

Fluid-Rock Characterization for NMR Well Logging and Special Core Analysis

2nd Annual Report

October 1, 2005 – September 30, 2006

George J. Hirasaki (gjh@rice.edu)

and

Kishore K. Mohanty (mohanty@uh.edu)

Issued: February 2007

DE-FC26-04NT15515

Project Officer:
Chandra Nautiyal, Tulsa

Contract Officer:
Thomas J. Gruber, Pittsburg

Rice University
6100 Main Street
Houston, TX 77005

University of Houston
4800 Calhoun Road
Houston, TX 77204-4004

DISCLAIMER* — The Disclaimer must follow the title page, and must contain the following paragraph:

"This report was prepared as an account of work sponsored by an agency of the United States Government. Neither the United States Government nor any agency thereof, nor any of their employees, makes any warranty, express or implied, or assumes any legal liability or responsibility for the accuracy, completeness, or usefulness of any information, apparatus, product, or process disclosed, or represents that its use would not infringe privately owned rights. Reference herein to any specific commercial product, process, or service by trade name, trademark, manufacturer, or otherwise does not necessarily constitute or imply its endorsement, recommendation, or favoring by the United States Government or any agency thereof. The views and opinions of authors expressed herein do not necessarily state or reflect those of the United States Government or any agency thereof."

ABSTRACT

Abstract for Project

NMR well logging provides a record of formation porosity, permeability, irreducible water saturation, oil saturation and viscosity. In the absence of formation material, the NMR logs are interpreted using default assumptions. Special core analysis on core samples of formation material provides a calibration between the log response and the desired rock and/or fluid property. The project proposes to develop interpretations for reservoirs that do not satisfy the usual assumptions inherent in the interpretation. Also, NMR will be used in special core analysis to investigate the mechanism of oil recovery by wettability alteration and the relative permeability of non-water-wet systems.

Some common assumptions and the reality of exceptional reservoirs are listed in the following and will be addressed in this project.

- (1) *Assumption:* in situ live crude oil and OBM have a relaxation time proportional to temperature/viscosity as correlated from stock tank oils. *Reality:* methane and ethane relax by a different mechanism than for dead oil and GOR is a parameter; carbon dioxide does not respond to proton NMR but influences oil and gas viscosity and relaxation rates.
- (2) *Assumption:* the in situ hydrocarbons have a relaxation time equal to that of the bulk fluid, i.e. there is no surface relaxation as if the formation is water-wet. *Reality:* Most oil reservoirs are naturally mixed-wet and drilling with oil-based mud (OBM) sometimes alters wettability. If the formation is not water-wet, surface relaxation of the hydrocarbon will result.
- (3) *Assumption:* OBM filtrate has the properties of the base oil. *Reality:* OBM filtrate often has some level of the oil-wetting additives and in some cases has paramagnetic particles. It may also have dissolved gas.
- (4) *Assumption:* the magnetic field gradient is equal to that of the logging tool. *Reality:* paramagnetic minerals may result in internal magnetic field gradient much greater than that of the logging tool.
- (5) *Assumption:* pores of different size relax independently. *Reality:* clay lined pores can have significant diffusional coupling between microporosity and macroporosity.

Abstract for 2nd-Annual Report

Progress is reported on Tasks: (1.1) Properties of live reservoir fluids, (2.1) Extend the diffusion editing technique and interpretation, (2.4) Interpretation of systems with diffusional coupling between pores, (2.5) Quantify the mechanisms responsible for the deviation of surface relaxivity from the mean value for sandstones and carbonates. and (3) Characterization of pore structure and wettability.

TABLE OF CONTENTS

| | |
|---|-----|
| DISCLAIMER..... | 2 |
| ABSTRACT..... | 3 |
| EXECUTIVE SUMMARY | 5 |
| Subtask 1.1 Properties of live reservoir fluids | 9 |
| Subtask 2.1 Extend the diffusion editing technique and interpretation..... | 23 |
| Subtask 2.4 Interpretation of systems with diffusional coupling between pores..... | 45 |
| Subtask 2.5 Quantify the mechanisms responsible for the deviation of surface relaxivity from the mean value for sandstones and carbonates. | 59 |
| Task 3: Characterization of pore structure and wettability. | 111 |
| NMR 1-D Profiling | 193 |

EXECUTIVE SUMMARY

NMR High Pressure Measurements for Natural Gas Mixtures

The work presented below shows the status of NMR high pressure measurements. So far, a manifold has been built for making NMR measurements at high pressures up to 5000 psi. Furthermore, a diffusion-editing pulse sequence has been tested at ambient pressure for appropriate criteria in choosing parameters for the NMR measurement. The tests were done with a crude oil and suggest that a parameter selection technique developed by Flaum (2006) is appropriate, with the parameters chosen such that they apply to the mode relaxation time and diffusivity (as opposed to the log-mean). This is likely applicable to high pressure NMR measurements of gas mixtures planned in the future. Finally, separate relaxation time and diffusivity measurements are shown for methane gas at elevated pressure for comparison with values from other investigators. Methane relaxation times that correspond to the expected trend from the literature have been obtained, but the reproducibility is suspect and is yet to be established. The diffusivity shows consistency; however the value is 20% less than the correlated value from Prammer, et al.(1995). Data is not available at 30 °C, the temperature in the present measurements, but a 20% deviation is within the bounds of the fit of the correlation to experimental data.

A Pulsed Field Gradient with Diffusion Editing (PFG-DE) NMR Technique for Emulsion Droplet Size Characterization

This paper describes a nuclear magnetic resonance (NMR) technique, pulsed field gradient with diffusion editing (PFG-DE), to quantify drop size distributions of brine/crude oil emulsions. The drop size distributions obtained from this technique were compared to results from the traditional pulsed field gradient (PFG) technique. The PFG-DE technique provides both transverse relaxation (T_2) and drop size distributions simultaneously. In addition, the PFG-DE technique does not assume a form of the drop size distribution. An algorithm for the selection of the optimal parameters to use in a PFG-DE measurement is described in this paper. The PFG-DE technique is shown to have the ability to resolve drop size distributions when the T_2 distribution of the emulsified brine overlaps either the crude oil or the bulk brine T_2 distribution. Finally, the PFG-DE technique is shown to have the ability to resolve a bimodal drop size distribution.

NMR Diffusional Coupling: Effects of Temperature and Clay Distribution

The interpretation of Nuclear Magnetic Resonance (NMR) measurements on fluid-saturated formations assumes that pores of each size relax independently of other pores. However, diffusional coupling between pores of different sizes may lead to false interpretation of measurements and thereby, a wrong estimation of formation properties. The objective of this study is to provide

a quantitative framework for the interpretation of the effects of temperature and clay distribution on NMR experiments. In a previous work, we established that the extent of coupling between a micropore and macropore can be quantified with the help of a coupling parameter (α) which is defined as the ratio of characteristic relaxation rate to the rate of diffusive mixing of magnetization between micro and macropore. The effect of temperature on pore coupling is evaluated by proposing a temperature dependent functional relationship of α . This relationship takes into account the temperature dependence of surface relaxivity and fluid diffusivity. The solution of inverse problem of determining α and microporosity fraction for systems with unknown properties is obtainable from experimentally measurable quantities.

Experimental NMR measurements on reservoir carbonate rocks and model grainstone systems consisting of microporous silica gels of various grain sizes are performed at different temperatures. As temperature is increased, the T_2 spectrum for water-saturated systems progressively changes from bimodal to unimodal distribution. This enhanced pore coupling is caused by a combined effect of increase in water diffusivity and decrease in surface-relaxivity with temperature. Extent of coupling at each temperature can be quantified by the values of α . The technique can prove useful in interpreting log data for high temperature reservoirs.

Effect of clay distribution on pore coupling is studied for model shaly sands made with fine silica sand and bentonite or kaolinite clays. The NMR response is measured for two cases in which clay is either present as a separate, discrete layer or homogeneously distributed with the sand. For layered systems, T_2 spectrum shows separate peaks for clay and sand at 100% water saturation and a sharp $T_{2,cutoff}$ could be effectively applied for estimation of irreducible saturation. However, for dispersed systems a unimodal T_2 spectrum is observed and application of 33ms $T_{2,cutoff}$ would underestimate the irreducible saturation in the case of kaolinite and overestimate in the case of bentonite. The inversion technique can still be applied to accurately estimate the irreducible saturation.

Paramagnetic Relaxation in Sandstones: Distinguishing T_1 and T_2 Dependence on Surface Relaxation, Internal Gradients and Dependence on Echo Spacing

Sandstones have T_1/T_2 ratio of 1.6, on the average. Clean silica has a T_1/T_2 ratio of about 1.3. If T_2 changes with echo spacing in a homogeneous applied magnetic field, the change is interpreted to be due to diffusion in internal gradients. We demonstrate that when the paramagnetic material is iron, the increase in the T_1/T_2 ratio above that of clean silica is due to diffusion in internal gradient. Furthermore, when the paramagnetic sites are small enough, no dependence on echo spacing is observed with conventional low-field NMR spectrometers. Echo spacing dependence is observed when the paramagnetic

materials become large enough or form a 'shell' around each silica grain such that the length scale of the region of induced magnetic gradients is large compared to the diffusion length during the time of the echo spacing.

The basis for these assertions is a series of experiments and calculations described below. A solution of hydrated Fe^{3+} ion has a T_1/T_2 ratio of unity. Aqueous dispersions of paramagnetic magnetite particles ranging from 4 nm to 110 nm have T_1/T_2 increasing with particle size. No echo spacing dependence is observed. Larger (25nm and 110 nm) magnetite particles coated on 50 μm silica grains have no echo spacing dependence for lower concentration of particles but show echo spacing dependence for larger concentrations. Largest (2,600 nm) magnetite particles mixed with fine sand have echo spacing dependence and T_1/T_2 greater than 2.

These experimental observations are being interpreted by theoretical calculations. The magnetite particles are modeled as paramagnetic spheres. Paramagnetic particles on the surface of silica grains are modeled as individual particles at low concentrations. At high surface concentrations, they are modeled as a thin, spherical shell of paramagnetic material. Calculations show that the system transitions from motionally averaging (no dependence on echo spacing) to localization regime (dependent on echo spacing) at high surface concentration of paramagnetic particles.

NMR Well Logging and Special Core Analysis for Fluid-Rock Characterization

Characterization of pore structure and wettability has been completed on six carbonate samples. The vug size, distribution and interconnection vary significantly in these six samples. The thin sections have been characterized through their pore size distribution, two-point correlation function, chord number distribution, lineal path function and fractal dimension. The power spectrum from Fourier transform has been computed. The three-dimensional pore structures have been reconstructed for two carbonates and one sandstone sample. Single phase permeability and NMR response has been measured for all the samples. The relative permeability, NMR response and electrical conductivity have been measured for three samples.

NMR 1-D Profiling

T_2 profiles can be generated by implementing the rapid acquisition with relaxation enhancement (RARE) pulse sequence. The RARE sequence is a multi-echo imaging sequence used to construct a one-dimensional profile of T_2 relaxation times. Experimental parameters, such as sample size, gradient strength and duration, and the number and spacing of the acquired data points, must be selected to ensure that useful information can be extracted from the profiles. The sample must be centered within the Maran's sweet spot. The gradient strength relates the precession frequency to sample position. Attenuation due to diffusion is dependent on the product of gradient strength (g)

and duration (d). Therefore, g and d should be selected in order to reduce the amount of the relaxation due to diffusion. The dwell time (DW), or spacing between acquired data points, needs to be selected so that the sample plus a small region above and below is resolved by the experiment. The number of data points collected per echo will influence the image resolution; as more points are collected per echo, the resolution will increase. Experiments were performed on both a water sample and a layered water-squalane (C-30 oil, $\mu = 22$ cP) system using the RARE sequence. T_2 was calculated by fitting the decaying profiles to a single exponential model. The difference between the T_2 profiles acquired via RARE and the T_2 of the bulk samples found using CPMG is due to diffusion and thus needs to be minimized.

Task 1. Properties of reservoir fluids
Subtask 1.1 Properties of live reservoir fluids

NMR High Pressure Measurements for Natural Gas Mixtures

Arjun Kurup and George Hirasaki

Abstract

The work presented below shows the status of NMR high pressure measurements. So far, a manifold has been built for making NMR measurements at high pressures up to 5000 psi. Separate relaxation time and diffusivity measurements are shown for methane gas at elevated pressure for comparison with values from other investigators. Methane relaxation times approaching the expected trend from the literature have been obtained. However the relaxation times obtained are consistently smaller than reported values. The measured diffusivity is consistent within the measurements in this work; however the value is 20% less than the correlated value from Prammer, *et al.* (1995). The diffusivity data do not appear to match the correlation within the scatter of the data. The reason for this is unknown.

Introduction

This report discusses steps in preparation for making NMR measurements of high pressure gas mixtures. The anticipated samples are mixtures of methane, ethane, propane, nitrogen, and carbon dioxide, components that are often present in significant quantities in natural gas reservoirs (McCain 1990). The present document recounts measurements of relaxation times (T_1 and T_2) and diffusivity of methane gas, to validate the high pressure apparatus by confirmation with values available in the literature.

The measurements mentioned here are motivated by downhole NMR logging measurements. NMR well-logging of gas reservoirs provides NMR response (some combination of relaxation times, T_1 and T_2 , and diffusivity) as a function of depth in the reservoir. The NMR response must then be correlated to state properties like density and temperature. NMR properties of methane have been studied, both in the laboratory setting (Gerritsma *et al.* 1971, Lo 1999, Dawson 1966, Oosting and Trappeniers 1971, Harris 1978), and in natural gas reservoirs (Prammer *et al.* 1995, Akkurt *et al.* 1996). For the purposes of reservoir evaluation, it has been previously assumed that the presence of non-methane components can be accounted for simply by the gas density (Akkurt *et al.* 1996). However as Fig. 1 shows, different gases show different NMR behavior (T_1 relaxation time in Fig. 1) for the same normalized density (Zhang 2002). Thus, non-methane components of natural gas require distinct treatment.

Based on theory that postulates NMR relaxation results from binary collisions between molecules (Bloom *et al.*, 1967; Gordon, 1966), Zhang (2002) presented a model for relaxation of gas mixtures based on the relaxation behavior of each gas in the mixture. The resulting expression is

$$T_{1,i} = \sum_{j=1}^n \rho_j \frac{\hbar^2 N_A}{4\pi^2 I_{\perp i} C_{\text{eff},i}^2} \sqrt{\frac{2}{\pi k}} \frac{\sigma_{i-j}}{\sqrt{T \mu_{i-j}}} . \quad (1)$$

In this equation, $T_{1,i}$ is the T_1 relaxation time of the i^{th} component in the mixture, ρ_j is the partial molar density of the j -th component of the mixture, \hbar is Planck's constant divided by 2π , N_A is Avogadro's number, k is Boltzmann's constant, T is the temperature, I_{\perp} is the moment of inertia in the direction perpendicular to the axis of the molecule, and C_{eff} is a quantity describing coupling between nuclear and molecular angular momentum. The other quantities in Eq. 1 are defined by one of the following equations (Zhang 2002),

$$\mu_{i-j} = \frac{1}{m_i} + \frac{1}{m_j} \quad (2.a)$$

and

$$\sigma_{i-j} = \frac{300}{T} \sqrt{\sigma_{j-j}(300K) * \sigma_{i-i}(300K)} . \quad (2.b)$$

In Eq. 2.a, m_i and m_j are the atomic masses of the two colliding molecules. In Eq. 2.b, σ refers to the collision cross-section for angular momentum transfer.

In practice, Eq. 1 can be simplified to (Zhang 2002)

$$T_{1,i} = \sum_{j=1}^n \rho_j \frac{G_{ij}}{T^{1.5}} \quad (3)$$

where G_{ij} is a binary interaction term that collects the constants in Eq. 1. Eq. 3 does, however keep the temperature dependence explicit, incorporating the temperature dependence of σ , the binary collision parameter, from Eq. 2.b.

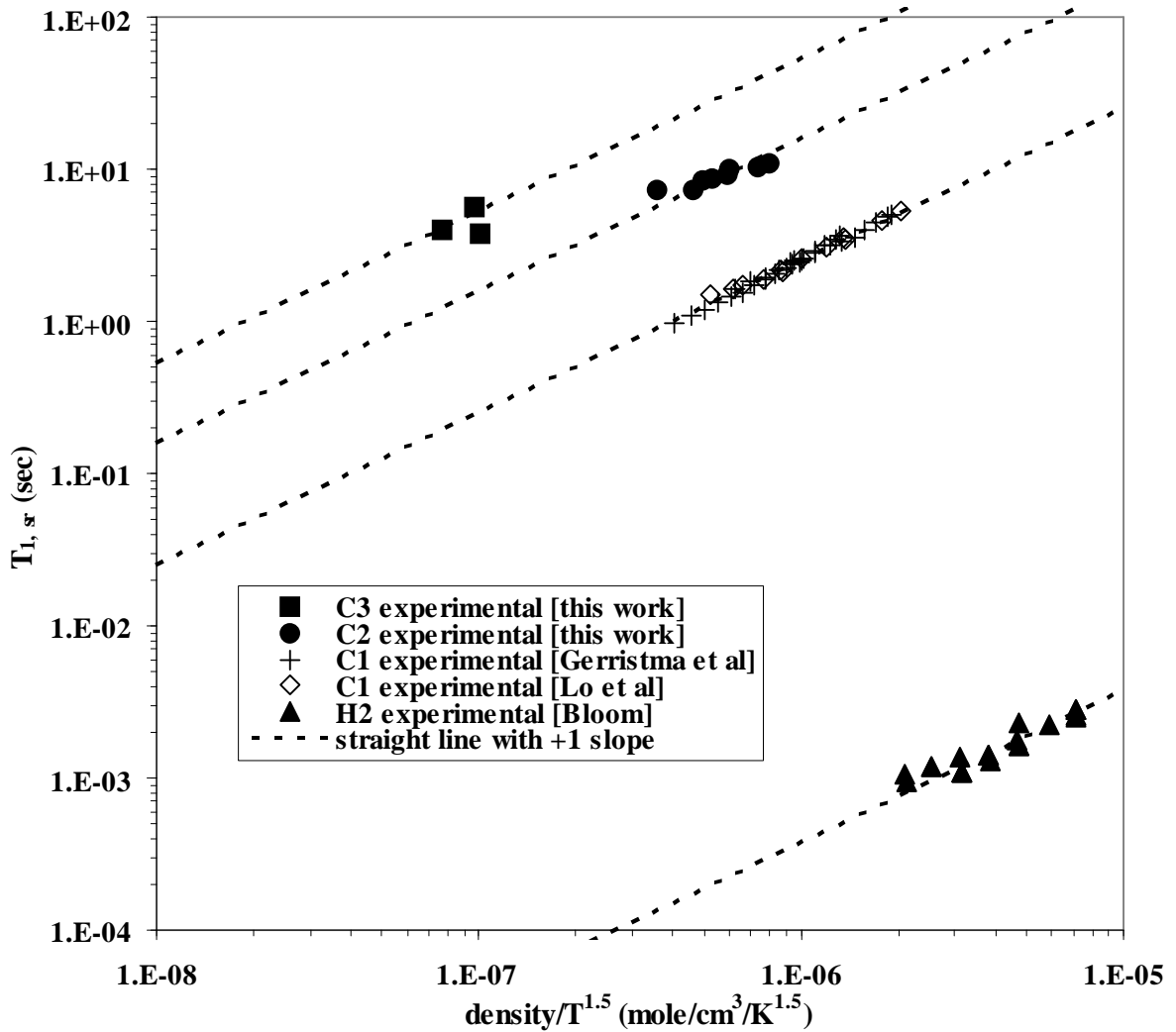


Figure 1: Relaxation behavior of various pure gases as a function of density and temperature. Reproduced from Zhang 2002.

The model in Eq. 1 was then verified by comparison with data by Rajan, *et al.* (1975) for up to approximately 5 atmospheres of pressure for two methane mixtures, one with carbon dioxide and one with nitrogen (Zhang 2002). The aim of the present work is to obtain experimental data for more generalized gas mixtures containing other natural gas components and to make measurements at more elevated pressures.

The expression in Eq. 3 was used to calculate the relaxation behavior of a few specified natural gas mixtures of methane and ethane using the binary interaction terms G_{ij} reported in Zhang (2002). Fig. 2 shows the expected relaxation response of three methane-ethane mixtures, compared to the behavior

correlated for the individual gases. Fig. 3 shows the calculated response for a methane-ethane-propane mixture.

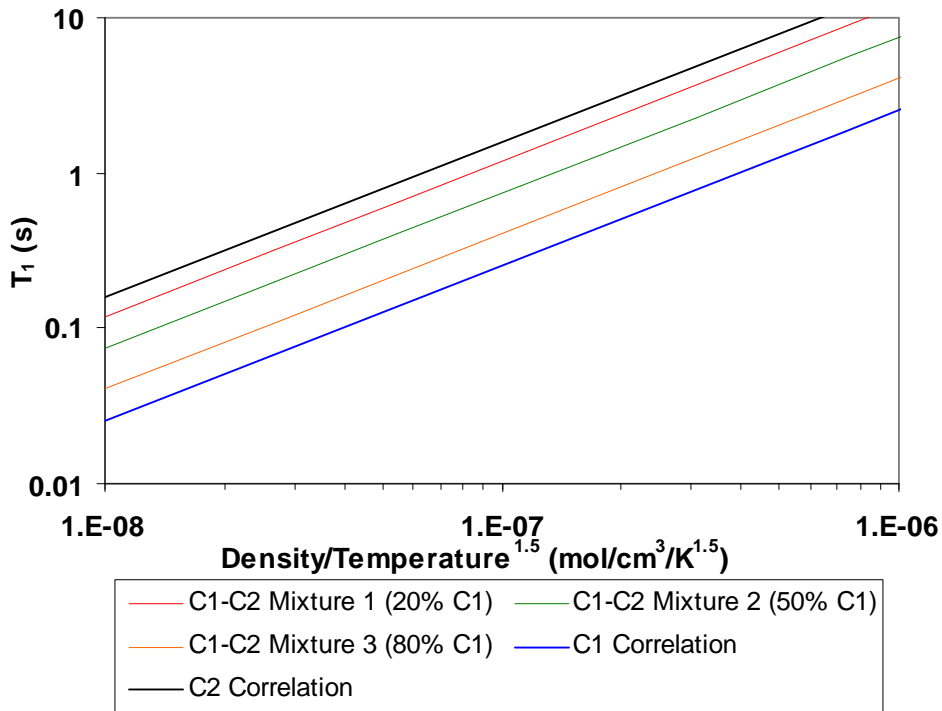


Figure 2: Calculated relaxation behavior of methane(C1)-ethane(C2) mixtures with relation to correlations for methane and ethane

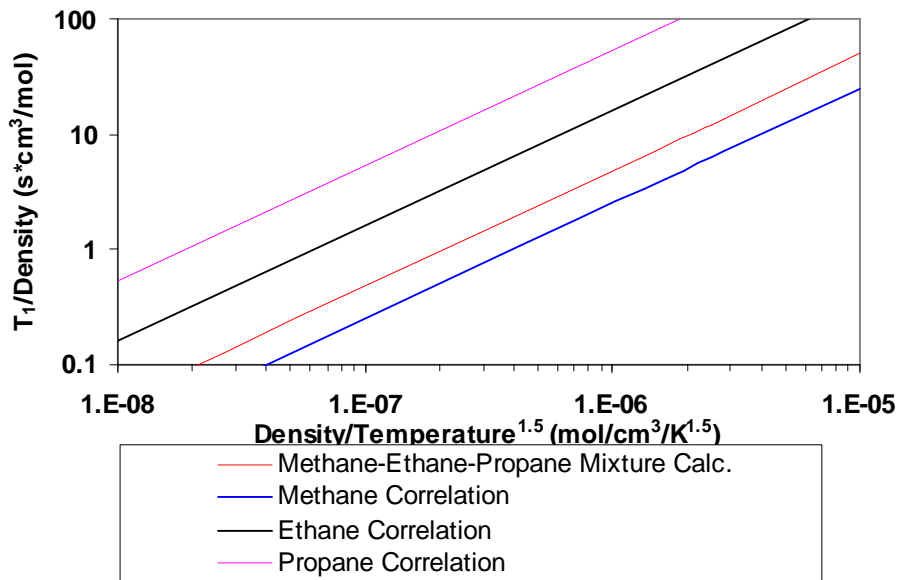


Figure 3: Calculated relaxation behavior of methane-ethane-propane mixture (80% methane, 13.5% ethane, 6.5% propane) in possession with relation to correlations for methane, ethane, and propane

Equipment and Capabilities

The NMR spectrometer used for the work mentioned here is a 2 MHz bench-top MARAN apparatus. It is equipped with one-dimensional gradient coils, which provides a linear spatial magnetic field gradient for use in diffusion evaluations. The pulse sequences used are standard sequences: inversion recovery for measuring T_1 , CPMG for measuring T_2 , and a pulsed-field gradient (PFG) stimulated-echo sequence for measuring diffusivity.

For high pressure measurements with gases, a manifold was built from stainless steel fittings, manufactured by Swagelok. A schematic of the manifold and its ports, which form the NMR high pressure system, is shown in Fig. 4. A few statements regarding the features of the NMR high pressure system follow. First, gas cylinders with appropriate gas or gas mixture are connected to the inlet side of the apparatus. The inlet line is equipped with an oxygen scavenger (Matheson model 6411) to remove traces of oxygen from the contents of the gas cylinder. Oxygen is a paramagnetic contaminant and could detrimentally affect measured NMR relaxation times if not removed. The oxygen scavenger is rated for a maximum pressure differential of 90 psi between inlet and outlet. Second, the manifold is equipped with a vacuum line. This is used to evacuate the system prior to injection of gases at elevated pressure. The line is connected to a mechanical vacuum pump, with a trap, cooled by dry ice (freezing point of $-78.5\text{ }^{\circ}\text{C}$) in isopropanol. Furthermore, to prevent accidental exposure of the vacuum line to high pressure, the vacuum line is double-valved. The third feature is the two lines to two hand pressure generation pumps (hand pumps), models 87-6-5 and 62-6-10 manufactured by High Pressure Equipment Company. These hand pumps can be used to increase the system pressure beyond tank pressure by compressing the system volume. The fourth feature of the high pressure NMR system is the pressure gauges that allow monitoring of pressure during NMR measurements. One gauge is a pressure transducer manufactured by Sensometrics, Inc. coupled to the manifold using an adapter and connected to a digital readout meter. Both the adapter and meter (model DP41-S) are made by Omega. The entire system also outlets to a vent to safely remove gases after measurements are complete. Another safety feature is the relief lines in the system. A check valve in the relief line for the vacuum portion protects the vacuum side from overpressurization; the check valve opens to the vent line should any positive pressure occur in the vacuum line. The relief line of the high-pressure portion of the manifold also discharges into the vent. However in this case, relief is provided by a diaphragm-type blowout valve manufactured by Autoclave Engineers, where the diaphragm is designed to yield at pressures greater than 5000 psi. The final component of the system is the NMR pressure vessel, manufactured by Temco, Inc. It will be described in the following paragraph. A photograph of the NMR high pressure system is shown in Fig. 5. The system is rated to 5000 psi pressure, except the vacuum line (designed for running at subatmospheric pressure) and the inlet line, where the gas cylinder is

rated to at least the initial cylinder pressure and the oxygen scavenger is rated to 3000 psi.

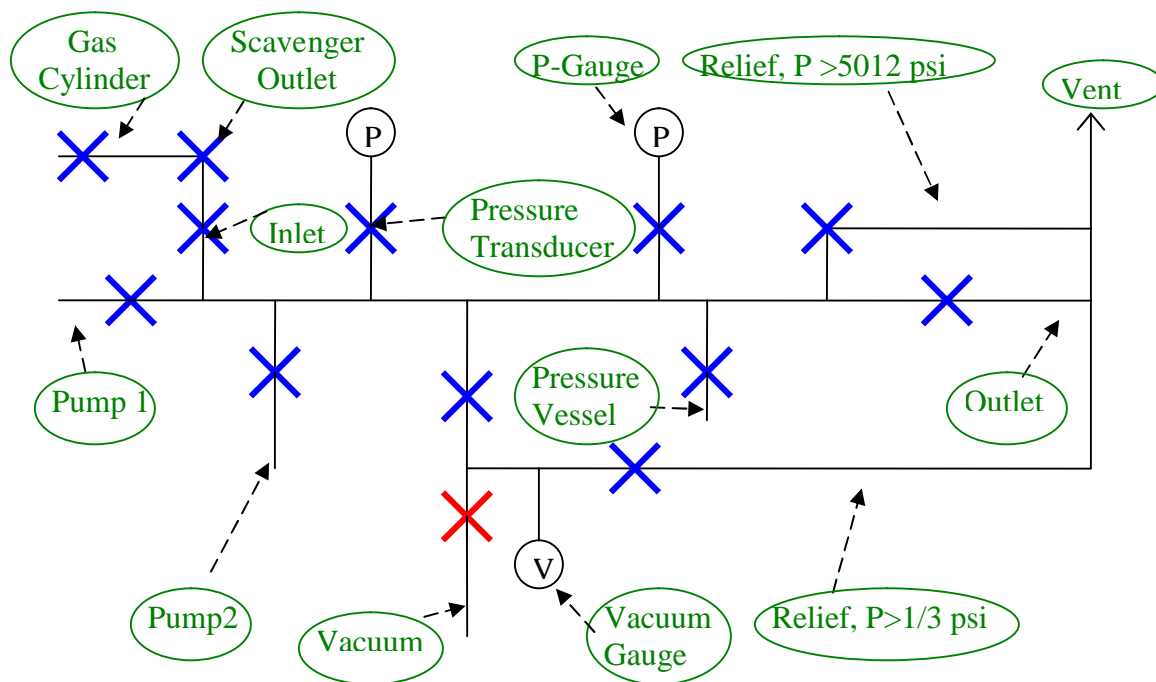


Figure 4: Schematic of manifold and attachments for preparing gases for NMR analysis

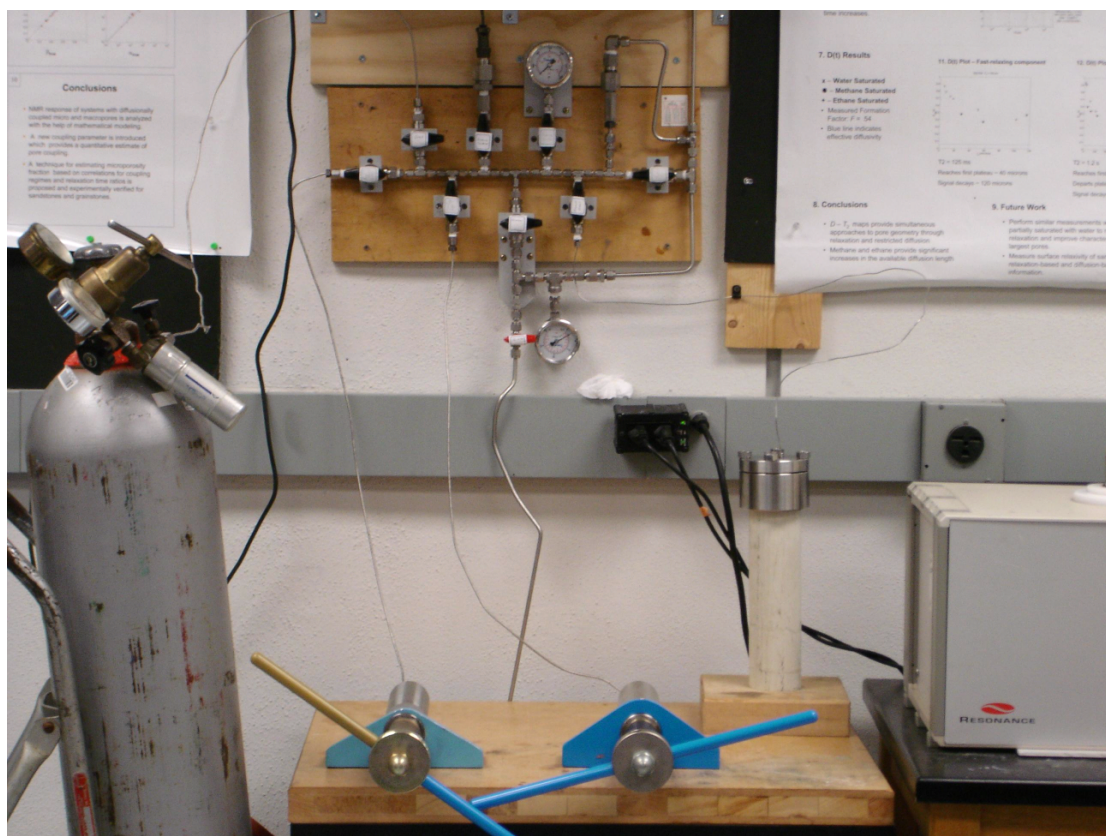


Figure 5: Photograph of high pressure NMR system, including gas cylinder, hand pumps, and NMR pressure vessel.

The NMR pressure vessel is the component of the high pressure NMR system that is placed in the MARAN 2 MHz instrument to make NMR measurements. A diagram of the design of the NMR pressure vessel is shown in Fig. 6. As shown, the pressure vessel has three layers. The outermost layer is the pressure-bearing surface, made of fiberglass in an epoxy matrix. The middle layer seals the system and connects it to the manifold. The top of this portion of the NMR pressure vessel is a stainless steel flange. The flange has ports at the top which connect to a line from the manifold and o-rings that contact the inside of the PEEK liner. The PEEK liner is the body of the NMR pressure vessel, as the inner layer is contained inside it. The middle layer is sealed at the bottom with a stainless steel end piece capped with an o-ring. The inner layer consists of two PEEK cylinders, one that allows gas to pass along a small orifice along its axis and the other serving as a sample chamber (which is aligned in the magnetic field of the MARAN 2 MHz instrument) with a hollow region of approximately 12.9 ml where the measured gas resides. The NMR pressure vessel, like the manifold is rated to 5000 psi.

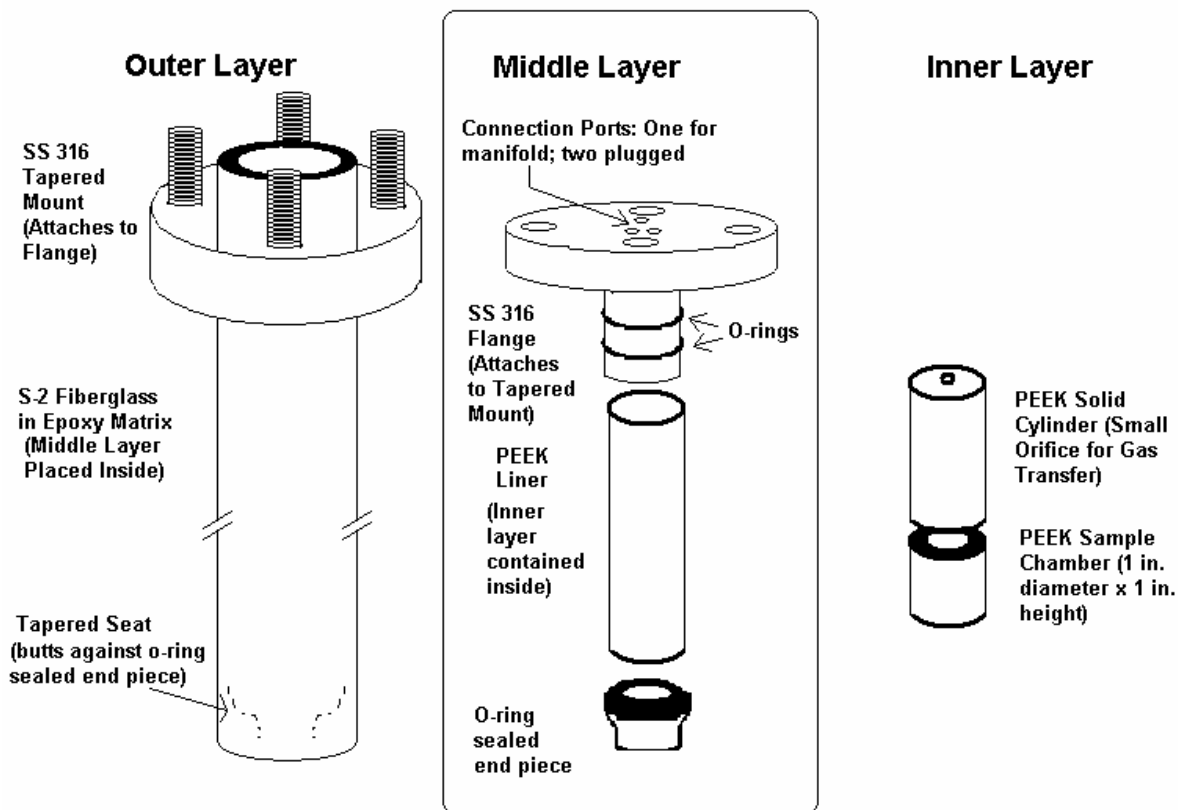


Figure 6: Drawing of Temco ® NMR pressure vessel

Prior to use, the manifold and pressure vessel were tested under pressure. First, the NMR high pressure system was tested with water in the system. Pressures up to 5000 psig were achieved. The high-pressure relief line was found to

operate correctly during this test because the diaphragm failed (as designed) at slightly beyond 5000 psig. The manifold, without the NMR pressure vessel, was found to maintain pressure when tested under pressure at 4500 psig. However, when the NMR pressure vessel is incorporated, a leak of approximately 10 psi/hr is presently being observed at pressures near 2000 psia. Several attempts to stop the leak have proven unsuccessful. Nonetheless, the magnitude of the leak was deemed to be acceptable for measurements to proceed. This assessment can be made by calculating the effect of variations in pressure (due to the leak) on NMR measurements. When this calculation was made, the difference in NMR measurements (of relaxation times or diffusivity) was found to be 2% or less for the majority of the pressure variations observed so far. (This determination was made using Eqs. 4 and 5, shown in the following section.) Thus, the effect of the leak is deemed to be acceptable for NMR measurements.

Elevated Pressure NMR Measurements with Methane

Using the high pressure NMR apparatus shown in Figs. 4-6, NMR measurements are currently in progress with methane gas. NMR T_1 , T_2 , and diffusion measurements have been performed. Data for methane are available in the literature, and the purpose of the present methane measurements is validation of the apparatus described in the previous section. Relaxation time measurements thus far have fallen within approximately 10% of the expected value, but show a bias toward short relaxation times. It appears that oxygen (paramagnetic contaminant) is still present in the methane sample for the cases considered. Diffusion measurements provide a methane diffusivity that is approximately 20% below the expected correlation, the reason for which is yet to be determined.

Before taking the data obtained into consideration, the default procedures used to prepare the high pressure NMR apparatus for making a gas measurements follow:

1. Evacuation of system to remove air, especially to reduce oxygen content. (This step is disregarded in cases where an experiment begins at an elevated pressure obtained in a previous measurement.)
2. Pressurization to small elevated pressure (typically approximately 500 psi) and purging this pressure to slightly above atmospheric pressure (typically approximately 20-50 psig). This step is repeated for a desired number of rounds (typically 3-5 rounds)
3. Pressurization of system to up to gas cylinder pressure, controlling the gas cylinder regulator pressure.
4. Final pressurization using the hand pressure generation pumps

Note that steps 2 and 3 must be performed carefully to allow any oxygen in the methane sample enough time to contact the oxygen scavenger. Once the steps above are taken, the sample is ready for NMR measurements.

In relaxation time (T_1 and T_2) measurements, the response of NMR signal amplitude is measured as a function of time. The resultant data is said to be in the time domain. The acquired data is then inverted, converting the time-domain data to the relaxation time (T_1 or T_2) domain. For T_2 , the large number of time-domain data points is parsed before the conversion to the T_2 -domain is performed. The parsing process, called “sampling and averaging”, reduces the computational load in the conversion with minimal sacrifice to data quality (Chuah 1996). Due to fewer data points in T_1 measurements, no parsing process is necessary.

The time domain data obtained thus far show an anomaly illustrated in Fig. 7. At early times in CPMG measurements, a sharp dip occurs in the observed T_2 response. This phenomenon is also present in the T_1 response, but is not readily visible in the corresponding time-domain data. Therefore in analyzing the relaxation times for methane, the early time data was truncated. The analysis was done either in the time domain or relaxation domain. In the time domain, the early-time data corresponding to the observed anomaly was removed before fitting the data to a straight line in semilog scale. In the relaxation domain, all the data is first inverted. Then the logarithmic mean of the peak observed for large relaxation times is retained, removing contributions from artifacts at shorter relaxation times. Since both resulting relaxation times, in both time and relaxation time domains, using only longer-time data, they are demarcated with a suffix, “long”.

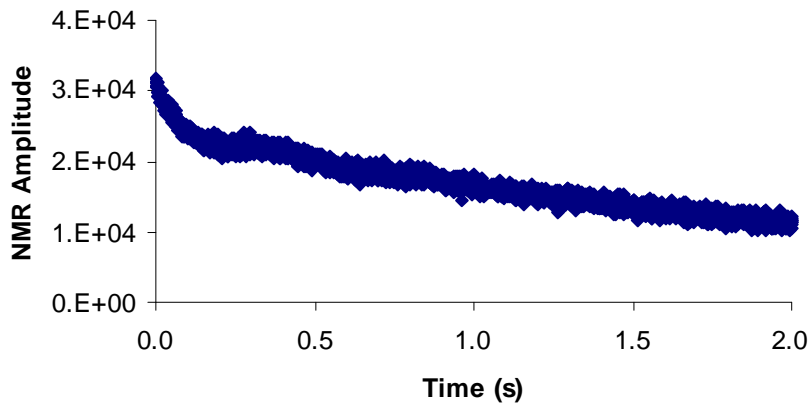


Figure 7: Typical T_2 measurement for methane at elevated pressures, illustrates faster decay at early times

The results are shown in Figs. 8-9 (for T_1) and Figs. 10-11 (for T_2). Figs. 8 and 10 show results analyzed in the time domain, whereas Figs. 9 and 11 are for the relaxation time domain. Figs. 8-11 show two correlations for T_1 (Lo 1999, Prammer, et al. 1995, respectively), which should be valid for T_2 as well:

$$T_1 (s) = 1.57 \times 10^5 \frac{\rho}{T^{1.5}} \quad (4)$$

$$T_1 (s) = 2.5 \times 10^4 \frac{\rho}{T^{1.17}} \quad (5)$$

In these equations, ρ is the density (g/cm^3) and T is the temperature in Kelvin.

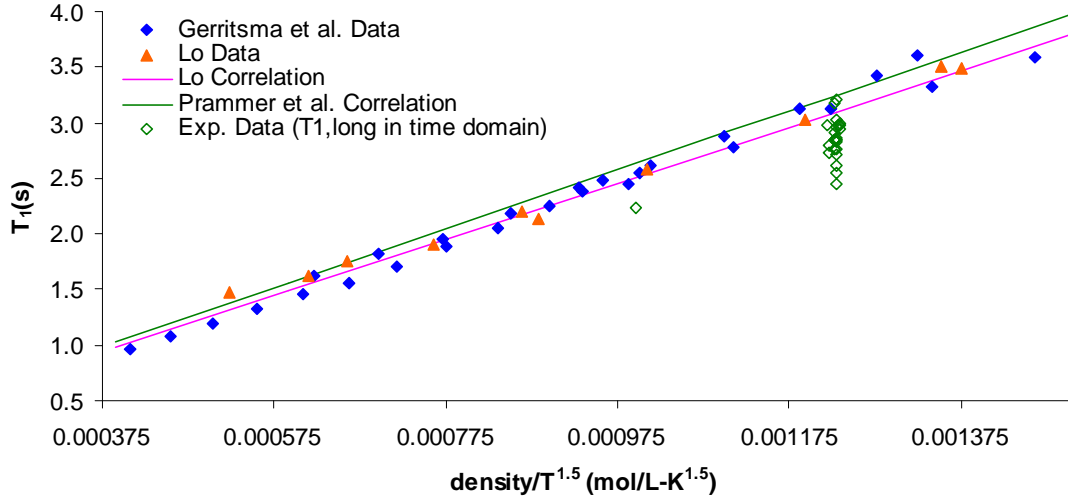


Figure 8: NMR T_1 measurements (time domain) compared with literature data and correlations

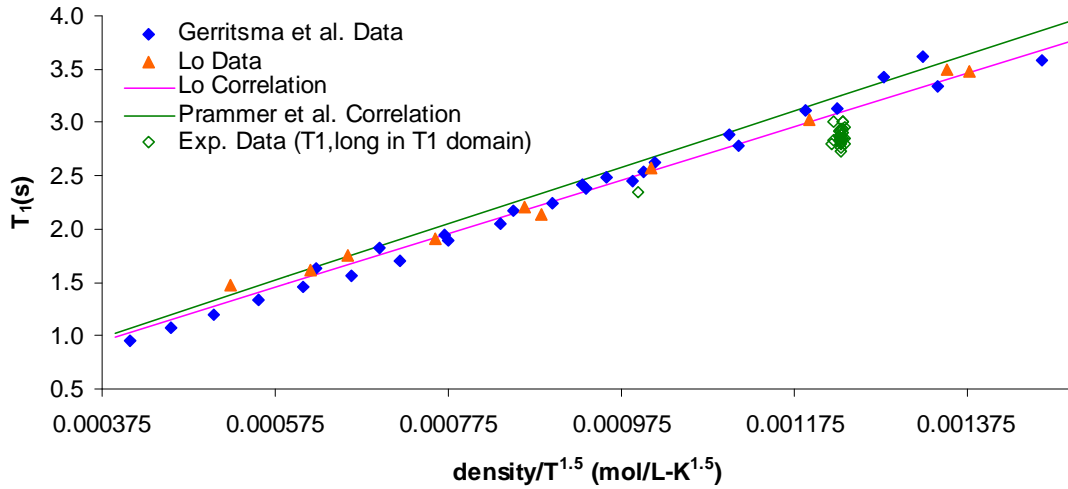


Figure 9: NMR T_1 measurements (T_1 domain) compared with literature data and correlations

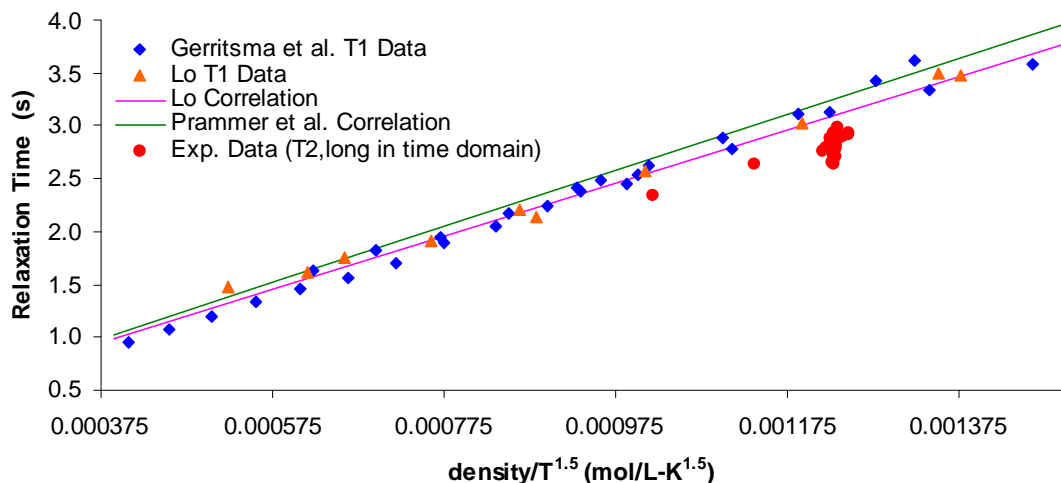


Figure 10: NMR T_2 measurements (time domain) compared with literature data and correlations

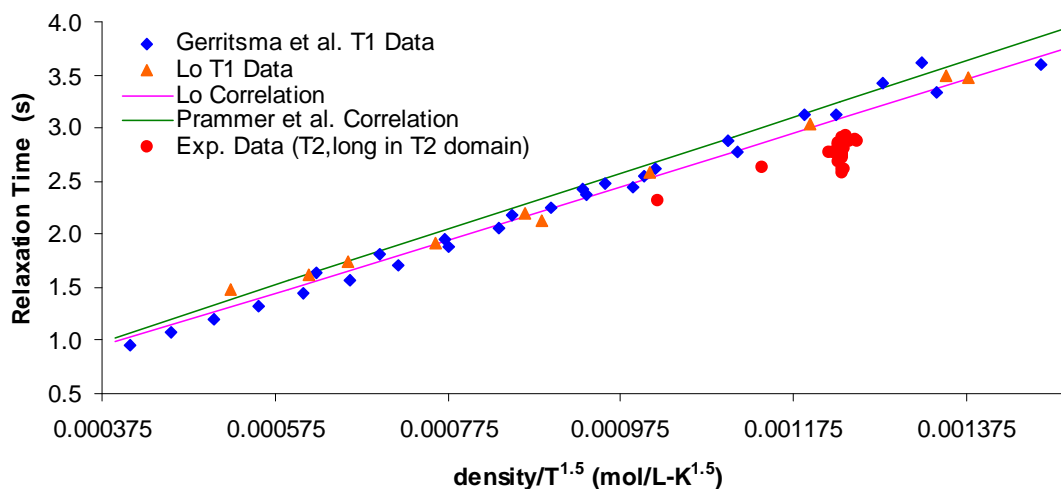


Figure 11: NMR T_2 measurements (T_2 domain) compared with literature data and correlations

The relaxation times in Figs. 8-11 are near expected values, but are consistently below the correlation lines. This may be because of remaining oxygen contamination. This is especially likely because Figs. 8-11 include two cases where the oxygen scavenger was not used in the procedures. Since no distinguishable difference was noted in relaxation times with or without the oxygen scavenger, this suggests that traces of oxygen in the methane cylinder are not removed. Furthermore, although the pressure differential across the oxygen scavenger can be as high as 90 psi according to manufacturer specifications, pressure differentials as low as 20 psi were used without yielding a significantly closer match to the existing correlations. These observations suggest that the oxygen scavenger is not operating correctly even though it remained sealed until the start of methane measurements mentioned above.

Despite these remaining issues, the data also demonstrate an expected result, namely the equality of T_1 and T_2 . This was assessed by taking the difference ($T_1 - T_2$) for several cases where T_1 and T_2 measurements were done in tandem. Often multiple T_2 measurements are done for one T_1 measurement. In such cases, the difference ($T_1 - T_2$) is calculated for each of the values of T_2 . The results are shown in Table 1 for 28 such differences ($T_1 - T_2$). Table 1 shows the mean and standard deviation for these cases. Note that zero relaxation time difference ($T_1 - T_2$) falls with the standard deviation from the mean value. Hence, T_1 and T_2 can be said to be equal because their difference ($T_1 - T_2$) is not statistically distinguishable from zero.

Table 1: Relaxation time difference for time and relaxation time domain

| Case | Relaxation Time Difference ($T_1 - T_2$) (s) |
|------------------------|--|
| Time Domain | -0.06±0.22 |
| Relaxation Time Domain | 0.08±0.13 |

In addition to the relaxation time measurements, NMR diffusion measurements were also made using a standard pulsed-field gradient (PFG) stimulated echo sequence. The data are shown in Table 2. The relevant parameters are also shown. Eq. 6 (Prammer, *et al.*, 1995),

$$D \text{ (cm}^2/\text{s)} = 8.5 * 10^{-7} \frac{T^{0.9}}{\rho}, \quad (6)$$

shows a correlation for diffusivity of methane, where ρ is the density (g/cm^3) and T is the temperature in Kelvin. Using Eq. 6, the correlated value of diffusivity for the conditions in Table 3 is $1.40 \times 10^{-7} \text{ m}^2/\text{s}$, which is 20% higher than the values in Table 2.

Table 2: Summary of diffusivity measurements on methane

| P (psig) | δ (ms) | Δ (ms) | Gradient List (G/cm) | D (m^2/s) |
|----------|---------------|---------------|----------------------|-----------------------------|
| 1980 | 3.65 | 15 | 0, 0.8 to 5 G/cm | 1.15×10^{-7} |
| 1980 | 3.65 | 15 | 0, 0.8 to 5 G/cm | 1.13×10^{-7} |
| 1981 | 3.65 | 15 | 0, 0.8 to 5 G/cm | 1.17×10^{-7} |
| 1982 | 3.65 | 15 | 0, 0.8 to 5 G/cm | 1.11×10^{-7} |
| 1985 | 3.65 | 15 | 0, 0.8 to 5 G/cm | 1.10×10^{-7} |
| 1980 | 3.40 | 17 | 0, 0.8 to 5 G/cm | 1.11×10^{-7} |

The data in Table 2 is plotted against available data in the literature in Fig. 12. The diffusivity data for methane obtained here appears to be below the correlation line by a greater degree than data from other investigators. The reason for this is yet unknown since the presence of oxygen is not expected to affect the measured diffusivity. Furthermore, restricted diffusion (which would result in a lower diffusivity than expected) is not expected to be significant given the size of the NMR sample chamber.

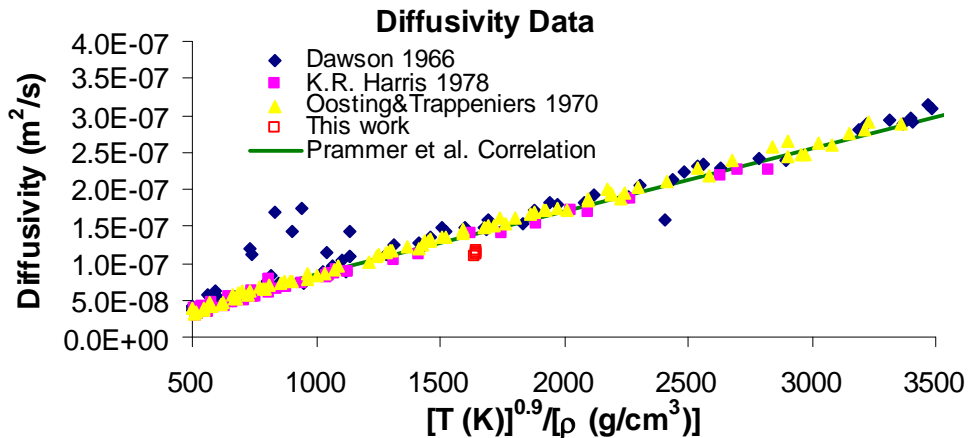


Figure 12: NMR diffusivity measurements compared with literature data and correlation

Conclusions and Future Directions

So far, an NMR high pressure apparatus has been built. Validation measurements on methane gas are in progress. Generally, relaxation and diffusion measurements yield data that approach, but do not match, existing methane correlations. It appears that the oxygen scavenger in use does not adequately remove oxygen from the methane cylinder, which could explain the anomalies in the relaxation time data. Therefore, a new oxygen scavenger is in the process of being acquired. For diffusion measurements, some other factors appear to be at work. When these issues are resolved, measurements can begin on four elevated-pressure gas mixtures available in the laboratory. Three of these mixtures consist of methane and ethane at different compositions, whereas the fourth also includes propane.

References:

Akkurt, R., Vinegar, H.J., Tutunjian, P.N., and Guillory, A.J. "NMR Logging of Natural Gas Reservoirs". *The Log Analyst*. **November-December**. 33 (1996).

- Bloom, M., Bridges, F., and Hardy, W. N. "Nuclear Spin Relaxation in Gaseous Methane and Its Deuterated Modifications": *Canadian Journal of Physics*. **45**, 3533 (1967).
- Chuah, T. L., *Estimation of Relaxation Time Distribution for NMR CPMG Measurements*. M.S.Thesis, Rice University, Houston, Texas (1996).
- Dawson, R. *Self-Diffusion in Methane*. Ph.D. Thesis, Rice University, Houston (1966).
- Gerritsma, C.J., Oosting, P.H., and Trappeniers, N.J. "Proton-Spin-Lattice Relaxation and Self-Diffusion in Methanes II: Experimental Results for Proton-Spin-Lattice Relaxation Times." *Physica*. **51**. 381 (1971).
- Gordon, R.G. "Nuclear Spin Relaxation in Gases". *Journal of Chemical Physics*. **44**. 228 (1966).
- Harris, K.R. "The Density Dependence of the Self-Diffusion Coefficient of Methane at -50°, 25°, and 50°C". *Physica*. **94A**. 448 (1978).
- Lo, S.-W. *Correlations of NMR Relaxation Time with Viscosity/Temperature, Diffusion Coefficient and Gas/Oil Ratio of Methane-Hydrocarbon Mixtures* Ph.D. Thesis, Rice University, Houston (1999).
- McCain Jr., William D. *The Properties of Petroleum Fluids*. (2nd Ed.) PennWell Books. Tulsa (1990).
- Oosting, P.H. and Trappeniers, N.J. "Proton-Spin-Lattice Relaxation and Self-Diffusion in Methanes: IV Self-Diffusion in Methane" *Physica*. **51**. 418 (1971)
- Prammer, M.G., Mardon, D., Coates, G.R., and Miller, M.N. "Lithology-Independent Gas Detection by Gradient-NMR Logging". Paper 30562, presented at the SPE ATCE. Dallas (1995)
- Rajan, S., Lalita, K., and Babu, S. "Intermolecular Potentials from NMR Data. I: CH₄-N₂ and CH₄-CO₂". *Canadian Journal of Physics*. **53**. 1624 (1975).
- Zhang, Y. *NMR Relaxation and Diffusion Characterization of Hydrocarbon Gases and Liquids*. Ph.D. Thesis, Rice University, Houston (2002).

Task 2. Estimation of fluid and rock properties and their interactions from NMR relaxation and diffusion measurements

Subtask 2.1 Extend the diffusion editing technique and interpretation...

A Pulsed Field Gradient with Diffusion Editing (PFG-DE) NMR Technique for Emulsion Droplet Size Characterization

Clint P. Aichele, Mark Flaum, Tianmin Jiang, George J. Hirasaki, and Walter G. Chapman

Abstract

This paper describes a nuclear magnetic resonance (NMR) technique, pulsed field gradient with diffusion editing (PFG-DE), to quantify drop size distributions of brine/crude oil emulsions. The drop size distributions obtained from this technique were compared to results from the traditional pulsed field gradient (PFG) technique. The PFG-DE technique provides both transverse relaxation (T_2) and drop size distributions simultaneously. In addition, the PFG-DE technique does not assume a form of the drop size distribution. An algorithm for the selection of the optimal parameters to use in a PFG-DE measurement is described in this paper. The PFG-DE technique is shown to have the ability to resolve drop size distributions when the T_2 distribution of the emulsified brine overlaps either the crude oil or the bulk brine T_2 distribution. Finally, the PFG-DE technique is shown to have the ability to resolve a bimodal drop size distribution.

1. Introduction

Emulsions are dispersions of one liquid in another, immiscible liquid. Emulsions have widespread applications in the petroleum industry, especially during crude oil production. Specifically, the drop size distributions of brine/crude oil emulsions are used to understand and quantify emulsion formation and stability mechanisms. Drop size distributions are also useful for quantifying properties of emulsions such as viscosity and stability [1]. This paper addresses techniques used to measure drop size distributions of brine/crude oil emulsions using nuclear magnetic resonance (NMR).

Historically, researchers have attempted to measure drop size distributions of emulsions using techniques including microscopy, light scattering, Coulter counting, and nuclear magnetic resonance [1-4]. For brine/crude oil emulsions, nuclear magnetic resonance is a superior technique because it is not destructive to the emulsion, it considers the entire sample, and it is not restricted by the fact that brine/crude oil emulsions do not transmit an appreciable amount of light. Traditionally, NMR has been used to measure drop size distributions of emulsions according to the technique developed by Packer and Rees [5]. The Packer-Rees technique incorporates the idea of restricted diffusion established by Neuman [6] and refined by Murday and Cotts [7] for diffusion in spheres.

The method presented by Packer and Rees relies on the assumption that the drops in emulsions are distributed in size according to the lognormal

distribution. This restriction often results in the loss of valuable information about the actual emulsion drop size distribution. Therefore, techniques have been developed and discussed in the literature that are designed to yield more general information about drop size distributions of emulsions, independent of the assumption that the drops are lognormally distributed [8].

This paper presents a new technique that provides both the T_2 and drop size distributions of brine/crude oil emulsions simultaneously. This paper also presents an algorithm that can be used to calculate parameters for both PFG-DE and PFG experiments for a variety of emulsion conditions. The PFG-DE technique involves a two dimensional inversion with regularization much like that used for obtaining diffusivity and transverse relaxation information [9, 10]. The drop size distributions obtained from the PFG-DE technique are compared to drop size distributions obtained from the stimulated echo pulsed field gradient (PFG) technique [11]. In this paper, the PFG-DE technique is shown to be useful for obtaining drop size distributions when the T_2 distribution of the emulsified brine overlaps either the bulk brine or crude oil T_2 distribution. Finally, the utility of the PFG-DE technique is particularly observed when the drop size distribution of the emulsion is more complicated, such as when the distribution is bimodal.

2. Experimental Methods

The NMR measurements discussed in this paper were performed on a 2 MHz Maran Ultra spectrometer at 30°C. The following sections contain the pulse sequences and experimental methods that were used in this work.

2.1 Carr-Purcell-Meiboom-Gill (CPMG)

The Carr-Purcell-Meiboom-Gill (CPMG) pulse sequence can be used to obtain transverse relaxation information about an emulsion sample [12, 13].

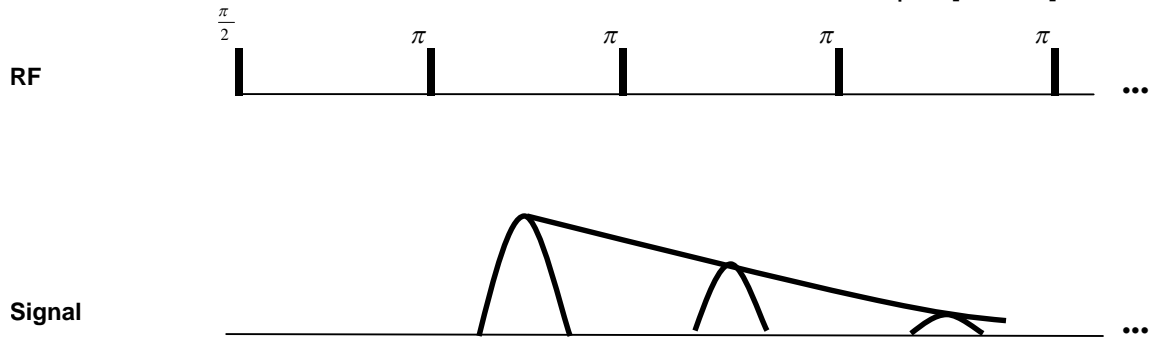


Figure 1: Carr-Purcell-Meiboom-Gill (CPMG) pulse sequence (adapted from Pena [1]).

After obtaining the T_2 distribution, the resulting drop size distribution can be determined according to Equation 1 [1].

$$d_i = 6 \rho \left(\frac{1}{T_{2,i}} - \frac{1}{T_{2,bulk}} \right)^{-1} \quad (1)$$

The surface relaxivity, ρ , is determined either by combining a CPMG and PFG measurement or by performing a PFG-DE measurement. The bulk transverse relaxation time of the fluid that is confined in the drops is given by $T_{2,bulk}$. The CPMG measurement is fast with duration usually equal to 10 minutes. Most importantly, the shape of the drop size distribution obtained from the CPMG technique is not assumed. For these reasons, Equation 1 is useful for determining drop size distributions of emulsions when the transverse relaxation distribution of the emulsified brine is separated from both the crude oil distribution and the bulk brine distribution.

2.2 Pulsed Field Gradient (PFG)

The pulsed field gradient (PFG) stimulated echo technique has been shown to facilitate the characterization of emulsion drop size distributions [1, 11].

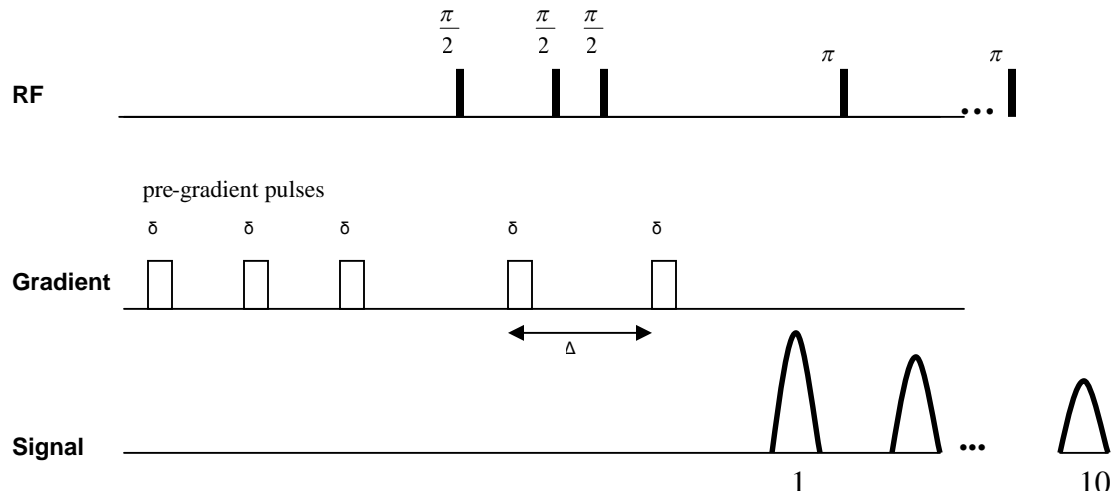


Figure 2: Pulsed field gradient (PFG) pulse sequence with stimulated echoes and pre-gradient pulses [11]. The amplitudes of the first 10 echoes are fit by linear regression to obtain the amplitude of the first echo.

Figure 2 shows the pulsed field gradient pulse sequence with stimulated echoes and pre-gradient pulses. Three to nine pre-gradient pulses should be used to make the final two gradient pulses identically shaped. In the work discussed in this paper, the gradient strength values were manipulated in each experiment to facilitate attenuation of the emulsion signal. The amplitude of the first echo was obtained by linearly fitting the amplitudes of the first ten echoes, thereby increasing the signal:noise ratio (SNR) of the measurement.

The attenuation decay in a PFG measurement is coupled with the model developed by Murday and Cotts [7] for diffusion in spheres to obtain the drop size distribution of the emulsion. The model for attenuation of the signal of fluid confined in spheres is given by Equations 2 – 4 [6, 7].

$$R_{sp} = \exp \left\{ -2 \gamma_g^2 g^2 \sum_{m=1}^{\infty} \frac{1}{\alpha_m^2 (\alpha_m^2 r^2 - 2)} \left[\frac{2 \delta}{\alpha_m^2 D_{DP}} - \frac{\Psi}{(\alpha_m^2 D_{DP})^2} \right] \right\} \quad (2)$$

$$\Psi = 2 + \exp(-\alpha_m^2 D_{DP} (\Delta - \delta)) - 2 \exp(-\alpha_m^2 D_{DP} \delta) - 2 \exp(-\alpha_m^2 D_{DP} \Delta) + \exp(-\alpha_m^2 D_{DP} (\Delta + \delta)) \quad (3)$$

The gyromagnetic ratio is given by γ_g , the gradient strength is g , D_{DP} is the diffusivity of the fluid in the dispersed phase, r is the radius of the emulsion droplet, Δ is the time between gradient pulses, δ is the gradient pulse duration, and α_m is the m^{th} positive root of Equation 4.

$$\frac{1}{\alpha r} J_{3/2}(\alpha r) = J_{5/2}(\alpha r) \quad (4)$$

J_k is the Bessel function of the first kind with order k . The overall attenuation of the emulsion has been shown to be a function of the attenuation of both the continuous and dispersed phases [8].

$$R_{emul} = (1 - \kappa) R_{DP} + \kappa R_{CP}; \quad 0 \leq \kappa \leq 1.0 \quad (5)$$

The fraction of the attenuation from the continuous phase is given by the parameter, κ .

$$\kappa = \left[1 + \frac{\sum (f_i)_{DP} \exp \left[\frac{-\Delta}{(T_{2,i})_{DP}} \right]}{\sum (f_i)_{CP} \exp \left[\frac{-\Delta}{(T_{2,i})_{CP}} \right]} \right]^{-1} \quad (6)$$

The attenuation of the continuous phase, R_{CP} , is expressed as the bulk attenuation of the continuous phase.

$$R_{CP} = \exp \left(-\gamma^2 g^2 D_{CP} \delta^2 \left(\Delta - \frac{\delta}{3} \right) \right) \quad (7)$$

The attenuation of the dispersed phase, R_{DP} , is given by Equation 8 [5].

$$R_{DP} = \frac{\int_0^{\infty} p(r) R_{sp(r)} dr}{\int_0^{\infty} p(r) dr} \quad (8)$$

The volume weighted drop size distribution, $p(r)$, is the lognormal probability density function [1].

$$p(r) = \frac{1}{2 r \sigma (2 \pi)^{1/2}} \exp \left(-\frac{(\ln(2 r) - \ln(d_v))^2}{2 \sigma^2} \right) \quad (9)$$

The volume based mean is given by d_v and the width of the distribution is σ .

The PFG technique involves obtaining attenuation of the signal as a function of gradient strength and subsequently fitting the attenuation to the predicted attenuation according to the restricted diffusion model. For this work, a

nonlinear least squares algorithm with optimization in MatLab was used to perform the fitting.

2.3 Pulsed Field Gradient with Diffusion Editing (PFG-DE)

The standard PFG pulse sequence that was previously discussed can be modified to include several thousand 180° pulses at the end of the gradient sequence to gather transverse relaxation information [9, 10].

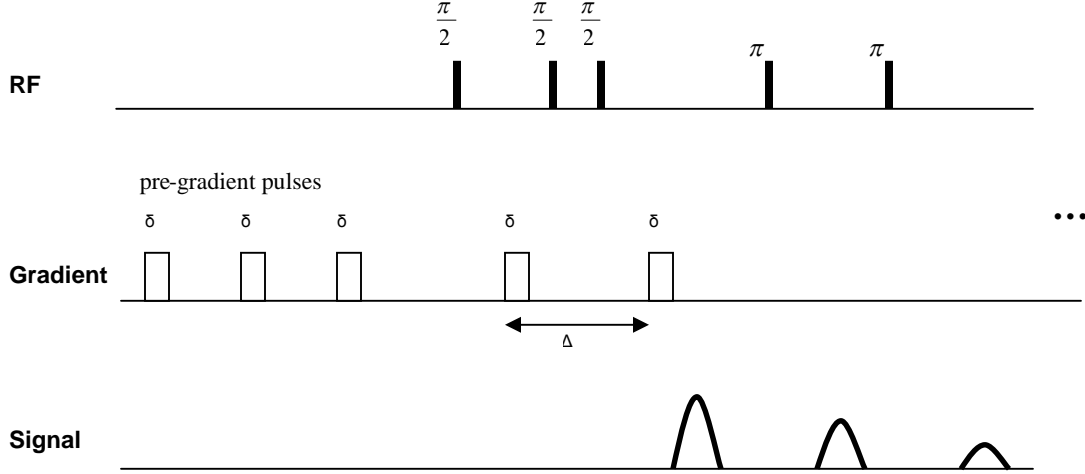


Figure 3: Pulsed field gradient with diffusion editing (PFG-DE) pulse sequence (adapted from Flaum [9]).

Similar to the standard PFG technique, the gradient values are manipulated to facilitate attenuation due to restricted diffusion. However, the PFG-DE technique acquires thousands of echoes, thus resulting in the attainment of both diffusion and transverse relaxation information.

The magnetization obtained with the PFG-DE technique is given by Equation 10 [9].

$$M(g, t) = \iint f(r, T_2) \exp\left(-\frac{t}{T_2}\right) R_{sp}(\Delta, \delta, g, r) \exp\left(-\frac{\Delta + \delta}{T_1} - 2\delta \left(\frac{1}{T_2} - \frac{1}{T_1}\right)\right) dr dT_2 \quad (10)$$

The attenuation of the brine drops according to Equations 2 – 4 is given by R_{sp} . The distribution of both drop size and transverse relaxation, $f(r, T_2)$, is determined using a two dimensional inversion with regularization [9, 10].

2.4 Parameter Selection

The parameters that are used in both the PFG and PFG-DE techniques are obtained by solving the series model for restricted diffusion in spheres given by Murday and Cotts [7, 9]. Specifically, the primary parameters that affect both the PFG-DE and PFG measurements are the gradient spacing (Δ), gradient duration (δ), and gradient strength (g). Both physical and equipment constraints must be accounted for when determining the parameters for a given experiment. Selection of the gradient spacing must be made based on the range of sizes of the drops expected in the sample and the SNR of the system. To distinguish

restricted diffusion from free diffusion, the dimensionless diffusion time must be greater than or equal to 1.0 [9].

$$\frac{2 D \Delta}{r^2} \geq 1.0 \quad (11)$$

If Δ is too small, the measurement will not be sensitive to large drops. If Δ is too large, the SNR will be low.

$$\frac{r^2}{2 D} \leq \Delta \leq 0.3 T_2 \quad (12)$$

After Δ is established, the gradient duration, $\bar{\delta}$, is calculated. The minimum value of the gradient duration is instrument specific, and the maximum value is based on an established rule of thumb [9].

$$\delta_{\min} \leq \delta \leq 0.2 \Delta \quad (13)$$

With the gradient spacing and duration calculated, the gradient values which achieve the desired attenuation can be calculated using the previously described series model for restricted diffusion in spheres. Ideally, for a given sphere size, the attenuation should range from 0.99 to 0.01 [9].

Figure 4 illustrates the relationship between the parameters in a given experiment.

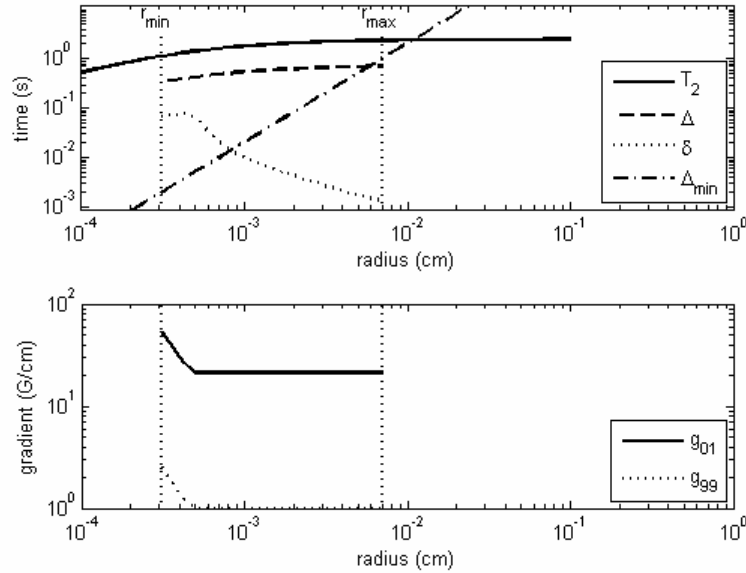


Figure 4: Example of parameters calculated for PFG-DE and PFG measurements. These parameters were calculated with ($\rho = 0.5 \mu\text{m/s}$, $D_{\text{brine}} = 2.45 \times 10^{-9} \text{m}^2/\text{s}$, $T_{2,\text{bulk}} = 2.48 \text{s}$, and $\Delta/T_2 = 0.3$).

In the top figure, the solid curve shows the T_2 distribution of the dispersed fluid. The dashed curve is the gradient spacing, Δ , and the dotted curve is the gradient duration, $\bar{\delta}$. The minimum gradient spacing, Δ_{\min} , is shown as the dashed-dotted line in the top figure, as determined by the lower constraint on Δ . When the calculated Δ falls below Δ_{\min} , the measurement is no longer sensitive to restricted diffusion, thus resulting in the maximum drop size, r_{max} . The minimum detectable

drop size, r_{\min} , is calculated based on the maximum gradient duration and maximum gradient strength of the instrument. Finally, the bottom figure contains the range of gradient values that should be used to facilitate the desired amount of attenuation ranging from 1% signal remaining, g_{01} , to 99% signal remaining, g_{99} . In this work, 25 logarithmically spaced gradient values were calculated for each parameter set. For all PFG and PFG-DE measurements discussed in this paper, 32 scans were used with the echo spacing equal to 600 μs and the relaxation delay equal to 10 s.

Using a technique developed by Flaum [9], multiple sets of parameters can be used to characterize the entire drop size range ($r_{\min} - r_{\max}$). This technique, referred to as masking, incorporates multiple parameter sets with each set consisting of one Δ value, one δ value, and a logarithmically spaced list of gradient strength values. After the data have been collected, the results from each set are combined to obtain information about the entire drop size range. The sensitivity of each parameter set is limited by the SNR of the instrument. The masking technique applies to both drop size information and transverse relaxation information. The masking technique weights the most sensitive drop size ranges of each parameter set based on the SNR of the measurement to gain the most accurate information about the range of drop sizes. Similarly, the transverse relaxation information is masked according to the gradient spacing. In this work, transverse relaxation times shorter than half of the gradient spacing were truncated. If the emulsion is known to be unimodal, only one experimental set of parameters needs to be used. However, if the drop size distribution of the emulsion is broad or multi-modal, multiple parameter sets should be employed to characterize the entire drop size range.

2.6 Emulsion Preparation

The emulsions considered in this work were prepared using a Couette flow device. The rotating, inner cylinder was composed of Torlon with radius, $r_T = 19.1$ mm. The stationary, outer cylinder was composed of glass with radius, $r_g = 21.6$ mm.

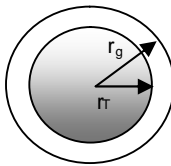


Figure 5: Cross section of the Couette flow device. Note that $r_T/r_g = 0.88$.

The rotational speed of the inner cylinder was adjusted depending on the desired experimental conditions, and the shear rate is given by Equation 14.

$$\gamma = \frac{2 \pi \omega r_T}{(r_g - r_T)} \quad (14)$$

The rotational speed of the inner cylinder is given by ω . The temperature of all measurements was maintained at 30° C. For all of the emulsions discussed, the dispersed phase was ASTM certified synthetic seawater, and the emulsions were

classified as water/oil. Two different oils were used for the continuous phase, denoted as either Crude Oil A or Crude Oil B.

3. Results

The following sections contain three different cases that show the usefulness of the PFG-DE technique. The first case illustrates a situation when the T_2 distribution of the emulsified brine overlaps the bulk brine T_2 distribution. The second case illustrates the situation when the T_2 distribution of the emulsified brine overlaps the T_2 distribution of the crude oil. Finally, the third case illustrates the ability of the PFG-DE technique to resolve a bimodal drop size distribution.

3.1 Emulsified Brine T_2 Distribution Overlaps the Bulk Brine T_2 Distribution

Drop size distributions of brine/Crude Oil A emulsions were obtained using the CPMG, PFG-DE, and PFG techniques. Figure 6 shows the T_2 distribution of an emulsion that was formed by combining 10 mL of brine with 40 mL of Crude Oil A with viscosity equal to 15 cP. Shear was applied to the emulsion with $\dot{\gamma} = 1.3 \times 10^3 \text{ s}^{-1}$ for 10 minutes.

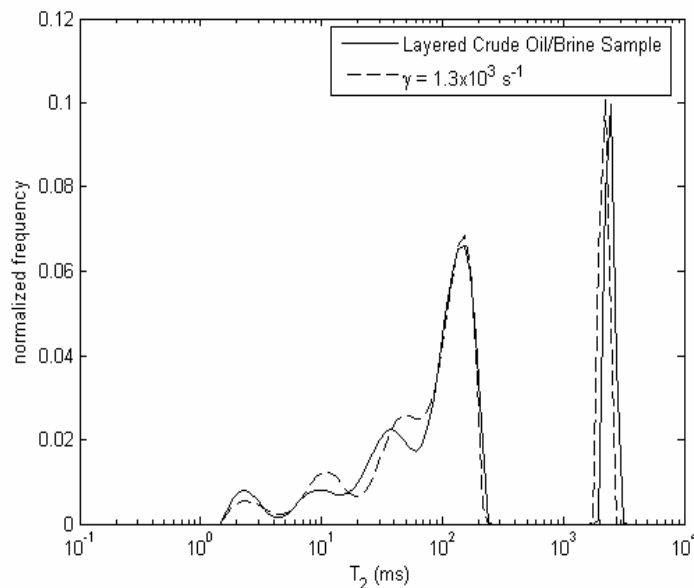


Figure 6: T_2 distribution of an emulsion with $\dot{\gamma} = 1.3 \times 10^3 \text{ s}^{-1}$ for 10 minutes. Note the proximity of the emulsified brine T_2 distribution to the bulk brine T_2 distribution.

Figure 6 shows the overlap of the emulsified brine T_2 distribution and the bulk brine T_2 distribution. Figure 7 shows the drop size distribution that was obtained by using the emulsified brine T_2 distribution in conjunction with Equation 1.

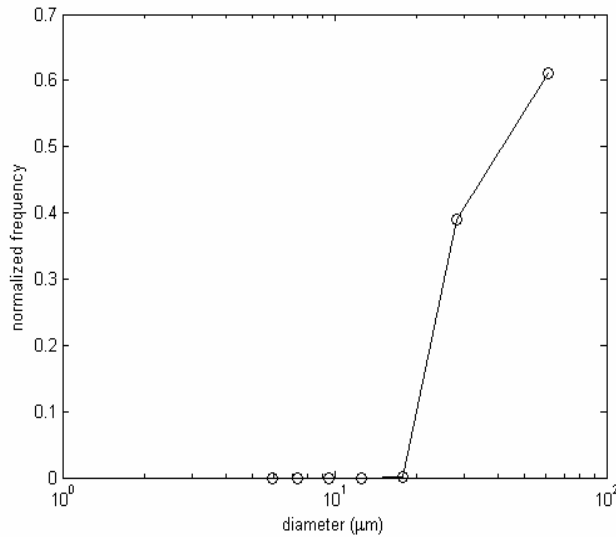


Figure 7: Drop size distribution obtained from transverse relaxation data. Note the increase in the width of the distribution that was caused by the approach of the emulsified brine T_2 distribution to the bulk brine T_2 distribution.

The drop size distribution in Figure 7 illustrates the error that is introduced when using Equation 1 if the T_2 distribution of the emulsified brine is close to the bulk brine T_2 distribution. Equation 1 assumes that the transverse relaxation distribution of the bulk brine is single valued. Experimentally, the bulk brine exhibits a finite range of T_2 values. Therefore, the emulsified brine can overlap the bulk brine distribution, thus causing a significant increase in the uncertainty of the drop size distribution. In addition, Equation 1 requires the use of the surface relaxivity, which was obtained from Equation 15.

$$\rho = \frac{d_v}{6} \left(\frac{1}{T_{2,brine}} - \frac{1}{T_{2,bulk}} \right) \quad (15)$$

The volume weighted mean diameter, d_v , and the corresponding T_2 value of the brine, $T_{2,brine}$, were obtained from a PFG-DE measurement. For this brine/crude oil system, the surface relaxivity was determined to be 0.5 $\mu\text{m/s}$.

The PFG-DE and PFG techniques were performed on the same emulsion. With the input values of $T_{2,bulk} = 2.48$ s, $\rho = 0.5$ $\mu\text{m/s}$, and $\Delta/T_2 = 0.3$, the following parameters were calculated based on the previously discussed parameter selection method: $\Delta = 598$ ms, $\delta = 5.7$ ms, and $g = 1 - 10$ G/cm. These parameters were calculated to be sensitive to drop diameters in the range, 20 $\mu\text{m} - 100$ μm .

Unlike the CPMG technique, the PFG-DE technique does not rely on the T_2 distribution to generate the drop size distribution. Figure 8 contains the two dimensional map that was generated using the PFG-DE technique.

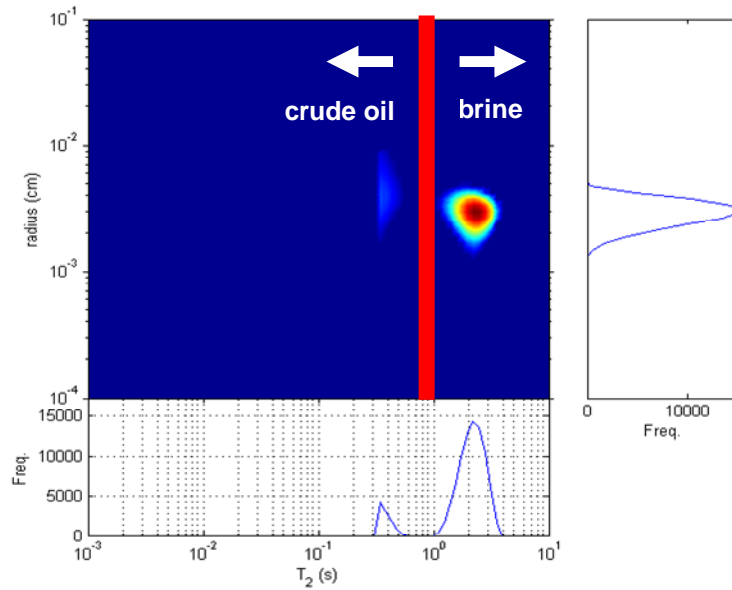


Figure 8: Two dimensional map produced from the PFG-DE technique. Note the separation of the Crude Oil A and brine in terms of transverse relaxation. Only brine contributes to the drop size distribution.

The brine and Crude Oil A contributions are separated with respect to the T_2 distribution, thereby making the drop size distribution only dependent on the brine contribution. In addition, the transverse relaxation contribution from the crude oil has been minimized as a result of the choice of the gradient spacing. The PFG technique was performed to confirm the drop size distribution obtained from the PFG-DE technique, and the results are shown in Figure 9.

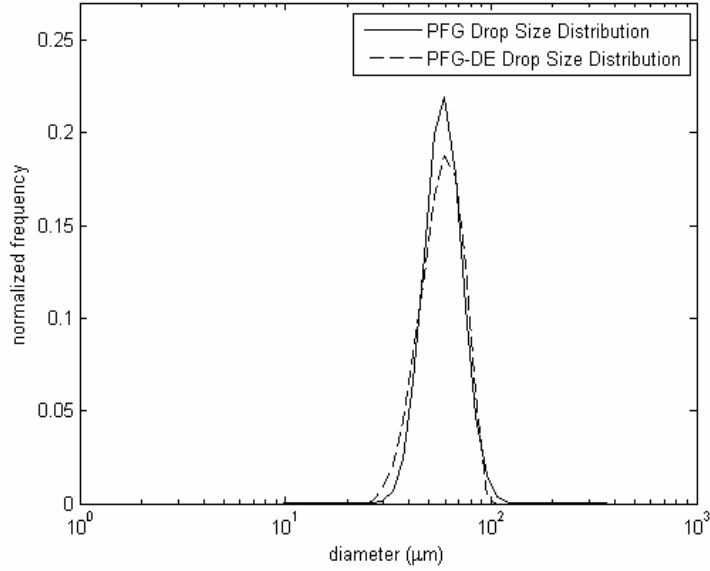


Figure 9: Comparison of drop size distributions obtained from the PFG-DE and PFG techniques. The drop size distribution from the PFG-DE technique given by the mean and one standard deviation on either side of the mean [45, 59, 72] μm agrees well with the traditional PFG technique, [47, 58, 72] μm .

Because the PFG-DE technique yields a discrete drop size distribution and the PFG technique yields a continuous probability density function, a relationship must be established between the results of the two techniques. The cumulative distribution can be written according to Equation 16.

$$P(d) = \sum_{j=1}^{j=i} f_j \quad (16)$$

The normalized frequency obtained from the PFG-DE technique is given by f_j . Because the probability density function is lognormal with equal increments of the logarithm of the diameter, the cumulative distribution can further be written in terms of the normalized frequency from the PFG-DE technique.

$$\Delta P_i = d_i p(d_i) \Delta(\log(d_i)) = f_i \quad (17)$$

The probability density function is denoted by $p(d_i)$. Thus, the results from both techniques can be accurately plotted on the same figure. Figure 9 reveals the agreement between the PFG-DE and PFG techniques for the drop size distribution of this emulsion. Unlike the CPMG technique as shown in Figure 7, the PFG-DE and PFG techniques have the ability to resolve the drop size distribution when the T_2 distribution of the emulsion overlaps the bulk brine T_2 distribution. Table 1 contains a summary of this comparison.

Table 1: Summary of results for the brine/Crude Oil A emulsion with $\gamma = 1.3 \times 10^3 \text{ s}^{-1}$.

| Method | $\frac{d_v}{e^\sigma}$ (μm) | d_v (μm) | $d_v e^\sigma$ (μm) |
|--------|--|-------------------------|----------------------------------|
| PFG-DE | 45 | 59 | 72 |
| PFG | 47 | 58 | 72 |

3.2 Emulsified Brine T_2 Distribution Overlaps the Bulk Crude Oil T_2 Distribution

If the T_2 distribution of the emulsified brine overlaps the T_2 distribution of the crude oil in the emulsion, the transverse relaxation data cannot be used to obtain the drop size distribution of the emulsion. An emulsion was prepared by combining 5 mL of brine with 20 mL of Crude Oil B with viscosity equal to 1 cP. The emulsion was sheared for five minutes with $\gamma = 3.2 \times 10^3 \text{ s}^{-1}$. Figure 10 contains the T_2 distribution of the emulsion showing the overlap of the emulsified brine and crude oil T_2 distributions.

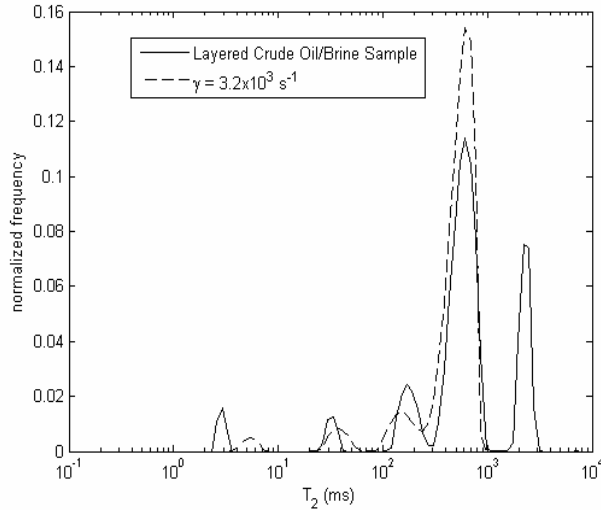


Figure 10: Overlap of emulsion and Crude Oil B T_2 distributions.

The solid curve in Figure 10 is the T_2 distribution of the layered Crude Oil B/brine sample, and the dashed curve is the T_2 distribution of the emulsion. Because the emulsified brine and Crude Oil B T_2 distributions are not separable, Equation 1 cannot be used to calculate the drop size distribution.

The parameters for the PFG-DE technique were calculated based on ($T_{2,\text{bulk}} = 2.48 \text{ s}$, $\rho = 0.3 \text{ } \mu\text{m/s}$, and $\Delta/T_2 = 0.3$), and the values were: $\Delta = 552 \text{ ms}$, $\delta = 28 \text{ ms}$, and $g = 1 - 13 \text{ G/cm}$. The parameters were sensitive to drop diameters in the range, $5 - 50 \text{ } \mu\text{m}$. The two dimensional map obtained from the PFG-DE technique is shown in Figure 11.

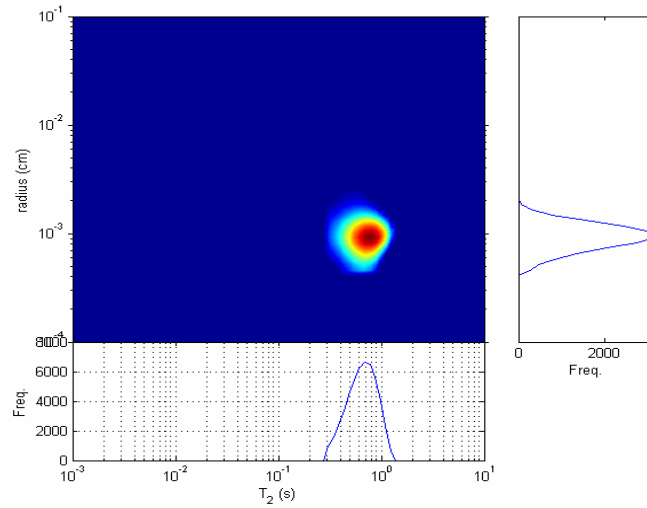


Figure 11: Two dimensional map of brine/Crude Oil B emulsion. The emulsified brine and Crude Oil B T_2 distributions overlap, but the Crude Oil B does not contribute to the drop size distribution because the Crude Oil B signal attenuated significantly.

Figure 11 shows that the drop size distribution of the brine phase was extracted using the PFG-DE technique even though the T_2 distributions of the emulsified brine and Crude Oil B overlap. The lack of contribution of the Crude Oil B to the drop size distribution is evident when considering the attenuation of the emulsion as shown in Figure 12.

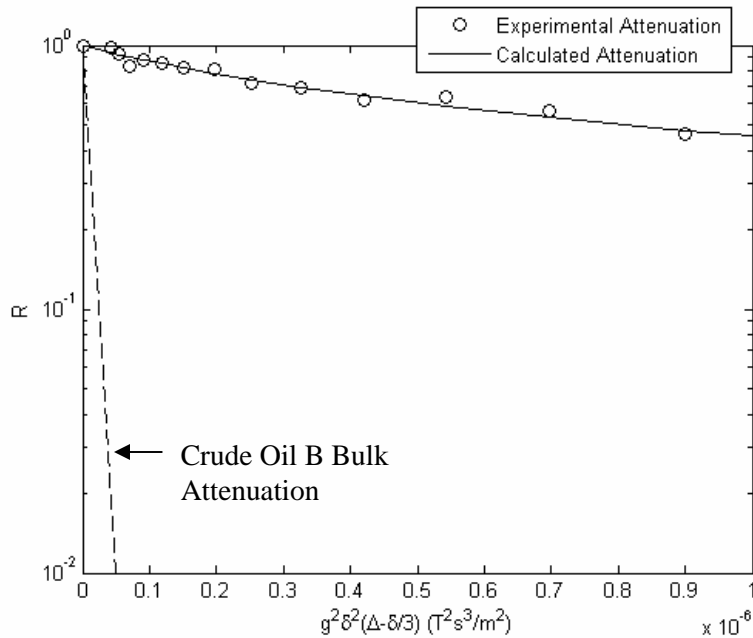


Figure 12: Experimental and predicted attenuation for the brine/Crude Oil B emulsion ($\Delta = 552$ ms, $\delta = 28$ ms, and $g = 1 - 13$ G/cm). Note that the Crude Oil B does not contribute to the attenuation of the signal of the emulsion, thereby facilitating the separation of the Crude Oil B and brine contributions.

Figure 12 shows that the Crude Oil B does not significantly contribute to the attenuation of the signal of the emulsion based on Equation 7. The signal of the Crude Oil B is negligible after the second gradient pulse; therefore, the brine and Crude Oil B contributions can be separated.

The PFG measurement was performed using the same parameters as those used for the PFG-DE measurement, and the comparison of the drop size distributions is shown in Figure 13.

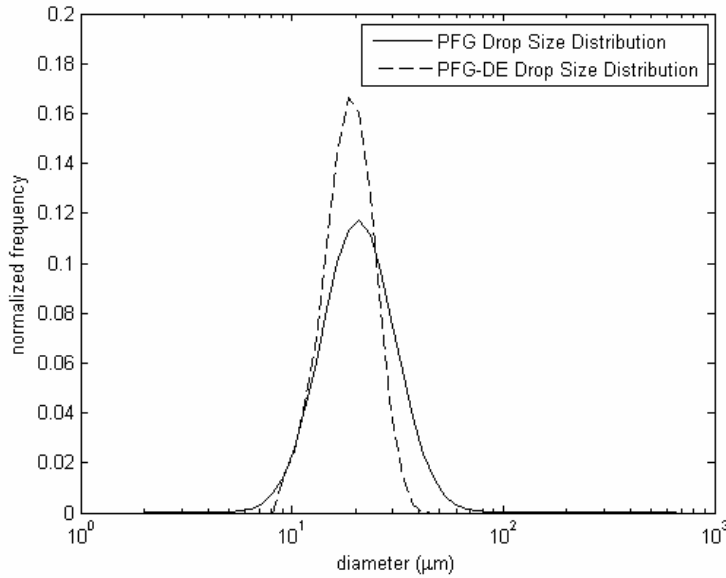


Figure 13: Comparison of drop size distributions obtained from the PFG-DE and PFG techniques. The drop size distribution from the PFG-DE technique, [14, 19, 24] μm , agrees well with the traditional PFG technique [14, 21, 31] μm .

Figure 13 shows that the means of the drop size distributions are in agreement for the two techniques, while the widths of the distributions are slightly different. The difference in the widths of the distributions is likely caused by the assumption of the PFG technique that the drop size distribution is lognormal. The PFG-DE technique is not restricted by the assumption that the drop size distribution is lognormal. Table 2 contains a summary of the results for this brine/Crude Oil B emulsion.

Table 2: Summary of results for the brine/Crude Oil B emulsion with $\gamma = 3.2 \times 10^3 \text{ s}^{-1}$.

| Method | $\frac{d_v}{e^\sigma}$ (μm) | d_v (μm) | $d_v e^\sigma$ (μm) |
|--------|--|-------------------------|----------------------------------|
| PFG-DE | 14 | 19 | 24 |
| PFG | 14 | 21 | 31 |

3.3 Bimodal Drop Size Distribution

The PFG-DE technique is particularly useful for determining the drop size distribution when the emulsion contains a bimodal drop size distribution. A bimodal drop size distribution was prepared by combining two independently formed emulsions. One emulsion was prepared by shearing 10 mL of brine with 40 mL of Crude Oil A. The shearing duration was 10 minutes with $\gamma = 2.3 \times 10^3 \text{ s}^{-1}$. An independent emulsion consisting of 10 mL of brine and 40 mL of Crude Oil A was formed with $\gamma = 1.3 \times 10^3 \text{ s}^{-1}$ and duration equal to 10 minutes. The PFG-

DE and PFG measurements were performed on both of the independent emulsions. From each independent emulsion, 25 mL was removed and combined into one glass sample vessel to form a bimodal drop size distribution. The PFG-DE measurement was performed on the combined emulsion.

By applying two different shear rates, it was expected that two different populations of drops would form. Therefore, two different parameter sets were constructed to characterize the two different drop size distributions. With $\gamma = 2.3 \times 10^3 \text{ s}^{-1}$, the expected range of drop diameters was 5 – 50 μm . To characterize this range of diameters, the following parameters were calculated using the previously described algorithm based on $T_{2,\text{bulk}} = 2.48 \text{ s}$, $\rho = 0.5 \mu\text{m/s}$, and $\Delta/T_2 = 0.3$: $\Delta = 470 \text{ ms}$, $\delta = 28 \text{ ms}$, $g = 1 - 21 \text{ G/cm}$. The PFG technique was also used to measure the drop size distribution of the emulsion, and the comparison is shown in Figure 14.

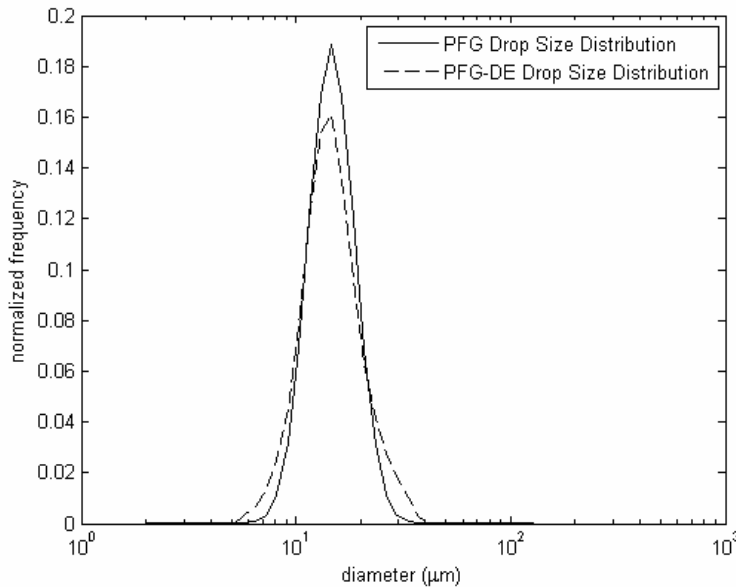


Figure 14: Comparison of drop size distributions with $\gamma = 2.3 \times 10^3 \text{ s}^{-1}$. The PFG-DE technique yielded a drop size distribution, [10, 15, 20] μm , that agreed with the PFG technique, [11, 15, 19] μm .

Figure 14 shows the agreement that was achieved between the PFG-DE technique and the PFG technique with $\gamma = 2.3 \times 10^3 \text{ s}^{-1}$.

With $\gamma = 1.3 \times 10^3 \text{ s}^{-1}$, the expected range of drop diameters was 30 – 100 μm . To characterize this range of diameters, the following parameters were calculated using the previously described algorithm based on $T_{2,\text{bulk}} = 2.48 \text{ s}$, $\rho = 0.5 \mu\text{m/s}$, and $\Delta/T_2 = 0.3$: $\Delta = 598 \text{ ms}$, $\delta = 5.7 \text{ ms}$, $g = 1 - 19 \text{ G/cm}$. The PFG technique was also used to measure the drop size distribution of the emulsion, and the comparison is shown in Figure 15.

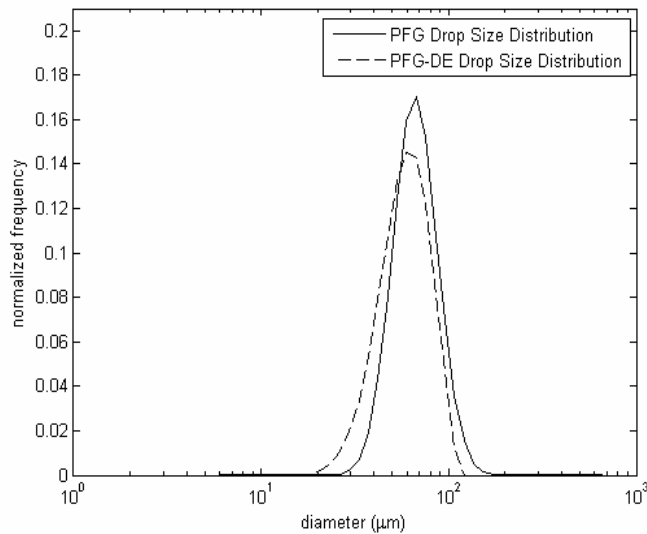
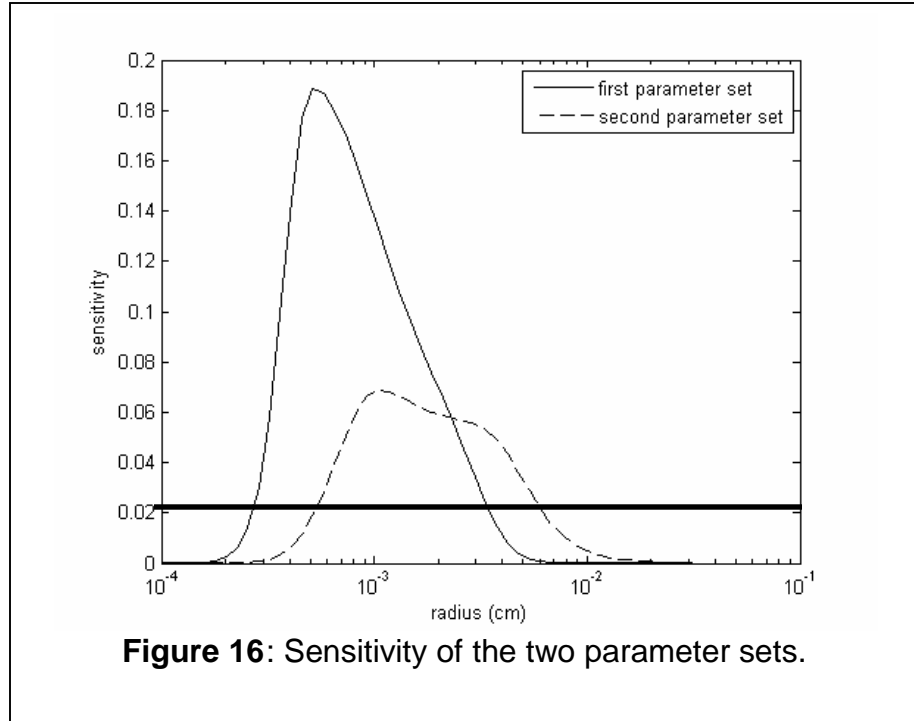


Figure 15: Comparison of drop size distributions with $\gamma = 1.3 \times 10^3 \text{ s}^{-1}$. The PFG-DE technique yielded a drop size distribution, [42, 60, 78] μm , that agreed with the PFG technique, [50, 66, 87] μm .

Figure 15 shows the agreement that was achieved between the PFG-DE and PFG techniques with $\gamma = 1.3 \times 10^3 \text{ s}^{-1}$.

An emulsion with a bimodal drop size distribution was formed by combining 25 mL of the emulsion with $\gamma = 2.3 \times 10^3 \text{ s}^{-1}$, with 25 mL of the emulsion with $\gamma = 1.3 \times 10^3 \text{ s}^{-1}$. The PFG-DE measurement of the bimodal emulsion consisted of two complete parameter sets: [$\Delta = 470 \text{ ms}$, $\delta = 28 \text{ ms}$, $g = 1 - 21 \text{ G/cm}$] and [$\Delta = 598 \text{ ms}$, $\delta = 5.7 \text{ ms}$, $g = 1 - 19 \text{ G/cm}$]. The masking technique developed by Flaum [9] was used to investigate the range of sizes of the bimodal distribution. The sensitivity of each parameter set is determined by the amount of noise in the measurement. Figure 16 illustrates the determination of the sensitive region of each parameter set by plotting the sum of the square of the difference in attenuation for different drop sizes as a function of drop size.



The horizontal line in Figure 16 was calculated using Equation 18 [9].

$$cutoff = 2 (\sigma_{noise})^2 N_{grad} \quad (18)$$

In this equation, the standard deviation of the noise is given by σ_{noise} and the number of gradients is given by N_{grad} . For this example, the value of the cutoff was calculated to be 0.02, as illustrated in Figure 16. The intersections of the horizontal line with the sensitivity curves designate the boundaries of the sensitivity of each parameter set. For example, the first parameter set, shown as the solid curve, is sensitive to drop diameters in the range, 5 μm – 70 μm . The first parameter set yielded the results shown in Figure 17.

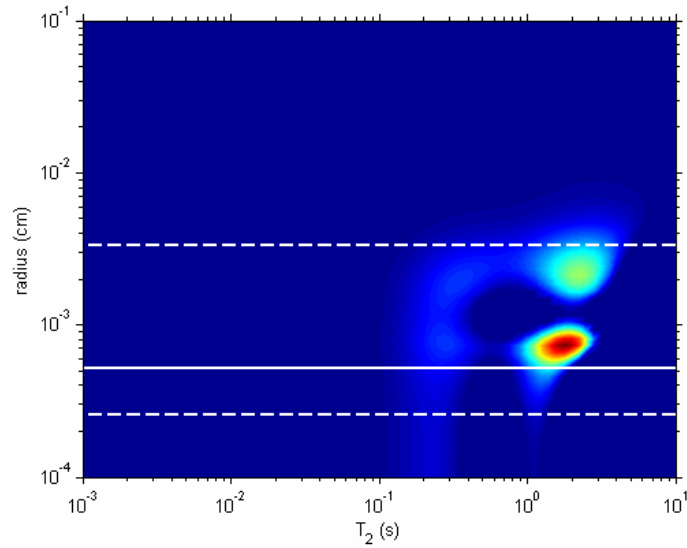


Figure 17: Two dimensional results from the first parameter set. The most sensitive drop size is indicated by the solid line while the limits of the sensitivity of the measurement are indicated by the dashed lines. Note that the population of smaller drops exists in the sensitive region.

Figure 17 shows the sensitive region obtained by using the first parameter set. The solid line indicates the drop size that the measurement is most sensitive to, and the dashed lines indicate the limits of the sensitivity of the measurement as given by Equation 18. Similarly, the second parameter set was performed on the emulsion to yield the results shown in Figure 18.

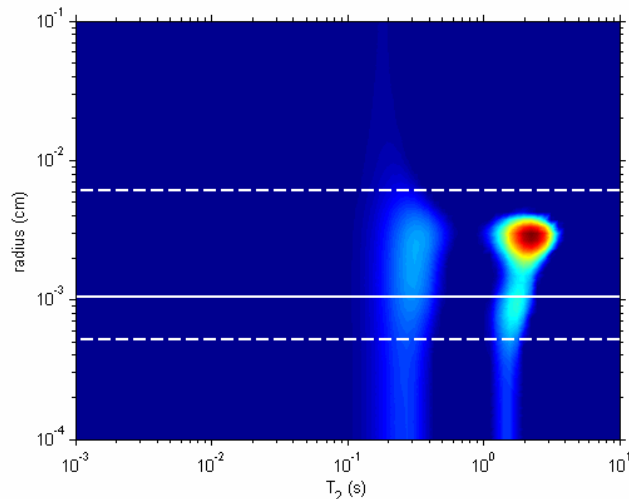


Figure 18: Two dimensional results from the second parameter set. Note that the larger population of drop sizes is present in the sensitive region.

The second parameter set is clearly sensitive to the larger population of drop sizes as shown in Figure 18.

In addition to masking the measurement according to the drop size, the masking procedure also truncates the transverse relaxation based on the gradient spacing, Δ , of the measurement. As mentioned in Section 2.4, all transverse relaxation times that are less than half of Δ are truncated. For this measurement, the limit for transverse relaxation times was set to 235 ms which was half of the shortest Δ , 470 ms. For this example, truncating the transverse relaxation merely diminishes the transverse relaxation contribution of the crude oil while the brine contribution is unaffected. Figure 19 shows the final result after masking both transverse relaxation and drop size.

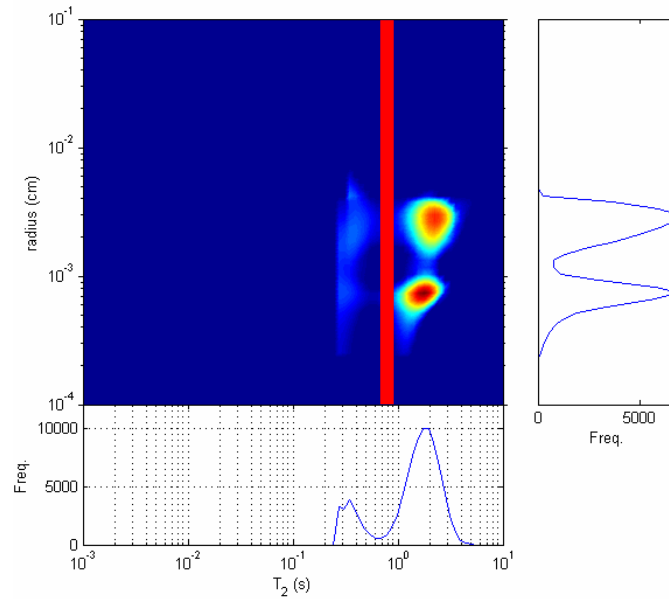


Figure 19: Two dimensional map of the bimodal drop size distribution after masking. The brine contribution to the drop size distribution was isolated according to the separation of the T_2 distributions.

The Crude Oil A and brine contributions were isolated according to the separation in terms of the T_2 distributions, and the resulting bimodal drop size distribution is given in Figure 20.

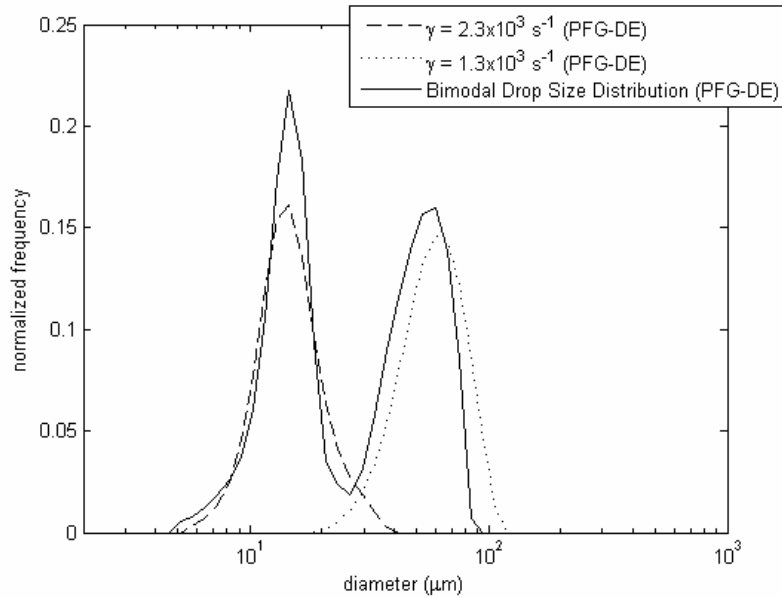


Figure 20: Comparison of unimodal drop size distributions with the bimodal drop size distribution obtained using the PFG-DE technique.

Figure 20 illustrates the ability of the PFG-DE technique to resolve the bimodal drop size distribution. The independently measured unimodal drop size distributions of each emulsion are plotted in conjunction with the bimodal drop size distribution. Figure 20 shows that the first population of sizes in the bimodal distribution, [11, 14, 17] μm , agrees with the PFG-DE measurement of the corresponding unimodal drop size distribution, [10, 15, 20] μm . In addition, the second population of drop sizes in the bimodal distribution, [39, 52, 65] μm , also agrees with the PFG-DE measurement of the corresponding unimodal distribution, [42, 60, 78] μm . These results show that the PFG-DE technique has the ability to resolve a bimodal drop size distribution which is in agreement with the independent, unimodal drop size distributions.

4. Conclusion

Based on the work presented in this paper, the PFG-DE technique has the ability to resolve drop size distributions of emulsions in different physical situations. In addition, the parameter selection algorithm developed by Flaum [9] facilitates accurate measurements of drop size distributions of emulsions. The results from the PFG-DE technique have been shown to agree with the traditional PFG technique for lognormal drop size distributions. The PFG-DE technique also has the ability to resolve more complicated drop size distributions such as bimodal drop size distributions. In general, the PFG-DE technique is useful because it provides both transverse relaxation and drop size distributions simultaneously, and it is not constrained by an assumed shape of the drop size distribution.

Acknowledgements

The authors would like to thank Dick Chronister, Waylon House, Dr. Alberto Montesi, Dr. Jeff Creek, Mike Rauschhuber, and Chevron for financial support.

References

1. Pena, A. and G.J. Hirasaki, *NMR Characterization of Emulsions*, in *Emulsions and Emulsion Stability*, J. Sjöblom, Editor. 2006, CRC: Boca Raton, FL.
2. Becher, P., *Emulsions: Theory and Practice*. 2001, New York: Oxford University Press.
3. Schramm, L.L., *Emulsions, Foams, and Suspensions: Fundamentals and Applications*. 2005: Wiley-VCH.
4. Sjöblom, J., *Encyclopedic Handbook of Emulsion Technology*. 2001, New York: Marcel Dekker.
5. Packer, K.J. and C. Rees, *Pulsed NMR Studies of Restricted Diffusion I. Droplet Size Distributions in Emulsions*. *Journal of Colloid and Interface Science*, 1972. **40**(2).
6. Neuman, C.H., *Spin Echo of Spins Diffusing in a Bounded Medium*. *Journal of Chemical Physics*, 1974. **60**: p. 4508-4511.
7. Murday, J.S. and R.M. Cotts, *Self-Diffusion Coefficient of Liquid Lithium*. *Journal of Chemical Physics*, 1968. **48**: p. 4938-4945.
8. Pena, A., *Enhanced Characterization of Oilfield Emulsions via NMR Diffusion and Transverse Relaxation Experiments*. *Advances in Colloid and Interface Science*, 2003. **105**: p. 103-150.
9. Flaum, M., *Fluid and Rock Characterization Using New NMR Diffusion-Editing Pulse Sequences and Two Dimensional Diffusivity- T_2 Maps*, in *Chemical and Biomolecular Engineering*. 2006, Rice University: Houston.
10. Hurlimann, M.D. and L. Venkataramanan, *Quantitative Measurement of Two Dimensional Distribution Functions of Diffusion and Relaxation in Grossly Inhomogeneous Fields*. *Journal of Magnetic Resonance*, 2002. **157**: p. 31-42.
11. Garisanin, T. and T. Cosgrove, *NMR Self-Diffusion Studies on PDMS Oil-in-Water Emulsion*. *Langmuir*, 2002. **18**: p. 10298-10304.
12. Carr, H.Y. and E.M. Purcell, *Effects of Diffusion on Free Precession in Nuclear Magnetic Resonance Experiments*. *Physical Review*, 1954. **94**: p. 630-638.
13. Meiboom, S. and D. Gill, *Modified Spin-Echo Method for Measuring Nuclear Relaxation Times*. *The Review of Scientific Instruments*, 1958. **29**: p. 688-691.

Task 2. Estimation of fluid and rock properties and their interactions from NMR relaxation and diffusion measurements

Subtask 2.4 Interpretation of systems with diffusional coupling between pores

NMR DIFFUSIONAL COUPLING: EFFECTS OF TEMPERATURE AND CLAY DISTRIBUTION

Vivek Anand, George J. Hirasaki, Rice University, USA

Marc Fleury, IFP, France

ABSTRACT

The interpretation of Nuclear Magnetic Resonance (NMR) measurements on fluid-saturated formations assumes that pores of each size relax independently of other pores. However, diffusional coupling between pores of different sizes may lead to false interpretation of measurements and thereby, a wrong estimation of formation properties. The objective of this study is to provide a quantitative framework for the interpretation of the effects of temperature and clay distribution on NMR experiments. In a previous work, we established that the extent of coupling between a micropore and macropore can be quantified with the help of a coupling parameter (α) which is defined as the ratio of characteristic relaxation rate to the rate of diffusive mixing of magnetization between micro and macropore. The effect of temperature on pore coupling is evaluated by proposing a temperature dependent functional relationship of α . This relationship takes into account the temperature dependence of surface relaxivity and fluid diffusivity. The solution of inverse problem of determining α and microporosity fraction for systems with unknown properties is obtainable from experimentally measurable quantities.

Experimental NMR measurements on reservoir carbonate rocks and model grainstone systems consisting of microporous silica gels of various grain sizes are performed at different temperatures. As temperature is increased, the T_2 spectrum for water-saturated systems progressively changes from bimodal to unimodal distribution. This enhanced pore coupling is caused by a combined effect of increase in water diffusivity and decrease in surface-relaxivity with temperature. Extent of coupling at each temperature can be quantified by the values of α . The technique can prove useful in interpreting log data for high temperature reservoirs.

Effect of clay distribution on pore coupling is studied for model shaly sands made with fine silica sand and bentonite or kaolinite clays. The NMR response is measured for two cases in which clay is either present as a separate, discrete layer or homogeneously distributed with the sand. For layered systems, T_2 spectrum shows separate peaks for clay and sand at 100% water saturation and a sharp $T_{2,cutoff}$ could be effectively applied for estimation of irreducible saturation. However, for dispersed systems a unimodal T_2 spectrum is observed and application of 33ms $T_{2,cutoff}$ would underestimate the irreducible saturation in the case of kaolinite and overestimate in the case of bentonite. The inversion technique can still be applied to accurately estimate the irreducible saturation.

INTRODUCTION

NMR well logging provides a useful technique for the estimation of formation properties such as porosity, permeability, irreducible water saturation, oil saturation and viscosity. The conventional interpretation of NMR measurements on fluid-saturated rocks assumes that the relaxation rate of fluid in a pore is directly related to the surface-to-volume ratio of the pore. In addition, each pore is assumed to relax independently of other pores so that the relaxation time distribution represents a signature of the distribution of pore sizes. Ramakrishan et al (1999) showed that such interpretation often fails if the fluid molecules in intra (micro) and intergranular (macro) pores are diffusively coupled with each other. The pore coupling effects can be particularly enhanced at high formation temperatures and a calibration for the estimation of irreducible saturations based on laboratory data at room temperature may not be suitable.

In a previous work (Anand and Hirasaki, 2005), we demonstrated that the extent of coupling in a pore model consisting of a micropore in contact with a macropore can be quantified with the help of a coupling parameter (α). α is defined as the ratio of characteristic relaxation rate of the pore to the rate of diffusional mixing of magnetization between micro and macropore i.e.

$$\alpha = \frac{\text{Characteristic relaxation rate}}{\text{Diffusion rate}} = \frac{\rho\beta L_2^2}{DL_1} \quad (1)$$

where ρ is the micropore surface relaxivity, β is the microporosity fraction, L_2 is the half length of the macropore and L_1 is the half width of the micropore (refer to figure 1 in reference 2). Numerical simulations show that as α decreases, coupling between micro and macropore increases and the T_2 response of the pore changes from bimodal to unimodal distribution. The amplitude of the faster relaxing (micropore) peak, ϕ , shows an empirical lognormal relationship with α .

$$\frac{\varphi}{\beta} = \frac{1}{2} \left[1 + \operatorname{erf} \left(\frac{\log \alpha - 2.29}{0.89\sqrt{2}} \right) \right] \quad (2)$$

The pore types can, thus, communicate through three coupling regimes: Total coupling ($\varphi = 0$), Intermediate coupling ($0 < \varphi < \beta$) and Decoupled ($\varphi = \beta$) regime. For systems with unknown physical and geometrical properties, the solution of inverse problem of determining α and β can be obtained from intersection of contours of constant φ and $T_{2,\text{macro}}/T_{2,\mu}$ in α and β parameter space (Figure 17 in reference 2). Here $T_{2,\text{macro}}$ and $T_{2,\mu}$ are the modes of the macropore and micropore peaks at 100% water and irreducible saturation respectively. The model was experimentally validated for pore coupling in several grainstones systems and clay lining pores in sandstones.

The purpose of this paper is to extend the earlier work to describe the effect of temperature and clay distribution on pore coupling. In the first section, a temperature dependent functional relationship of α is proposed by incorporating the temperature variation of surface relaxivity and fluid diffusion-coefficient. NMR measurements are performed at various temperatures with series of model grainstone systems and reservoir carbonate core at irreducible and 100% water saturation. Measurements at irreducible water saturation show that surface relaxivities for both systems decrease with temperature. The results for 100% water saturated systems illustrate that as temperature is increased, T_2 distributions gradually transition from bimodal to unimodal spectra suggesting an increase in pore coupling with temperature. Estimation of α theoretically predicts the transition of the systems between coupling regimes as temperature is increased. In the second section, diffusional coupling between free and irreducible water in shaly sands is studied as a function of distribution of clays with the sand. Model shaly sands are prepared in two ways such that the clays are either homogeneously dispersed with sand or present as a separate, discrete layer. NMR measurements at 100% and irreducible water saturation show that the free and irreducible water can be diffusively coupled or decoupled depending on the spatial separation between them.

EFFECT OF TEMPERATURE ON DIFFUSIONAL COUPLING

Relaxation rates of bulk fluids are strongly temperature sensitive due to the thermal modulation of translational and rotational correlation times. For fluids in porous media, relaxation is usually dominated by surface relaxation which can be temperature dependent. In addition, diffusional coupling between pores of different sizes can also increase with temperature due to increased diffusional transport of fluid molecules. Thus, the interpretation of temperature effect on NMR measurements in porous media needs to take into account the temperature variation of both surface relaxation and diffusional coupling.

The effect of temperature on pore coupling can be quantified by incorporating the temperature dependencies of surface relaxivity and diffusion coefficient in the functional relationship for α . Surface relaxation of fluid molecules in porous media is governed by two processes (Godefroy et al, 2001). First, translational motion of the fluid molecules near the paramagnetic sites at pore surface and second, exchange between surface and bulk molecules. The temperature dependence of surface relaxation arises from the thermal activation of the translational motion at the pore surface as well as increased exchange between surface and bulk fluid molecules. Quantitatively, the temperature dependence can be expressed as an Arrhenius relationship

$$\rho = \rho_0 \exp\left(\frac{\Delta E}{RT}\right) \quad (3)$$

where ΔE is the effective activation energy and R is the universal gas constant. Self-diffusion of bulk fluids is also a thermally activated process and the diffusion coefficient usually shows Arrhenius dependence with temperature,

$$D = D_0 \exp\left(-\frac{E_a}{RT}\right) \quad (4)$$

In the above equation, E_a is the activation energy for the diffusion process and D_0 is the diffusion coefficient at infinite temperature. Substituting equations (3) and (4) in the expression for α (equation 1) and grouping variables, a temperature dependent functional relationship of α can be given as

$$\alpha = \alpha_0 \exp\left(\frac{E_a + \Delta E}{R} \left(\frac{1}{T} - \frac{1}{T_0}\right)\right) \quad (5)$$

where α_0 is the value of coupling parameter at reference temperature T_0 . Thus, pore coupling can either increase or decrease with temperature if the difference in the activation energy for diffusion and relaxation process ($E_a + \Delta E$) is positive or negative, respectively.

Experimental Validation

The effect of temperature on NMR diffusional coupling is experimentally studied for two systems of porous media. The first system consists of a homologous series of microporous silica gels with varying grain diameters. The second system consists of a reservoir carbonate core with bimodal pore size distribution. For both systems NMR measurements are performed at total and irreducible water saturation as a function of temperature.

Silica Gels

Silica gels with mean grain radii of 118 μm (Medium Coarse), 55 μm (Very Fine) and 28 μm (Silt size) were obtained from Sigma Aldrich. The physical properties of the gels are given in Table 2 of reference 2. Figure 1 shows the T_2 distributions at 100% water saturation for the three silica gels at 30, 50, 75 and 95°C. At each temperature, the distributions are normalized with the pore volume (area under the curve) to account for the Curie Law. Figure 2 shows the normalized T_2 distributions at irreducible condition for the medium coarse silica gel at the above mentioned temperatures. The NMR apparatus has a response around 1 ms at high temperatures which has been subtracted from the distributions.

The increase in relaxation time at irreducible condition with temperature (Figure 2) shows that the surface relaxivity decreases as the temperature is increased. This result is in agreement with those obtained by Ramakrishnan et al (1999) who saw a similar increase in the relaxation time of water-saturated systems with temperature. The temperature behavior at 100% water saturation can now be interpreted keeping in mind the negative dependence of relaxivity on temperature. Each of the three silica gels in Figure 1 represents a different coupling scenario. The medium coarse silica gel is almost in decoupled regime ($\phi/\beta = 0.97$) at 30°C. As the temperature is increased, surface relaxivity decreases and diffusivity of water increases. As a result, coupling between micro and macropores increases and the system transitions from almost decoupled to intermediate coupling regime. This is evidenced by the reduction in the amplitude of the micropore peak and decrease in the relaxation time of the macropore with temperature. Very fine silica gel is in intermediate coupling regime at 30°C ($\phi/\beta = 0.24$). Increasing the temperature increases coupling so that the T_2 distribution changes from bimodal at 30°C to unimodal at higher temperatures. However, the increase in relaxation rate of the macropore due to coupling is exactly cancelled by the decrease in surface relaxation and thus the position of macropore peak remains unchanged. Silt size silica gel has a unimodal T_2 distribution at 30°C suggesting that the system is in total coupling regime ($\phi/\beta \sim 0$). Increase in temperature has no further effect on coupling but the corresponding decrease in surface relaxivity leads to a shift of T_2 distribution to longer relaxation times. The results demonstrate that temperature can have apparently different effects on the NMR response even though the systems may be governed by similar principles.

Reservoir Carbonate Core

The carbonate core studied is a Thamama reservoir carbonate with porosity 21.2% and water permeability of 13mD. Analysis of lithology shows that the carbonate is a packstone/wackestone with mainly moldic macroporosity in leached areas. The microporosity is predominantly inside pellets and mud. Figure 3 shows the T_2

distributions of the core at 100% and irreducible water saturation (oil saturated) for three temperatures of 25, 50 and 80°C. We can see that for 100% water-saturated core, as the temperature is increased amplitude of the micropore peak and relaxation time of the macropore decrease. This suggests that diffusional coupling between micro and macropores is increasing with temperature. Similar to the case for silica gels, the increase in pore coupling is due to increase in water diffusivity as well as decrease in surface relaxivity with temperature. The latter claim is based on the fact that the relaxation time of the residual water in the micropores of oil saturated core increases with temperature (lower panel of figure 3). An important implication of the results is that application of a sharp $T_{2,cutoff}$ based on a laboratory calibration at room temperature for the estimation of irreducible saturation may not be suitable for high temperature formations.

Discussion

Effect of temperature on pore coupling for the two systems can be analyzed quantitatively from the temperature variation of α . For silica gels, α at different temperatures can be calculated by including the temperature dependence of surface relaxivity and diffusivity in the definition of α for grainstone systems (Anand and Hirasaki, 2005),

$$\alpha_{\text{grain}}(T) = \frac{\rho(T)\beta R_g^2}{D(T)R_\mu} \quad (6)$$

Here R_g is the grain radius and R_μ is the micropore radius (75 Å for silica gels). The temperature variation of surface relaxivity is obtained from measurements at irreducible saturation (Figure 2). The estimates of self-diffusion coefficient of water as a function of temperature are obtained from the experimental data of Holz et al (2000). For the carbonate core, α is calculated using the inversion technique described earlier. Figure 4 shows the cross plot of the normalized micropore-peak amplitude (ϕ/β) with α for the three silica gels and carbonate core. It can be seen that α accurately predicts the transition of the different coupling regimes with temperature as the systems move downward along the empirical relationship (Equation 2). The microporosity fraction, estimated using the inversion technique, agrees within 5% average absolute deviation as shown in Figure 5. Thus, the technique can prove useful in accurately estimating formation properties for reservoirs at elevated temperatures.

EFFECT OF CLAY DISTRIBUTION ON PORE COUPLING

NMR well logging has evolved as a promising technology for the formation evaluation of shaly sands. Coates et al. (1994) proposed that the fast relaxing components of the T_2 spectrum in clayey rocks can be attributed to the water adsorbed on clays. This idea was further extended by Prammer et al. (1996) who

found that clays in sandstones exhibited specific transverse relaxation times proportional to their surface area and cation exchange capacity (CEC). Thus, they postulated that the position of fast relaxing T_2 peak can be used for clay typing. This claim was disputed by Matteson et al. (2000) who found that relaxation time of clay brine slurries is a function of compaction of clays. Since the degree of compaction of formation clays is usually not known, they argued that clay typing from T_2 measurements alone is not possible. In addition, they found that distinct peaks for clay bound and free water were not visible for the clay-brine slurries.

In order to understand the phenomenological factors causing the apparent differences, a systematic study of the relaxation characteristics of clay-sand systems was undertaken. Two systems of model shaly sands consisting of varying amount of either kaolinite or bentonite clay and fine sand were prepared. In the first system, the clays were uniformly dispersed (dispersed systems) with the sand such that the clays occupied the interstitial voids between the sand grains. For the second system, clays were present as a separate, discrete layer with the sand (laminated systems). NMR response of the systems was measured at 100% and irreducible water saturations.

Experimental Section

Fine sand (grain radius $50\mu\text{m}$), kaolinite and bentonite clays were obtained from Sigma Aldrich. The physical properties of the materials are given in Table 1. The dispersed and laminated systems were prepared in three sets such that the clay (either kaolinite or bentonite) constituted 0, 2, 5 and 10% of the total solid content. For each set, the systems were prepared at total and irreducible water saturation separately. The details for the preparation of the systems are included below.

Dispersed System

To prepare the dispersed system at 100% water saturation, 15 grams of fine sand was taken in a plastic centrifuge tube. The amount of either clay required to make the desired weight percentage content was added to the sand and the mixture was vigorously shaken to disperse the clay in the interstitial voids between the sand grains. 5 ml of 0.1M calcium chloride solution was added to the mixture to make thick slurries. The slurries were mixed with a glass rod to further homogenize the clays with the sand and then compacted at a relative centrifugal force (RCF) of 1500g. The small amount of supernatant water obtained after centrifuging was removed.

The dispersed systems at irreducible conditions were made by first preparing the water saturated slurries in a 1" by 1" teflon sleeve. The base of the sleeve was

sealed with a covering of teflon tape. 15 grams of sand and desired amount of either clay were mixed in the sleeve and the mixture was saturated with 5 ml of CaCl_2 solution. The slurries were then centrifuged in a Beckman rock core centrifuge at an air/water capillary pressure of 50psi (which also approximately corresponds to 1500g RCF) for 3 hours to drain the free water. The teflon base is permeable to water but prevents any grain loss during centrifugation.

Laminated System

15g of fine sand and 15ml calcium chloride solution were taken in a centrifuge tube and

compacted at 1500g RCF for half hour. The required amount of either clay was added to the sand and centrifuged for 3 hours to compact the systems. Since the sand had already settled before the introduction of clay, there was no elutriation of the clay with sand. Clay, thus, compacted as a laminated layer on top of the sand.

Laminated systems at irreducible conditions were prepared analogously to the dispersed systems at irreducible condition. 15 grams of sand was allowed to settle gravimetrically in 15ml calcium chloride solution in a 1" by 1" sleeve with a sealed base. The required amount of either clay was added to the sand and the systems were centrifuged at 50psi air/brine capillary pressure to drain the free water.

Results and Discussion

Fig 6 and 7 show the T_2 distributions of the dispersed and laminated kaolinite systems at 100% water saturation. Figures 8 and 9 show the corresponding distributions for the dispersed and laminated bentonite systems. For each case, the distributions at irreducible conditions are also shown for comparison. Analysis of the T_2 distributions in figures 6-9 shows that the systems exhibit different relaxation characteristics when the clays are dispersed or layered with sand. For the dispersed systems, the T_2 distributions at 100% water saturation show unimodal spectra. The laminated systems, on the other hand, show bimodal T_2 distributions at 100% water saturation. The fast and slow relaxing peaks in the bimodal distributions correspond to water in the clay and sand layer respectively. Note that the faster relaxation of water in bentonite (~4 ms) compared to that in kaolinite (~25ms) is due to the large interlayer surface area in swelling bentonite clay. Bimodal T_2 distributions for the laminated systems indicate that water populations in the clay and sand layer are decoupled. On the other hand, unimodal T_2 distributions for the dispersed systems indicate that water in the interstitial pores between clay and sand is diffusionally coupled. Figure 10 shows that the relaxation rate of water in dispersed systems shows a linear dependence with the clay content. Extrapolation of the linear relationship to zero clay fractions has an

intercept close to the relaxation rate of water in sand-only system. Thus, the relaxation rate of water in the dispersed systems can be expressed as

$$\frac{1}{T_2} = \frac{\rho_{\text{sand}} S_{\text{sand}} + \rho_{\text{clay}} S_{\text{clay}}}{V_{\text{total}}} \quad (7)$$

where $\rho_{\text{sand}} S_{\text{sand}}$ and $\rho_{\text{clay}} S_{\text{clay}}$ are the products of relaxivity and surface area for sand and clay respectively and V_{total} is the total volume of water. Since the relaxation rate is simultaneously influenced by both clay and sand surface areas, we do not observe distinct peaks for irreducible and free water.

A quantitative estimate of characteristic lengths required for the systems to be in coupled or decoupled regime can be obtained from the analysis of α for the systems. For coupled systems, α is given as (Anand and Hirasaki, 2005)

$$\alpha = \frac{\rho S_{\text{active}} / V_{\text{total}}}{D / L_2^2} \quad (8)$$

Since the surface area of the sand is negligible compared to that of the clays, relaxation at

the surface of the sand grains can be neglected in comparison to that on the clay surface

$$\rho S_{\text{active}} \approx \rho_{\text{clay}} S_{\text{clay}} \quad (9)$$

For total coupling regime α is less than 1. Thus,

$$L_2 < \sqrt{\frac{DV_{\text{total}}}{\rho_{\text{clay}} S_{\text{clay}}}} \quad (10)$$

for totally coupled regime. For decoupled regime α is greater than 50 (based on $\phi/\beta = 0.97$ in equation 2). Thus,

$$L_2 > \sqrt{\frac{50DV_{\text{total}}}{\rho_{\text{clay}} S_{\text{clay}}}} \quad (11)$$

for decoupled regime. From the values of relaxivity and surface area of the clays (Table 1), we find that the characteristic diffusion length for total coupling regime should be less than 15 μm and 5 μm for kaolinite and bentonite respectively. Since these values are of the order of the interstitial pores between the sand grains with grain radius of 50 μm , irreducible and free water in dispersed systems are coupled with each other. For the decoupled regime, the diffusion length should be greater than 110 μm and 35 μm for kaolinite and bentonite respectively. Since the separation between clay and sand layer is of the order of two centimeters in the

laminated systems, we observe distinct peaks for the irreducible clay water and free water.

Estimation of Irreducible water saturation

Irreducible water for the sand-clay systems consists of both clay bound and capillary bound water. The two populations are in close physical proximity and thus, relax at same rates due to fast diffusional exchange (Allen et al, 1998). If, however, the distance between the irreducible and free water is large, the two populations can relax independently with distinct relaxation times. This was experimentally demonstrated for the laminated systems which showed separate peaks for clay and sand layers at 100% water saturation. Thus, for laminated systems a sharp cutoff is applicable to partition the T_2 distributions into the irreducible and free water fractions. Note that in the model shaly sands considered in this study, there will be an overestimation of irreducible water if a sharp $T_{2,cutoff}$ is applied at the valley between clay and sand peak. This is due to the additional compaction of the clays during centrifugation as the water squeezes out of the clay layer.

The dispersed systems, on the other hand, are in coupled regime and the application of a sharp $T_{2,cutoff}$ to estimate the irreducible water would give wrong estimates. For example, application of conventional 33 ms cutoff would overestimate the irreducible saturation in the case of bentonite and underestimate in the case of kaolinite particularly for cases with high clay content. The coupled response necessitates the application of inversion technique for accurate estimation of irreducible saturation. Since the systems are in total coupled regime, the irreducible saturation is given by the ratio of modes of relaxation time peaks at irreducible saturation and 100% water saturation (Anand and Hirasaki, 2005),

$$\beta = \left(\frac{T_{2,\mu}}{T_{2,macro}} \right)_{\alpha < 1} \quad (12)$$

Figure 11 shows the cross plot of the irreducible saturation obtained using equation (12) with that obtained experimentally from NMR measurements at irreducible saturation. The estimates fall within 4% of the average absolute deviation proving the applicability of the technique. The higher irreducible saturation for bentonite systems than for kaolinite is due to the presence of interlayer water.

These experiments also explain the apparent differences in the results reported by Matteson et al (2000) and Prammer et al (1996). The absence of peak at fast relaxation time for the clay slurries which can be interpreted as clay bound water is due to fast diffusional exchange between clay bound and free water. However,

when clays are present as laminated layers or as pore filling masses, the separation between irreducible water and free water is large enough to decouple the NMR responses. Thus, some sandstones can display distinct peaks for clay and free water with the clay response being proportional to the CEC of the clay, as was indeed observed by Prammer et al (1996).

CONCLUSIONS

NMR diffusional coupling between micro and macropores is studied for the effects of temperature and clay distribution. The effect of temperature on pore coupling is quantified by incorporating the temperature dependence of surface relaxivity and diffusion coefficient in the definition of coupling parameter (α). NMR measurements with model grainstones and carbonate core show that the systems transition to more strongly coupled regimes with rise in temperature. This increase in coupling is quantified by a decrease in values of α with temperature. The results also explain the anomalous decrease in relaxation time of macropore with temperature even as relaxivity decreases. Inversion technique is applied to obtain accurate estimates of irreducible saturation for the systems at all temperatures.

Diffusional coupling between irreducible and free water in shaly sands is determined by the distribution of clays with the sand. Experiments with model shaly sands show that irreducible and free water are coupled when clays are dispersed with sand and decoupled when clays form a lamination on sand. From the values of α required for systems to be in coupled and decoupled regimes, a quantitative estimate of the characteristic diffusion lengths can be obtained. Application of inversion technique accurately estimates irreducible saturation for the dispersed case.

REFERENCES

- 1) Allen, D.F. et al. (1998), "Petrophysical Significance of the Fast Components of the NMR T_2 spectrum in Shaly Sands and Shales", *SPE 49307*, SPE ATCE, LA
- 2) Anand, V. and Hirasaki, G.J. (2005), "Diffusional Coupling between Micro and Macroporosity for NMR Relaxation in Sandstones and Grainstones", *Proceedings of SPWLA 46th Annual Logging Symposium*, New Orleans, LA.
- 3) Coates, G.R. et al (1994), "Applying Pulse Echo NMR to Shaly Sand Formation Evaluation", *paper presented at 1994 SPWLA Convention*, Tulsa, Oklahoma.
- 4) GodeFroy, S. et al. (2001), "Temperature Effect on NMR Surface Relaxation", *SPE 71700*, presented at SPE ATCE, LA (30 Sep-3 Oct).
- 5) Holz, M. et al (2000), "Temperature dependent self-diffusion coefficients of water and six selected molecular fluids for calibration in accurate ^1H NMR PFG

measurements”, *Physical Chemistry Chemical Physics*, Web published, 3rd October.

- 6) Matteson, A. et al (2000), “NMR Relaxation of Clay/Brine Mixtures”, *SPE Reservoir Eval & Eng*, 3(5), 408-413.
- 7) Prammer, M.G. et al (1996), “Measurements of Clay-Bound Water and Total Porosity by Magnetic Resonance”, *The Log Analyst*, 37, No 6, 61.
- 8) Ramakrishnan, T.S. et al (1999), “New Interpretation Methodology Based on Forward Models for Magnetic Resonance in Carbonates”, *Proceedings of SPWLA 40th Annual Logging Symposium*, May 30-June 3.

ACKNOWLEDGEMENTS

The authors would like to acknowledge US DOE DF-PS26-04NT1551 and the Consortium on Processes in Porous media (Baker Hughes, BP, Chevron Texaco, Conoco Philips, Core Labs, Exxon Mobil, Halliburton, Kerr McGee, Marathon, Oil Chem, PTS Labs, Schlumberger, Shell and Statoil) for the financial support.

Table 1: Physical Properties of Fine Sand, Kaolinite and Bentonite clays.

| | Sand | Kaolinite | Bentonite |
|----------------------------------|------|-----------|-----------|
| Surface Area (m ² /g) | 0.2 | 19 | 38 |
| Relaxivity (μm/sec) | 4.7 | 1.4 | 9.2 |

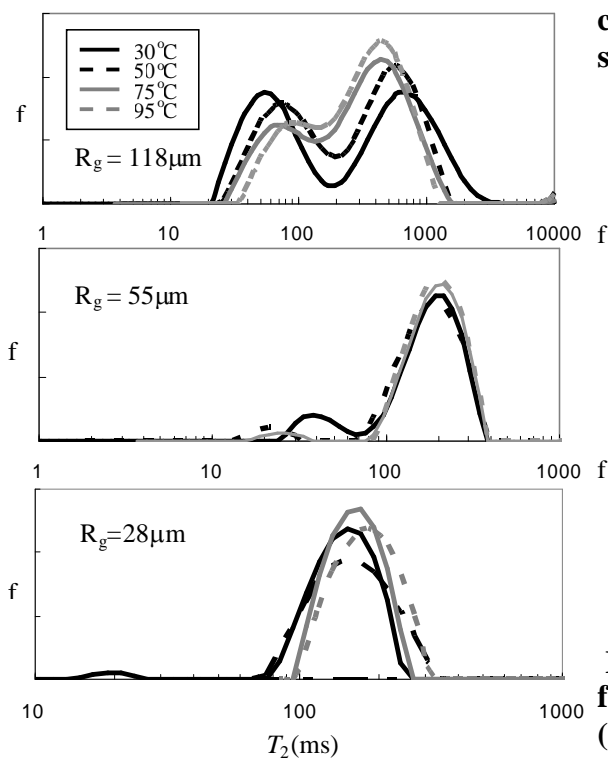


Fig 1: T_2 distributions of silica gels at 100% water saturation and at 30, 50, 75 and 95°C.

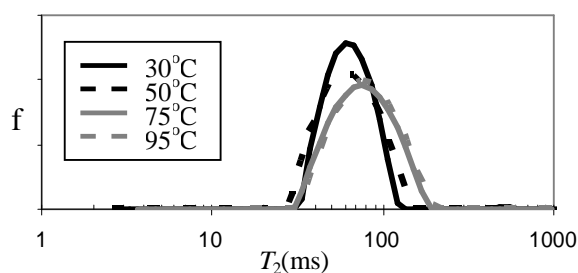


Fig 2: T_2 distributions of the medium coarse silica gel at irreducible water saturation and at 30, 50, 75 and 95°C.

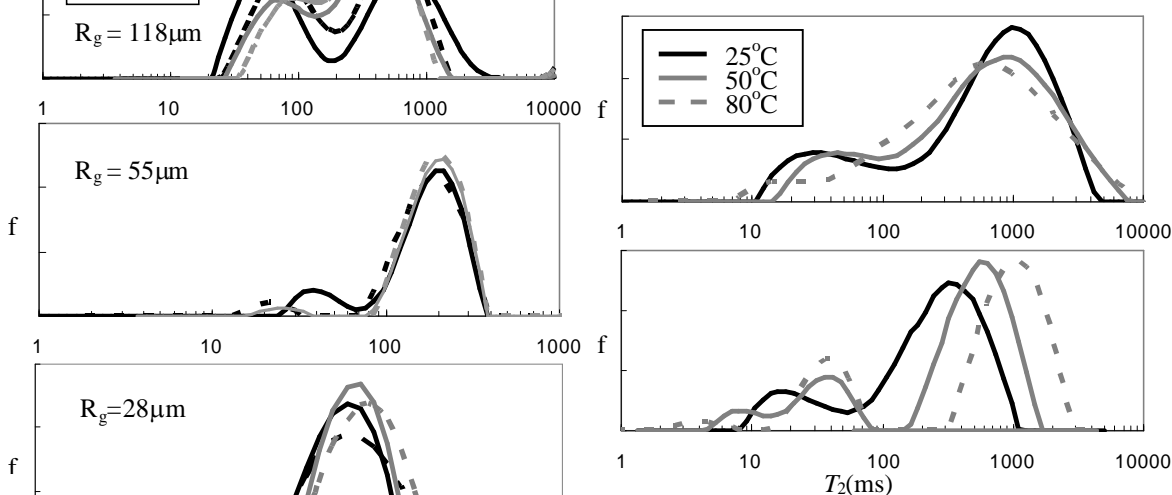


Fig 3: T_2 distributions of the Thamama formation carbonate core at 100% water saturation (upper panel) and irreducible water saturation (lower panel) at 25, 50 and 80°C.

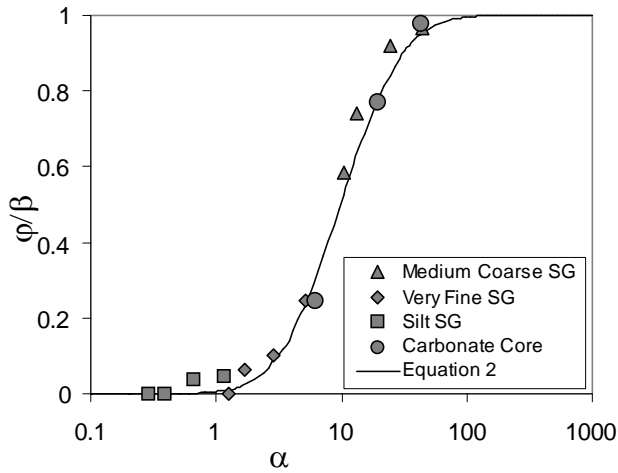


Fig 4: Cross plot of normalized micropore peak amplitude for different systems with α .

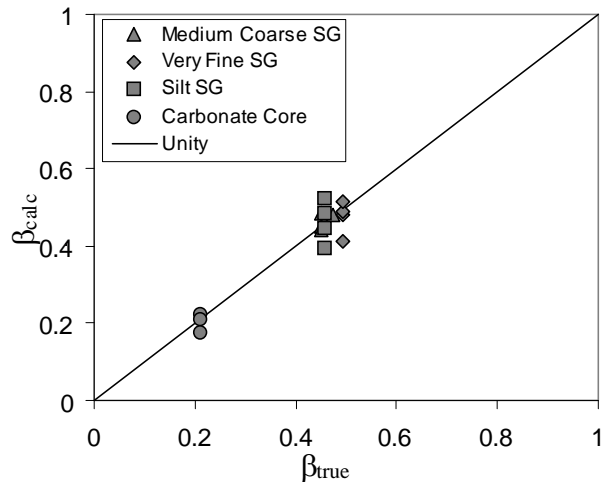


Fig 5: Comparison of the microporosity fraction calculated using the inversion technique and measured experimentally for silica gels and carbonate core.

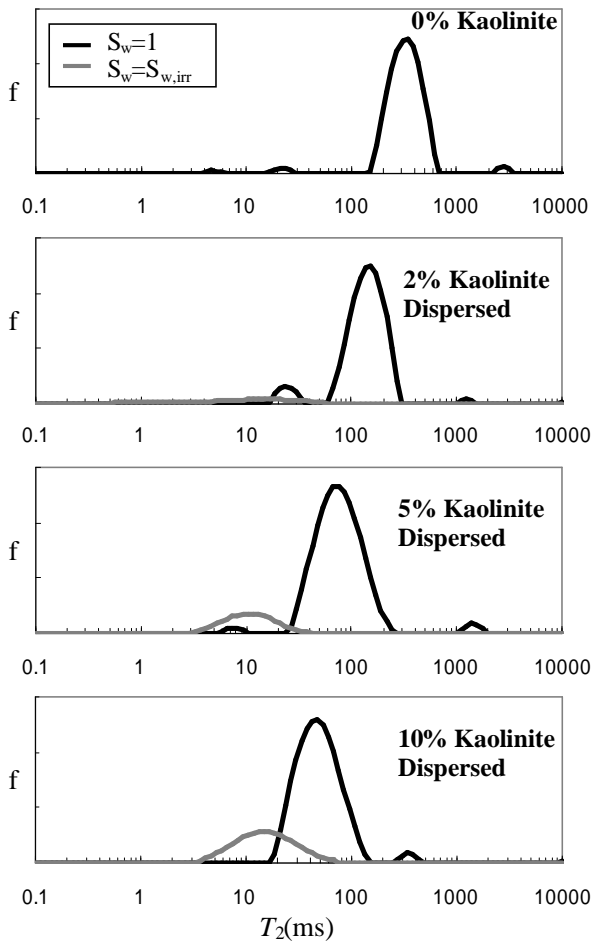


Fig 6: T_2 distribution of dispersed kaolinite-sand systems for different clay weight fractions.

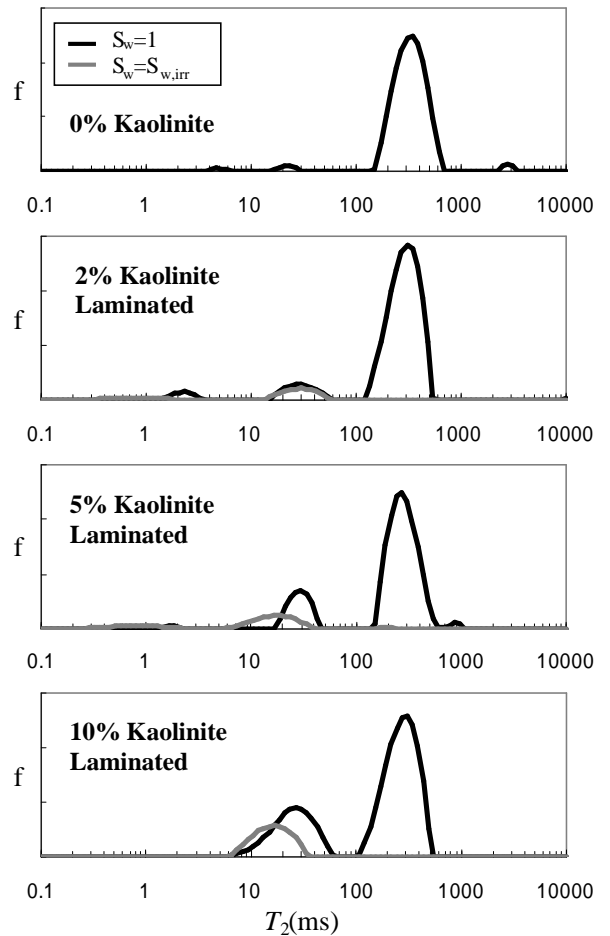


Fig 7: T_2 distributions of laminated kaolinite-sand systems for different clay weight fractions.

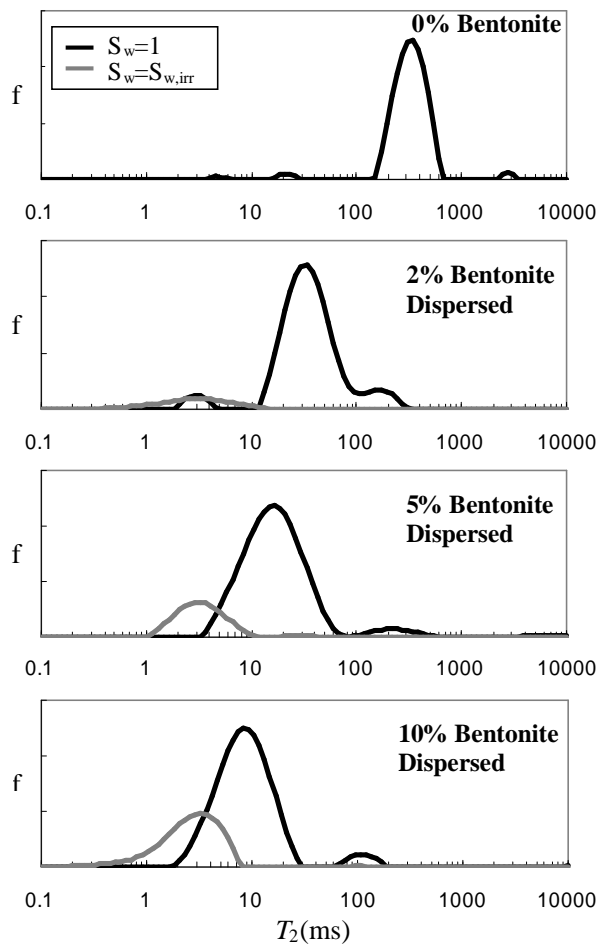


Fig 8: T_2 distributions of dispersed bentonite-sand systems for different clay weight fractions.

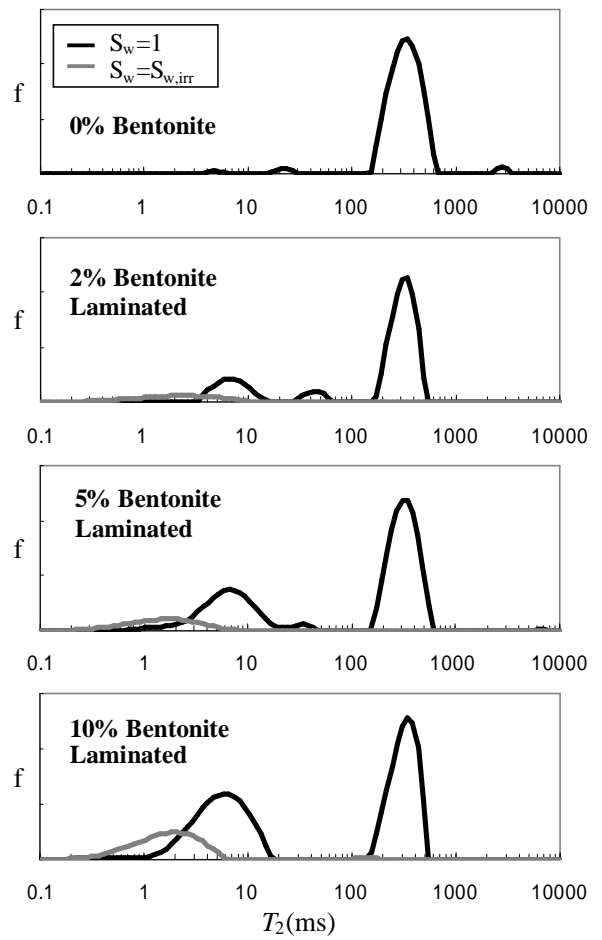


Fig 9: T_2 distributions of laminated bentonite-sand systems for different clay weight fractions.

Subtask 2.5 Quantify the mechanisms responsible for the deviation of surface relaxivity from the mean value for sandstones and carbonates.

Paramagnetic Relaxation in Sandstones: Distinguishing T_1 and T_2 Dependence on Surface Relaxation, Internal Gradients and Dependence on Echo Spacing

**Vivek Anand, George J. Hirasaki
Rice University**

Abstract

Sandstones have T_1/T_2 ratio of 1.6, on the average. Clean silica has a T_1/T_2 ratio of about 1.3. If T_2 changes with echo spacing in a homogeneous applied magnetic field, the change is interpreted to be due to diffusion in internal gradients. We demonstrate that when the paramagnetic material is iron, the increase in the T_1/T_2 ratio above that of clean silica is due to diffusion in internal gradient. Furthermore, when the paramagnetic sites are small enough, no dependence on echo spacing is observed with conventional low-field NMR spectrometers. Echo spacing dependence is observed when the paramagnetic materials become large enough or form a 'shell' around each silica grain such that the length scale of the region of induced magnetic gradients is large compared to the diffusion length during the time of the echo spacing.

The basis for these assertions is a series of experiments and calculations described below. A solution of hydrated Fe^{3+} ion has a T_1/T_2 ratio of unity. Aqueous dispersions of paramagnetic magnetite particles ranging from 4 nm to 16 nm have T_1/T_2 increasing with particle size. No echo spacing dependence is observed. Larger (25nm and 110 nm) magnetite particles coated on 50 μm silica grains have no echo spacing dependence for lower concentration of particles but show echo spacing dependence for larger concentrations. Largest (2,600 nm) magnetite particles mixed with fine sand have echo spacing dependence and T_1/T_2 greater than 2.

These experimental observations are being interpreted by theoretical calculations. The magnetite particles are modeled as paramagnetic spheres. Paramagnetic particles on the surface of silica grains are modeled as individual particles at low concentrations. At high surface concentrations, they are modeled as a thin, spherical shell of paramagnetic material. Calculations show that the system transitions from motionally averaging to localization regime at high surface concentration of paramagnetic particles.

I. Introduction

NMR relaxation measurements have become an important tool to estimate petrophysical properties of rocks. The relaxation of fluids in pores of sedimentary

rocks is primarily governed by magnetic interactions of the fluid molecules with the paramagnetic particles at the pore surfaces. However, the relaxation mechanisms at pore surfaces are not understood completely. Kleinberg et al. (1993) studied the low field (2MHz) NMR response of several sandstones and found that the T_1/T_2 ratio varied over a large range of 1 to 2.6. For most cases, no echo spacing dependence of the T_2 relaxation was observed. Based on these and other observations, Kleinberg et al. (1994) suggested that contribution of scalar interaction between fluid molecules and surface paramagnetic sites to transverse relaxation leads to a T_1/T_2 ratio greater than unity. While scalar coupling is an important relaxation mechanism for paramagnetic Mn^{2+} ions, it is not so for ferric ions and the T_1/T_2 ratio of protons in ferric solutions is unity (Morgan et al., 1959, Soloman, I., 1955). Thus, scalar coupling alone can not explain the T_1/T_2 ratio of sandstones when the predominant paramagnetic mineral is iron.

In addition, several studies with fluid-saturated sandstones and porous media have reported a strong dependence of transverse relaxation on echo spacing (Zhang et al., 2001, Fantazzini et al., 2005). However, the dependence is not quadratic as predicted by the classical Bloch formula but rather quasi-linear. A theoretical and experimental understanding of the principles governing the relaxation characteristics of the sedimentary rocks is, thus, needed for accurate interpretation of NMR measurements.

We explain that the observed range of T_1/T_2 ratios and echo spacing dependence of transverse relaxation in sandstones can arise due to diffusion in internal magnetic field inhomogeneities. Internal field inhomogeneities are induced due to differences in magnetic susceptibility of the pore fluids and paramagnetic minerals on the pore surfaces. Figure 1 shows the magnetic field lines in the presence of a paramagnetic sphere of unit radius with susceptibility 10^6 times that of the surrounding medium. The field lines concentrate around the equator and the poles of the paramagnetic sphere. In porous media large field inhomogeneities can occur around corners or sharp discontinuities in pore system (Zhang et al., 2003, Brown et al., 1993). Diffusion of fluid molecules in such inhomogeneous fields leads to additional relaxation of transverse magnetization due to dephasing. The additional relaxation is called secular relaxation and is defined as the difference in the transverse and longitudinal relaxation rates,

$$\frac{1}{T_{2,sec}} = \frac{1}{T_2} - \frac{1}{T_1} \quad (1)$$

At present, there is no exact theory which treats restricted diffusion in porous media in a general inhomogeneous field. However, the simplest case of diffusion in constant gradient in idealized pore geometries has been extensively studied in the past. De Swiet et al (1993) described three characteristic length scales that characterize secular relaxation in a constant gradient g :

- 1) Pore structural length, L_s

- 2) Dephasing length L_g defined as the distance over which the spins have to diffuse in order to dephase by 1 radian given as

$$L_g = \sqrt[3]{\frac{D}{\gamma g}} \quad (2)$$

where D is the diffusivity of the fluid and γ is the proton gyromagnetic ratio

- 3) Diffusion length, L_d , defined as

$$L_d = \sqrt{D\tau_E} \quad (3)$$

where τ_E is the echo spacing for CPMG pulse sequence. Depending on the smallest length scales, secular relaxation can be classified into three relaxation regimes of motionally averaging, localization and free diffusion. We demonstrate that the conditions for the relaxation regimes can be extended for general inhomogeneous fields in terms of three characteristic time scales. The characteristic time scales are independent of the particular choice of field distribution and determine the characteristics of secular relaxation e.g. echo spacing dependence and T_1/T_2 ratio.

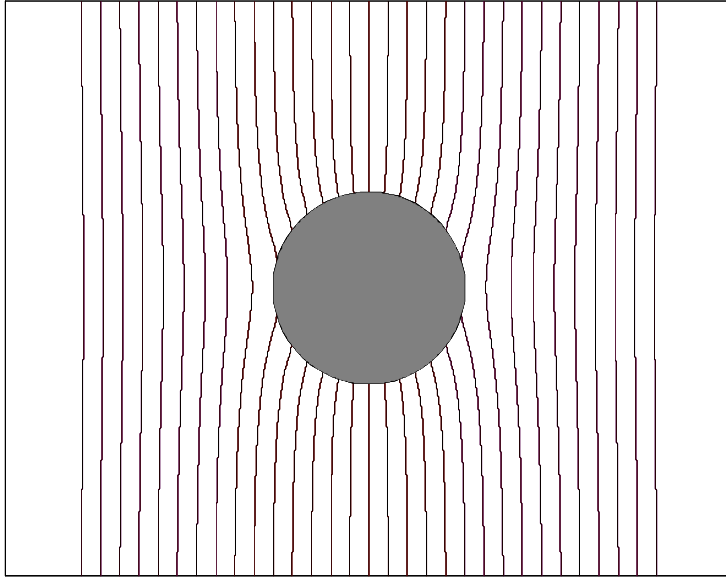


Figure 1: Magnetic field lines in the presence of paramagnetic sphere with magnetic susceptibility 10^6 times that of the surrounding medium. The field lines are mostly concentrated around the poles and the equator of the sphere.

This report is organized as follows. In section II, we provide a generalized theory of relaxation regimes in inhomogeneous fields. The theory is independent of the particular choice of inhomogeneous field distribution. The two special cases of secular relaxation in constant gradient and relaxation by paramagnetic particles are described for each regime to explain the correspondence between the characteristic parameters. In section III, random walk simulations of secular

relaxation in inhomogeneous fields induced by paramagnetic particles are shown to quantitatively explain the characteristics of the relaxation regimes. In section IV, a series of NMR measurements with paramagnetic magnetite particles spanning a size range of almost four orders of magnitude are described that physically explore the relaxation regimes. The simulation and experimental results of sections III and IV form the basis for explaining the relaxation characteristics in sandstones.

II. Generalized Secular Relaxation Theory

Transverse relaxation due to dephasing in magnetic field inhomogeneities induced either internally due to susceptibility differences or externally due to applied gradients is characterized by three time scales

1) time taken for significant dephasing, τ_H , defined as the inverse of the spread of the Larmor frequencies ($\delta\omega$) existing in the system

$$\tau_H = \frac{1}{\delta\omega} \quad (4)$$

2) diffusional correlation time, τ_R , defined as the time taken to diffusively average the inhomogeneities.

$$\tau_R = \frac{L^2}{D} \quad (5)$$

where L is the characteristic length of field inhomogeneity in the system and

3) half echo spacing used in CPMG pulse sequence, τ_E , given as

$$\tau_E = \frac{TE}{2} \quad (6)$$

where TE is the echo spacing for the CPMG sequence. Decay of transverse magnetization can be characterized by three relaxation regimes based on the smallest of the three characteristic time scales:

A. Motionally Averaging regime

Motionally averaging regime is characterized by fast diffusion of the protons such that the inhomogeneities in magnetic field are motionally averaged. This occurs when the diffusional correlation time is much smaller compared to half echo spacing and the time taken for significant dephasing due to presence of field inhomogeneities. Mathematically, the conditions of motionally averaging regime are

$$\begin{aligned} \tau_R &\ll \tau_H \\ \tau_R &\ll \tau_E \end{aligned} \quad (7)$$

An important characteristic of the motionally averaging regime is that the secular relaxation rate is independent of the echo spacing. Since the diffusional correlation time is much smaller than the echo spacing, field inhomogeneities are motionally averaged in time much smaller compared to the echo spacing.

A.1 Motionally averaging in constant gradient

For the case of restricted diffusion in constant gradient g in a one dimensional pore of structural length L_s , the spread in Larmor frequencies and correlation time are given as

$$\delta\omega = \gamma g L_s \quad (8a)$$

$$\tau_R = \frac{L_s^2}{D} \quad (8b)$$

using $L=L_s$ in equation (5). Substituting equations (8) in equations (7), we obtain the conditions for motionally averaging in constant gradient in terms of the characteristic length scales

$$L_s \ll L_g \quad (9)$$

$$L_s \ll L_d$$

Equations (9) imply that motionally averaging regime is observed when pore structural length is small compared to the diffusion length during time τ_E (L_d) and the dephasing length (L_g) defined in equations (2) and (3) respectively. Thus, the spins typically diffuse several times the pore size during the measurement and any magnetic field inhomogeneities are motionally averaged by their motion.

Neumann (1974) derived the expression for secular relaxation rate in motionally averaging regime by assuming the distribution of phase shifts to be Gaussian given as

$$\frac{1}{T_{2,\text{sec}}} = \frac{L_s^4 \gamma^2 g^2}{120D} \quad (10a)$$

Using equations (8), equation (10a) can be expressed in terms of characteristic parameters

$$\frac{1}{T_{2,\text{sec}}} = \frac{1}{120} (\delta\omega)^2 \tau_R \quad (10b)$$

Thus, the relaxation rate shows a quadratic dependence on the field inhomogeneity ($\delta\omega$) in the motionally averaging regime. The quadratic dependence on field inhomogeneity was also derived for an arbitrary field in one-dimensional restricted geometry by Tarczón et al (1985).

A.2 Motionally averaging in internal fields induced by spherical paramagnetic particles

A paramagnetic particle of magnetic susceptibility different from that of the surrounding medium induces internal magnetic field gradients when placed in an external magnetic field. Potential theory can be used to estimate the induced internal fields in idealized geometries. The field induced by a paramagnetic sphere of radius R_0 placed in an external magnetic field is given as (Menzel, 1955)

$$\frac{\vec{B}}{|\vec{B}_0|} = \cos \theta \left(1 + \frac{2(k-1)R_0^3}{(k+2)r^3} \right) \vec{r} - \sin \theta \left(1 - \frac{(k-1)R_0^3}{(k+2)r^3} \right) \vec{\theta} \quad (11)$$

where $k = (1 + \chi_{\text{sphere}}) / (1 + \chi_{\text{medium}})$, χ_{sphere} and χ_{medium} are the magnetic susceptibility of the sphere and medium respectively. θ is the azimuthal angle from the direction of \vec{B}_0 and r is the radial distance from the centre of the paramagnetic sphere. $\vec{\theta}$ and \vec{r} are the unit vectors in the azimuthal and radial direction respectively.

Thus, the component of the induced field along the direction of external field B_0 induced by a sphere of radius R_0 is given as

$$B_\delta = B_0 \left(\frac{k-1}{k+2} \right) (3 \cos^2 \theta - 1) \frac{R_0^3}{r^3} \quad (12)$$

We consider only the component of the internal field along the external magnetic field since this determines the precession frequency (Brown et al, 1993). Figure 2 shows the contour plots of dimensionless internal magnetic field defined as

$$B_\delta^* = \frac{B_\delta}{[(k-1)/(k+2)]B_0} = \left(\frac{3 \cos^2 \theta - 1}{r^{*3}} \right) \quad (13)$$

where the radial distance r^* is normalized with respect to the radius of the paramagnetic sphere.

$$r^* = \frac{r}{R_0} \quad (14)$$

The internal field is maximum at the surface of the particle (positive at poles and negative at equator) and falls as the cube of the radial distance from the center. Thus, the range of Larmor frequencies in the system is the difference in the polar and equatorial fields at the surface of the sphere

$$\delta\omega = \frac{3(k-1)}{(k+2)} \gamma B_0 \quad (15)$$

The diffusional correlation time is defined as the time taken by spins to diffuse a characteristic length scale of field inhomogeneity. Thus, for the case of the induced fields in the presence of a paramagnetic sphere, the correlation time is the time to diffuse a distance of the order of radius of the sphere (R_0)

$$\tau_R = \frac{R_0^2}{D} \quad (16)$$

The conditions for motionally averaging regime require that the correlation time be much smaller than the time for inhomogeneous dephasing and echo spacing. In terms of the system parameters, motionally averaging regime is observed for paramagnetic relaxation when the following conditions are satisfied

$$\frac{R_0^2}{D} \ll \tau_H = \frac{1}{\delta\omega} = \frac{(k+2)}{3(k-1)\gamma B_0} \quad (17)$$

$$\frac{R_0^2}{D} \ll \tau_E$$

The quantum-mechanical outer sphere theory (Gillis et al., 1987) suggests that when conditions for motionally averaging are satisfied, the secular relaxation rate is given by

$$\frac{1}{T_{2,OS}} = \frac{4}{9} f (\overline{\delta\omega})^2 \tau_R = \frac{16}{45D} f \left(\frac{(k-1)}{(k+2)} \gamma B_0 R_0 \right)^2 \quad (18)$$

where f is the volume fraction of the paramagnetic particles and $\overline{\delta\omega}$ is the root mean square frequency at the surface of the sphere given as

$$\overline{\delta\omega} = \sqrt{\frac{4}{5} \frac{(k-1)}{(k+2)}} \gamma B_0 \quad (19)$$

Equation (18) is derived by solving quantum mechanical equations for the “flip rates” of the protons using time dependent perturbation theory (Gillis et al., 1987). Note the similar functional form of the secular relaxation rate predicted by the outer sphere theory (equation 18) and equation 10b.

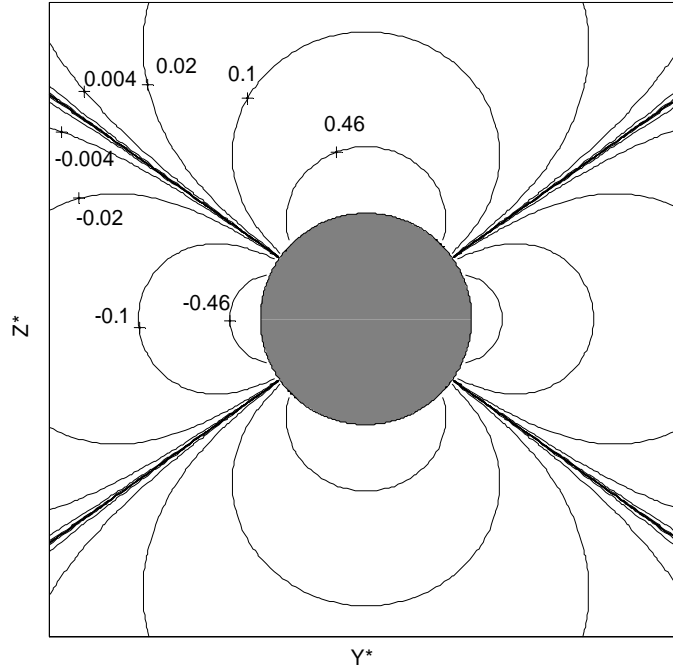


Figure 2: Contour plots of z component of internal magnetic field (dimensionless) induced by a unit paramagnetic sphere in a vertical plane passing through the center of the sphere. The external magnetic field is applied in the vertical z direction.

B. Free diffusion regime

Free diffusion regime is valid when half echo-spacing is the smallest of the characteristic time scales. The effect of restriction as well as large field inhomogeneities is not felt by the spins in the time of echo formation. Thus, the spins dephase as if diffusing in an unrestricted medium. The conditions for free diffusion regime state

$$\begin{aligned}\tau_E &\ll \tau_H \\ \tau_E &\ll \tau_R\end{aligned}\quad (20)$$

B.1 Free diffusion in constant gradient

For the case of diffusion in constant gradient in a pore, free diffusion regime of transverse relaxation may arise for small echo spacings such that the spins do not experience the restriction effects. The conditions for free diffusion inside a pore of length L_s can be obtained in terms of characteristic length scales defined in equations (2) and (3) by substituting equation (8) in equation (20) given as

$$\begin{aligned}L_d &\ll L_g \\ L_d &\ll L_s\end{aligned}\quad (21)$$

Thus, the free diffusion regime arises when the diffusion distance in τ_E is much small compared to dephasing length and pore length. In this regime, the secular relaxation is given by the classical Bloch expression (Carr and Purcell, 1954) for unrestricted diffusion in a constant gradient

$$\frac{1}{T_{2,\text{sec}}} = \frac{\gamma^2 g^2 \tau_E^2 D}{3}\quad (22)$$

The relaxation rate, thus, shows a quadratic dependence with echo spacing as long as the conditions for free diffusion regime are satisfied.

B.2 Free diffusion in internal fields induced by paramagnetic particles

The free diffusion regime has been described as the “weak magnetization regime ($\delta\omega \cdot \tau_E < 1$)” in the medical resonance imaging (MRI) literature mentioned below.

The regime arises physically when weakly magnetized paramagnetic particles are used as contrast agents for medical imaging or in biological tissues with iron rich cells or deoxygenated red blood cells. Jenson and Chandra (2000) derived the expression for the secular relaxation in weak field inhomogeneities by assuming a Gaussian field correlation function. Their solution was modified by Brooks et al (2001) to calculate the relaxation rate by weakly magnetized paramagnetic particles which is given as

$$\frac{1}{T_{2,\text{FD}}} = \frac{2.25 f (\overline{\delta\omega})^2 \tau_E^2}{\tau_R} = \frac{9}{5} f \left[\frac{(k-1)}{(k+2)} \gamma B_0 \right]^2 \tau_E^2 \frac{D}{R_0^2}\quad (23)$$

The above expression (called the Mean Gradient Diffusion Theory, MGDT) shows the similar quadratic dependence of secular relaxation rate on the echo spacing as the expression for unrestricted diffusion in constant gradient (equation 22). However, the relaxation rate shows an inverse squared dependence on the paramagnetic particle size which is opposite to that in the motionally averaging

regime (equation 18). This is because the mean squared internal field gradient given as

$$\langle g^2 \rangle = \frac{9 \overline{f(\delta\omega)^2}}{\gamma^2 R_0^2} \quad (24)$$

decreases with the increase in particle size (Brooks et al., 2001). The mean gradient in equation (24) is calculated by integrating the square of gradient of the magnetic field induced by a single paramagnetic particle (equation 11) over infinite space.

C. Localization Regime

Localization regime of secular relaxation arises when dephasing time is small compared to the diffusion correlation time and half echo spacing. The conditions for localization regime are

$$\begin{aligned} \tau_H &\ll \tau_R \\ \tau_H &\ll \tau_E \end{aligned} \quad (25)$$

C.1 Localization regime in constant gradient

Using equations (8) for $\delta\omega$ and τ_R for restricted diffusion in constant gradient in a pore of length L_s , equation (25) reduce to the following equations in special cases

$$\begin{aligned} L_g &\ll L_d \\ L_g &\ll L_s \end{aligned} \quad (26)$$

The dephasing length is the smallest characteristic length in the localization regime. Thus, the spins typically dephase a large amount during the measurement time and do not contribute to the total magnetization. The signal comes primarily from the spins near the boundaries which see smaller change in magnetic field due to reflection (Sen et al., 1999). Localization regime is most difficult to treat theoretically because of the presence of large gradients. De Swiet et al. (1993) have shown that at long times, the echo amplitude decays as

$$\frac{M(g, \tau_E)}{M_0} = c \frac{L_g}{L_s} e^{-a_1 (L_d/L_g)^2} \quad (27)$$

where $a_1=1.0188\dots$ and $c=5.8841\dots$ for parallel plates. The exponent is independent of the pore geometry but the prefactor is modified for other geometries.

C.2 Localization regime in internal fields induced by paramagnetic particles

Secular relaxation in localization regime has also been discussed in the MRI literature. The regime arises physically for relaxation in presence of strongly magnetized contrast agents such as superparamagnetic particles for which $\delta\omega\tau_E > 1$. Gillis et al (2002) proposed a semi-empirical model for decay in internal fields induced by strongly magnetized spheres. In their model, the region surrounding the paramagnetic particle is divided in two regions: an inner region with very strong internal gradients and an outer region with only weak gradients. The boundary radius (R') between the inner and outer region is related to the system parameters as (Gillis et al., 2002)

$$\frac{R'}{R_0} = \left(\frac{\overline{\delta\omega\tau_E}}{a + bf\overline{\delta\omega\tau_E}} \right)^{1/3} \quad (28)$$

Since the gradients in outer region are weak, Gillis et al. (2002) suggested that relaxation can be described by theory for relaxation by weakly magnetized particles. Thus, the relaxation rate in the outer region ($r > R'$) is given by equation (23) with a modification to account for the excluded volume of the inner region shown below

$$\frac{1}{T_{2,Loc}} = \frac{2.25f(\overline{\delta\omega})^2\tau_E^2}{\tau_R} \left(\frac{\overline{\delta\omega\tau_E}}{a + bf\overline{\delta\omega\tau_E}} \right)^{-5/3} \quad (29)$$

where a and b are adjustable parameters. Gillis et al. (2002) calculated the values of the parameters a ($=1.34$) and b ($=0.99$) by fitting equation (29) to numerical simulations of transverse relaxation in the presence of strongly magnetized particles.

In the inner region ($r < R'$), the spins experience very strong gradient and dephase very fast. Due to very fast relaxation, they do not contribute much to the macroscopic relaxation rate and equation (29) can provide a good measure of relaxation rate for strongly magnetized particles.

D. Parametric representation of relaxation regimes

The asymptotic regimes of secular relaxation are schematically shown in figure 3 as a function of two dimensionless parameters: $\delta\omega\tau_R$ and $\delta\omega\tau_E$. The boundaries between the asymptotic regimes are drawn at the equality between the characteristic times. Thus, the regimes are typically valid in the regions away from the boundaries.

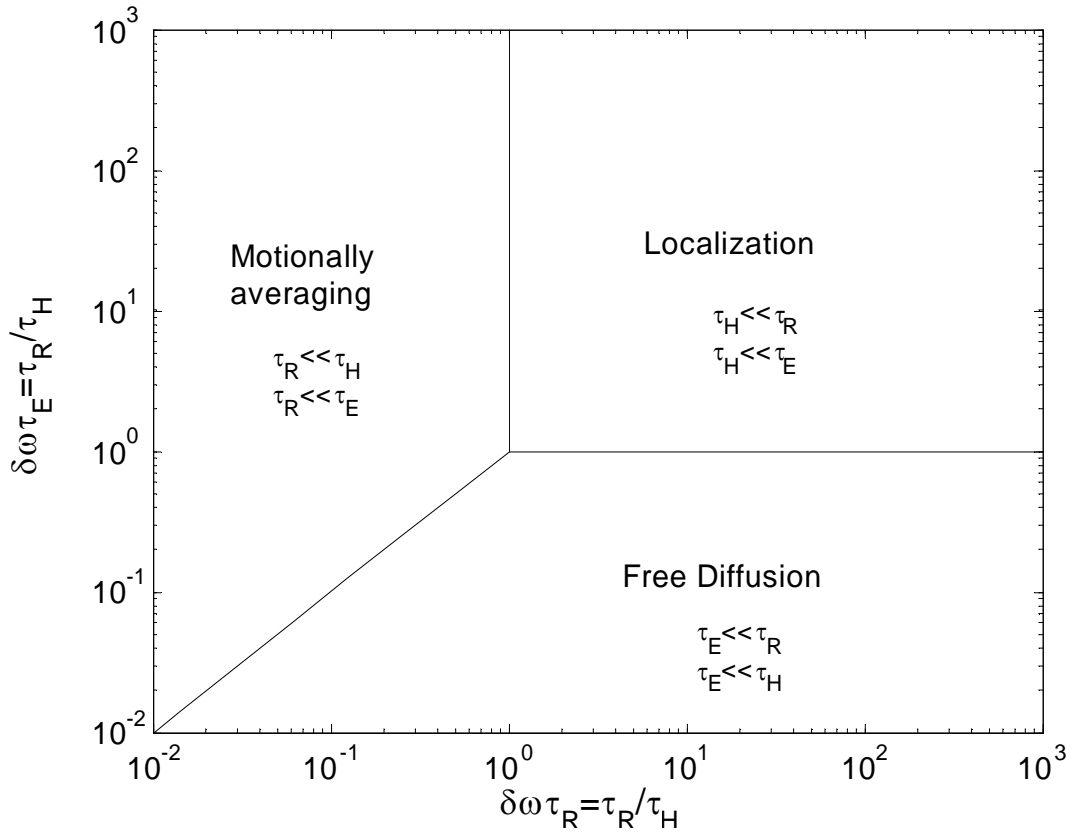


Figure 3: Schematic diagram of asymptotic relaxation regimes in the $(\delta\omega\tau_R, \delta\omega\tau_E)$ parameter space.

III. Random Walk simulations

The decay of transverse relaxation due to diffusion in inhomogeneous fields is studied with the help of random walk simulations. The simulations provide a convenient method to quantitatively study the characteristics of asymptotic regimes. We begin by numerically simulating the secular relaxation in inhomogeneous field induced in the annular region of a paramagnetic particle. Surface relaxation at the inner radius (R_0) and outer radius (R_e) of the annulus is neglected. Measurement of spin-echoes by CPMG pulse sequence technique with ideal pulses is simulated.

The relaxation of transverse magnetization (M) in an inhomogeneous field B_z after the application of first $\pi/2$ pulse is given by the Bloch- Torrey equations

$$\frac{\partial M}{\partial t} = -i\gamma B_z M - \frac{M}{T_{2,B}} + D\nabla^2 M \quad (30)$$

where D is the diffusivity of the fluid and $T_{2,B}$ is the bulk relaxation time. No surface relaxation at the inner and outer boundaries implies

$$\vec{n} \cdot \nabla M = 0 \text{ at } r = R_0. \quad (31)$$

$$\vec{n} \cdot \nabla M = 0 \text{ at } r = R_e. \quad (32)$$

Here r is the radial distance from the center and \vec{n} is the outward pointing normal.

By substituting $M = M_x + iM_y$ and $M = m \cdot e^{\left(-i\omega_0 t + \frac{-t}{T_{2B}}\right)}$ (where $\omega_0 = \gamma B_0$), equation (30) can be expressed as

$$\frac{\partial m}{\partial t} = -i\gamma B_{\alpha} m + D\nabla^2 m \quad (33)$$

where $B_{\alpha} = B_z - B_0$. m represents the transverse magnetization with the precession at Larmor frequency (ω_0) and bulk relaxation factored out (Zhang and Hirasaki, 2003)

Let us now introduce the following dimensionless variables

$$r^* = \frac{r}{R_e}, \quad t^* = \frac{t}{t_0}, \quad m^* = \frac{m}{M_0}$$

where t_0 is a characteristic time and M_0 is the initial magnetization. Substituting the dimensionless variables and equation (12) for field induced by a paramagnetic sphere in (33), we get

$$\frac{\partial m^*}{\partial t^*} = -i \frac{(3 \cos^2 \theta - 1)}{r^{*3}} \left(\frac{\gamma B_0 (k-1)}{(k+2)} \left(\frac{R_0}{R_e} \right)^3 t_0 \right) m^* + N_D \nabla^{*2} m^* \quad (34)$$

where dimensionless group N_D is defined as

$$N_D = \frac{D t_0}{R_e^2} \quad (35)$$

Now, the characteristic time t_0 is chosen such that the coefficient of the second term in equation (34) is unity. Thus,

$$t_0 = \left[\frac{(k+2)}{\gamma B_0 (k-1)} \right] \frac{1}{f} \quad (36)$$

where f is the volume fraction of the paramagnetic particle given as

$$f = \left(\frac{R_0}{R_e} \right)^3 \quad (37)$$

The term in parenthesis in the expression for t_0 (equation 36) is the reciprocal of the equatorial frequency shift (magnitude) at the surface of the paramagnetic sphere. This can be verified by using $\theta = \pi/2$ and $r = R_0$ in equation (12).

$$\Rightarrow \delta\omega_{eqt} = \frac{(k-1)\gamma B_0}{(k+2)} \quad (38)$$

Thus, t_0 can be expressed as reciprocal of the product of equatorial frequency shift and the volume fraction.

$$\Rightarrow t_0 = \frac{1}{\delta\omega_{eqt}.f} \quad (39)$$

Equation (39) is used to normalize secular relaxation rates for the experimental systems as described in Section IV. The dimensionless parameter, N_D , can also be expressed in terms of system parameters by substituting equation (36) in equation (35)

$$N_D = \frac{Dt_0}{R_e^2} = \frac{(k+2)DR_e}{(k-1)\gamma B_0 R_0^3} \quad (40)$$

Thus, the governing Bloch equation in dimensionless form becomes

$$\frac{\partial m^*}{\partial t^*} = -i \frac{(3\cos^2\theta - 1)}{r^{*3}} m^* + N_D \nabla^{*2} m^* \quad (41)$$

The dimensionless boundary conditions are

$$\frac{\partial m^*}{\partial r^*} = 0 \text{ at } r^* = 1 \quad (42)$$

$$\frac{\partial m^*}{\partial r^*} = 0 \text{ at } r^* = \frac{R_0}{R_e} \quad (43)$$

In addition, the application of π pulse at dimensionless half-echo time τ_E^* reverses the y component of the magnetization. Thus,

$$m^* |_{t^*_-} = \overline{m^*} |_{t^*_+} \quad \text{at } t^* = \tau_E^*, 3\tau_E^*, 5\tau_E^* \dots \tau_E^* \quad (44)$$

τ_E^* is the dimensionless echo spacing given as

$$\tau_E^* = \tau_E / t_0. \quad (45)$$

A. Algorithm

A continuous random walk algorithm is applied to model T_2 relaxation of spins (equations 41-45) diffusing in an inhomogeneous internal field $B_{\delta z}(r, \theta)$ (Weisskoff et al, 1994). The random-walkers are initially distributed uniformly in an annular region of spherical paramagnetic particle. The outer radius was taken to be 20 times the radius of the concentric paramagnetic particle ($R_e = 20R_0$). Since the magnetic field falls as the cube of the particle radius, the field becomes negligible in the region greater than 10 times the inner radius. Thus, an outer radius of $20R_0$ is sufficient to avoid any boundary effects (Weisskoff et al, 2000).

The walkers start with a zero initial phase. In dimensionless time step dt^* , the n^{th} walker at a position (r^*, θ^*) accumulates a phase of $\Delta\phi_n = \omega^*(r^*, \theta^*) dt^*$. The dimensionless Larmor frequency ω^* is given as

$$\omega^*(r^*, \theta^*) = \frac{\omega(r, \theta)}{1/t_0} = \frac{(3 \cos^2 \theta - 1)}{r^{*3}} \quad (46)$$

After every time step dt^* , the stochastic diffusion of the proton is simulated by choosing a random displacement with zero mean and standard deviation $\sqrt{2N_D dt^*}$ in the x, y and z directions in Cartesian coordinates. The clock is incremented by dt^* after every time step.

At the time of the application of π pulses $t^* = \tau_E^*, 3\tau_E^*, 5\tau_E^* \dots$, the phases of all random walkers is inverted. Perfect reflection at the inner and outer boundaries is simulated by returning the walker to the same position if the next displacement takes it outside the boundaries. The echo intensity at times $t^* = 2\tau_E^*, 4\tau_E^*, 6\tau_E^* \dots$ is evaluated by averaging the phases of all walkers

$$M(t^*) = \frac{1}{N} \sum_{n=1}^N \exp(i\phi_n(t^*)) \quad (47)$$

where N is the number of walkers and $\phi_n(t^*)$ is the phase of the n^{th} walker at time t^* . The dimensionless relaxation rate is calculated from the slope of exponential fit to the simulated echo intensities. However, magnetization decay is multi-exponential for simulations such that $\delta\omega\tau_R > 100$. For such cases, relaxation rate is calculated from the slowest rate of the multi-exponential decay.

There are two simulation parameters which should be appropriately chosen to ensure the accuracy of the solution

1. Number of walkers (N_w) – Number of walkers determines the statistical noise in the simulations. Simulations with different number of walkers showed that $N=10,000$ gives a good accuracy ($<0.1\%$ average absolute deviation from the analytical solutions) and a reasonable amount of computational time.
2. Time step (dt^*) – The value of the time step should be so chosen such that the dimensionless diffusion length in time step dt^* is less than any dimensionless characteristic length of the system. Since the radius of the paramagnetic particle sphere is the smallest characteristic length, dt^* was chosen such that

$$\sqrt{2N_D dt^*} \ll \frac{R_0}{R_e} \quad (48)$$

B. Validation

The random walk simulations are validated for unrestricted and restricted diffusion in constant gradient by comparing with the known analytical expressions for transverse relaxation in the two cases.

B.1 Unrestricted Diffusion in constant gradient

For unrestricted diffusion in a constant gradient, echo attenuation due to diffusion follows an exponential decay with a time constant given by the Bloch formula

(equation 22). Figure 4 shows the comparison between the analytical and the simulated echo decay for the case of $g=100\text{G/cm}$ and $\tau_E = 2\text{ms}$. The two solutions match within 0.1% absolute average deviation indicating the validity of the algorithm. The algorithm was validated for more cases and for each case the solutions matched within good agreement.

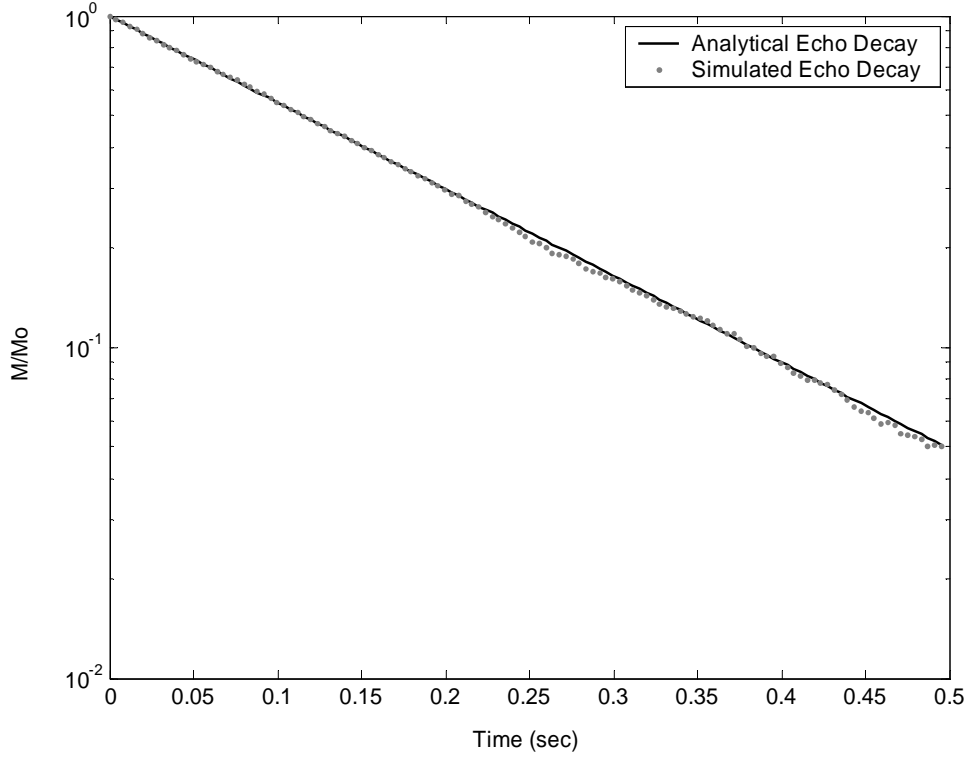


Figure 4: Comparison of analytical and simulated echo decay for **unrestricted diffusion in constant gradient**. The parameters used in the simulations are $g=100\text{G/cm}$, $\tau_E = 2\text{ms}$, $N_w=10,000$ and $dt=0.1\mu\text{s}$.

B.2 Restricted Diffusion in constant gradient

For the case of restricted diffusion, random walk simulations are validated by comparing with the analytical expression for transverse relaxation in constant gradient inside a sphere. In the motionally averaging regime, relaxation due to diffusion in a constant gradient g in a sphere of radius R_s is given as (Neumann, 1974)

$$\frac{1}{T_2} = \frac{8R_s^4 \gamma^2 g^2}{175D} \quad (49)$$

The simulations are done in terms of dimensionless variables by normalizing the spatial variables with the radius of the sphere (R_s). Thus, the normalized characteristic lengths (equations 2 and 3) are given as

$$L_g^* = \frac{L_g}{R_s} = \frac{1}{R_s} \sqrt[3]{\frac{D}{\gamma g}} \quad (50)$$

$$L_d^* = \frac{L_d}{R_s} = \frac{1}{R_s} \sqrt{D\tau_E} \quad (51)$$

The temporal variable is normalized with a characteristic time (t_c) defined as

$$t_c = \frac{1}{\gamma g R_s} \quad (52)$$

t_c defines the characteristic time for relaxation in constant gradient in contrast to t_0 (equation 36) which was defined for relaxation in the presence of paramagnetic particle. The expression for t_c is derived by following the same procedure as was used to derive t_0 expect that the inhomogeneous field ($B_{\delta z}$) is for a constant gradient given as

$$B_{\delta z} = gz \quad (53)$$

Secular relaxation due to diffusion in constant gradient with $L_g^* = 1.2$ and 1.5 is numerically simulated. For each case, two values of $L_d^* = 2$ and 3 (i.e two echo spacings) are chosen. The values of L_g^* and L_d^* were chosen greater than one so that the systems are in motionally averaging regime and relaxation rate is given by equation (49) normalized by characteristic rate $1/t_c$. Figures 5 and 6 show the comparison between simulated and analytical echo decay for two cases with $L_g^* = 1.2$ and 1.5 respectively. The two cases of $L_d^* = 2$ and 3 are shown in the upper and lower panel of the figures. For all cases, the simulated and analytical echo amplitudes match very well (<1% absolute average deviation) indicating the validity of the numerical technique.

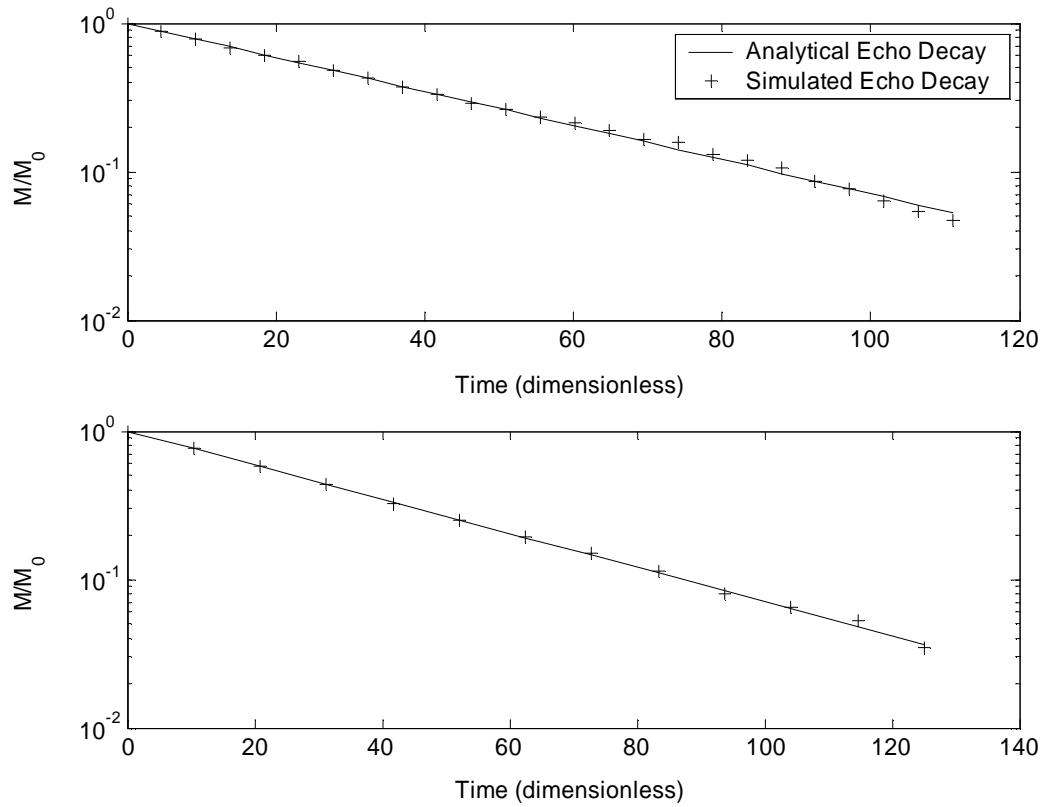


Figure 5: Comparison of simulated and analytical echo decays for **restricted diffusion in a sphere** with constant gradient. The parameters used in the simulations are $L_g^* = 1.2$ and $L_d^* = 2$ (upper panel) and $L_d^* = 3$ (lower panel). Lesser number of points in the lower figure is due to smaller sampling rate with larger L_d^* . The analytical rate is given by equation (49) normalized by $1/t_c$.

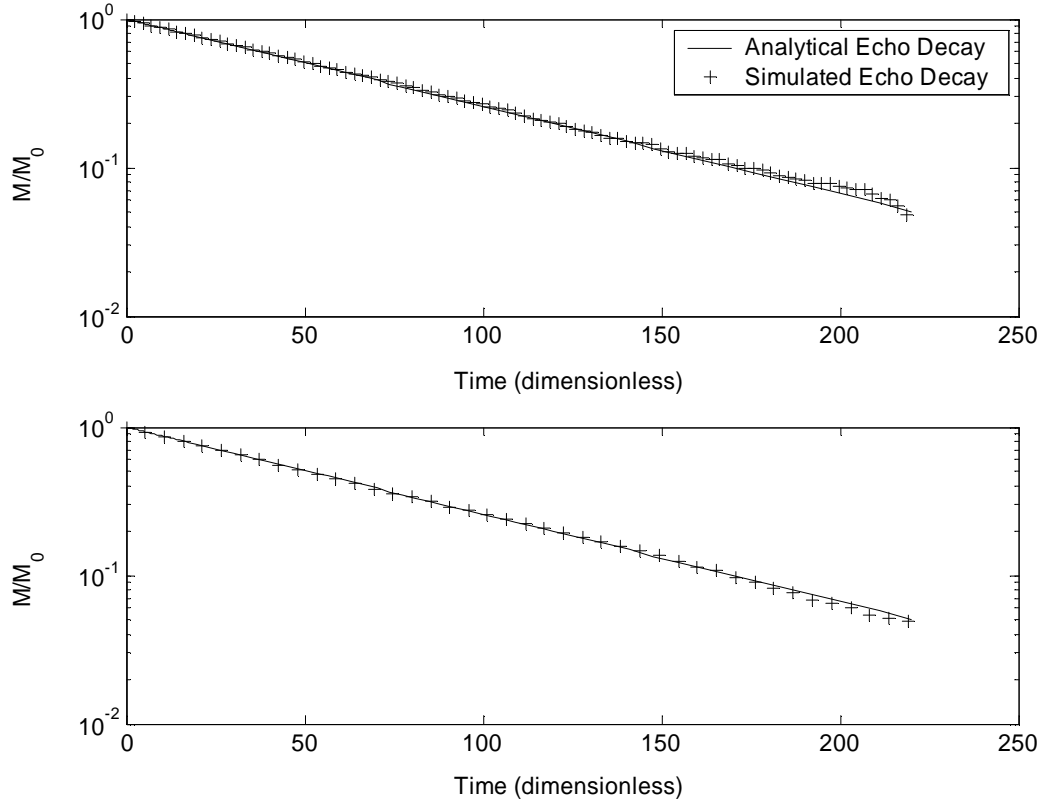


Figure 6: Comparison of simulated and analytical echo decays for **restricted diffusion in a sphere** with constant gradient. The parameters used in the simulations are $L_g^* = 1.5$ and $L_d^* = 2$ (upper panel) and $L_d^* = 3$ (lower panel). Lesser number of points in the lower figure is due to smaller sampling rate with larger L_d^* . The analytical rate is given by equation (49) normalized by $1/t_c$.

C. Results

We now present the results for random walk simulations of secular relaxation in the presence of paramagnetic particles. Secular relaxation of protons in the presence of paramagnetic particle of susceptibility 0.2 (SI units) and radius ranging from 20nm to 2 μ m is simulated. The value of susceptibility is representative of magnetite. The external magnetic field B_0 corresponds to a proton Larmor frequency of 2MHz. For each particle size, simulations with different values of half echo spacing are performed to study the echo spacing dependence of secular relaxation in different regimes. Thus, the simulations span the entire $(\delta\omega\tau_R, \delta\omega\tau_E)$ parameter space of figure 3.

Figure 7 shows the plot of simulated dimensionless relaxation rates as a function of $\delta\omega\tau_R$ for different cases of $\delta\omega\tau_E$ where $\delta\omega$ is the equatorial frequency shift given by equation (38). The solid black line is the plot of theoretical relaxation rate (equation 18) in the motionally averaging regime normalized by the characteristic rate $1/t_0$ (Brooks et al, 2001)

$$\frac{1}{T_{2,\text{sec}}^D} = \frac{t_0}{T_{2,\text{OS}}} = \frac{16}{45} \delta\omega\tau_R \quad (\tau_R \ll \tau_E, \tau_H) \quad (54)$$

The superscript “D” refers to dimensionless relaxation rate. The dotted line is the normalized relaxation rate (equation 23) given by mean gradient diffusion theory valid in the free diffusion regime (Brooks et al., 2001)

$$\frac{1}{T_{2,\text{sec}}^D} = \frac{t_0}{T_{2,\text{FD}}} = \frac{9(\delta\omega)\tau_E^2}{5\tau_R} = \frac{9(\delta\omega)^2\tau_E^2}{5\delta\omega\tau_R} \quad (\tau_E \ll \tau_R, \tau_H) \quad (55)$$

The dash-dotted lines are the plots of normalized relaxation rates (equation 29) given by modified mean field gradient theory (Brooks et al., 2002) valid in the localization regime given as

$$\frac{1}{T_{2,\text{sec}}^D} = \frac{t_0}{T_{2,\text{Loc}}} = \frac{9(\delta\omega)^2\tau_E^2}{5\delta\omega\tau_R} \left(\frac{\sqrt{4/5}\delta\omega\tau_E}{a + bf\sqrt{4/5}\delta\omega\tau_E} \right)^{-5/3} \quad (\tau_H \ll \tau_E, \tau_R) \quad (56)$$

The dashed line marks the boundaries $\delta\omega\tau_R=1$ and $\delta\omega\tau_E=1$ that delineate the asymptotic regimes.

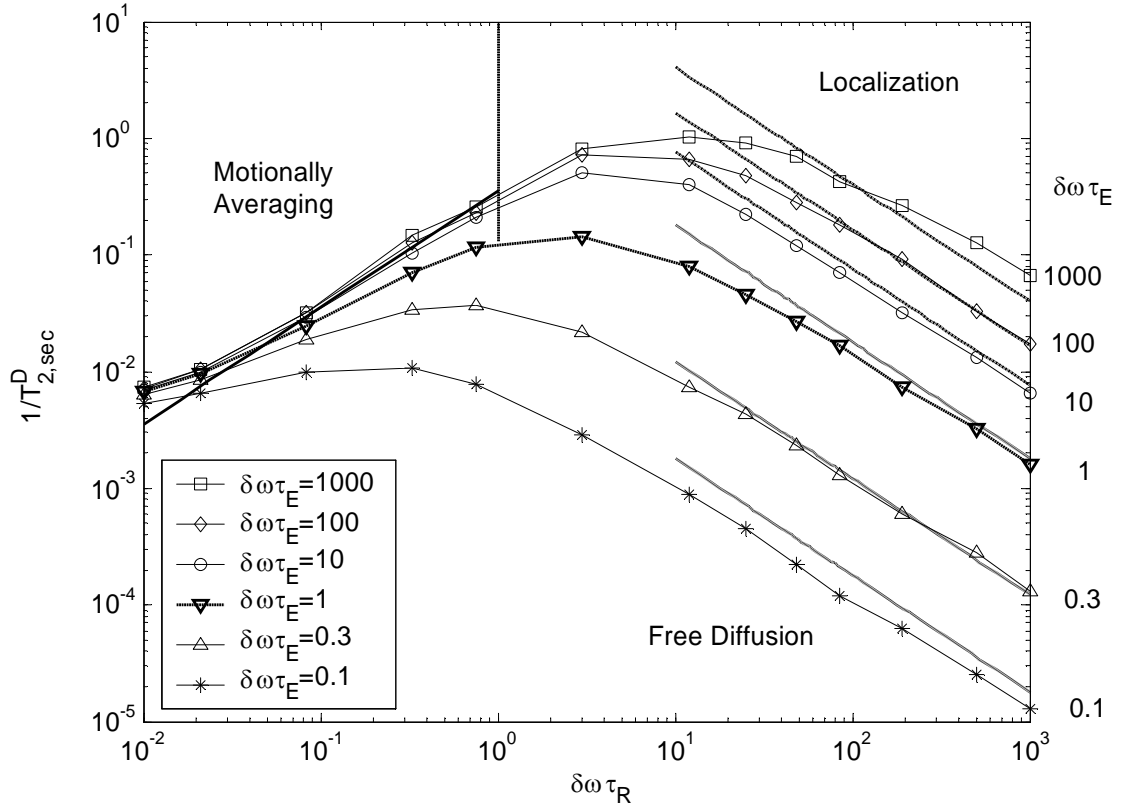


Fig 7: Plot of simulated secular relaxation rate (dimensionless) with $\delta\omega\tau_R$ as a function of $\delta\omega\tau_E$. The parameters used in the simulations are $f=1.25 \cdot 10^{-4}$, $k=1.2$, $B_0= 496$ Gauss. The solid, dashed and dotted line are the theoretically estimated secular relaxation rates according to the outer sphere theory (equation 54), modified mean gradient diffusion theory (equation 55) and mean gradient diffusion theory (equation 56) plotted in the respective regimes of validity.

As was shown in Figure 3, the secular relaxation is characterized by three asymptotic regimes based on the values of $\delta\omega\tau_R$ and $\delta\omega\tau_E$. For $\delta\omega\tau_R < 1$ and sufficiently large values of $\delta\omega\tau_E \gg 1$ in figure 7, **motionally averaging regime** is visible. The secular relaxation rates are independent of the echo spacing and increase with particle size. The theoretically predicted outer-sphere relaxation rates (equation 54) match well with the simulations as long as $\delta\omega\tau_R \ll 1$.

For $\delta\omega\tau_R > 1$ and large values of $\delta\omega\tau_E \gg 1$, **localization regime** exists. The secular relaxation rate shows strong dependence on echo spacing. In addition, the dependence of the relaxation rate on the correlation time (and thus the particle size) is inversed compared to that in the motionally averaging regime. The relaxation rates now decrease with the particle size. This is because as the particle size increases, the average internal field gradient decreases according to

equation (24). For $\delta\omega\tau_R \gg 1$, the simulated relaxation rates match well with the predictions of modified MGDT (equation 56).

The **free diffusion regime** is valid for the smaller echo spacings $\delta\omega\tau_E < 1$ as long as $\delta\omega\tau_E < \delta\omega\tau_R$. Since the decay is only weak in the free diffusion regime (Sen et al., 1999), the simulated relaxation rates are significantly smaller than the ones in localization or motionally averaging regime. For $\delta\omega\tau_R > 1$, the relaxation rates show inverse dependence on the particle size due to decrease in magnetic field gradient with particle size. The simulated rates match well with the predictions of the mean gradient diffusion theory (equation 55).

Now, let us study the characteristics of the secular relaxation rate in the $(\delta\omega\tau_R, \delta\omega\tau_E)$ parameter space. Figure 8 shows the contour plots of the dimensionless secular relaxation rate in the $(\delta\omega\tau_R, \delta\omega\tau_E)$ domain. The boundaries between the asymptotic regimes are shown by dashed lines. We notice that in the motionally averaging regime ($\delta\omega\tau_R \ll 1, \delta\omega\tau_E \gg 1$), the contour plots are almost parallel to the $\delta\omega\tau_E$ axis implying that the relaxation rates are independent of the echo spacing. Also, the rates increase with $\delta\omega\tau_R$ showing that the secular relaxation increases with particle size. In the localization and free diffusion regimes, the dependence of relaxation on $\delta\omega\tau_R$ is reversed and the rates decrease with particle size. In addition, the rates are echo spacing dependent. The contours are more closely spaced and have lesser slope in the free diffusion regime than in the localization regime. Thus, the dependence of the relaxation rate on the echo spacing is higher in free diffusion than in the localization regime.

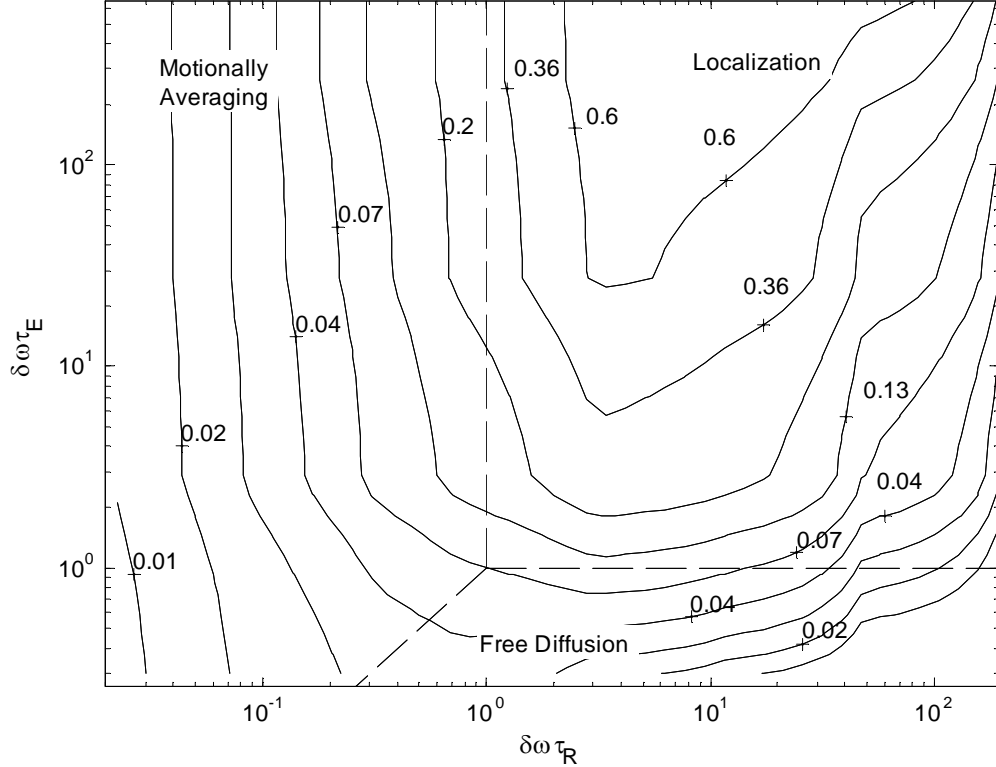


Figure 8: Contour plots of dimensionless secular relaxation rate in the $(\delta\omega\tau_R, \delta\omega\tau_E)$ parameter space.

The echo spacing dependence of the simulated rates in the different regimes needs to be quantitatively studied. Figure 9 shows the plot of simulated relaxation rate with dimensionless echo spacing $\delta\omega\tau_E$ for cases in which $\delta\omega\tau_R < 1$. The dashed curve shows the boundary $\delta\omega\tau_E = \delta\omega\tau_R$ delineating the free diffusion and motionally averaging regime. In the motionally averaging regime, the relaxation rates increase with particle size in accordance to the predictions of outer sphere theory. In addition, the relaxation rates are dependent on echo spacing in the free diffusion regime while they are independent of the echo spacing in the motionally averaging regime.

Figure 10 shows the plot of simulated relaxation rates with $\delta\omega\tau_E$ for cases in which $\delta\omega\tau_R > 1$. The dashed line shows the boundary $\delta\omega\tau_E = 1$ between the free diffusion and localization regime. Note the large decrease in the slope of relaxation rates as the systems transition from the free diffusion to the localization regime. In addition, the dependence of the relaxation rate on the echo spacing is almost linear in the localization regime.

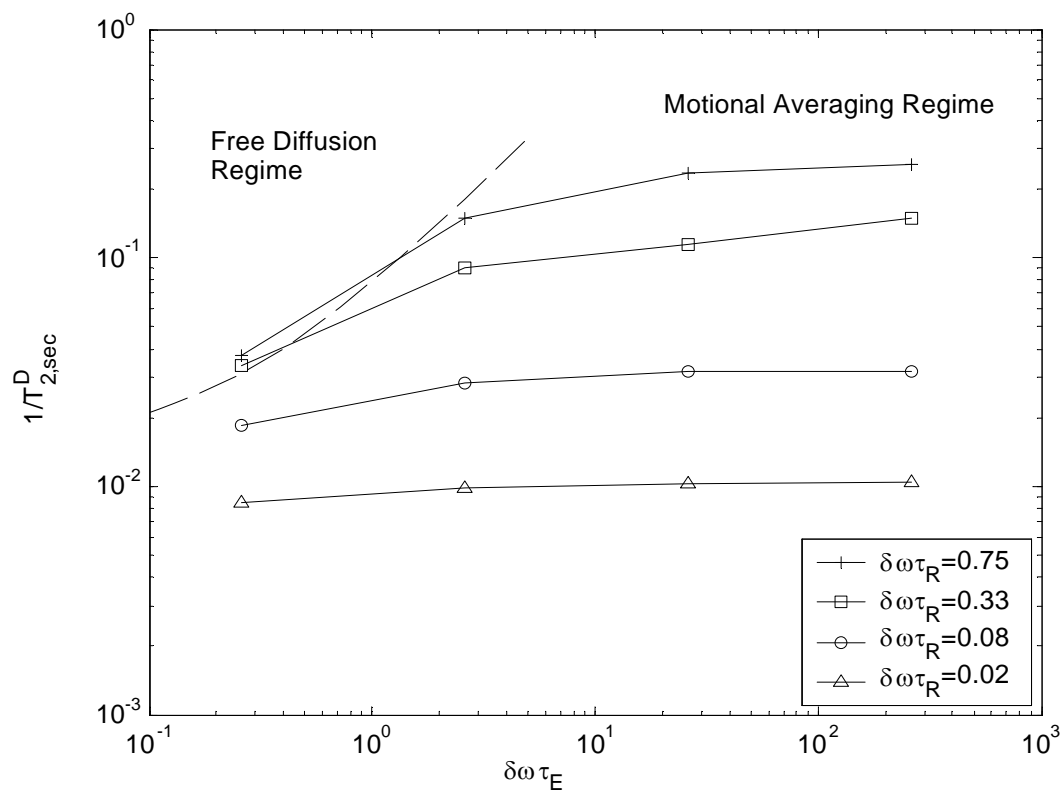


Figure 9: Plot of secular relaxation rates (dimensionless) with dimensionless echo spacing $\delta\omega\tau_E$ for $\delta\omega\tau_R < 1$. The dashed line is the boundary $\delta\omega\tau_E = \delta\omega\tau_R$ delineating the free diffusion and motionally averaging regime. The relaxation rates are almost independent of echo spacing in the motionally averaging regime.

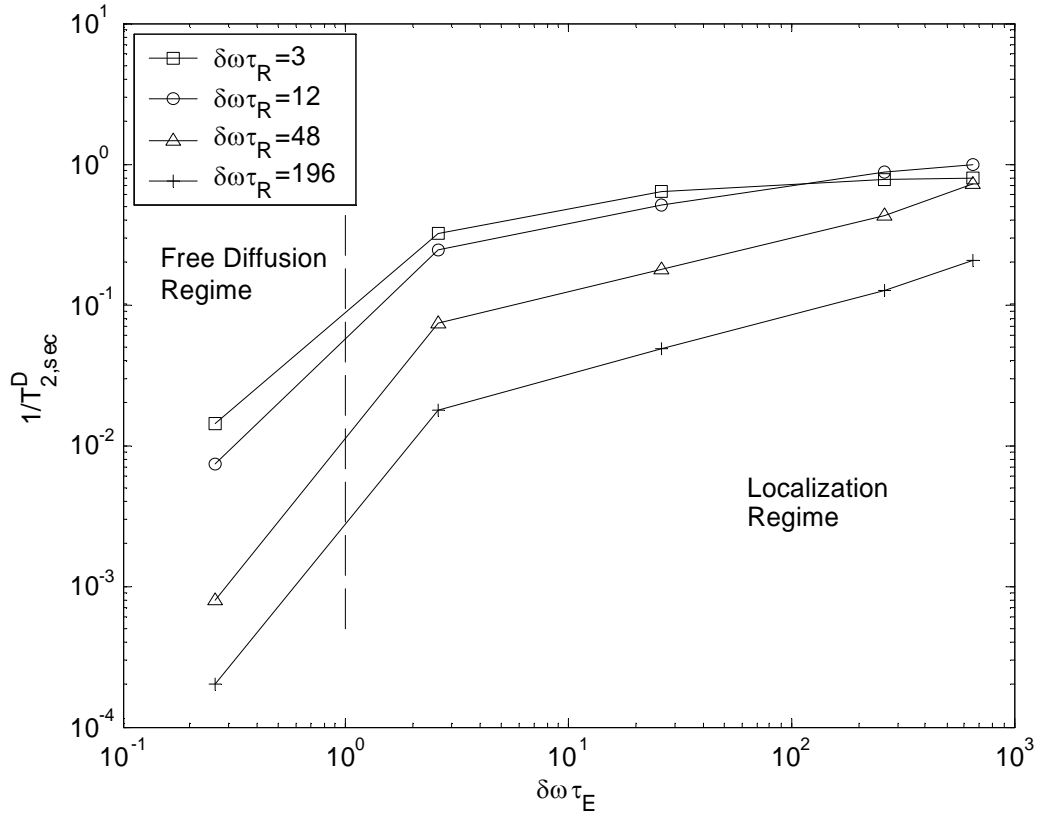


Figure 10: Plot of secular relaxation rates (dimensionless) with dimensionless echo spacing $\delta\omega\tau_E$ for $\delta\omega\tau_R \gg 1$. A dashed line is the boundary $\delta\omega\tau_E = 1$ delineating the free diffusion and localization regime. Note the linear dependence of the relaxation rate in the localization regime.

Note that even though the simulations were done for inhomogeneous field induced by a single paramagnetic particle, the above arguments would be qualitatively similar in other field distributions as well.

IV. Experimental

In the previous sections, we described the classification of different regimes of transverse relaxation based on three characteristic time (or corresponding length) scales. In the next section, we describe a series of proton relaxation measurement with paramagnetic particles spanning a size range from angstroms to microns. These measurements explain the characteristics of the relaxation regimes as a function of the length scale of field inhomogeneity. The section is organized in two subsections. In the first subsection, we describe the proton relaxation measurements with aqueous dispersions of paramagnetic particles of various sizes. The experiments help to quantitatively estimate the characteristic time scales for secular relaxation in the presence of paramagnetic particles. In the second subsection, experiments with sand coated with paramagnetic particles of various sizes are described.

A. Paramagnetic particles in solution

A.1 Ferric ion

The smallest paramagnetic particle studied was ferric ion (hydrated ionic radius 2.62Å, Bertini et al., 1993). Solutions of ferric chloride were made at various solute concentrations in 0.1N Hydrochloric acid. Acidic pH of the solutions prevents the formation of hydroxides. Proton longitudinal and transverse relaxation of the solutions was measured at 30°C. The T_2 relaxation was measured with different echo spacings to study the echo spacing dependence. Figure 11 shows the T_1 and T_2 relaxation rates of the aqueous solution of ferric ions as a function of the solution concentration.

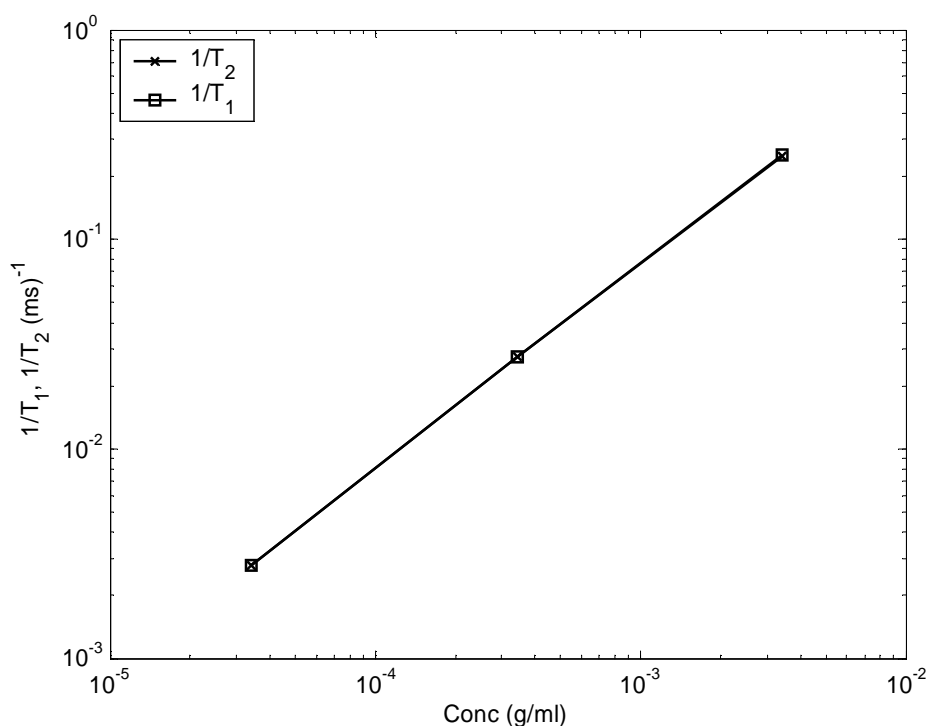


Figure 11: Longitudinal and Transverse relaxation rates of ferric chloride solutions as a function of the concentration of the solution.

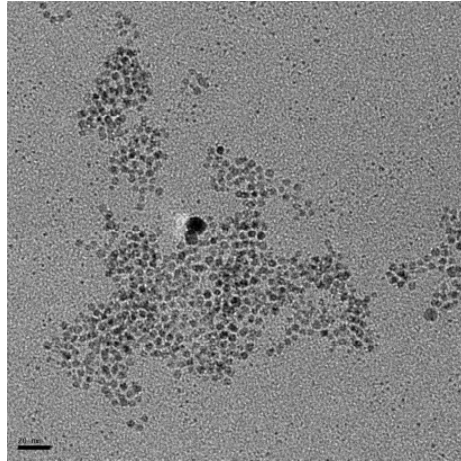
The relaxation rates of the ferric solutions increase linearly with the concentration. Furthermore, the T_1/T_2 ratio is unity and no echo spacing dependence of transverse relaxation is observed. T_1/T_2 ratio of unity implies that the secular relaxation does not contribute significantly to the transverse relaxation.

A.2 Polymer Coated Magnetite Nanoparticles

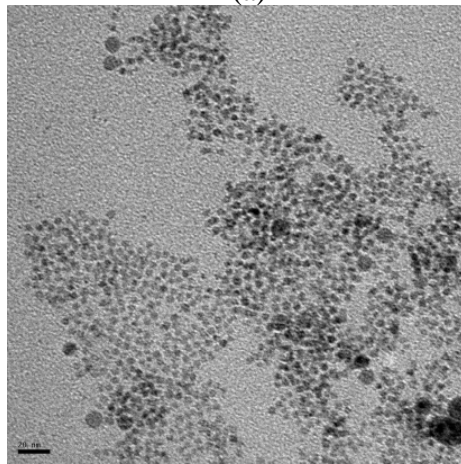
To explore a larger length of field inhomogeneity, NMR proton relaxation of aqueous dispersions of magnetite nanoparticles of various sizes was studied. Aqueous dispersions of the nanoparticles were obtained from Dr. V. Colvin's Lab.

The nanoparticles were synthesized by the pyrolysis of iron carboxylate salts in an organic solvent and subsequently dispersing the nanoparticles in water (Yu et al., 2004). Particles are then coated with a layer of a polymer which prevents agglomeration of the particles in external magnetic field due to interparticle dipole attraction. The size of the particles can be controlled by changing the time of reaction. Figure 12 shows the TEM images of 4nm, 9nm and 16nm magnetite particles (Agarwal, S., 2007) used in our study.

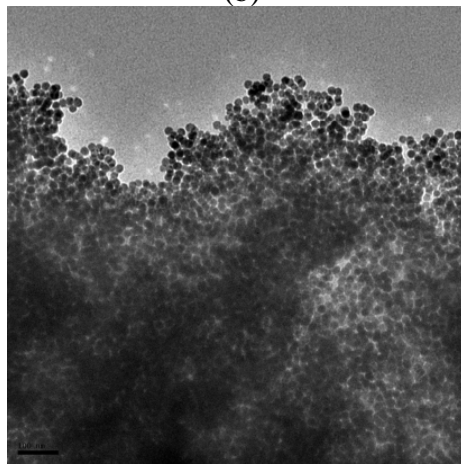
Proton relaxation rates of the aqueous dispersions were measured as a function of the concentration of the dispersion. Figure 13 shows the plots of longitudinal, transverse and secular relaxation rates with the concentration of the dispersion for the three particle sizes. The solid lines are the linear best fits of the experimental points. Once again, we notice that the relaxation rates increase linearly with the concentration of the paramagnetic particles. No echo spacing dependence of the T_2 relaxation is observed. In contrast to the ferric ions, however, the T_1/T_2 ratio is greater than one and increase monotonically with the particle size (Figure 14).



(a)



(b)



(c)

Figure 12: TEM images of magnetite nanoparticles. (a) 4nm magnetite (b) 9nm magnetite (c) 16nm magnetite (Agarwal,S., 2007).

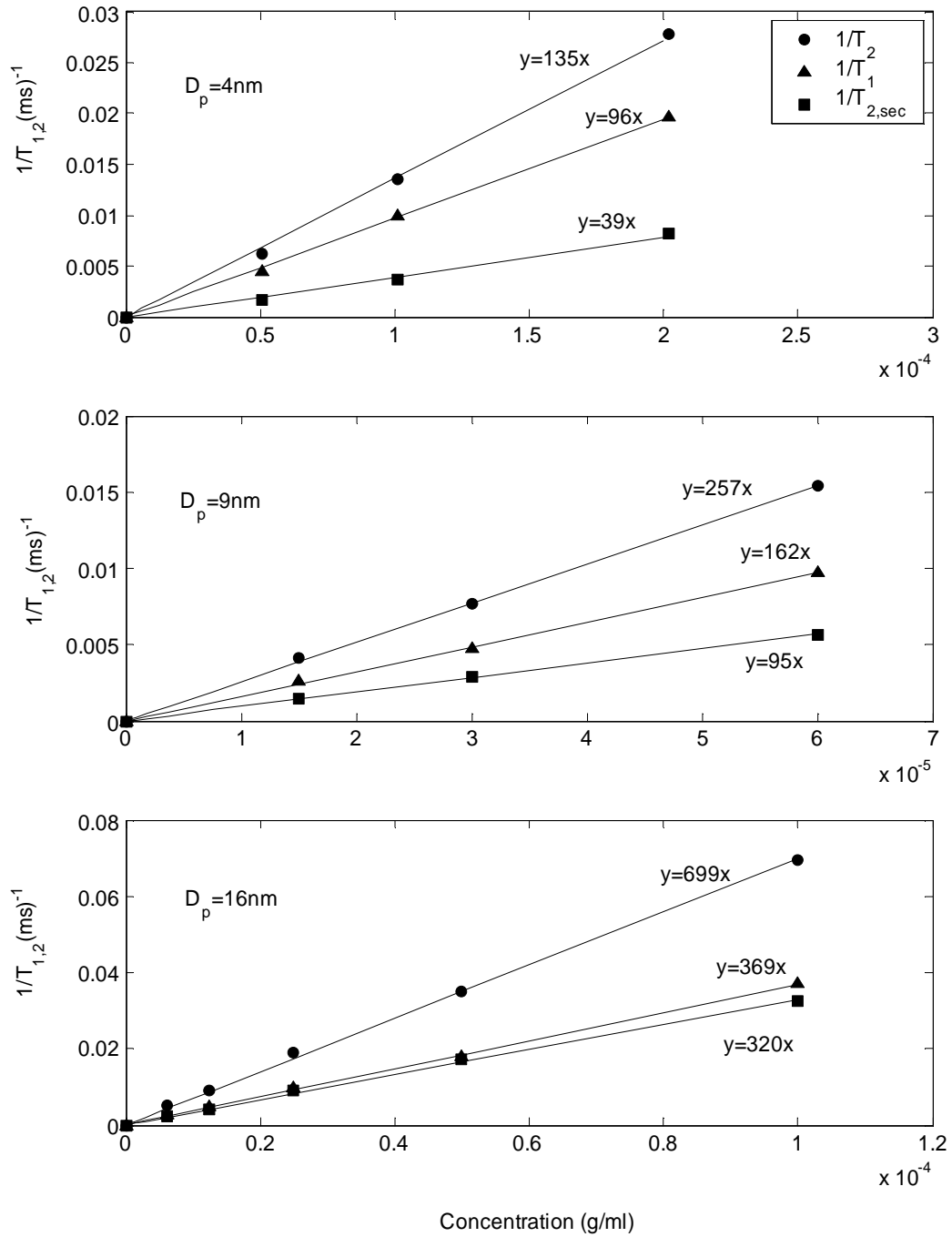


Figure 13: Plot of transverse, longitudinal and secular relaxation rates of aqueous dispersions of magnetite nanoparticles of three different sizes with the concentration of the dispersion. The diameter of the nanoparticles (D_p) and slopes of the linear best fits are also mentioned.

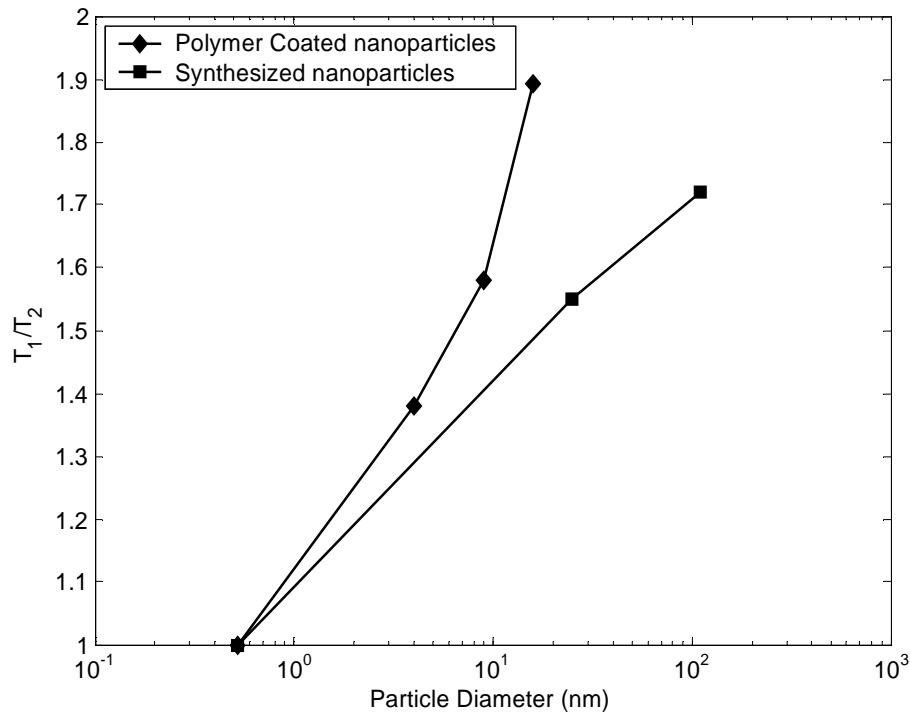


Figure 14: T_1/T_2 ratio of the aqueous dispersions of paramagnetic particles as a function of the particle size. The T_1/T_2 ratio increases with the particle size in the motionally averaging regime.

A.3. Magnetite nanoparticles coated with citrate ion

Positively charged magnetite nanoparticles of different sizes were synthesized using Massart's Method (1981). The aim of synthesizing positive charge nanoparticles is to adsorb them on the negatively charged silica surface by coulombic attraction. Thus, relaxation characteristics of model sandstones with paramagnetic particles adsorbed at different concentrations can be studied. This is not possible for the polymer coated nanoparticles since the coating prevents the particles from adsorbing on the sand surface. Here we will describe the relaxation characteristics of aqueous dispersions of the positively charged particles. NMR experiments with particles coated on sand will be described in a later section.

Let us first describe the experimental procedure used to obtain stable magnetite dispersions. Nanoparticles are synthesized by co-precipitation of magnetite from the aqueous solution of ferrous and ferric chloride using ammonium hydroxide (Massart, R., 1981). The precipitated magnetite is washed with 2M perchloric acid which makes the nanoparticles positively charged due to surface adsorption of protons (Massart, R., 1981). The positively charged particles can then be peptized in excess of water. The size of the particles can be controlled by changing the temperature of the reaction. At higher temperature, larger sized particles are obtained due to Oswald ripening. Figure 15 shows the particle size distribution

obtained by dynamic light scattering for two sets of nanoparticles. The average diameters of the particles for the two sets are 25nm and 110nm respectively. The 25nm particles are synthesized at 10°C while 110nm particles are synthesized at room temperature.

In the absence of external magnetic field, the positive charge on the particles helps to prevent the particles from agglomeration due to interparticle dipole attractions. However, the weak columbic repulsion is not sufficient to prevent agglomeration in the presence of external fields. Thus, the nanoparticles were stabilized by adding 1M sodium citrate in the volume ratio of 1%. Strong steric and columbic repulsion between citrate coated particles prevents them from agglomeration.

Proton relaxation rates of aqueous dispersions of the citrate coated particles were measured as a function of the concentration. Figure 16 shows the plots of longitudinal, transverse and secular relaxation rates with the concentration of the dispersion for the two particle sizes. The linear best fits of the experimental points and the corresponding slopes are also shown. The results are comparable to those for the aqueous dispersions of polymer coated magnetite. Relaxation rates are linearly dependent on the concentration of the dispersion and no echo spacing dependence of T_2 relaxation rates is observed. The T_1/T_2 ratio is also greater than one and increases with particle size (Figure 14).

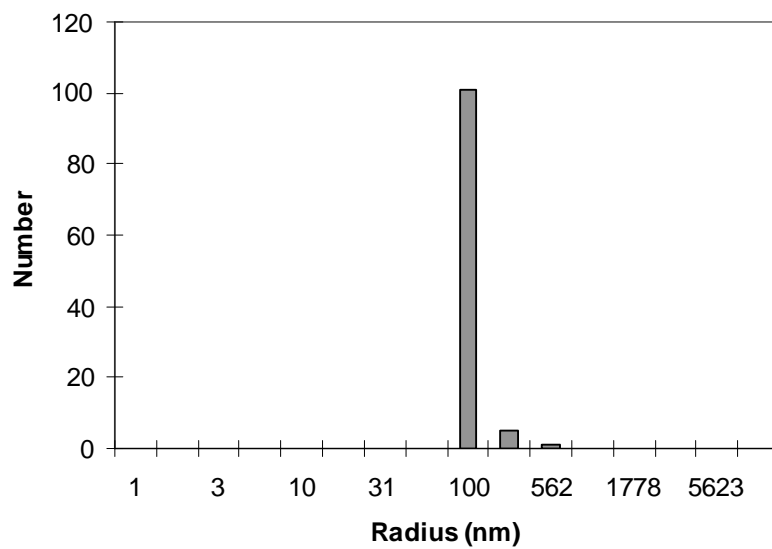
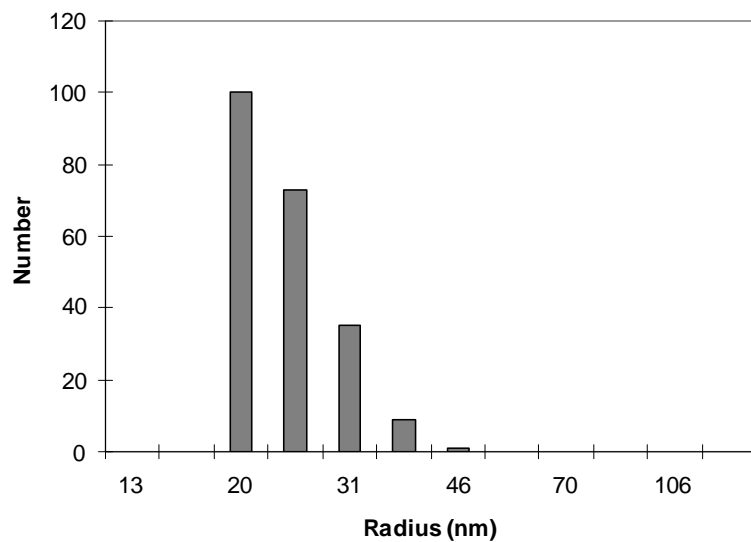


Fig 15: Particle size distribution of magnetite nanoparticles synthesized using Massart's method (1981). The average diameters of the particles are 25nm (upper panel) and 110nm (lower panel) respectively.

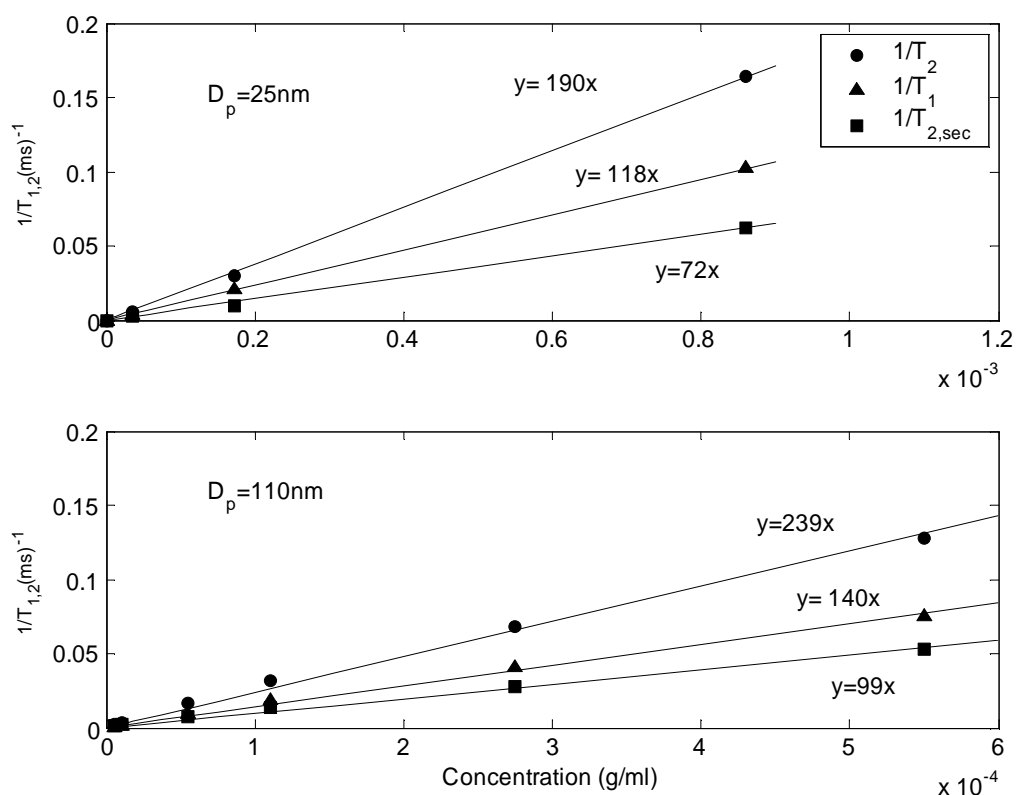


Figure 16: Plot of transverse, longitudinal and secular relaxation rates of aqueous dispersions of magnetite nanoparticles of two different sizes with the concentration of the dispersion. The radii of the nanoparticles (D_p) and slopes of the linear best fits are also mentioned.

A.4 Discussion

As was described earlier, secular relaxation can be characterized by three relaxation regimes depending on the smallest characteristic time scale. In the motionally averaging regime, secular relaxation is independent of echo spacing and increases with the particle size and concentration. Similar relaxation characteristics are also observed for aqueous dispersions of submicron paramagnetic particles. No echo spacing of transverse relaxation is observed and the T_1/T_2 ratio increases with the particle size. We, thus, hypothesize that the proton relaxation of the aqueous dispersions of (submicron) paramagnetic particles is in the motionally averaging regime.

Let us now quantitatively evaluate the characteristic time scales (τ_E, τ_R, τ_H) to prove the validity of the hypothesis. The value of half echo spacing (τ_E) is known from the experimental measurements. In our measurements, the smallest half echo spacing used was 0.2ms. The diffusional correlation time (τ_R) can be calculated from the radius of the paramagnetic particle (R_0) and diffusivity of water at 30°C ($\sim 2.5 \cdot 10^5 \text{ cm}^2/\text{sec}$) by using the following equation

$$\tau_R = \frac{R_0^2}{D} \quad (57)$$

Under the assumption of motionally averaging regime, the expression for the secular relaxation rate can be used to estimate $\delta\omega$ for the magnetite nanoparticles as shown below.

$$\frac{1}{T_{2,\text{sec}}} = \frac{16}{45} f \delta\omega^2 \tau_R \quad (58)$$

$$\Rightarrow \frac{1}{T_{2,\text{sec}}} = \frac{16\delta\omega^2 \tau_R C}{45d} \quad (59)$$

where C is the concentration of the dispersion and d is magnetite density. Thus, from the slopes of the plots between secular relaxation and the concentration given in figures 13 and 16, $\delta\omega$ can be evaluated for the various particle sizes. τ_H is obtained as the reciprocal of $\delta\omega$. Table 1 lists the characteristic time scales for the different particles. We notice that $\tau_R < \tau_H, \tau_E$ for all cases (except for 110nm particle for which $\tau_R \sim \tau_H$) and thus our earlier hypothesis of motionally averaging regime is justified.

Table 1: Characteristic Time scales for the ferric and magnetite nanoparticles.

| Time Scale (sec) | Fe3+ | 16nm | 9nm | 4nm | 25nm | 110nm |
|---------------------------|--------------------|-------------------|-------------------|-------------------|-------------------|-------------------|
| τ_R | $3 \cdot 10^{-11}$ | $3 \cdot 10^{-8}$ | $8 \cdot 10^{-9}$ | $2 \cdot 10^{-9}$ | $6 \cdot 10^{-8}$ | 10^{-6} |
| $\tau_{E,\text{minimum}}$ | $2 \cdot 10^{-4}$ | $2 \cdot 10^{-4}$ | $2 \cdot 10^{-4}$ | $2 \cdot 10^{-4}$ | $2 \cdot 10^{-4}$ | $2 \cdot 10^{-4}$ |
| τ_H | $2 \cdot 10^{-3}$ | $8 \cdot 10^{-8}$ | $8 \cdot 10^{-8}$ | $5 \cdot 10^{-8}$ | $2 \cdot 10^{-7}$ | 10^{-6} |

The condition $\tau_R \ll \tau_E$ implies that the magnetic field inhomogeneities are motionally averaged in time much smaller than τ_E . Thus, no dependence of T_2 relaxation on echo spacing is observed for the aqueous dispersions of ferric ions and magnetite nanoparticles. Additionally, the secular relaxation rate is proportional to the square of the radius of the paramagnetic particle in the motionally averaging regime. Due to very small size of the ferric ion, the secular relaxation contributes negligibly to the transverse relaxation and the T_1/T_2 ratio is unity. Secular relaxation, however, increases for the larger sized particles and contributes significantly to the T_2 relaxation. Thus, the T_1/T_2 ratio increases with particle size (provided the susceptibility remains same) as observed in Figure 14. The larger T_1/T_2 ratio for the polymer coated nanoparticles is probably due to a higher magnetic moment.

B. Paramagnetic particles on silica surface

Next, we will describe the proton relaxation for water-saturated fine sand coated with paramagnetic particles. Coated sand serves as a model to quantitatively understand the paramagnetic relaxation mechanisms in sandstones. Sand is coated with particles of various sizes and concentrations to explain the transition of the relaxation regimes as the length scale of field inhomogeneity increases. The theory is then applied to describe relaxation in North-Burbank sandstone which has strong internal gradients induced due to pore lining chlorite flakes (Zhang et al., 2003).

B.1 Sand coated with Ferric ions

Let us first describe the experimental protocol used to coat fine sand (Sigma Aldrich) with paramagnetic ferric ions. Fine sand (grain radius 50 μ m) was repeatedly washed with fresh batches of hydrochloric acid till the relaxation time of the washing acid stopped changing. Washing with acid helps to remove the paramagnetic particles already present on the sand surface. The sand was then exhaustively washed with deionized water and dried. A known quantity (15 grams) of the dried sand was kept in contact with acidic (pH 1) solutions of ferric chloride of known concentrations for 24 hours in a plastic bottle. The solid to liquid ratio (gm sand/ml) of the slurries was kept at 1:10. Low pH (<7) of the ferric solutions helps to prevent the formation of hydroxides and precipitation on the sand surface. To ensure uniform coating, the slurries were constantly rotated which prevents the sand from settling at the bottom. After 24 hours, the supernatant was removed and the coated sand was exhaustively washed with deionized water. This last step removes any remaining ferric ions in the pore liquid. Thus, the relaxation of the pore liquid can only be attributed to surface relaxation and diffusion in internal field gradients.

The surface concentration of the ferric ions can be estimated by measuring the quantity of the ferric ions deposited on a known surface area of sand as described. The BET surface area of sand (0.2 m²/g) was determined using N₂ adsorption at 77K. To estimate the deposited quantity, the relaxation time of the supernatant was measured. Using the calibration between the concentration of ferric ion solution and the relaxation rate (Figure 11), the concentration of the supernatant can be determined. The difference in the concentrations of the supernatant and initial coating solutions multiplied by the volume of the solution gives the quantity deposited on the sand surface.

Figure 17 shows the T_1 and T_2 distributions of the sand coated with ferric ions at various surface coverages expressed as surface area/ion. Table 2 lists the modes of the relaxation time distributions for the various cases. No echo spacing dependence of T_2 relaxation is observed and the T_1/T_2 ratio of coated sand is close to that of washed sand at all concentrations.

Table 2: Longitudinal and transverse relaxation times of water-saturated fine sand coated with ferric ions at different surface coverages (area/ferric ion).

| Concentration (Area/particle) | Washed sand | $0.3\text{nm}^2/\text{Fe}^{3+}$ | $0.09\text{nm}^2/\text{Fe}^{3+}$ | $0.03\text{nm}^2/\text{Fe}^{3+}$ |
|----------------------------------|----------------|---------------------------------|----------------------------------|----------------------------------|
| T_1 (ms) | 1587 | 471 | 372 | 294 |
| T_2 (ms) | 1260 | 378 | 294 | 233 |

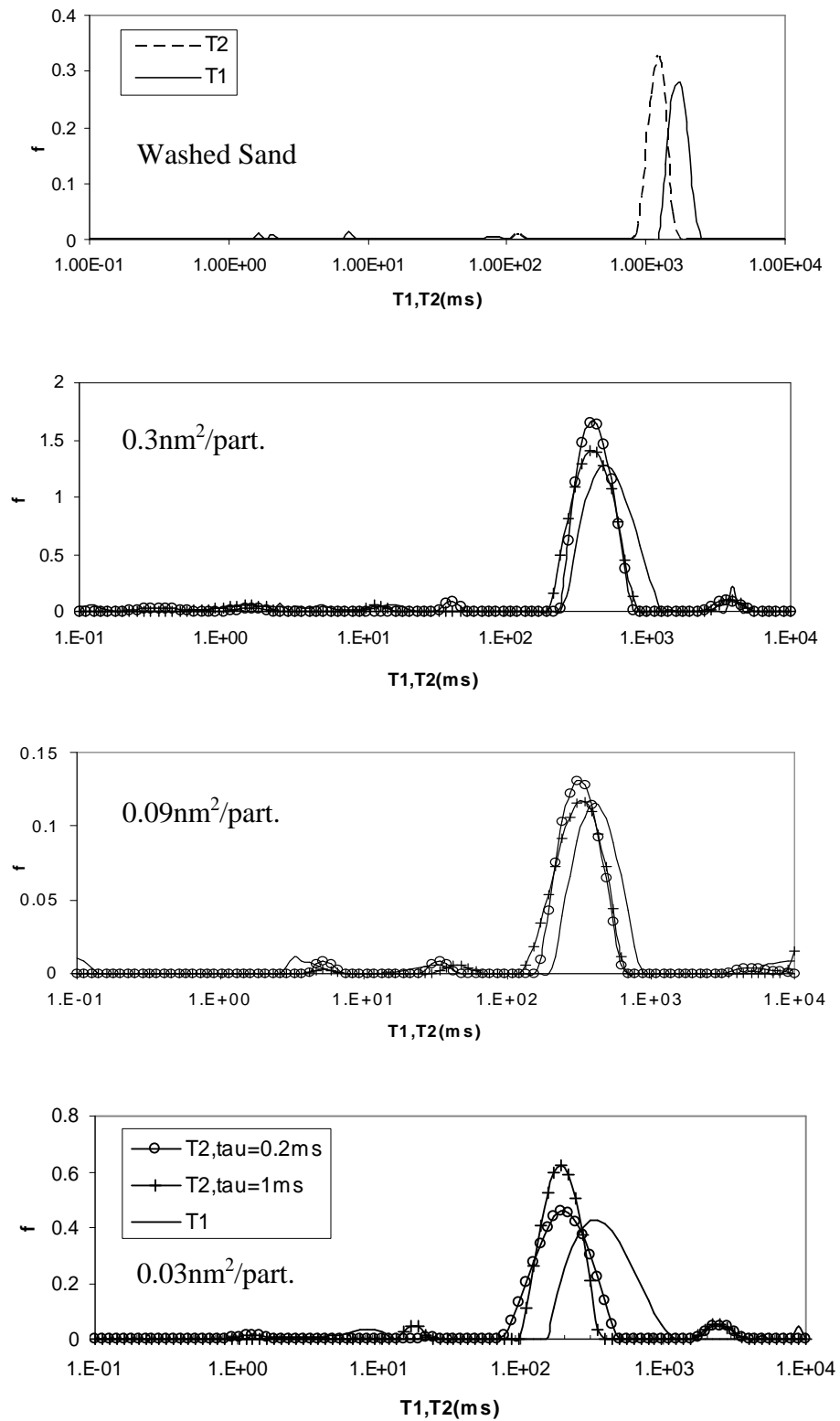


Figure 17: T_1 and T_2 distributions of fine sand coated with ferric ions at different surface concentrations.

B.2 Fine Sand coated with magnetite nanoparticles

Known quantity of fine sand was coated with 25nm and 110nm magnetite particles by following the same procedure as that for the ferric ions. The concentration of the coating dispersion was varied to obtain different surface concentrations of magnetite. Note that the coating is done with positively charged magnetite *not* coated with citrate ion. Figure 18 and 19 show the T_1 and T_2 distributions of water-saturated fine sand coated with 25nm and 110nm magnetite as a function of surface concentration. Table 3 and 4 lists the modes of the relaxation time distributions for the different cases.

We notice that at low surface concentrations of either 25nm or 110nm particles no echo spacing dependence of transverse relaxation is observed. At the highest concentration, however, an echo spacing dependence of T_2 relaxation is observed for both cases. As will be described in the interpretation section, this echo spacing dependence is observed because at high concentrations the particles form a shell around each silica grain such that the length scale of the region of induced magnetic gradients is large compared to the diffusion length during the time of the echo spacing.

Table 3: Longitudinal and transverse relaxation times of water-saturated fine sand coated with 25nm magnetite at different surface coverages.

| Concentration (Area/particle) | $3 \cdot 10^3 \text{ nm}^2/\text{particle}$ | $10^4 \text{ nm}^2/\text{particle.}$ | $9 \cdot 10^4 \text{ nm}^2/\text{particle.}$ |
|-----------------------------------|---|--------------------------------------|--|
| T_1 | 23.6 | 42 | 343 |
| T_2 ($\tau_E = 0.2\text{ms}$) | 18.7 | 29 | 215 |
| T_2 ($\tau_E = 0.5\text{ms}$) | 16.6 | 29 | 215 |
| T_2 ($\tau_E = 1\text{ms}$) | 11.7 | 29 | 215 |
| T_2 ($\tau_E = 2\text{ms}$) | 8.30 | 29 | 215 |

Table 4: Longitudinal and transverse relaxation times of water-saturated fine sand coated with 110nm magnetite at different surface coverages.

| Concentration (Area/particle) | 0.3 μm^2 /particle | 8 μm^2 /particle. | 30 μm^2 /particle. |
|-----------------------------------|-------------------------------|------------------------------|-------------------------------|
| T_1 | 24 | 95 | 613 |
| T_2 ($\tau_E = 0.2\text{ms}$) | 21 | 63 | 385 |
| T_2 ($\tau_E = 0.5\text{ms}$) | 20 | 63 | 385 |
| T_2 ($\tau_E = 1\text{ms}$) | 16.6 | 63 | 385 |
| T_2 ($\tau_E = 2\text{ms}$) | 14.8 | 63 | 385 |

B.3 Fine Sand with dispersed 2.4 μm magnetite

The length scale of field inhomogeneity can also be increased by increasing the size of the paramagnetic particle. Fine sand (15gms) was dispersed with 2.4 μm magnetite (Fischer Scientific) dispersions of known concentrations. Figure 20 shows the T_1 and T_2 distribution of water saturated fine sand with dispersed 2.4 μm magnetite at two concentrations. The corresponding modes of the relaxation time distributions for the two cases are listed in Table 5. Note a dependence of transverse relaxation on echo spacing is observed and the T_1/ T_2 ratio is greater than 2.

Table 5: Longitudinal and transverse relaxation times of water-saturated fine sand with dispersed 2.4 μm magnetite.

| Relaxation time (ms) | 2.7 cm^2 /particle. | 0.9 cm^2 /particle. |
|-----------------------------------|------------------------------|------------------------------|
| T_1 | 486.3 | 272 |
| T_2 ($\tau_E = 0.2\text{ms}$) | 215.4 | 75.6 |
| T_2 ($\tau_E = 0.5\text{ms}$) | 170.7 | 47.5 |
| T_2 ($\tau_E = 1\text{ms}$) | 135.3 | 37.6 |
| T_2 ($\tau_E = 2\text{ms}$) | 105.2 | 21.0 |

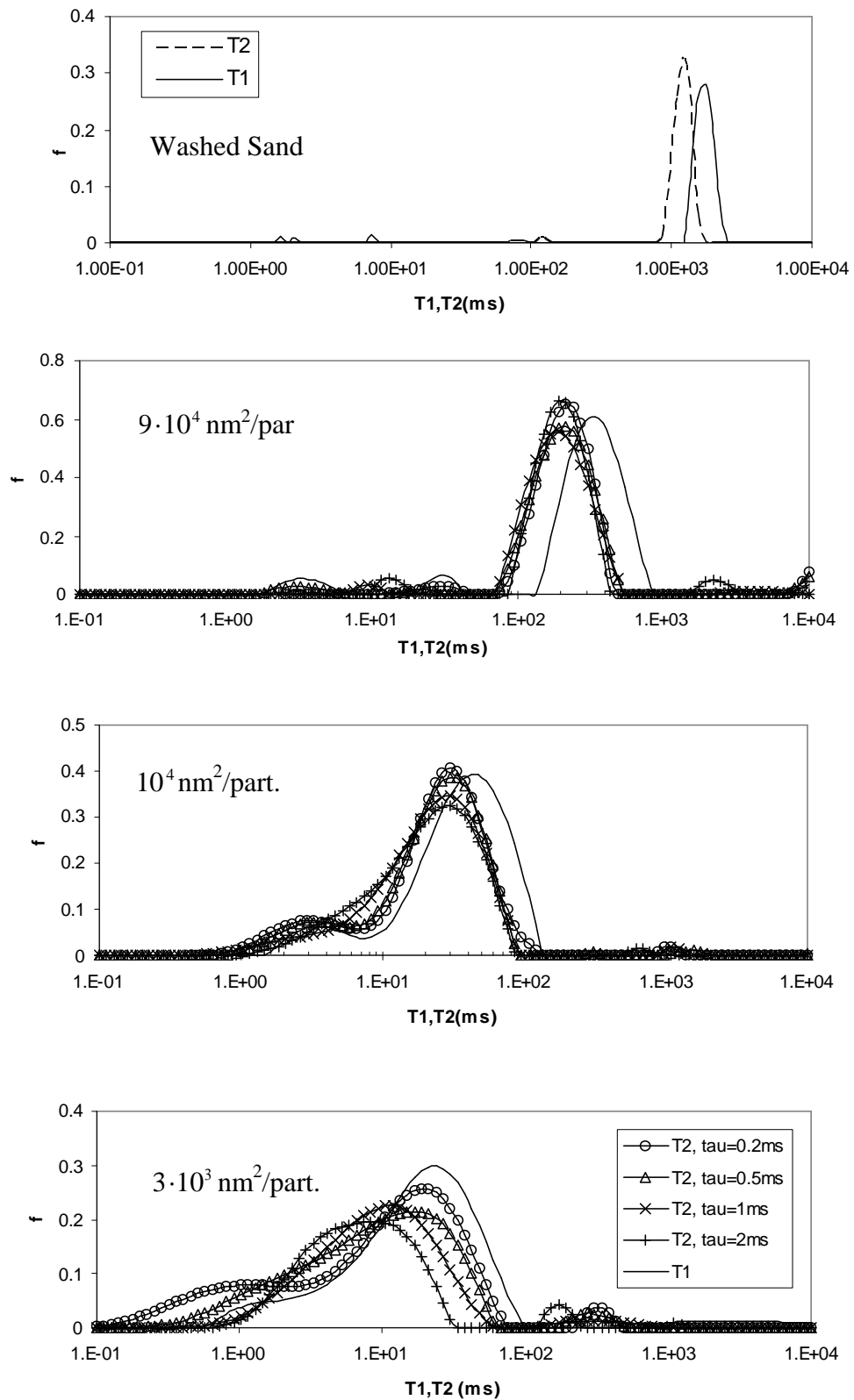


Figure 18: T_1 and T_2 distribution of water-saturated fine sand coated with 25nm magnetite nanoparticles at various concentrations.

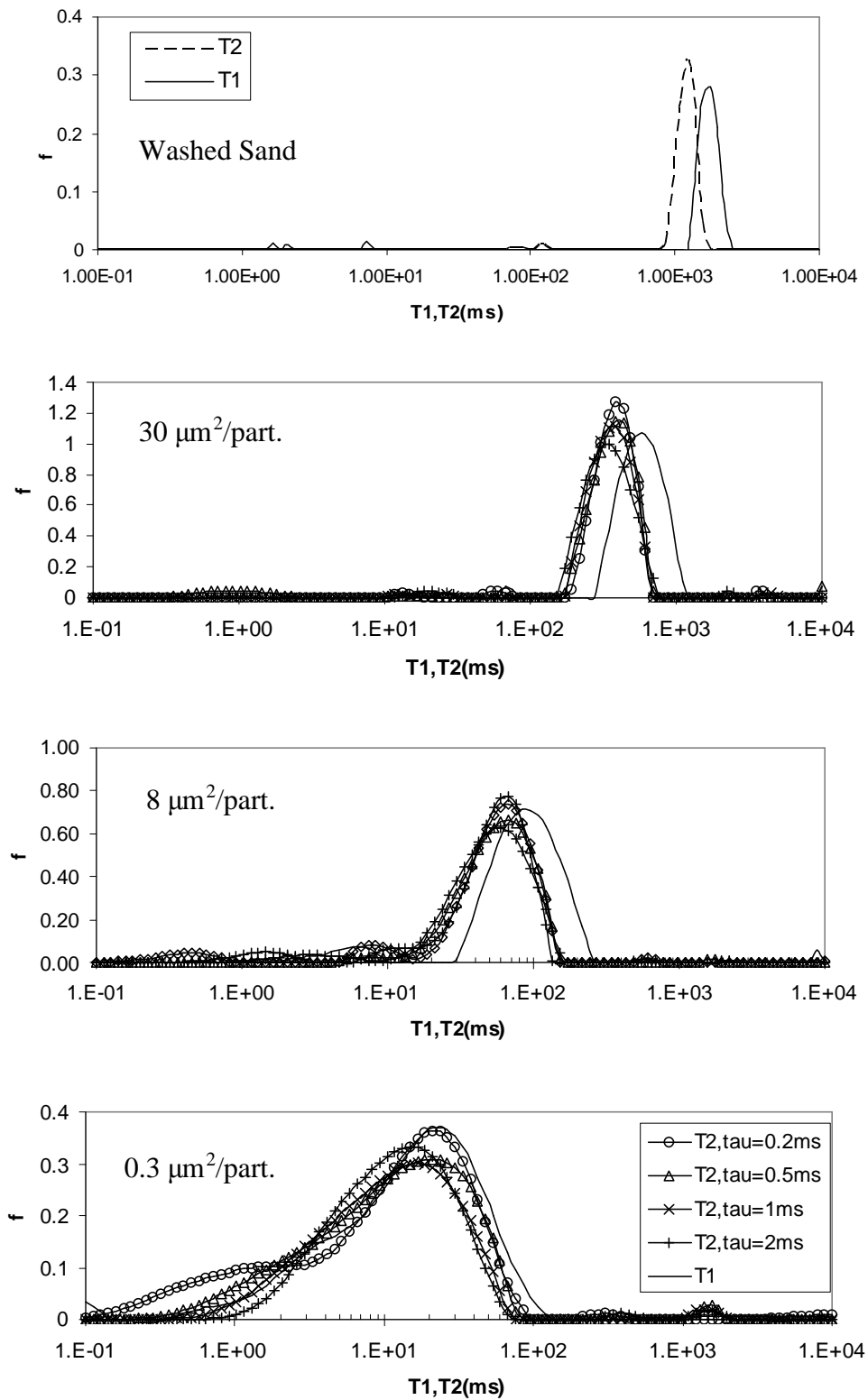


Figure 19: T_1 and T_2 distribution of water-saturated fine sand coated with 110nm magnetite nanoparticles at various concentrations.

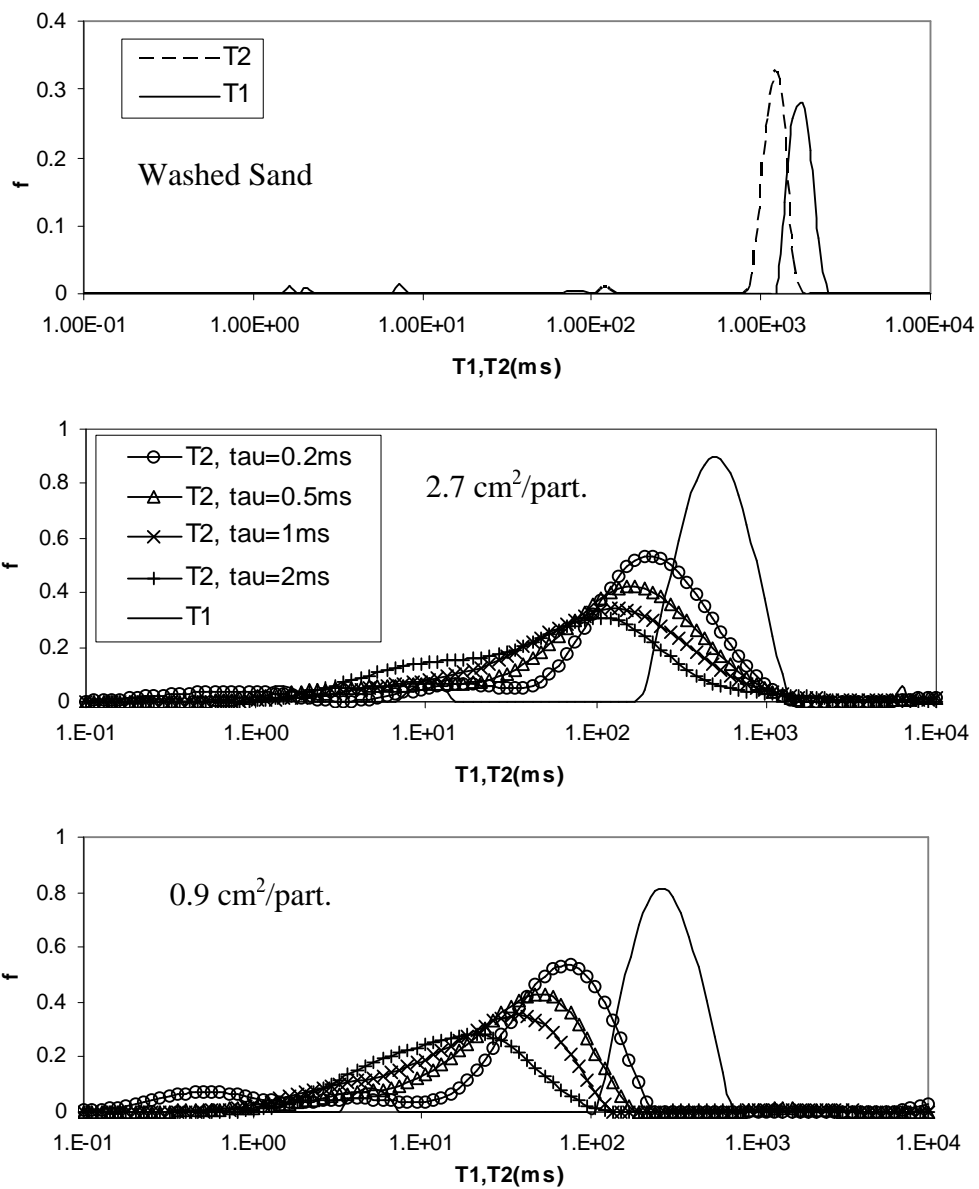


Figure 20: T_1 and T_2 distributions of fine sand with dispersed magnetite of diameter $2.4\mu\text{m}$ at two concentrations. Note, a large T_1/T_2 ratio and echo spacing dependence of transverse relaxation is observed.

B.4 Interpretation

The diverse experimental results can be understood in terms of the characteristic time scales and relaxation regimes discussed in the previous section.

Motionally Averaging Regime

Let us first discuss the case of sand coated with ferric ions at different concentrations. Similar to ferric ions in solution, no echo spacing of transverse relaxation is observed. Also, the T_1/T_2 ratios of coated sand (1.24, 1.26 and 1.25 for the three surface concentrations) are very close to the T_1/T_2 ratio of clean sand (1.26). The calculations of characteristic time scales (Table 1) show that the relaxation in the presence of angstrom size ferric ions is in motionally averaging regime. Thus, the secular relaxation is proportional to the square of the paramagnetic particle radius as postulated by outer sphere theory. Due to very small size of the paramagnetic ferric ion, the contribution of secular relaxation to the transverse relaxation is negligible. Consequently, the T_1/T_2 ratio remains same and no echo spacing dependence of T_2 relaxation is observed for paramagnetic relaxation by ferric ions.

The argument of motionally averaging regime can be extended to explain the relaxation characteristics of sand coated with 25nm and 110nm magnetite at low concentrations. The constraint of low concentration ensures that the internal fields induced by neighboring paramagnetic particles do not superpose. Thus, the protons dephase as if diffusing in the inhomogeneous field induced by a single paramagnetic particle. Figures 18 and 19 show that at low surface coverage of 25nm ($9 \cdot 10^4 \text{ nm}^2$, $10^4 \text{ nm}^2/\text{particle}$) and 110nm ($30 \text{ } \mu\text{m}^2$, $8 \text{ } \mu\text{m}^2/\text{particle}$), no echo spacing dependence of T_2 relaxation is observed and the T_1/T_2 ratio is close to that of the respective aqueous dispersions. At these surface coverages, the interparticle distance is greater than 10 times the radius of the particle and the internal fields induced by neighboring particles do not overlap. Thus, the length scale of field inhomogeneity is determined by the size of the paramagnetic particle. Motionally averaging regime of secular relaxation is observed and T_2 relaxation shows no echo spacing dependence. Additionally, the T_1/T_2 ratio of coated sand increases with the particle size (1.2 for ferric ions and 1.6 for 25nm particle). Thus, the earlier observation that the T_1/T_2 ratio increases with particle size (Figure 14) is also verified for paramagnetic particles adsorbed on sand surface.

Localization Regime

Now, let us analyze the results for the sand coated with high concentrations of the magnetite nanoparticles. At the highest surface coverage of 25nm ($3 \cdot 10^3 \text{ nm}^2/\text{particle}$) and 110nm particle ($0.3 \text{ } \mu\text{m}^2/\text{particle}$) in figures 8 and 9, an echo spacing dependence of T_2 relaxation is observed. This is because at high surface coverage, the particles form a 'shell' around each sand grain such that the length scale of the field inhomogeneity becomes large compared to the diffusion length during the time of the echo spacing. Consider a sand grain of

radius R_g coated with a paramagnetic shell of thickness δ . The internal field induced by the paramagnetic shell can be calculated by subtracting the field induced by sphere of radius R_g from the field induced by a concentric sphere of radius $R_g + \delta$. Thus, the internal field contribution of only the spherical shell survives. The internal field induced by a paramagnetic shell at a radial distance r is given as

$$B_\delta = \frac{(k-1)B_0(3\cos^2\theta-1)}{(k+2)} \left[\frac{(R_g + \delta)^3}{r^3} - \frac{R_g^3}{r^3} \right], r > R_g + \delta \quad (60)$$

$$\approx \frac{(k-1)B_0(3\cos^2\theta-1)}{(k+2)} \frac{3\delta R_g^2}{r^3}, \delta \ll R_g$$

Thus, the range of frequencies in the system at the surface of the spherical shell is

$$\delta\omega_{\text{shell}} \approx \frac{(k-1)\gamma B_0}{(k+2)} \frac{9\delta}{R_g} \quad (61)$$

The frequency range is proportional to the ratio of the thickness of paramagnetic shell to radius of the sand grain. As a validation of this relationship, consider the limiting case of field induced by an infinite plane i.e. $R_g \rightarrow \infty$. An infinite plane of susceptibility different from that of the surrounding medium when placed in external field does not induce any field gradients since the field lines still remain parallel. This is also quantitatively verified by equation (61) which shows $\delta\omega \rightarrow 0$ as $R_g \rightarrow \infty$.

Comparing equation (61) with equation (15) for induced frequencies by a single paramagnetic particle, we notice that the frequency range for a paramagnetic shell decreases by a factor $(3\delta/R)$. However, the length scale to which the inhomogeneity extends is proportional to the sand grain radius rather than the paramagnetic particle radius. Thus, the diffusional correlation time becomes proportional to the square of the sand grain radius rather than the radius of the paramagnetic particle. Since the radius of sand grain is typically much larger than the radius of the coating paramagnetic particle, τ_R is much larger than τ_H . The system thus experiences localization regime (or for some cases free diffusion if $\tau_E < \tau_H$) of transverse relaxation and an echo spacing dependence of transverse relaxation is observed.

Table 6 shows the characteristic time scales for a paramagnetic shell of diameter 25nm and 110 nm on a sand grain of 50 μ m. τ_R is calculated using $R = 50\mu$ m in equation (57) and τ_H is calculated as the reciprocal of $\delta\omega$ for the two paramagnetic particles listed in Table 1. Notice that $\tau_H < \tau_R$, τ_E proving the conditions for localization are satisfied. Thus, an echo spacing dependence of T_2 relaxation is observed at high surface concentrations of 25nm and 110nm particles.

Table 6: Characteristic time scales for relaxation in sand coated with 25nm and 110nm magnetite at high surface concentrations.

| Time Scale (sec) | 25nm | 110nm |
|--------------------|---------------------|-------------------|
| τ_R | 1 | 1 |
| $\tau_{E,minimum}$ | $2 \cdot 10^{-4}$ | $2 \cdot 10^{-4}$ |
| τ_H | $5.2 \cdot 10^{-5}$ | $5 \cdot 10^{-5}$ |

Localization regime can also be observed for relaxation in the presence of large paramagnetic particles with large diffusional correlation time. This is case for relaxation in sand with dispersed 2.4 μ m magnetite. The values of the characteristic times are mentioned in Table 7. ($\delta\omega$ is assumed to be same as for 110nm particles). The conditions for localization regime ($\tau_H < \tau_R$, τ_E) are satisfied and thus, an echo spacing dependence of transverse relaxation is observed as shown in Figure 20.

Table 7: Characteristic time scales for relaxation in sand with dispersed 2.4 μ m magnetite

| Time Scale (sec) | 2.4 μ m |
|--------------------|-------------------|
| τ_R | $6 \cdot 10^{-4}$ |
| $\tau_{E,minimum}$ | $2 \cdot 10^{-4}$ |
| τ_H | 10^{-6} |

Regimes of paramagnetic relaxation in sandstones

The experimental results of figures 17, 18 and 19 explain the observed range of T_1/T_2 ratio in sandstones with no echo spacing dependence of T_2 relaxation (Kleinberg et al.,1993). In the motionally averaging regime, relaxation due to diffusion in inhomogeneous fields induced by paramagnetic particles increases with the size and susceptibility of the paramagnetic particle. Thus, the presence of paramagnetic minerals of various sizes and susceptibilities on pore surfaces can result in a range of T_1/T_2 ratios. Since the diffusional correlation time is much smaller than the time for echo formation in motionally averaging regime, no echo spacing dependence of the T_2 relaxation would be observed. The lack of dependence of transverse relaxation on echo spacing, thus, does not necessarily imply that relaxation is not influenced by diffusion effects.

In sandstones, the localization regime can arise due to the presence of large paramagnetic particles such as clays. An example of such a system is North-Burbank sandstone which has macropores lined with chlorite clay flakes. Zhang

et al. (2003) modeled the gradients induced in a pore lined with clay flakes such that the flakes form micropores that open to a larger macropore. They found that large field gradients are concentrated around the sharp corners of the clay flakes and in the micropores between clay flakes. The gradients also extend considerably in the macropore although the strength is not as high as in micropores. Fluid molecules in the micropore and macropore are, however, coupled by diffusion (Anand et al., 2005). Thus, in general the molecules experience gradients that are intermediate to those in the micro and macropores.

Figure 21 shows the T_1 and T_2 distributions of two water-saturated North Burbank sandstone cores. The T_2 distributions are shown as a function of echo spacings. Once again, a large T_1/T_2 ratio is observed and the T_2 distributions show echo spacing dependence. These observations are expected for the localization regime of transverse relaxation in the presence of large internal field gradients. The logmean longitudinal and transverse relaxation times for the cores are listed in Table 8.

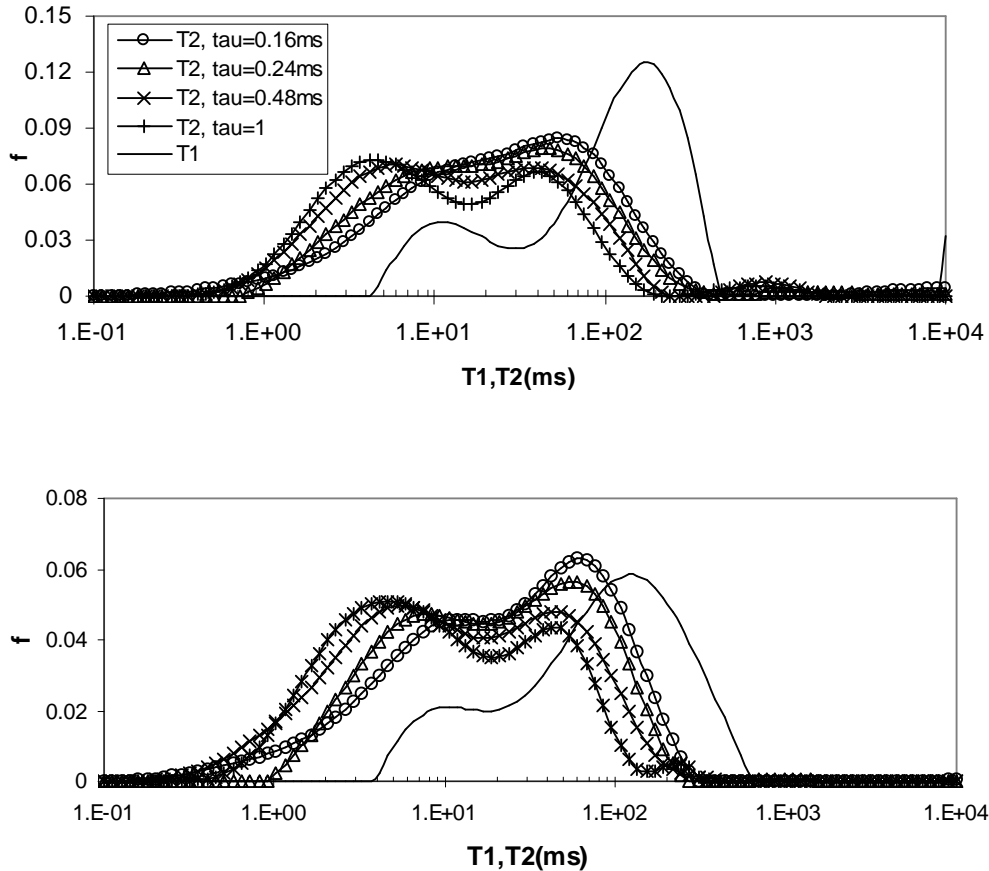


Figure 21: T_1 and T_2 distributions of water saturated North Burbank sandstone cores 1 and 2.

Table 8: Longitudinal and Transverse relaxation times of water saturated NB.

| Relaxation time (ms) | Core 1 | Core 2 |
|------------------------------------|--------|--------|
| T_1 | 87.5 | 64.2 |
| T_2 ($\tau_E = 0.16\text{ms}$) | 23.6 | 20.2 |
| T_2 ($\tau_E = 0.24\text{ms}$) | 20.5 | 19.0 |
| T_2 ($\tau_E = 0.48\text{ms}$) | 14.4 | 11.4 |
| T_2 ($\tau_E = 0.96\text{ms}$) | 11.7 | 10.4 |

To validate that the cores are in localization regime, let us quantitatively estimate the values of the characteristic time scales. The pore size distribution obtained from mercury porosimetry (Anand et al., 2005) shows that the average macropore radius is $24\mu\text{m}$ assuming a pore body to throat ratio of 3. Since the inhomogeneous fields extend throughout the entire pore, diffusional correlation time is given as

$$\tau_R = \frac{R^2}{D} = \frac{(24 \cdot 10^{-4})^2}{2.5 \cdot 10^{-5}} \sim 0.2 \text{ sec} \quad (62)$$

According to Zhang (2001), the range of dimensionless internal field gradient (G^*) in a clay lined pore is 28. The dimensionless gradient can be made dimensional using the following equation

$$G = \frac{\delta\chi}{4\pi} \frac{B_0}{w} G^* \quad (63)$$

where G, G^* are the dimensional and dimensionless internal field gradients respectively, $\delta\chi = \chi_{\text{chlorite}} - \chi_{\text{fluid}}$ and w is the width of the clay flake. Thus, the range of frequencies in the pore of length L_s is

$$\delta\omega \sim \gamma GL_s \quad (64)$$

Using $\chi_{\text{chlorite}} = 104 \cdot 10^{-6}$ (cgs units, Zhang et al., 2001), $w = 0.2\mu\text{m}$, $R_p = 24\mu\text{m}$, we get

$$\delta\omega \sim 3 \cdot 10^5 \text{ rad/sec} \quad (65)$$

Thus, the characteristic dephasing time is

$$\tau_H = \frac{1}{\delta\omega} \sim 3 \cdot 10^{-6} \text{ sec} \quad (66)$$

Since $\tau_E \geq 10^{-4}$ sec, $\tau_H \ll \tau_E$, τ_R satisfying the conditions for the localization regime.

The experimental results can be summarized on the plot of the asymptotic relaxation regimes in $(\delta\omega\tau_R, \delta\omega\tau_E)$ parameter space. Figure 22 shows the dimensionless secular relaxation rates in the $(\delta\omega\tau_R, \delta\omega\tau_E)$ parameter space for the various experimental systems studied. The values of coordinates are calculated from the values of characteristic time scales mentioned in Tables 1, 6

and 7. The corresponding experimental rates are normalized by a characteristic rate defined as

$$\frac{1}{t_0} = f \cdot \delta\omega \quad (67)$$

where f is the volume fraction of the paramagnetic particles. The values of f and $\delta\omega$ used in the calculation are mentioned in Appendix A. For comparison, the contours of dimensionless relaxation rates predicted by theoretical expressions for the three asymptotic regimes are also plotted. A good quantitative agreement between the theoretically predicted rates and experimentally measured rates is observed for all cases.

The relaxation characteristics of the experimental systems in Figure 22 can be explained in terms of the asymptotic regimes. The aqueous dispersions of nanoparticles (open circles) and coated sand at low surface concentrations (open triangles) fall in motionally averaging regime. Thus no echo spacing is observed and T_1/T_2 ratio increase with particle size. Experiments with sand coated at high concentrations of 25nm (open inverted triangles) and 110nm (open squares) lie in localization regime. Thus, an echo spacing dependence of the T_2 relaxation is observed. Similarly, North Burbank sandstone (solid circles) and sand with dispersed 2.4 μm magnetite (solid diamonds) also fall in localization regime and display an echo spacing dependence.

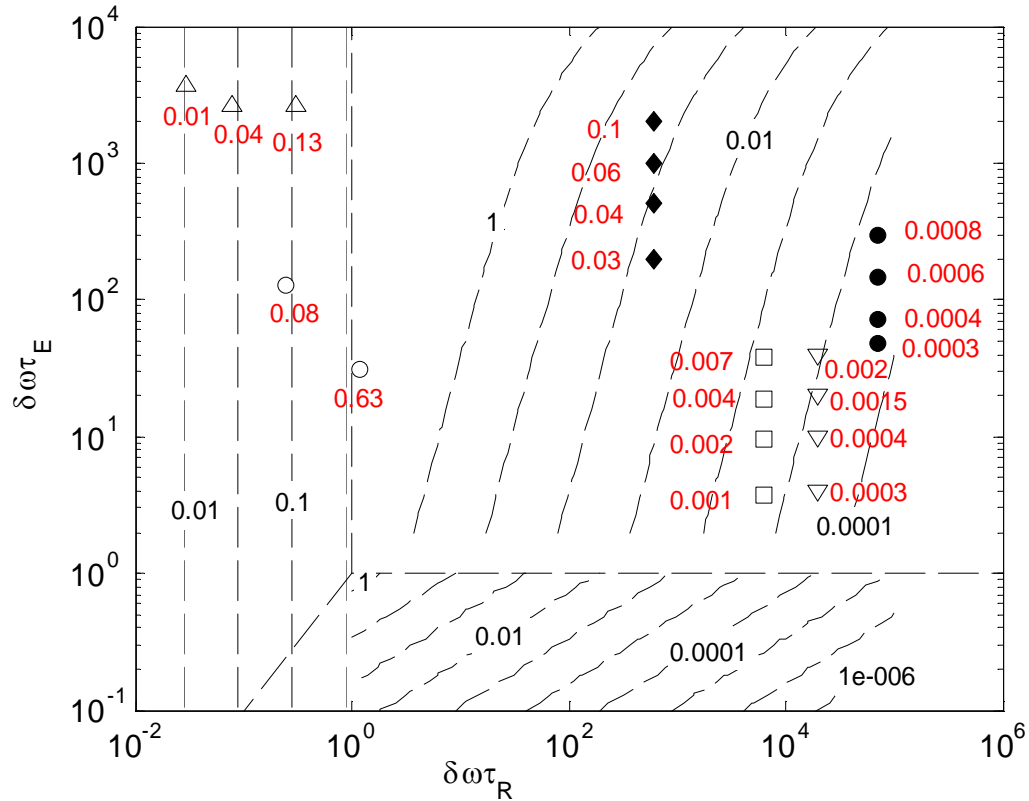


Figure 22: Parametric representation of experimentally measured secular relaxation rates for various systems in the $(\delta\omega\tau_R, \delta\omega\tau_E)$ parameter space. (Δ) aqueous dispersion of 4nm, 9nm, 16nm particles (\circ) sand coated with dilute concentrations of 25nm and 110nm particles (\square) sand coated with high surface concentration of 25nm (∇) sand coated with high surface concentration of 110nm, (\blacklozenge) sand with dispersed 2.4 μ m magnetite (\bullet) North Burbank sandstone.

In figure 23 we plot the secular relaxation rates with the echo spacing for the several cases of localization regimes observed in figures 18-21. The solid lines represent linear fit between the relaxation rates and the echo spacing. As was shown by the random walk simulations, the echo spacing dependence of secular relaxation in the localization regime is almost linear and not quadratic. These results thus explain the earlier observations of Brown et al. (1993) and Fantazzini et al. (2005) who found a quasi-linear dependence of transverse relaxation on the echo spacing in porous media.

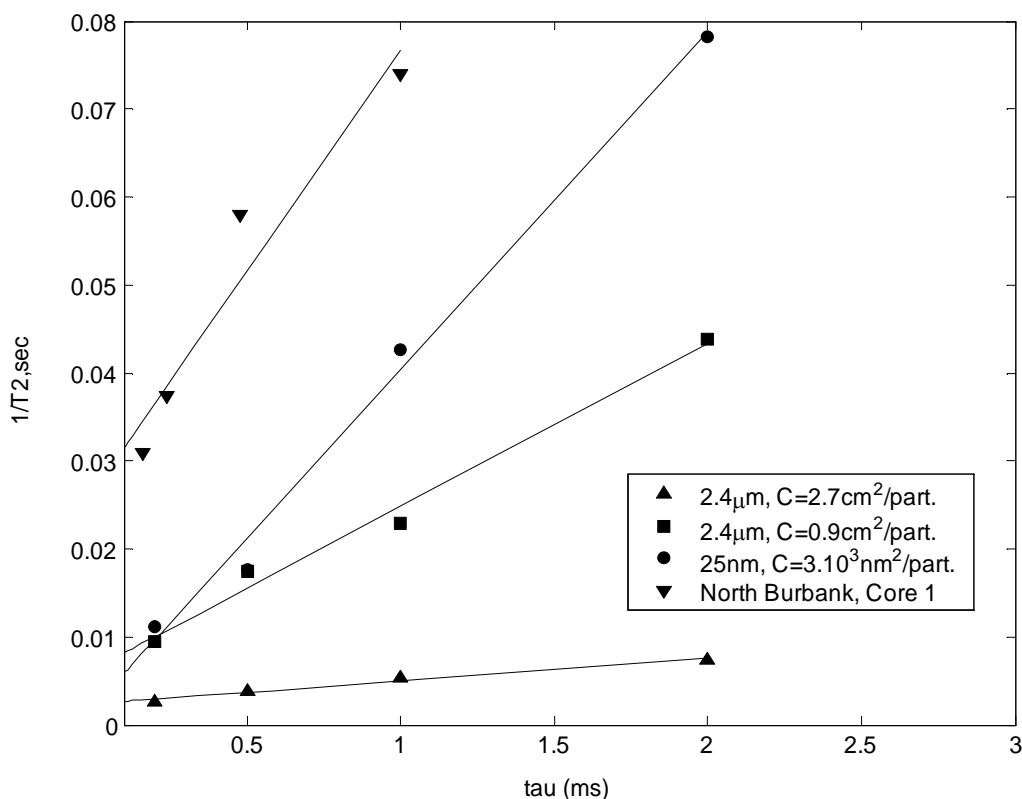


Figure 23: Plot of secular relaxation rates with echo spacing for different cases of localization regime. The solid lines are the linear best fits of the experimental points.

Conclusions

Diffusion of spins in magnetic field inhomogeneities leads to additional transverse relaxation due to dephasing called secular relaxation. Random walk simulations of proton relaxation in the presence of paramagnetic particles show that secular relaxation is characterized by three time scales: diffusional correlation time (τ_R), time for significant dephasing (τ_H) and half echo spacing of the CPMG sequence (τ_E). The smallest characteristic time determines the classification of secular relaxation into three asymptotic regimes of motionally averaging, localization and free diffusion. This classification of relaxation regimes using characteristic time scales is independent of the particular choice of inhomogeneous field distribution.

The asymptotic regimes show different relaxation characteristics. In the motionally averaging regime, field inhomogeneities are averaged due to fast diffusion in time much smaller than τ_E . Thus, no echo spacing dependence of transverse relaxation is observed. Additionally, the relaxation rate increases with the length scale of field inhomogeneity. In the free diffusion regime, secular relaxation rate shows quadratic dependence on the echo spacing. However, the dependence on the length scale of inhomogeneity is inversed and the relaxation rate decrease with the increase in size of the paramagnetic particle. This is

because the average gradient decreases with the increase in particle size. In the localization regime, relaxation rate shows a quasi- or sub-linear dependence on echo spacing. The dependence on field inhomogeneity length scale is inversed. The characteristics of the relaxation regimes can be demonstrated in a single contour map of dimensionless relaxation rate in $(\tau_R/\tau_H, \tau_E/\tau_H)$ parameter space.

The relaxation characteristics of asymptotic regimes can also provide explanation for the diverse NMR characteristics observed in fluid-saturated sandstones. A large range of T_1/T_2 ratio in sandstones with no echo spacing dependence of T_2 relaxation observed by Kleinberg et al. (1993) can arise in the motionally averaging regime. The quasi or sub-linear dependence of the T_2 relaxation on echo spacing shown in the experiments of Zhang et al. (2001) and Brown et al. (1995) can arise in the localization regime. Thus, the calculation of characteristic time scales can provide a quantitative understanding of paramagnetic relaxation in sandstones.

References:

- 1) Agarwal, S., 2007, Ph.D. Thesis, Rice University.
- 2) Anand, V. and Hirasaki, G.J., 2005, "Diffusional Coupling between micro and macropores for NMR relaxation in Sandstones and Carbonates", Proceedings of the 46th Annual SPWLA symposium, New Orleans, LA.
- 3) Bertini, I., Capozzi, F., Luchinat, C. and Xia, Z., 1993, "Nuclear and Electron Relaxation in $\text{Fe}(\text{OH}_2)_6^{3+}$ ", Journal of Physical Chemistry, 97, p 1134-1137.
- 4) Brooks, R.A., Moyny F. and Gillis, P., 2001, "On T_2 Shortening by Weakly Magnetized Particles: The Chemical Exchange Model", Magnetic Resonance in Medicine, Vol 45, p 1014-1020.
- 5) Brown, R.J.S. and Fantazzini, P., 1993, "Conditions for initial quasilinear T_2^{-1} versus τ for Carr-Purcell-Meiboom-Gill NMR with diffusion and susceptibility differences in porous media and tissues", Physical Review B, 47, 22, p14823-14834.
- 6) Carr, H.Y. and Purcell, E.M., 1954, "Effects of Diffusion on Free Precession in Nuclear Magnetic Resonance Experiments", Physical Review, Vol 94, No 3, p 630-638.
- 7) DeSwiet, T.M and Sen, P., 1993, "Decay of nuclear magnetization by bounded diffusion in a constant field gradient", Journal of Chemical Physics, Vol 100, No 8, p 5597-5604.
- 8) Fantazzini, P and Brown, R.J.S, 2005, "Initially linear echo-spacing dependence of $1/T_2$ measurements in many porous media with pore scale inhomogeneous fields", Journal of Magnetic Resonance, Vol 17, p 228-235.
- 9) Gillis, P. and Koenig, S.H., 1987, "Transverse relaxation of Solvent Protons Induced by Magnetized Spheres: Application to Ferritin, Erythrocytes and Magnetite", Magnetic Resonance in Medicine, Vol 5, p 323-345.

- 10) Gillis, P., Moiny, F. and Brooks, R.A., 2002, "On T_2 -Shortening by strongly magnetized spheres: a partial refocusing model", *Magnetic Resonance in Medicine*, Vol 34, p 227-233.
- 11) Jenson, J.H. and Chandra, R., 2000, "NMR Relaxation in Tissues with Weak Magnetic Inhomogeneities", *Magnetic Resonance in Medicine*, Vol 44, p144-156.
- 12) Kleinberg, R.L. and Farooqui, S.A., 1993, " T_1/T_2 ratio and frequency dependence of NMR Relaxation in Porous Sedimentary Rocks", *Journal of Colloid and Interface Science*, 158, p195-198.
- 13) Kleinberg, R.L., Kenyon, W.E. and Mitra, P.P., 1994, "Mechanism of NMR Relaxation of Fluids in Rocks", *Journal of Magnetic Resonance Series A*, 108, p 206-214.
- 14) Lide, D.R., 1990-1991, "Handbook of Chemistry and Physics", CRC Press, 71st Edition.
- 15) Massart, R., 1981, "Preparation of Aqueous Magnetic Liquids in Alkaline and Acidic Media", *IEEE Transactions on Magnetics*, 17 (2), p 1247-1248.
- 16) Menzel, D.A., "Fundamental Formulas of Physics", Prentice Hall, New York, NY, 1955.
- 17) Morgan, L.O and Nolle, A.W., 1959, "Proton Spin Relaxation in Aqueous Solutions of Paramagnetic Ions II. Cr^{+++} , Mn^{++} , Ni^{++} , Cu^{++} and Gd^{+++} ", *Journal of Chemical Physics*, 31(2), p 365-368.
- 18) Neuman, C.H., 1974, "Spin echo of spins diffusing in a bounded medium", *Journal of Chemical Physics*, Vol 60, No. 11, p 4508-4511.
- 19) Sen, P.N., André, A and Axelrod, S, 1999, "Spins echoes of nuclear magnetization diffusing in a constant magnetic field gradient and in a restricted geometry", *Journal of Chemical Physics*, Vol 111, No. 14, p. 6548-6555.
- 20) Solomon, I., 1955, "Relaxation Processes in a System of Two Spins", *Physical Review*, 99(2), p 559-565.
- 21) Tarczozon, J.C. and Halerpin, W.P., 1985, "Interpretation of NMR Diffusion measurements in uniform and nonuniform field gradients", *Physical Review B*, Vol 32 (5), p2798-2807.
- 22) Weisskoff, R.M., Zuo, C.S., Boxerman, J.L. and Rosen, B.R., 1994, "Microscopic Susceptibility Variation and Transverse Relaxation: Theory and Experiment", *Magnetic Resonance in Medicine*, Vol 31, p 601-610.
- 23) Yu, W.W., Joshua, C., Yavuz, C.T. and Colvin, V.L., 2004, "Synthesis of monodisperse iron oxide nanocrystals by thermal decomposition of iron carboxylate salts, *Chemical Communication*, web published on 2nd Sept 2004.
- 24) Zhang, Q, 2001, "NMR Formation Evaluation: Hydrogen Index, Wettability and Internal Field Gradients", Ph.D. Thesis, Rice University.
- 25) Zhang, G.Q., Hirasaki, G.J., House, W.V., 2003, "Internal field gradients in porous media", *Petrophysics*, 42, p422-434.
- 26) Zhang, G.Q and Hirasaki, G.J., 2003, "CPMG relaxation by diffusion with constant magnetic field gradient in a restricted geometry: numerical

simulation and application”, Journal of Magnetic Resonance, Vol 163, p 81-91.

Appendix A

f is the volume fraction of the paramagnetic particles. The values of f are easily determined for the different cases. For the case of aqueous dispersion of the particles, f is given as

$$f = \frac{C}{d} \quad (A1)$$

where C is the concentration of the dispersion (g/ml). Magnetite density ($d=5.18\text{g/cm}^3$) is obtained from Lide et al. (CRC Press). For nanoparticle adsorbed on silica surface at low concentrations, f is given by the quantity of adsorbed paramagnetic material divided by magnetite density and pore volume. At high concentrations, f is approximately the solid matrix volume fraction since the particles are assumed to be forming a shell around sand grains. For North Burbank core, $f (=0.3)$ is obtained from the volumetric calculations of micro and macropore done by Zhang et al. (2001).

Table A1: f and $\delta\omega$ used for the computation of dimensionless relaxation rates for the various experimental systems.

| | 25nm $10^4, 9 \cdot 10^4 \text{ nm}^2/\text{part.}$ | 110nm $0.3, 8 \text{ cm}^2/\text{part.}$ | 2.4 μm $2.7, 0.9\text{cm}^2/\text{part}$ | North Burbank |
|--------------------------|--|---|--|------------------|
| f (dimensionless) | $2 \cdot 10^{-4}, 1 \cdot 10^{-5}$ | $2 \cdot 10^{-4}, 4 \cdot 10^{-5}$ | $1.3 \cdot 10^{-4}, 4 \cdot 10^{-4}$ | 0.3 |
| $\delta\omega$ (rad/sec) | $4 \cdot 10^6$ | 10^5 | 10^6 | $3 \cdot 10^5$ |

Task 3: Characterization of pore structure and wettability

NMR Well Logging and Special Core Analysis for

Fluid-Rock Characterization

Subcontract to Rice University on

DOE Award Number: DE-PS26-04NT15450-2C

Semi-Annual Report

Reporting Period Start Date: 4-1-2005

Reporting Period End Date: 9-30-2006

I. Tripathi, R. Pitchumani, & K. K. Mohanty

Oct 2006

University of Houston

4800 Calhoun Road

Houston, TX 77204-4004

Abstract

Characterization of pore structure and wettability has been completed on six carbonate samples. The vug size, distribution and interconnection vary significantly in these six samples. The thin sections have been characterized through their pore size distribution, two-point correlation function, chord number distribution, lineal path function and fractal dimension. The power spectrum from Fourier transform has been computed. The three-dimensional pore structures have been reconstructed for two carbonates and one sandstone sample. Single phase permeability and NMR response has been measured for all the samples. The relative permeability, NMR response and electrical conductivity have been measured for three samples.

TABLE OF CONTENTS

| | Page |
|----------------------|------|
| Cover Page | 111 |
| Abstract | 112 |
| Table of Contents | 113 |
| Introduction | 114 |
| Experimental Results | 115 |
| Conclusions | 192 |

I. Introduction

The goal of this research is to relate NMR measurements in a core to its pore structure and wettability and thus to permeability and relative permeability. In Task 3, 2D pore structures will be extracted from thin-sections. The oil/brine/rock compositions will be related to wettability as determined by contact angle goniometry and atomic force microscopy. Amott wettability will be measured to define core scale wettability. Brine and oil NMR response of the cores will be measured. NMR response of surfactant solution imbibed carbonate cores will also be measured. NMR response will be simulated from pore images and wettability. Mechanistic correlations will be developed between NMR response, wettability and pore structure. Such correlation will help NMR logging define the variation of pore structure and wettability through all logged wells.

In Task 4, NMR response will be related to permeability and relative permeabilities. Such a correlation can estimate the reservoir heterogeneity and multiphase flow in logged but non-cored wells. The relative permeability functions determine the time for water breakthrough and the rate of oil recovery. Water-oil imbibition relative permeability will be measured for each core plug. Electrical conductivity will be measured at end-point saturations. Pore network models developed in Task 3 will be used to estimate the relative permeabilities and electrical conductivity. Correlations will be made among the NMR response and transport properties. Simple, but mechanistic correlations will be developed for NMR response, permeability and relative permeability.

The project started in the last quarter of 2004. We have worked on four subtasks: pore structure, wettability, NMR response and relative permeability/electrical conductivity of six carbonate cores. The activities are described in the next section.

II. Experiments

Table 1. Porosity and permeability of core samples

| Sample | Permeability(mD) | Porosity (%) |
|-------------|------------------|--------------|
| Limestone 1 | 7 | 24.7 |
| Limestone 2 | 150 | 23.3 |
| 7536B | 0.08 | 4.55 |
| 2416 | 0.023 | 5.97 |
| 7626A | 140.17 | 19.5 |
| 7626B | 2313 | 24.4 |

Thin sections were obtained for six carbonate samples listed in Table 1. The thin sections were viewed by using a Nikon Opti-Phot-2 Optical Microscope at resolutions of 4X, 10X and 40X. The digital images were captured in a CCD camera, and the video output signal was sent to a PC by using a frame-grabber PCI card. A computer controlled microscope stage was installed for automated image capture (Figure 1). Using this stage 3500 images, each of 640 X 480 pixels, were taken to cover the entire thin section of about 1.5 cm X 1.0 cm at high resolution. These images were then stitched using the Fourier Phase Correlation Method applied to the overlap region between images adjacent to each other. This resulted in images of about 10000 X 15000 pixels for each of the 6 carbonate thin sections at 4X, 10X and 40X resolutions.

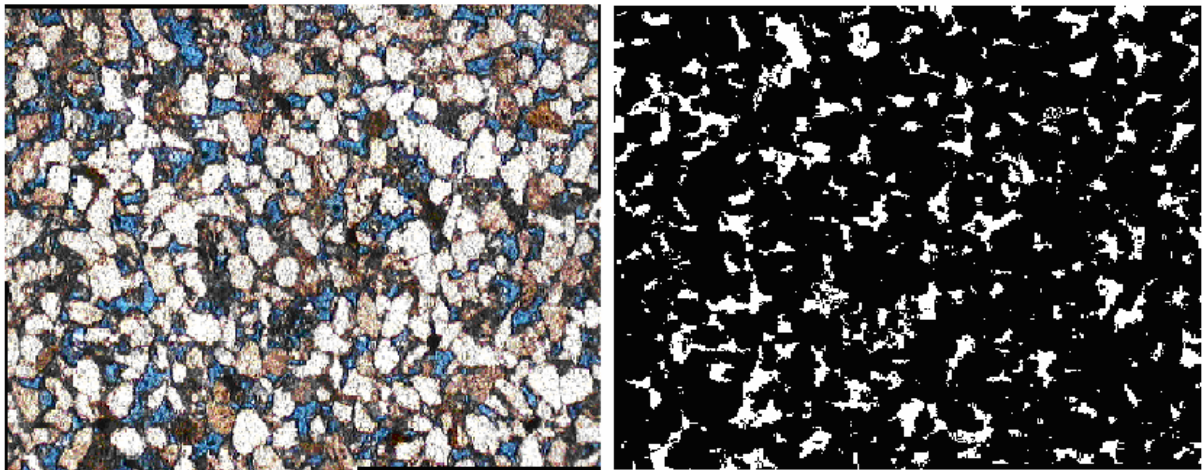
Table 2. Pixel sizes and resolution

| Optical Resolution | Microns/Pixel |
|--------------------|--------------------------|
| 4X | 3 μm /pixel |
| 10X | 1 μm /pixel |
| 40X | 0.3 μm /pixel |

Figure 1. Imaging apparatus



Figure 2. Color image to B/W image conversion



The phase correlation method is described for cylindrically shifted images. Let g_1 and g_2 be the overlapping sections of images to be stitched and their respective Fourier transforms be G_1 and G_2 . Then the phase correlation is defined as

$$d = F^{-1}\{e^{i(\phi_1 - \phi_2)}\}$$

where

$$G_j(\vec{f}) = |G_j(\vec{f})| e^{i\phi_j(\vec{f})}$$

For images shifted by a vector \vec{L} ,

$$g_2(\vec{r}) = g_1(\vec{r} + \vec{L})$$

and

$$G_2(\vec{f}) = G_1(\vec{f}) e^{i2\pi\vec{f}\cdot\vec{L}}.$$

The cross-correlation function d is a delta function given by

$$d = \delta(\vec{r} - \vec{L}).$$

Thus the exact \vec{L} can be found by using the cross-correlation function d . This d is calculated as a function of the position of g_2 with respect to g_1 . At near perfect alignment d is maximized. After the alignment, the images can be stitched in sequence to form a composite image. An efficient code was developed in MATLAB based on this method for stitching 3000 images.

Image segmentation is done on the composite images to convert them into a black and white image with pores as white and rock as black (Figure 2). This binary image can be analyzed for properties of the pore space described below.

2.1 Pore size distribution

Using erosion dilation algorithm we can identify each object in the pore space and calculate its area (in pixels), and a number of other characteristics like the diameter of the largest circle that can be fit completely inside that pore (called minimum diameter). Figure 3-14 show the percentage of pore space area associated with pores of a particular minimum diameter at the resolution of 1 $\mu\text{m}/\text{pixel}$ for the horizontal and vertical thin sections of each of the six carbonate samples.

Figure 3. Pore Size Distribution for Limestone 1 Horizontal Thin-Section

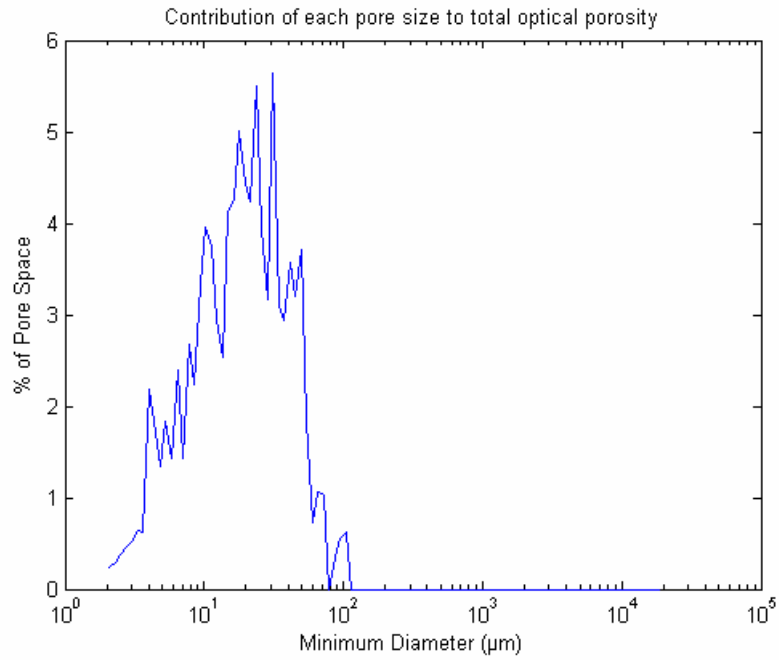


Figure 4. Pore Size Distribution for Limestone 1 Vertical Thin-Section

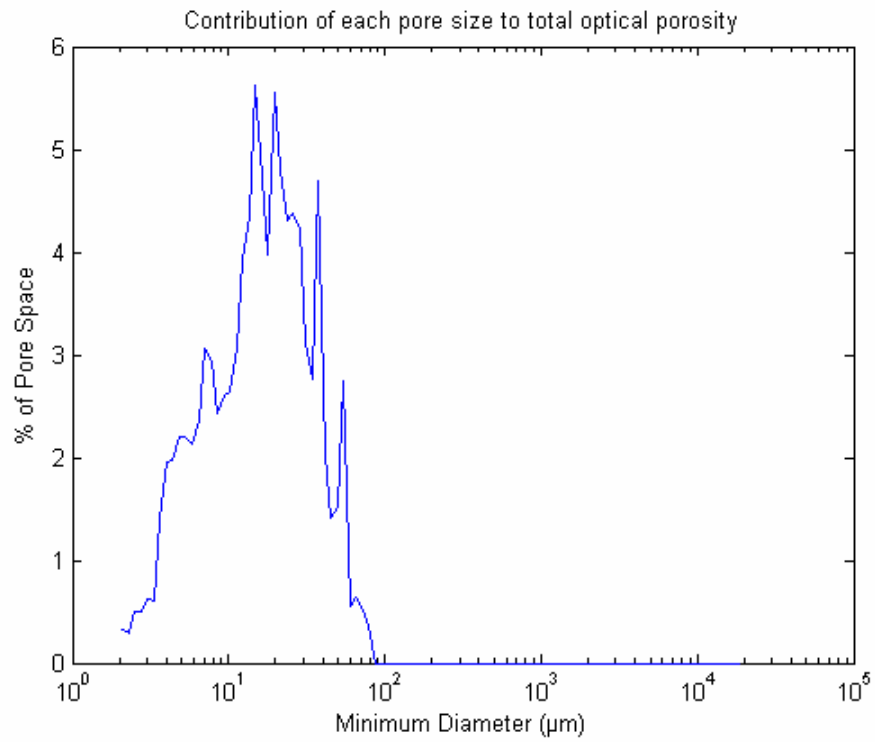


Figure 5. Pore Size Distribution for Limestone 2 Horizontal Thin-Section

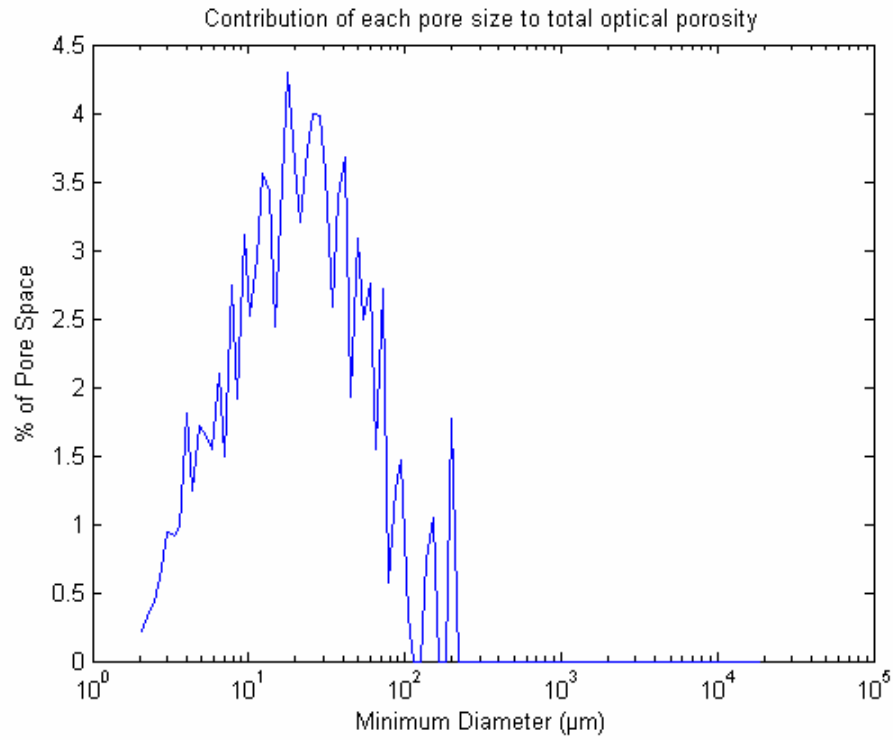


Figure 6. Pore Size Distribution for Limestone 2 Vertical Thin-Section

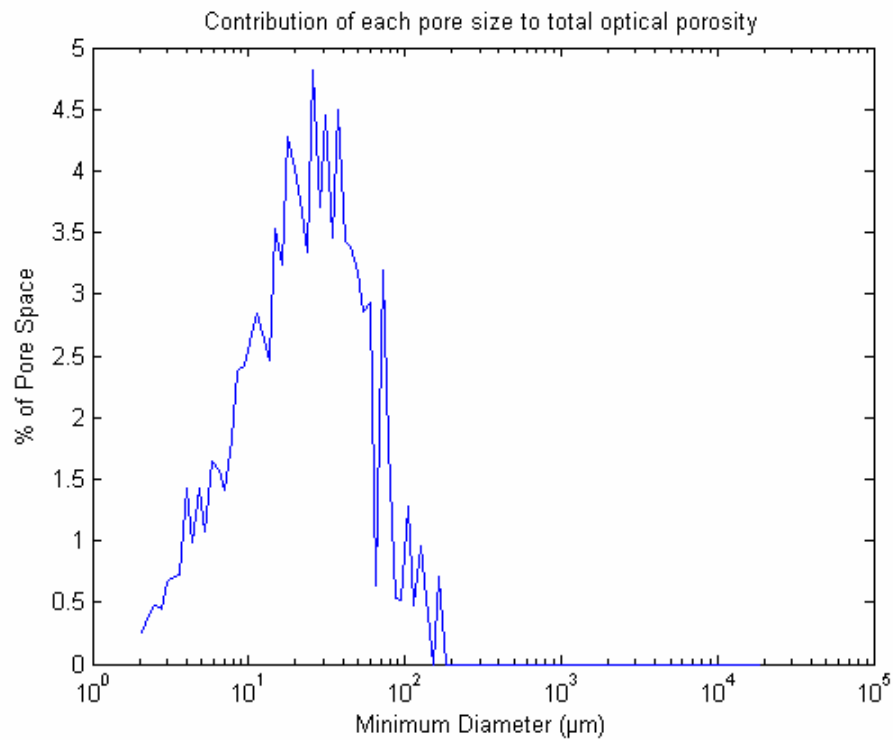


Figure 7. Pore Size Distribution for 7536B Horizontal Thin-Section

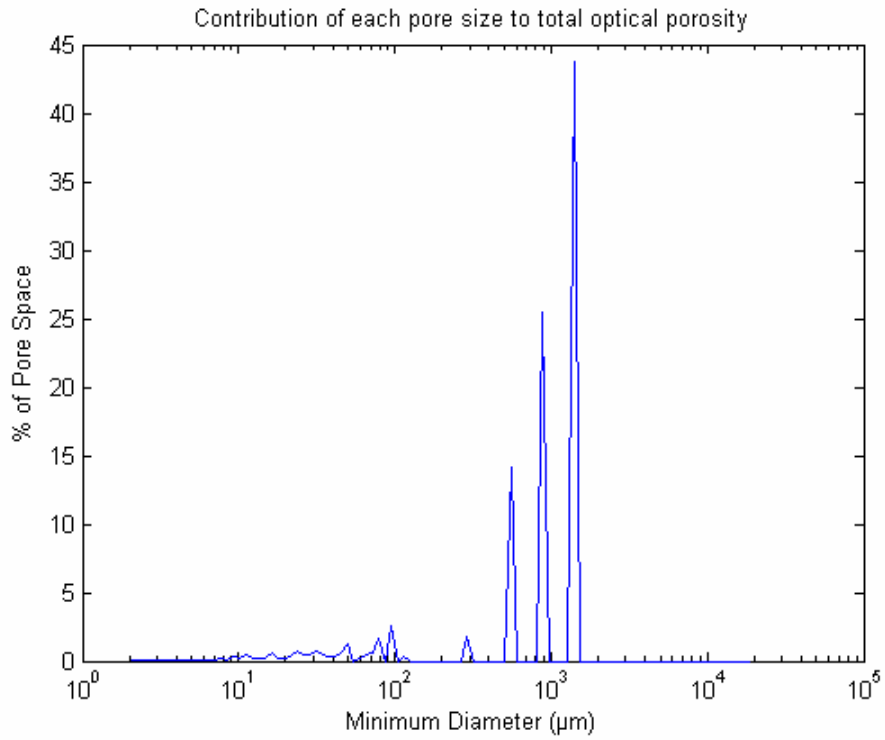


Figure 8. Pore Size Distribution for 7536B Vertical Thin-Section

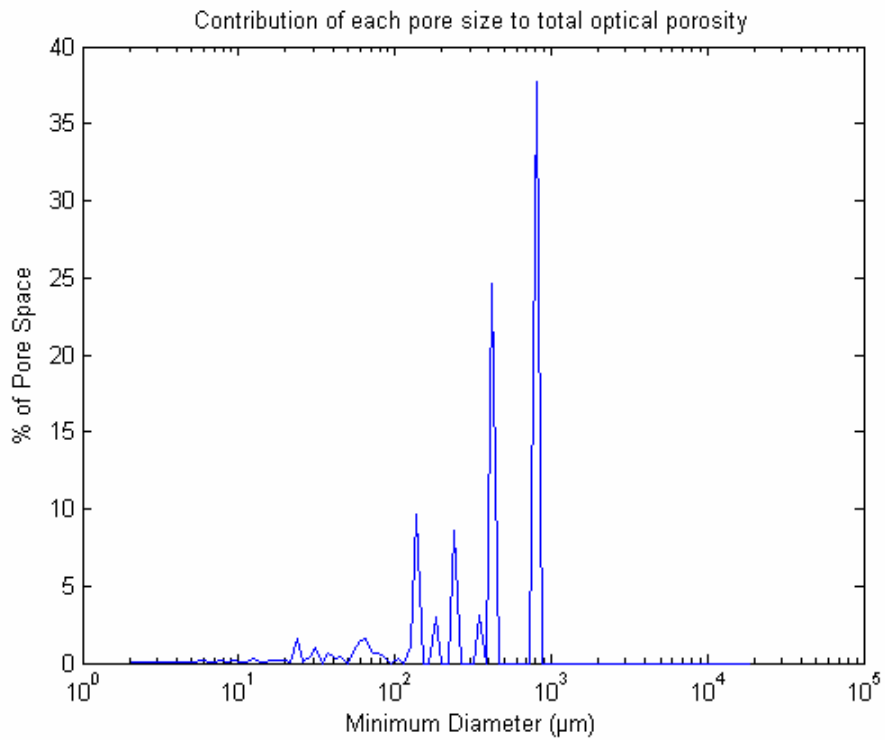


Figure 9. Pore Size Distribution for 2416 Horizontal Thin-Section

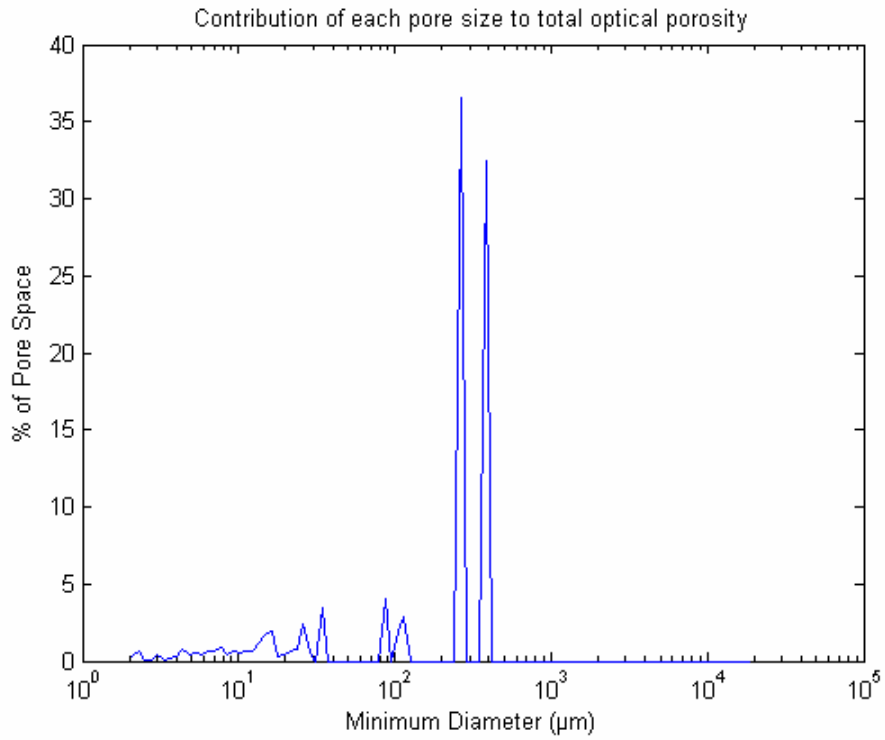


Figure 10. Pore Size Distribution for 2416 Vertical Thin-Section

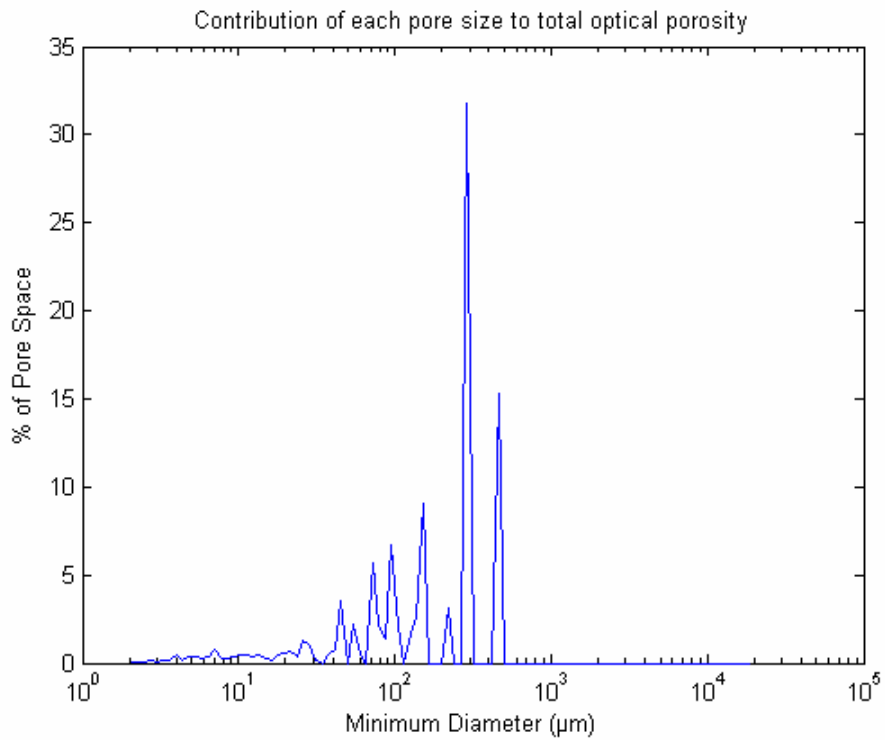


Figure 11. Pore Size Distribution for 7626A Horizontal Thin-Section

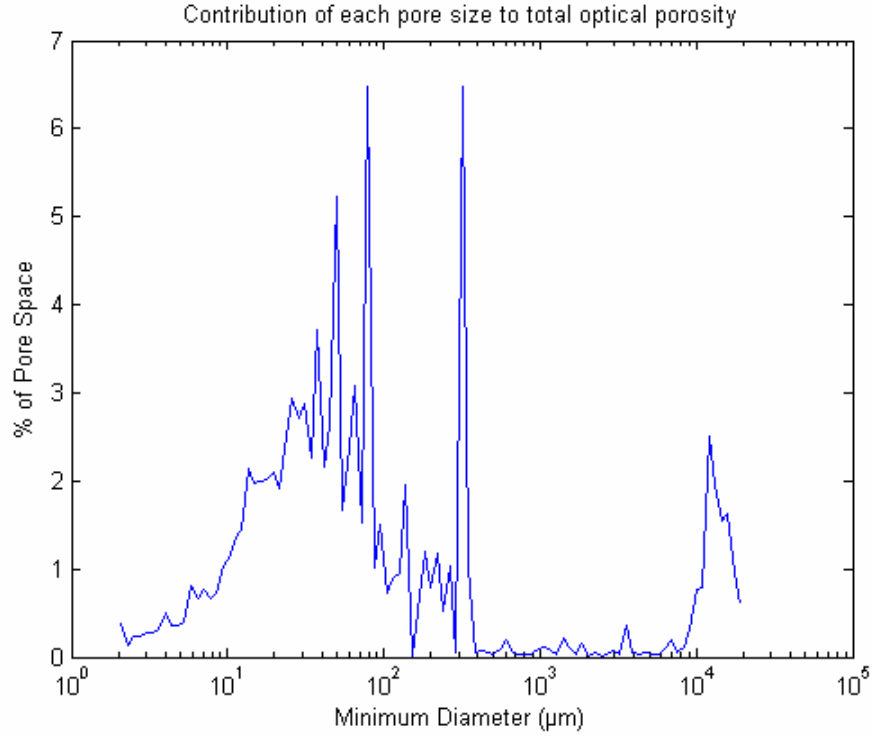


Figure 12. Pore Size Distribution for 7626A Vertical Thin-Section

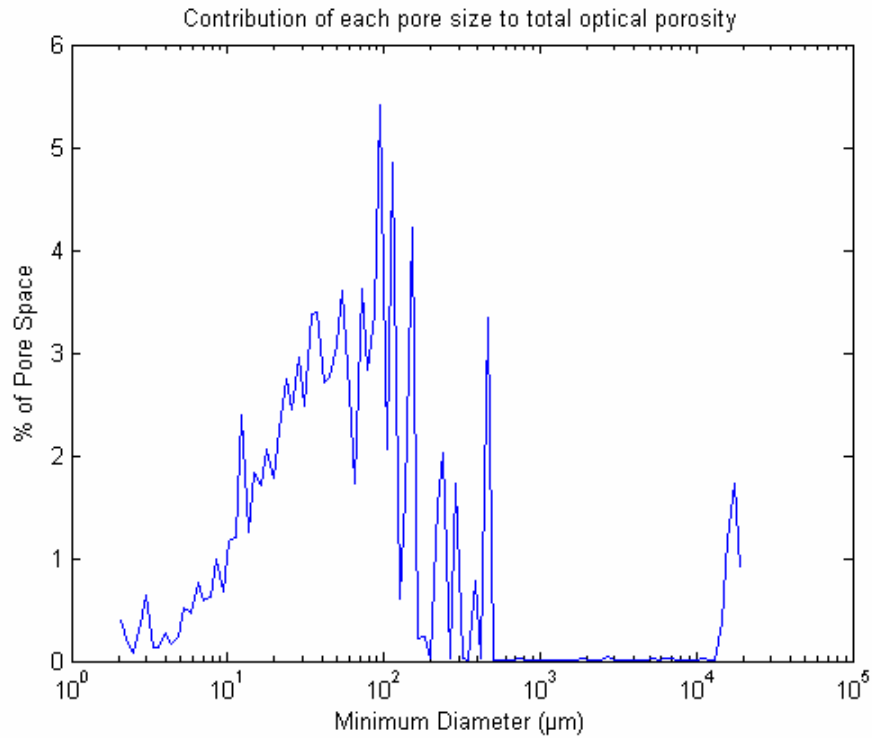


Figure 13. Pore Size Distribution for 7626B Horizontal Thin-Section

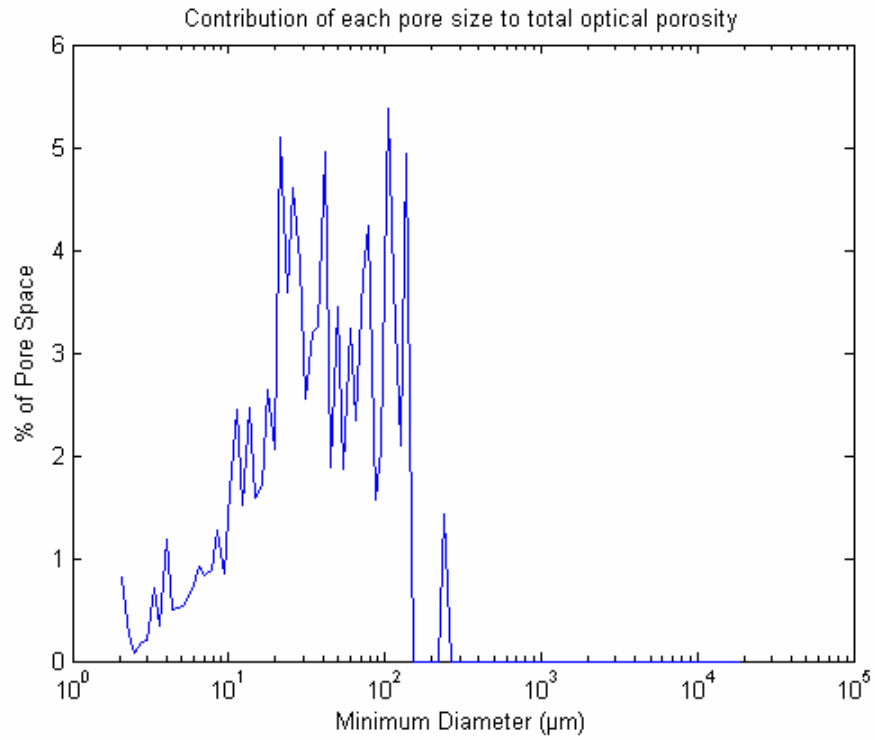
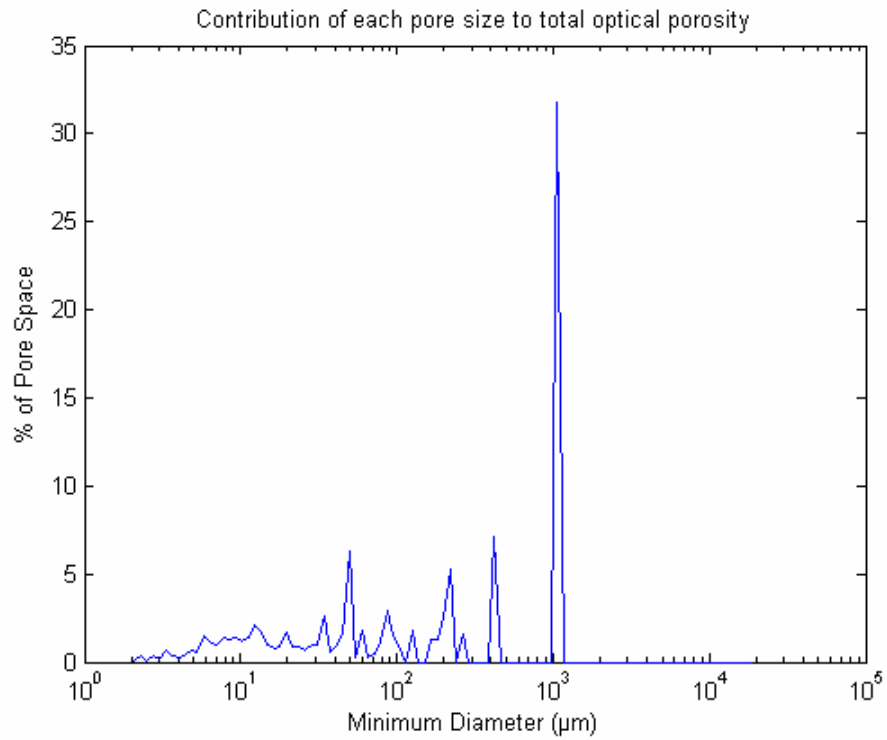


Figure 14. Pore Size Distribution for 7626B Vertical Thin-Section



The pore size distributions of vuggy carbonates show that most of the porosity of the sample is due to vugs in the size range of about 0.5 to 1 mm.. The packstones on the other hand have a well distributed porosity with a mean pore size of about 30 microns.

2.2 Porosity

The binary image is equivalent to a discrete phase function $Z(\underline{x})$ defined as

$$Z(\underline{x}) = \begin{cases} 1(\text{pore}) \\ 0(\text{rock}) \end{cases}.$$

The porosity (Φ) is then defined as the statistical average

$$\Phi = \langle Z(\underline{x}) \rangle.$$

The optical porosity of the thin section samples is dependent on the resolution of the image and the amount of micro-porosity present in the sample. If the sample has vugs then the optical porosity can even be greater than that of the whole core sample.

2.3 Autocorrelation function

The spatial autocorrelation function $S_2(\underline{r})$ is defined as the probability that two points at the distance r both lie in the pore phase when randomly selected from the image. This can be normalized by a function of porosity so that value of $S_2(\underline{r})$ ranges from 0 to 1. This normalized autocorrelation function is given by

$$S_2(\underline{r}) = \frac{\langle (Z(\underline{x}) - \langle Z \rangle)(Z(\underline{x} + \underline{r}) - \langle Z \rangle) \rangle}{\Phi - \Phi^2}$$

For an isotropic system without long range order

$$\begin{aligned} S_2(0) &= 1 \\ \lim_{r \rightarrow \infty} S_2(r) &= 0 \end{aligned}$$

Also for a digitized 2D medium

$$\left. \frac{dS_2(r)}{dr} \right|_{r=0} = -s/4$$

Where s = specific surface of the pore phase. Figure 15-26 show the two-point autocorrelation function for the six limestone samples at a resolution of 1 $\mu\text{m}/\text{pixel}$. The autocorrelation is calculated for both the horizontal and vertical sections along two perpendicular directions named X and Y.

Figure 15. Two Point Autocorrelation Function for Limestone 1 Horizontal Thin Section

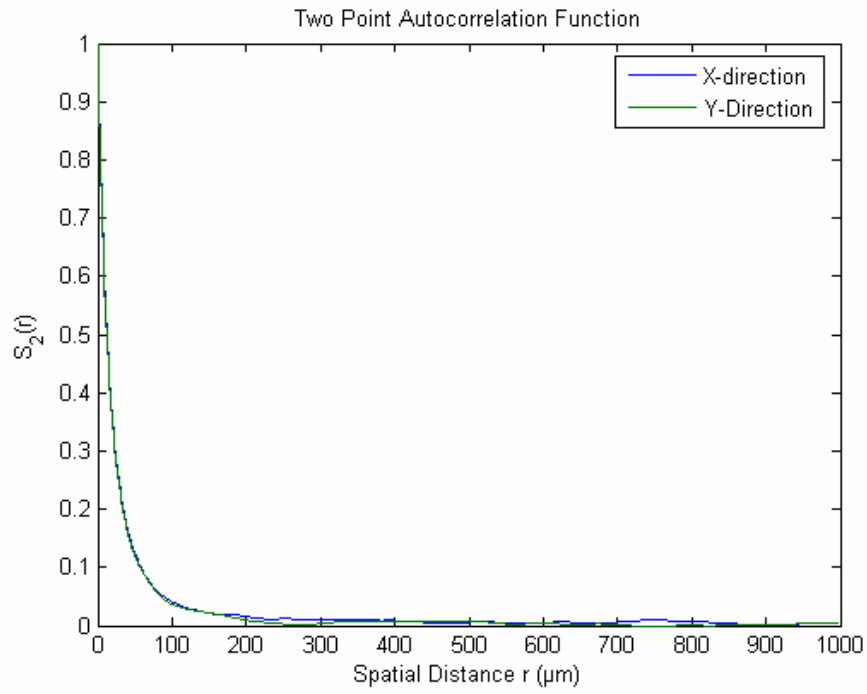


Figure 16. Two Point Autocorrelation Function for Limestone 1 Vertical Thin Section

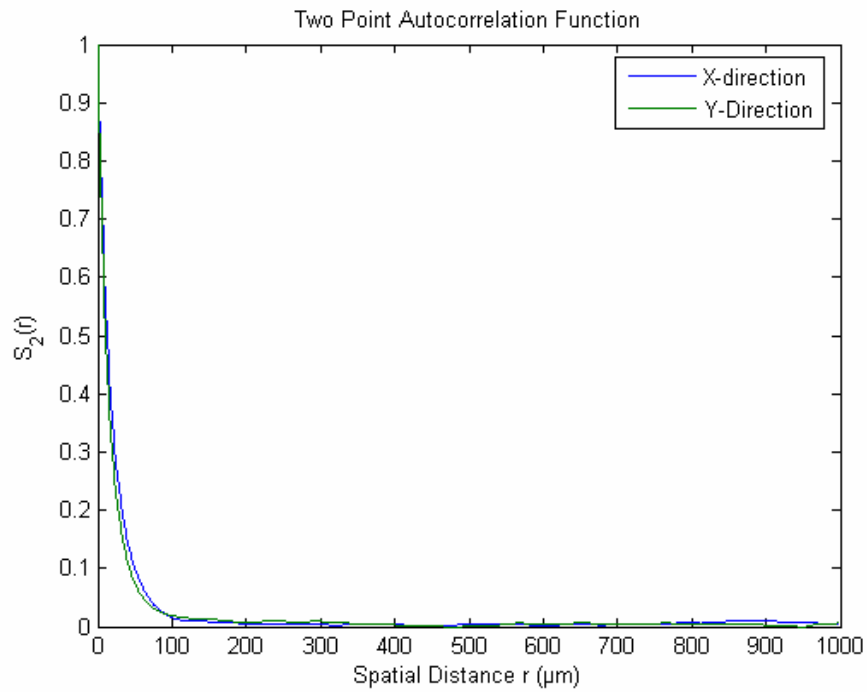


Figure 17. Two Point Autocorrelation Function for Limestone 2 Horizontal Thin Section

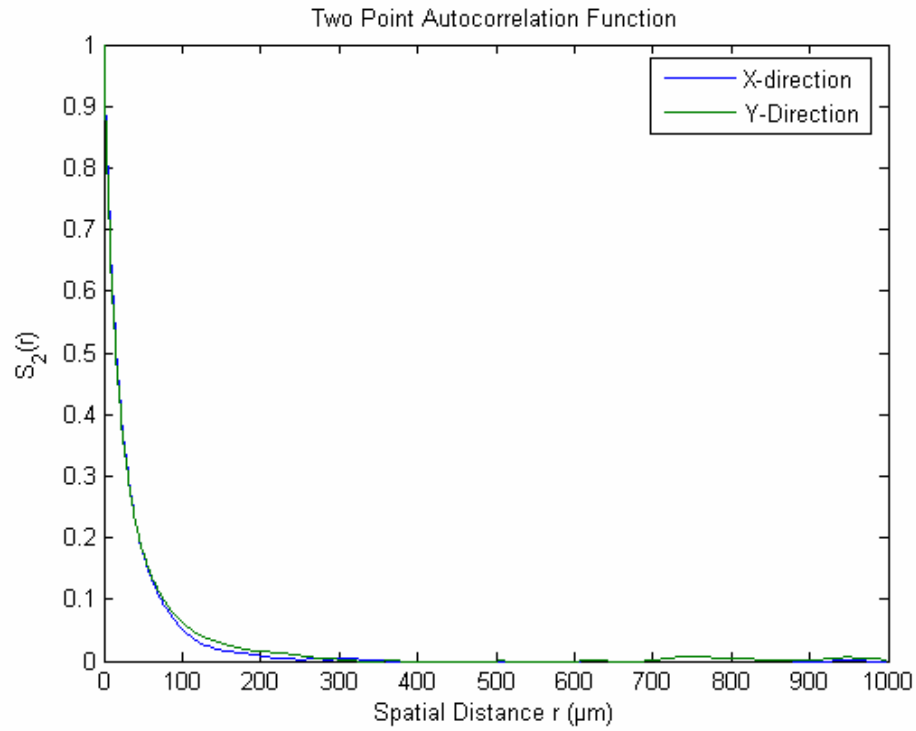


Figure 18. Two Point Autocorrelation Function for Limestone 2 Vertical Thin Section

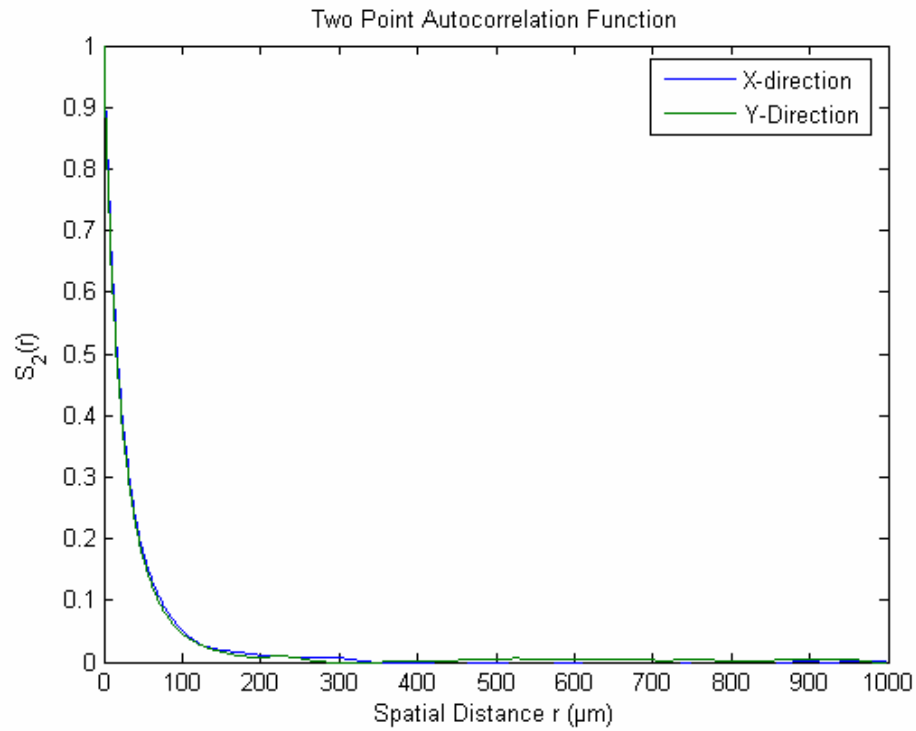


Figure 19. Two Point Autocorrelation Function for 7536 B Horizontal Thin Section

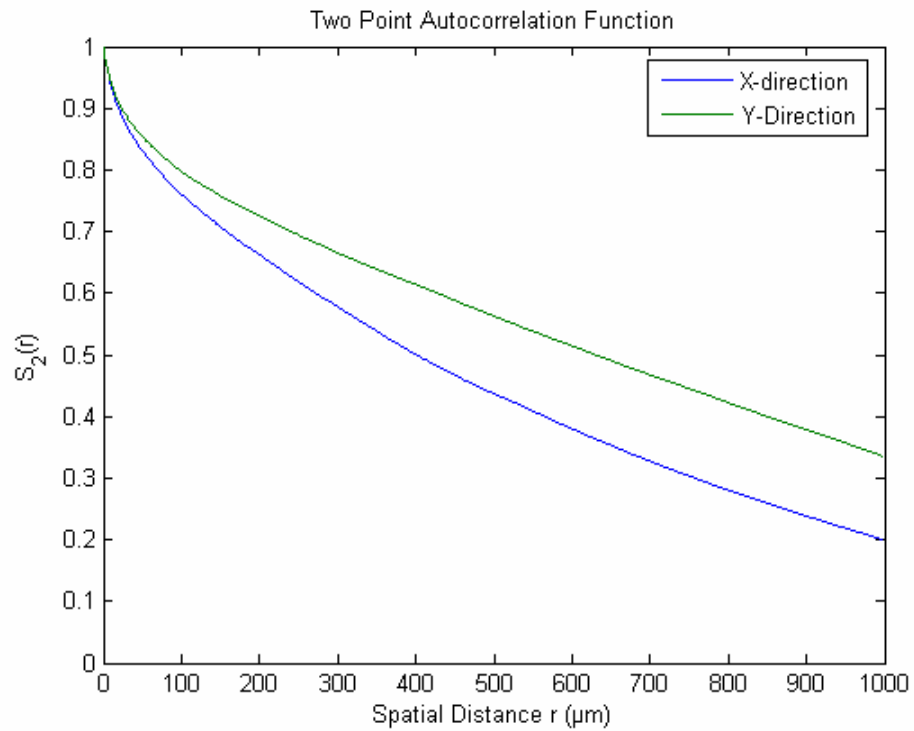


Figure 20. Two Point Autocorrelation Function for 7536B Vertical Thin Section

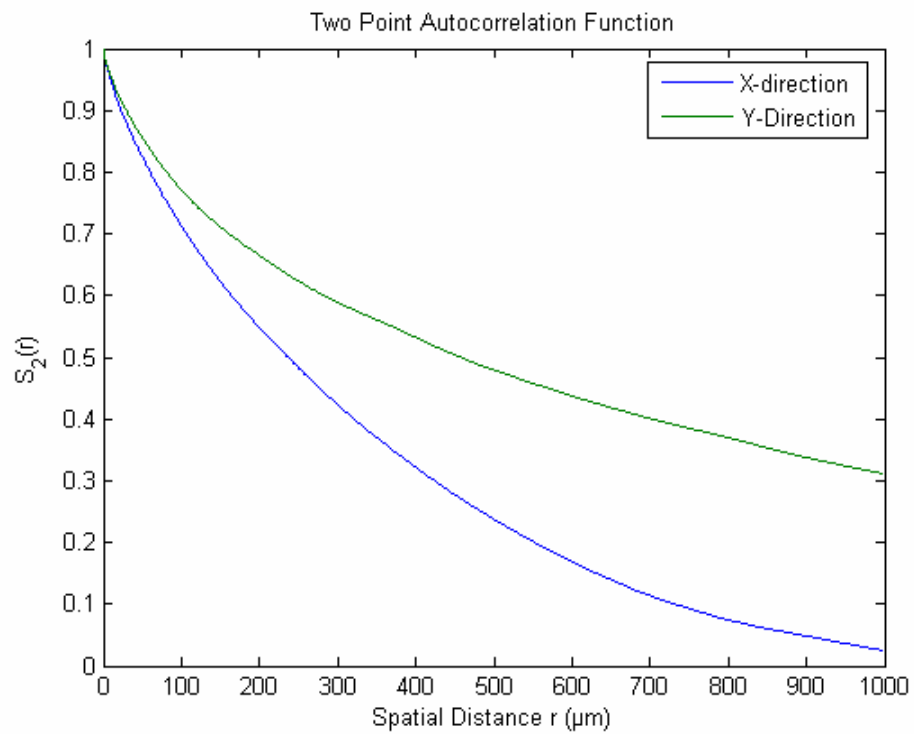


Figure 21. Two Point Autocorrelation Function for 2416 Horizontal Thin Section

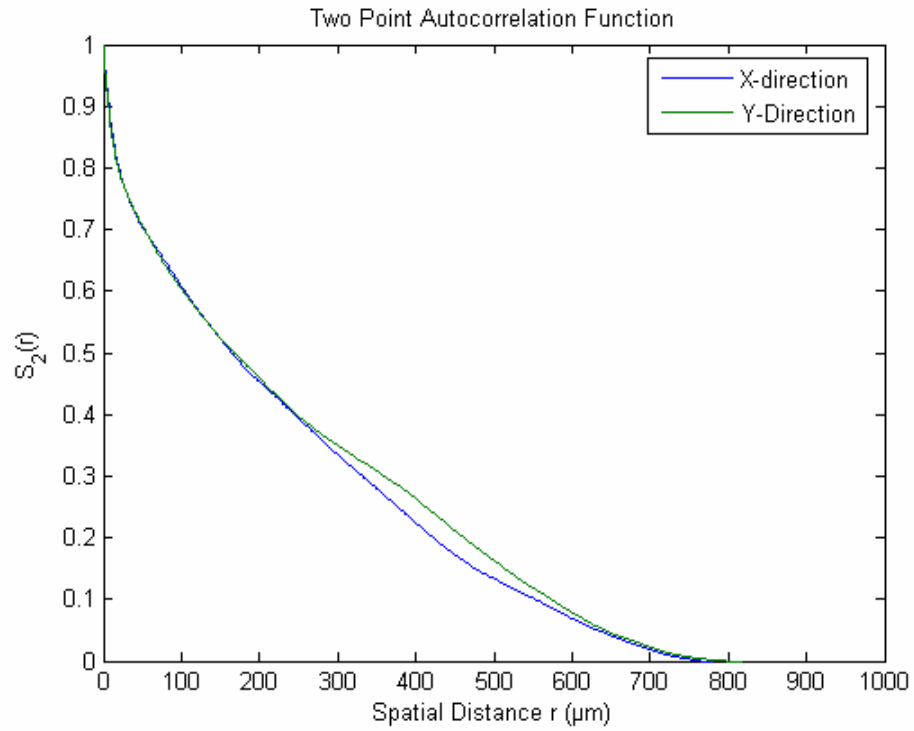


Figure 22. Two Point Autocorrelation Function for 2416 Vertical Thin Section

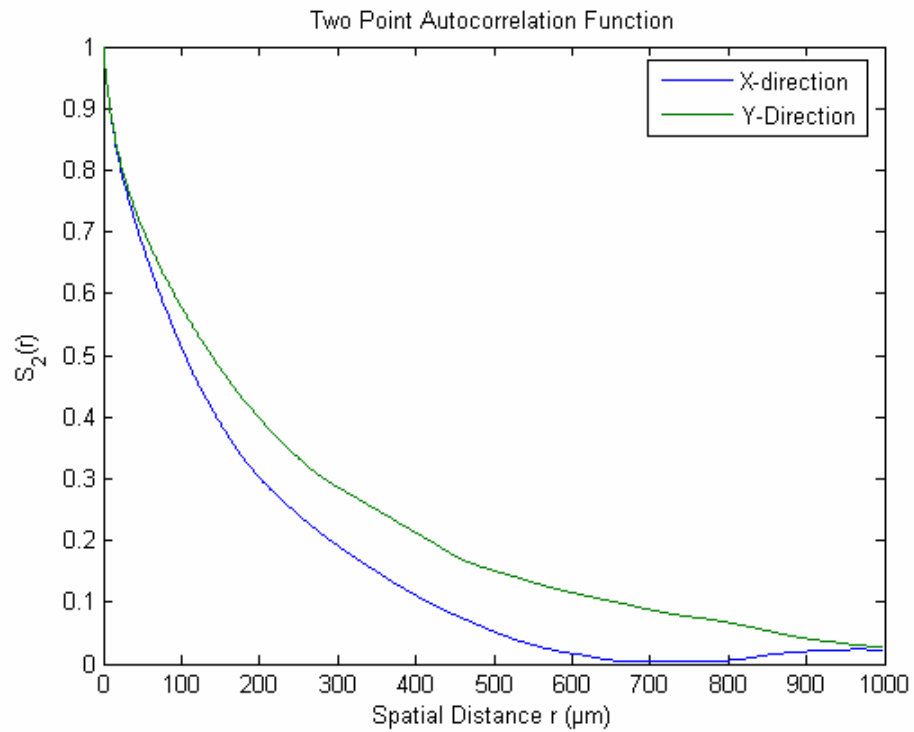


Figure 23. Two Point Autocorrelation Function for 7626A Horizontal Thin Section

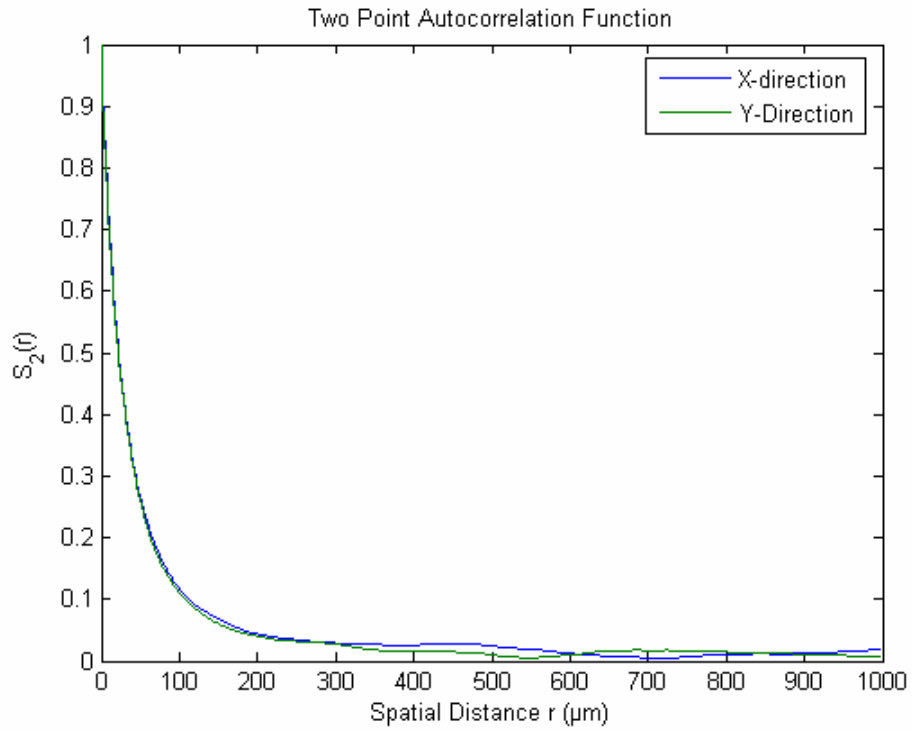


Figure 24. Two Point Autocorrelation Function for 7626A Vertical Thin Section

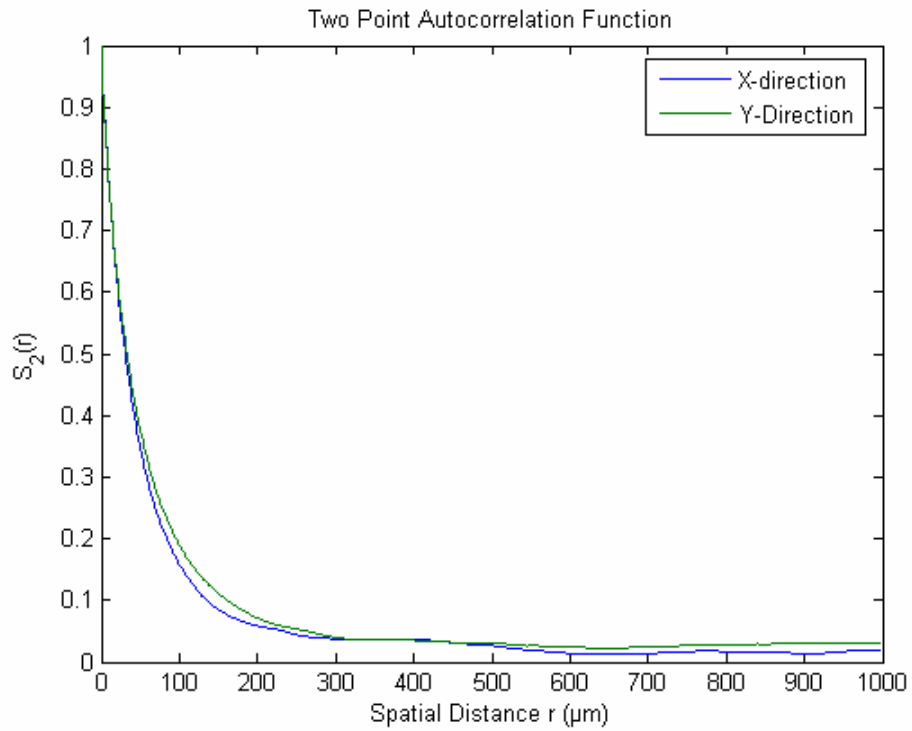


Figure 25. Two Point Autocorrelation Function for 7626B Horizontal Thin Section

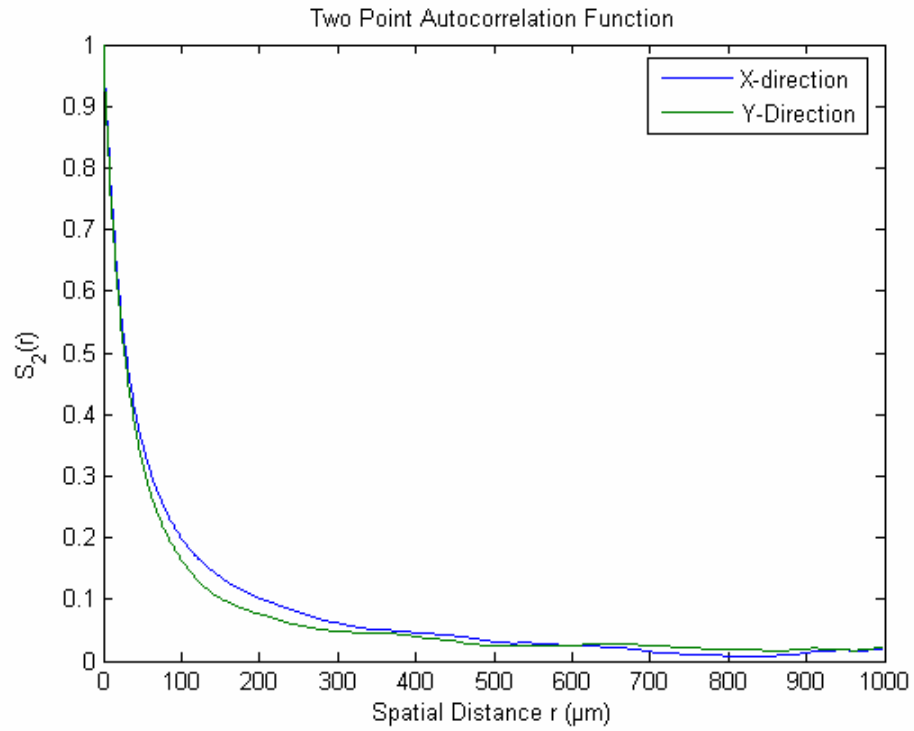
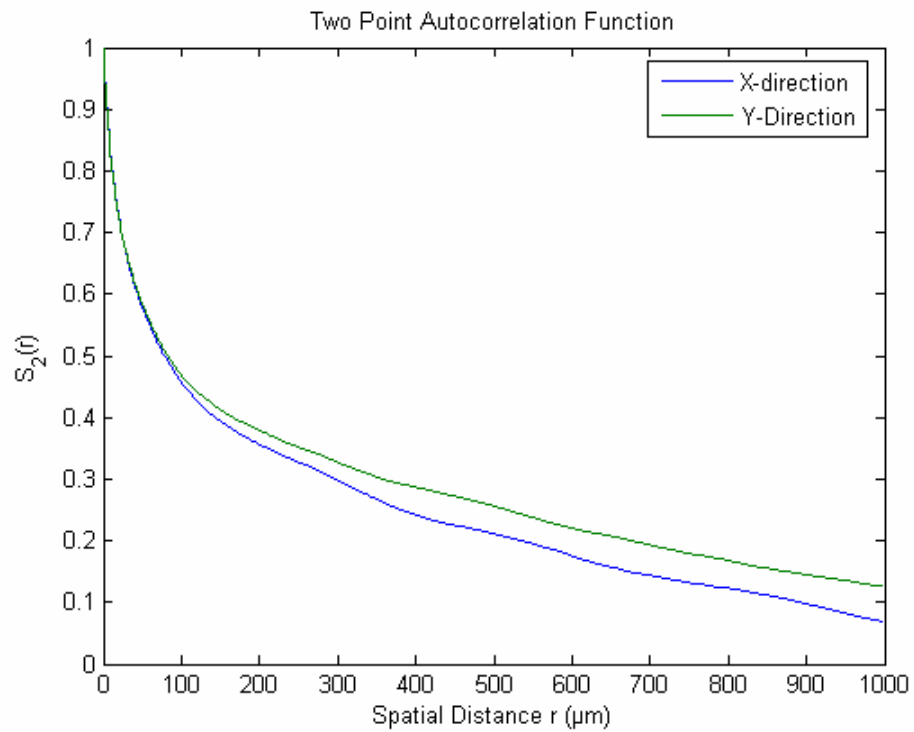


Figure 26. Two Point Autocorrelation Function for 7626B Vertical Thin Section



It is interesting to note that the two-point autocorrelation function does not go to zero at 1 mm distance for vuggy sample which indicates long range spatial correlations. On the other hand packstone samples show a correlation length of about 100 μm .

2.4 Lineal Path Function

The lineal path function for the pore phase $L(L)$ is defined as the probability of finding a line segment of length r entirely in the pore space when randomly thrown into the image. This is equivalent to the probability that a point can move a distance r along a direction without crossing phase boundary between rock and pore. Figure 27-39 show the Lineal path function for the six carbonate samples. The lineal paths are measured in two perpendicular directions named X and Y for the horizontal and vertical section for each sample at a resolution of 1 $\mu\text{m}/\text{pixel}$.

Figure 27. Lineal Path Function for Limestone 1 Horizontal Thin Section

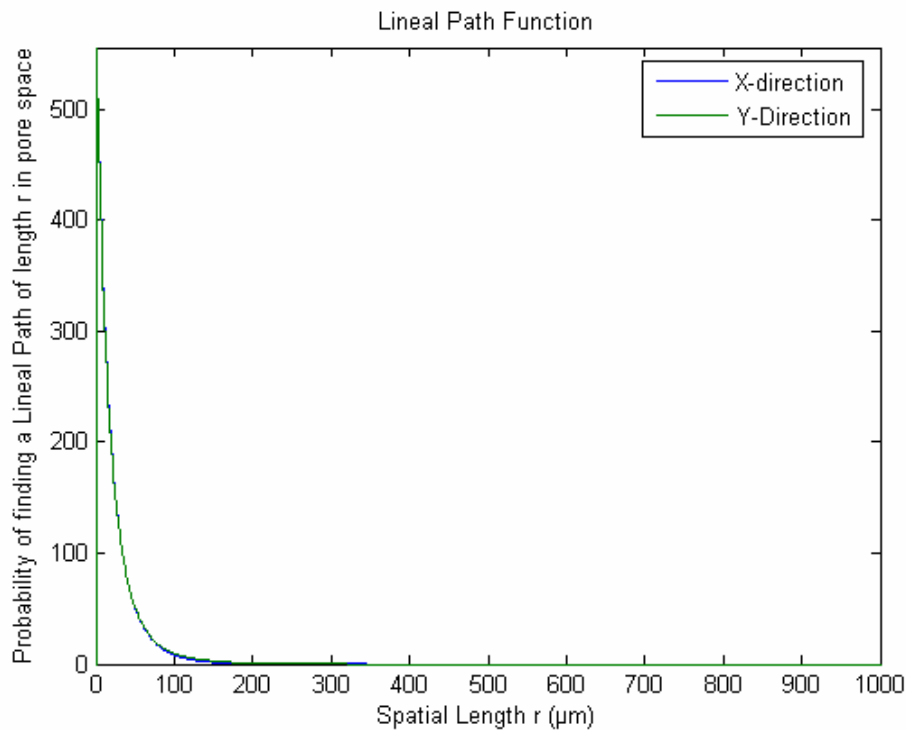


Figure 28. Lineal Path Function for Limestone 1 Vertical Thin Section

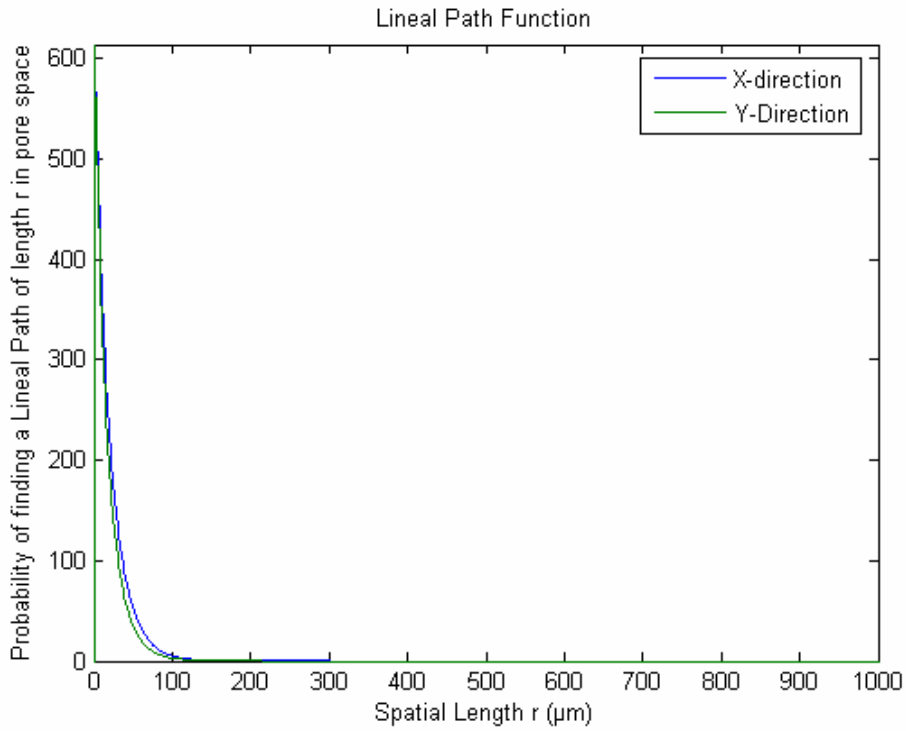


Figure 29. Lineal Path Function for Limestone 2 Horizontal Thin Section

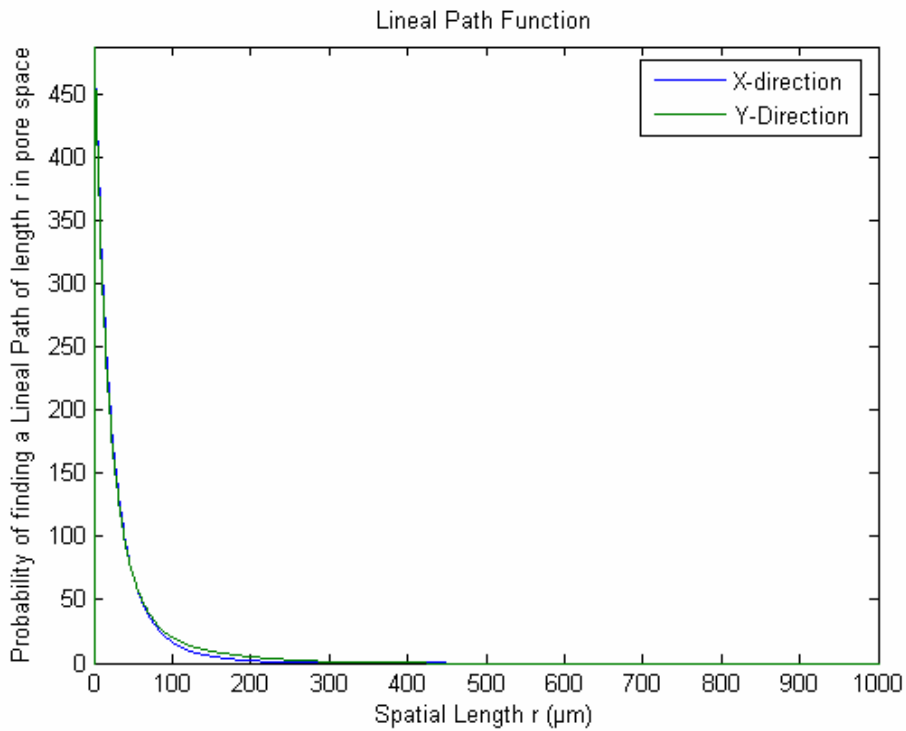


Figure 30. Lineal Path Function for Limestone 2 Vertical Thin Section

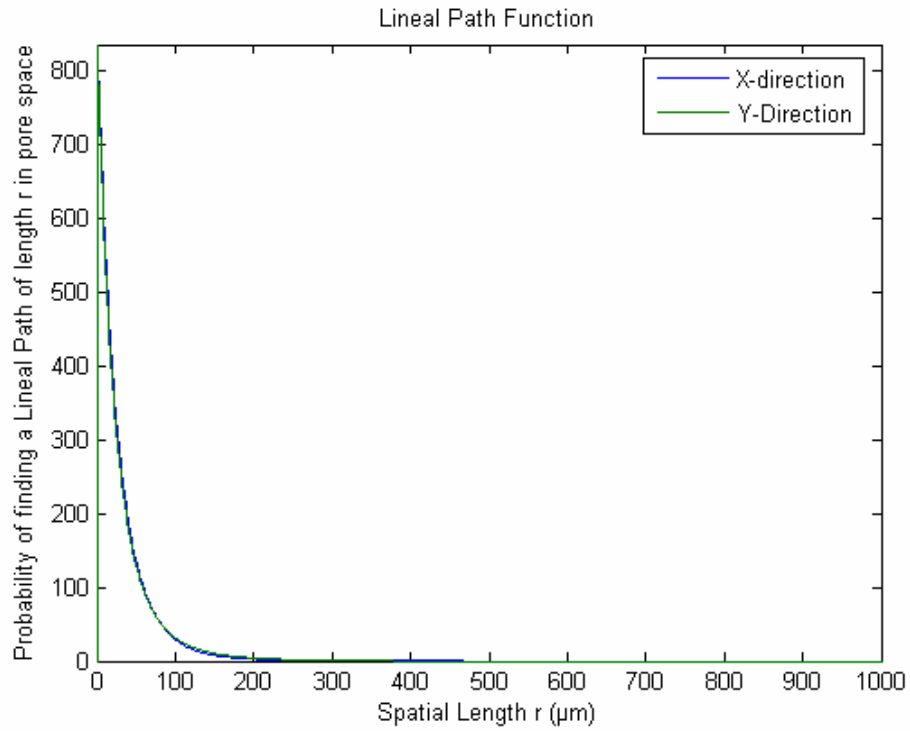


Figure 31. Lineal Path Function for 7536B Horizontal Thin Section

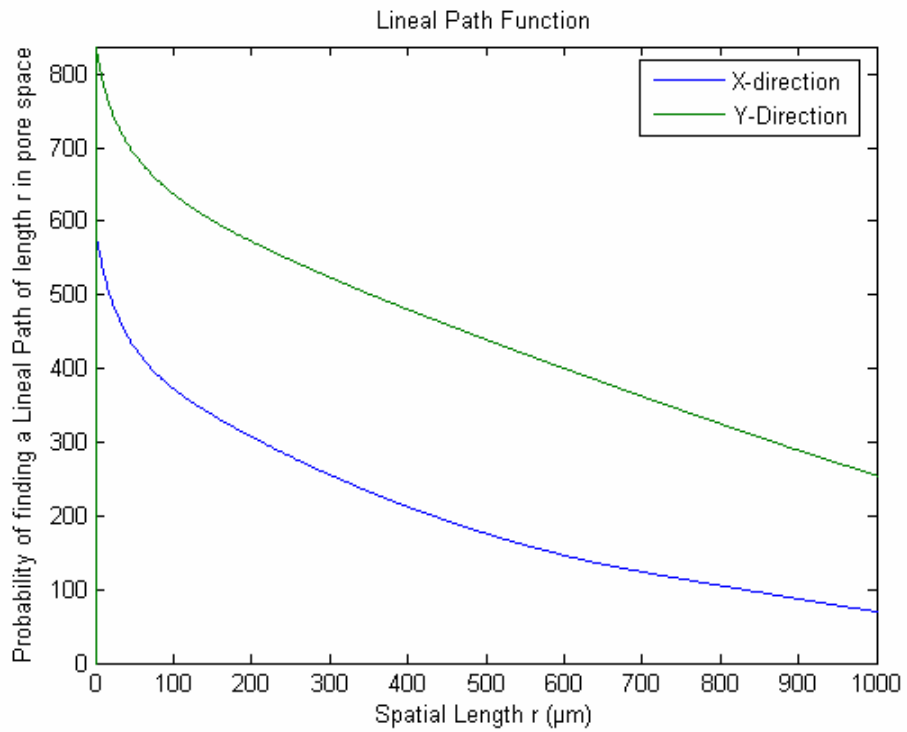


Figure 32. Lineal Path Function for 7536B Vertical Thin Section

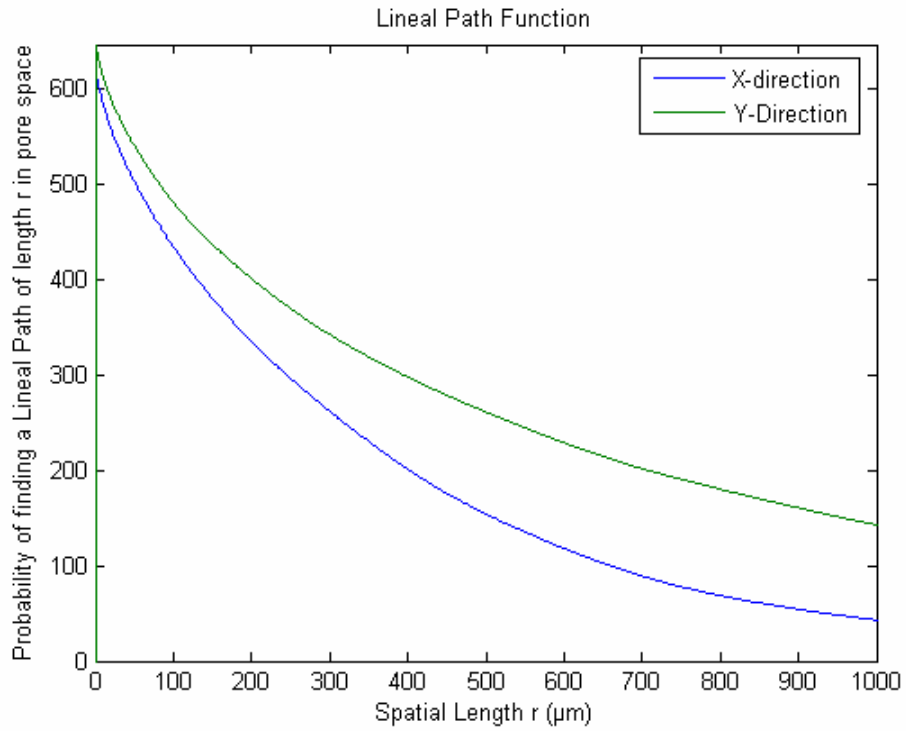


Figure 33. Lineal Path Function for 2416 Horizontal Thin Section

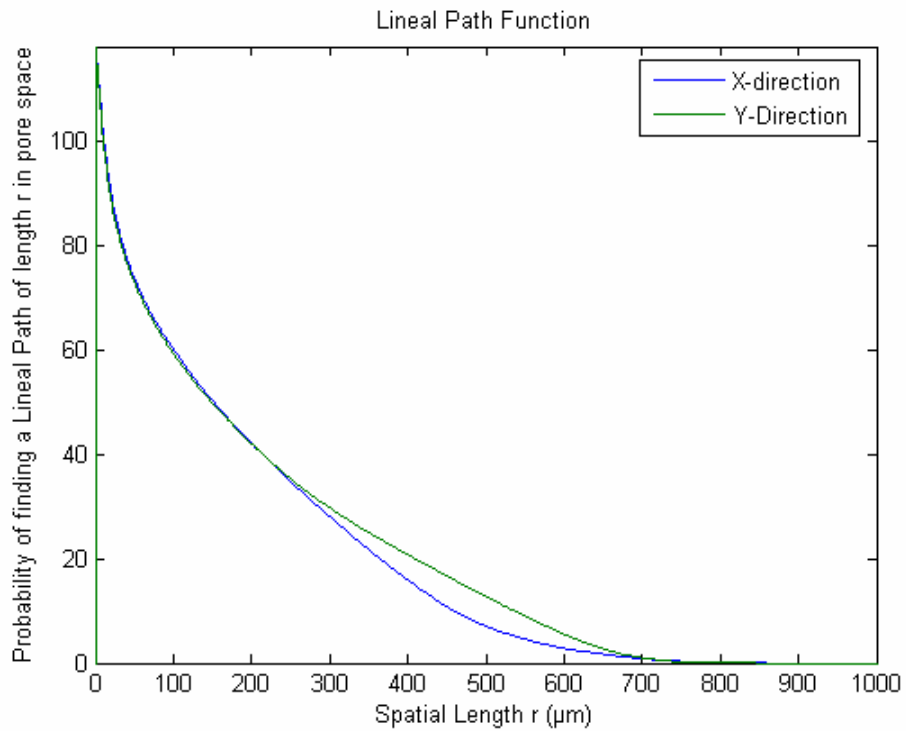


Figure 34. Lineal Path Function for 2416 Vertical Thin Section

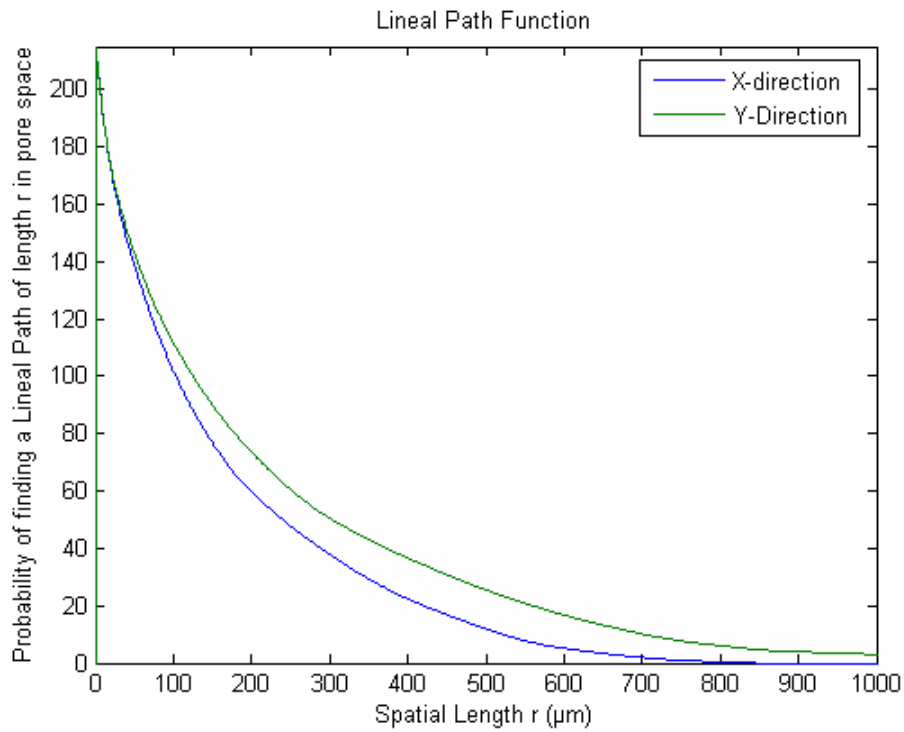


Figure 35. Lineal Path Function for 7626A Horizontal Thin Section

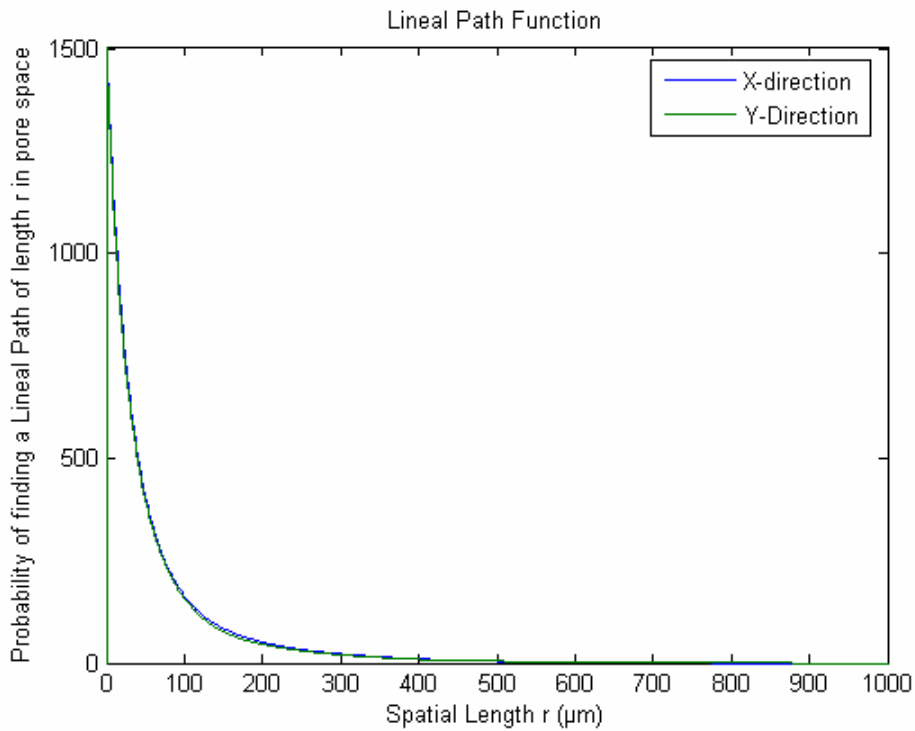


Figure 36. Lineal Path Function for 7626A Vertical Thin Section

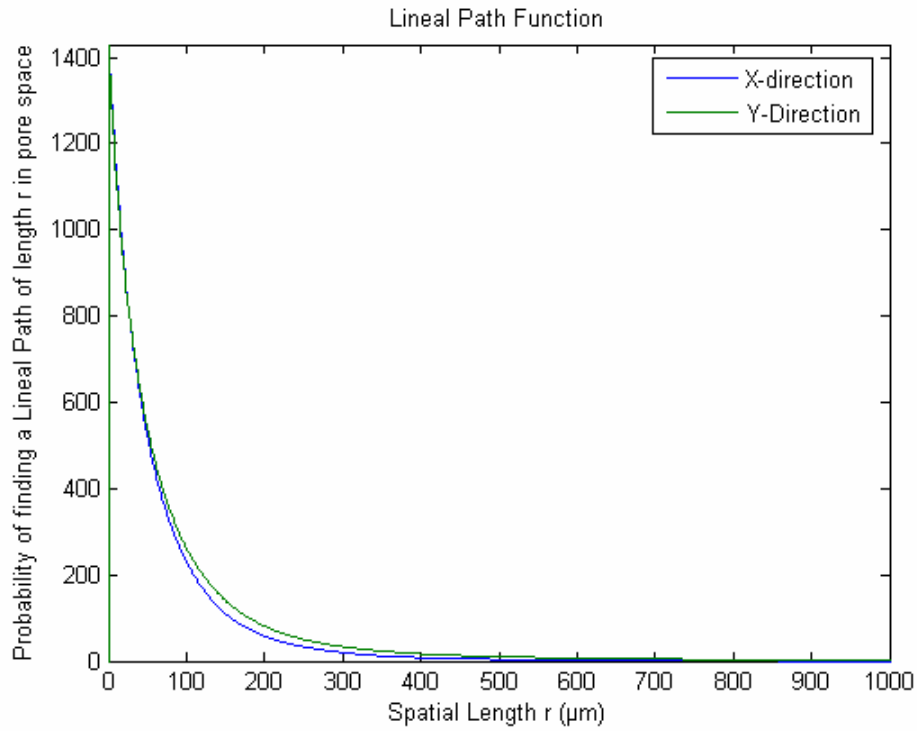


Figure 37. Lineal Path Function for 7626B Horizontal Thin Section

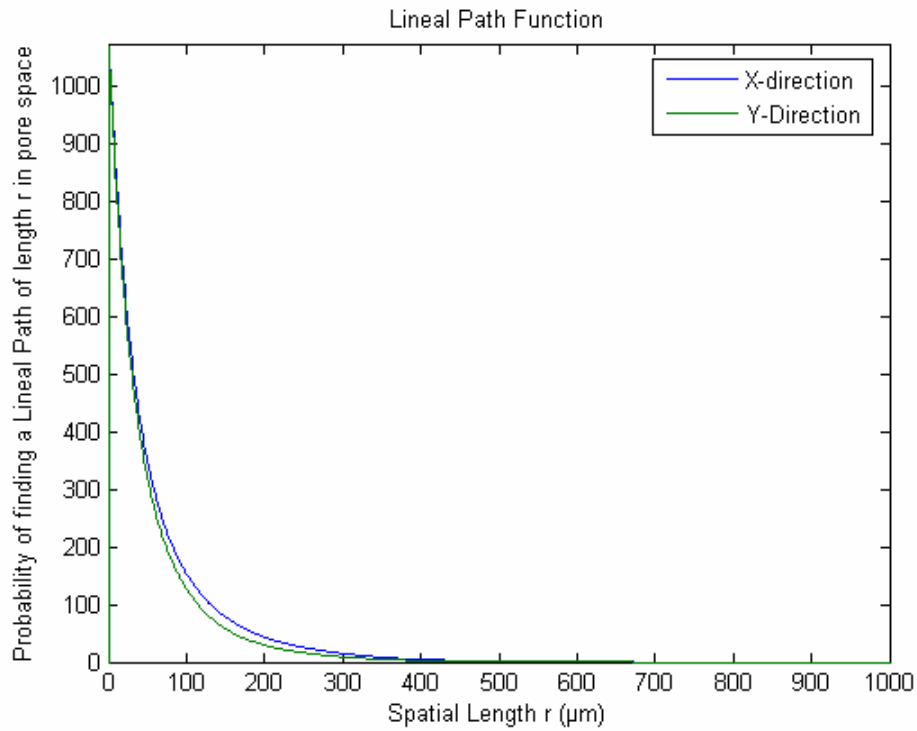
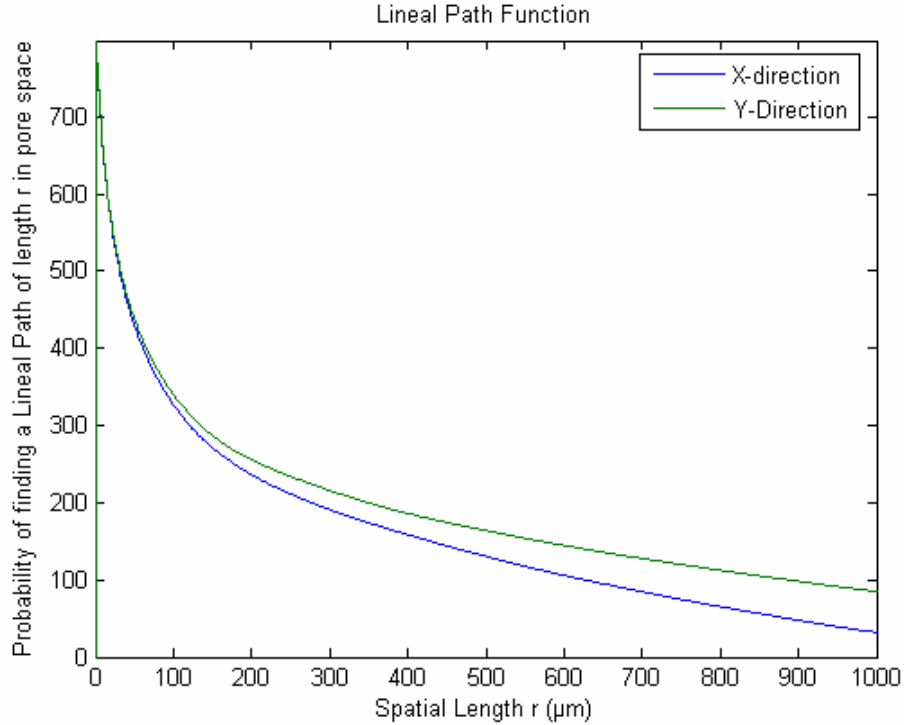


Figure 38. Lineal Path Function for 7626B Vertical Thin Section



2.5 Chord Length Distribution Function

Chord length probability distribution function for pore space, $p(r)$, is defined such that $p(r)dr$ is the probability of finding a chord of length between r and $r + dr$ in pore space. The mean chord length is the first moment of this probability distribution function given by

$$l_c = \int_0^{\infty} rp(r)dr$$

In general, for statistically isotropic systems

$$p(r) = \frac{l_c}{\phi} \frac{d^2L(r)}{dr^2}$$

Figure 39-50 show the chord length distribution function for all the carbonate samples for the horizontal and vertical sections at a resolution of $1 \mu\text{m}/\text{pixel}$. These are measured in two perpendicular directions named X and Y.

Figure 39. Chord Number Distribution for Limestone 1 Horizontal Thin Section

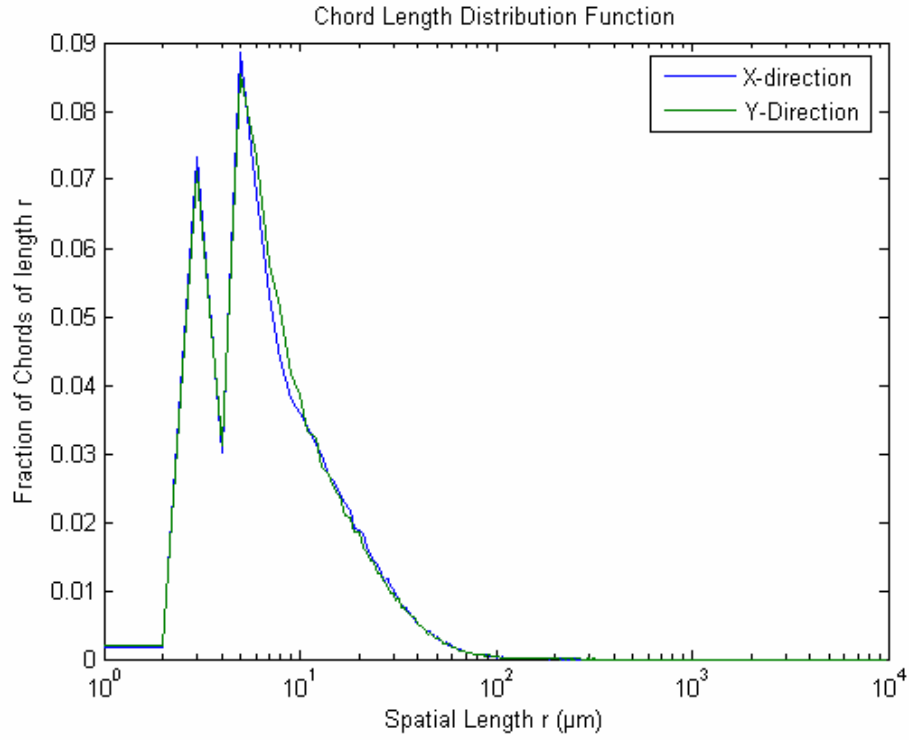


Figure 40. Chord Number Distribution for Limestone 1 Vertical Thin Section

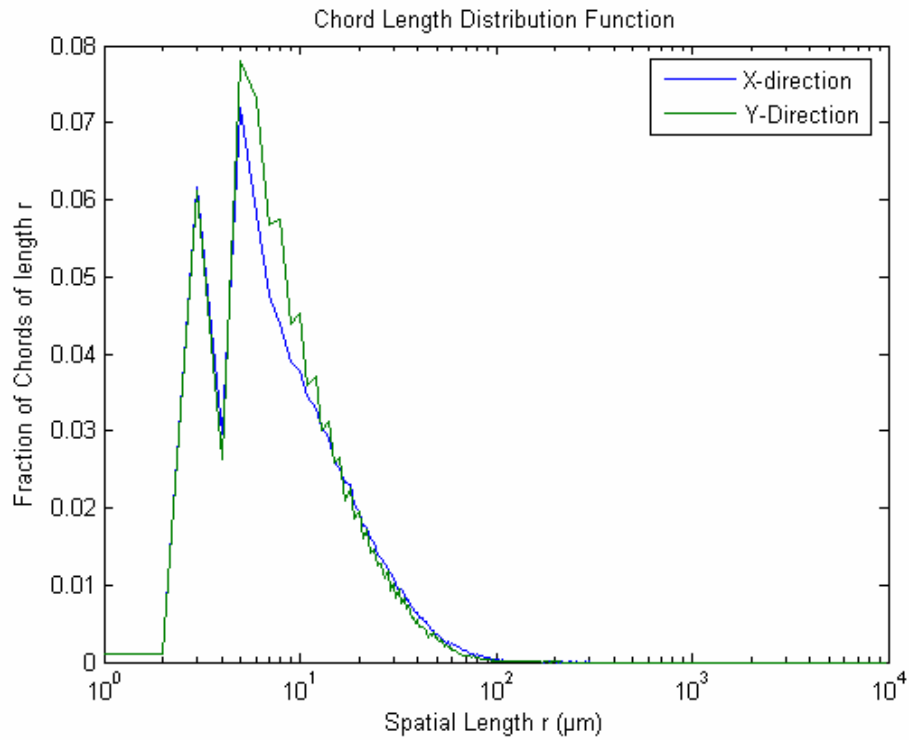


Figure 41. Chord Number Distribution for Limestone 2 Horizontal Thin Section

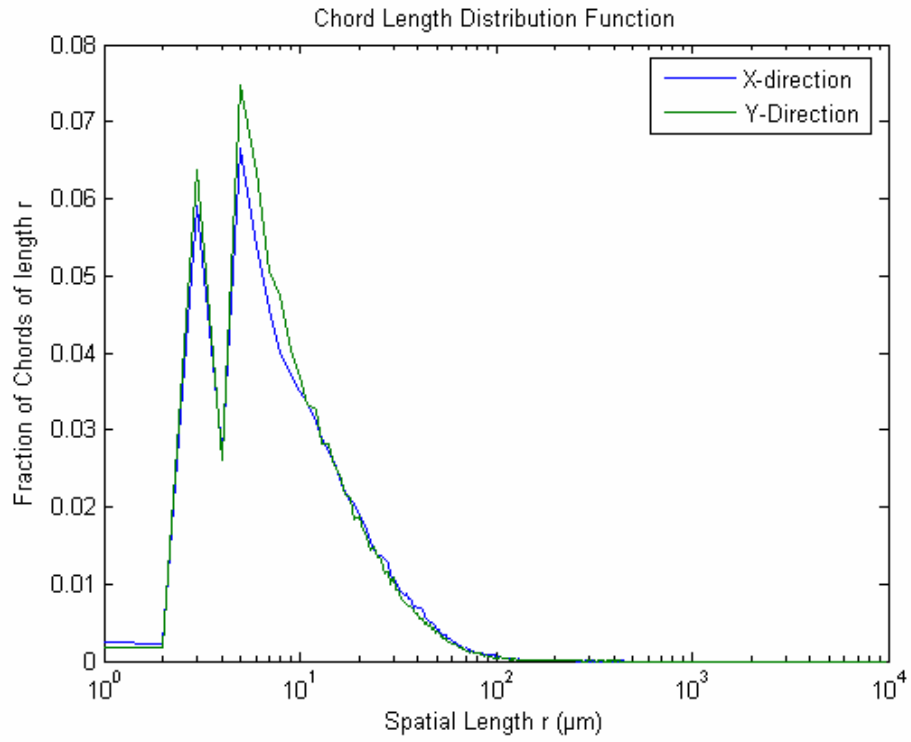


Figure 42 Chord Number Distribution for Limestone 2 Vertical Thin Section

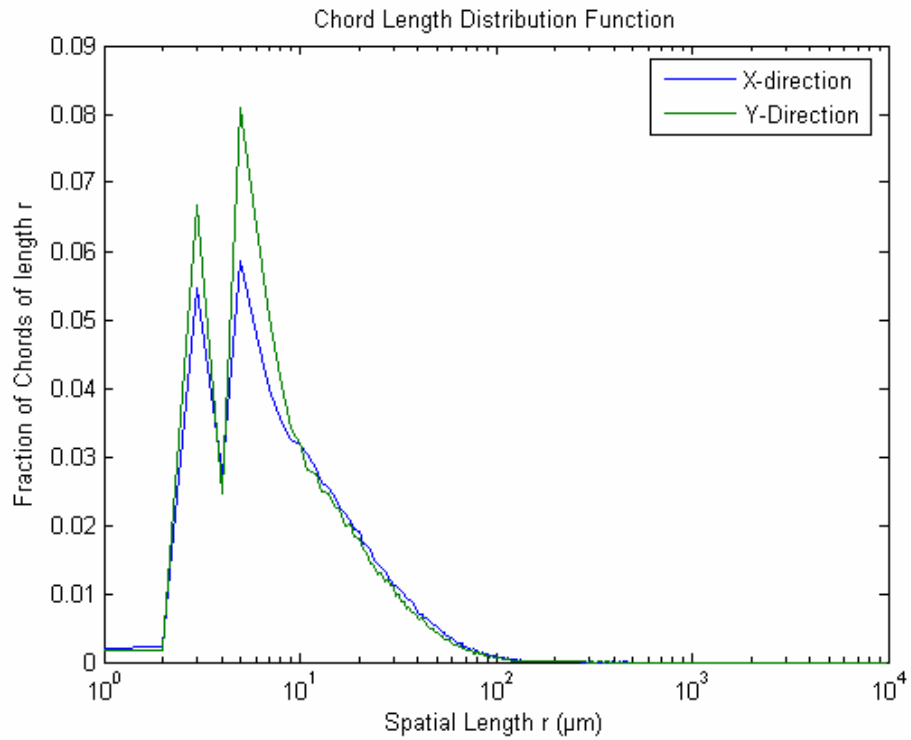


Figure 43 Chord Number Distribution for 7536 B Horizontal Thin Section

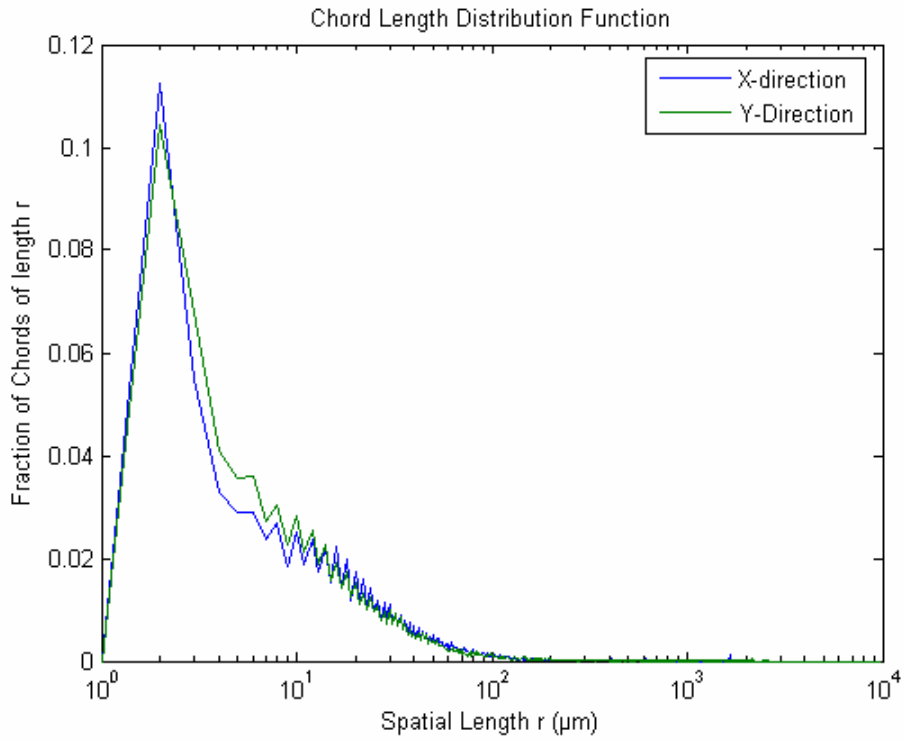


Figure 44 Chord Number Distribution for 7536 B Vertical Thin Section

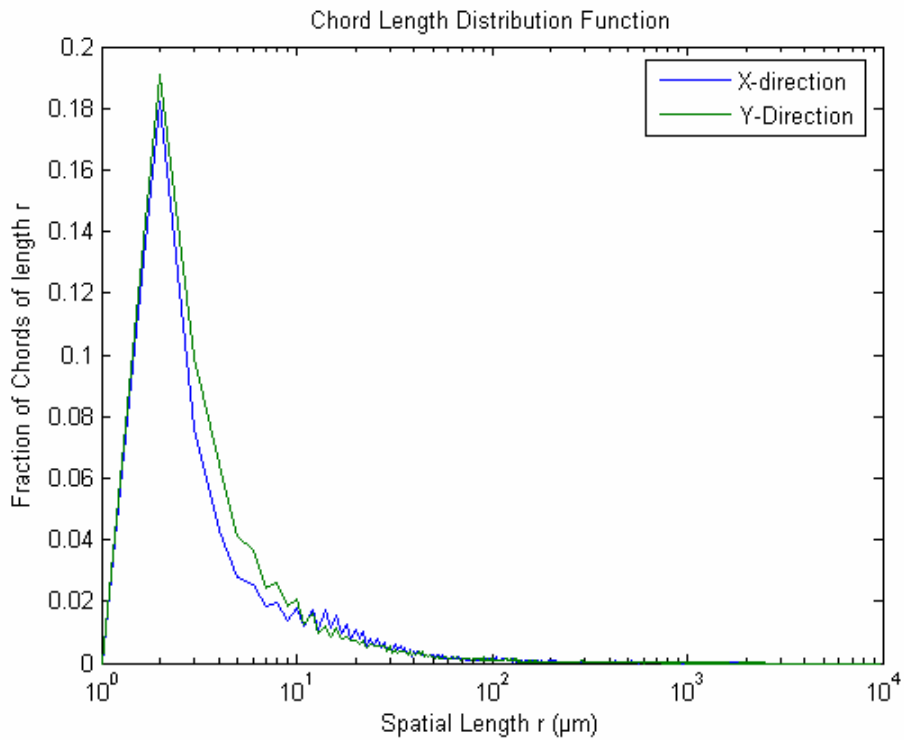


Figure 45 Chord Number Distribution for 2416 Horizontal Thin Section

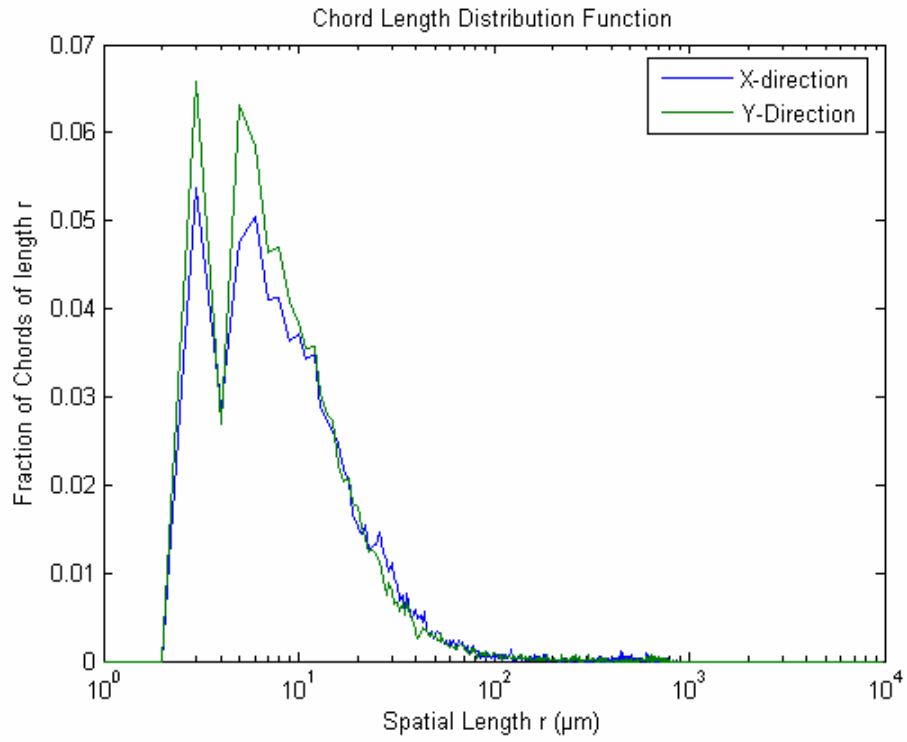


Figure 46 Chord Number Distribution for 2416 Vertical Thin Section

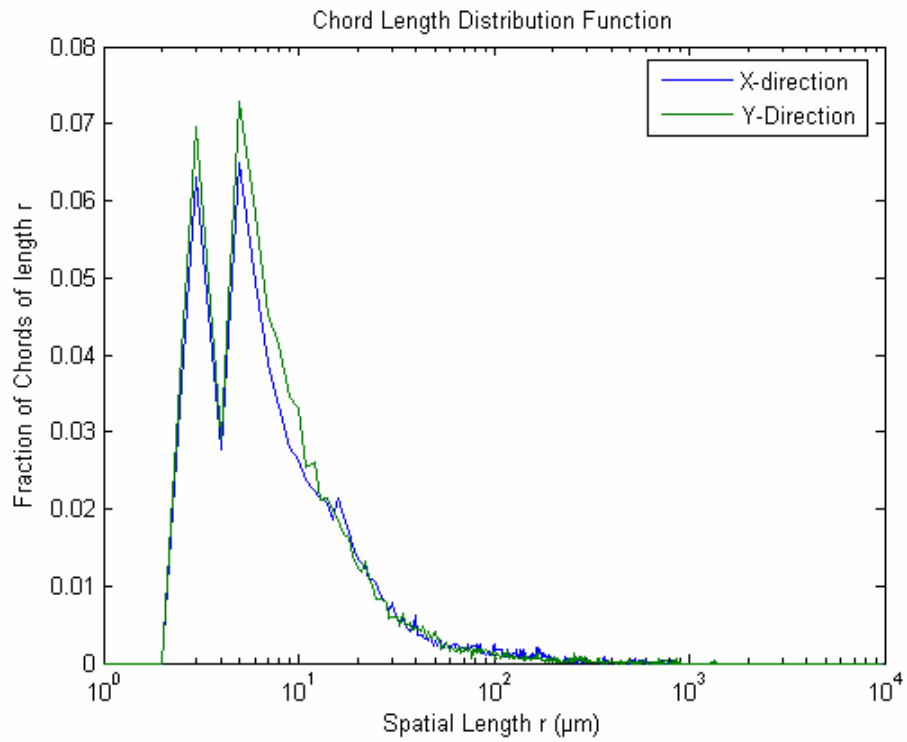


Figure 47 Chord Number Distribution for 7626A Horizontal Thin Section

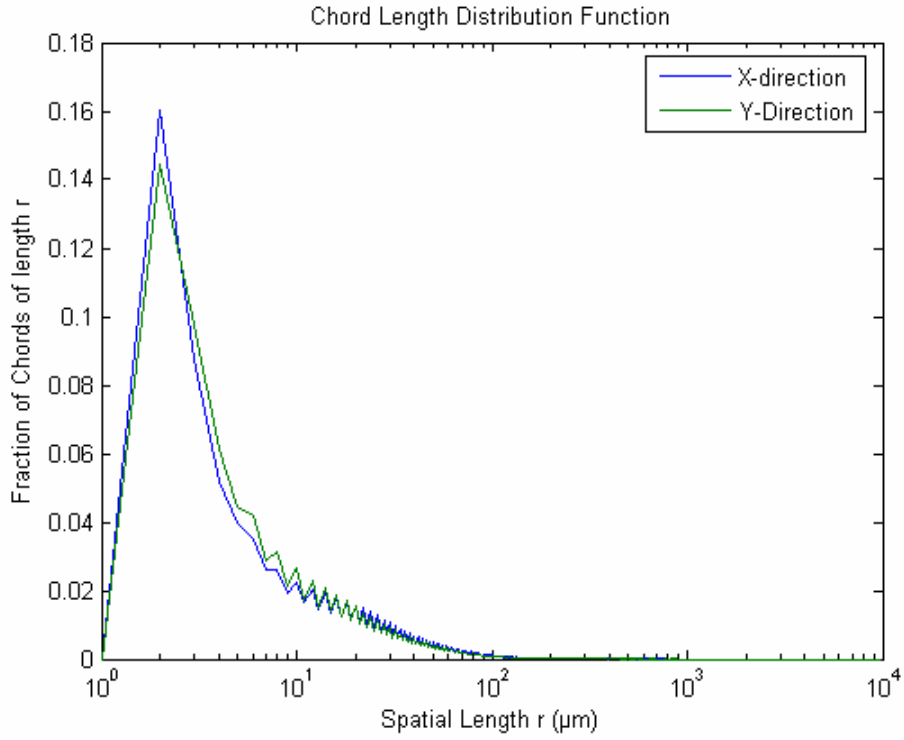


Figure 48 Chord Number Distribution for 7626A Vertical Thin Section

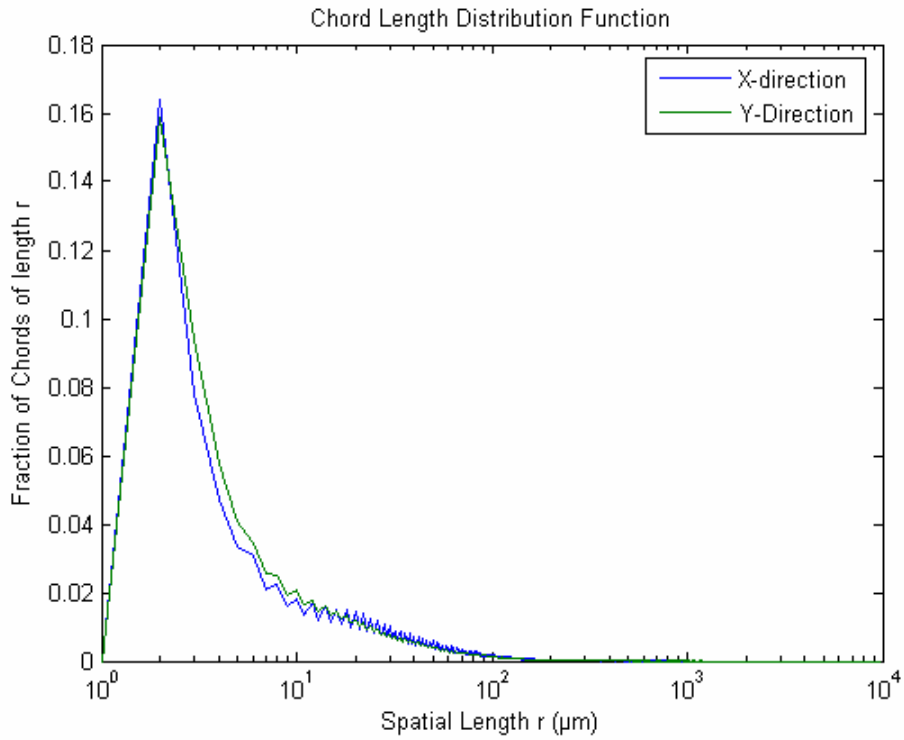


Figure 49 Chord Number Distribution for 7626B Horizontal Thin Section

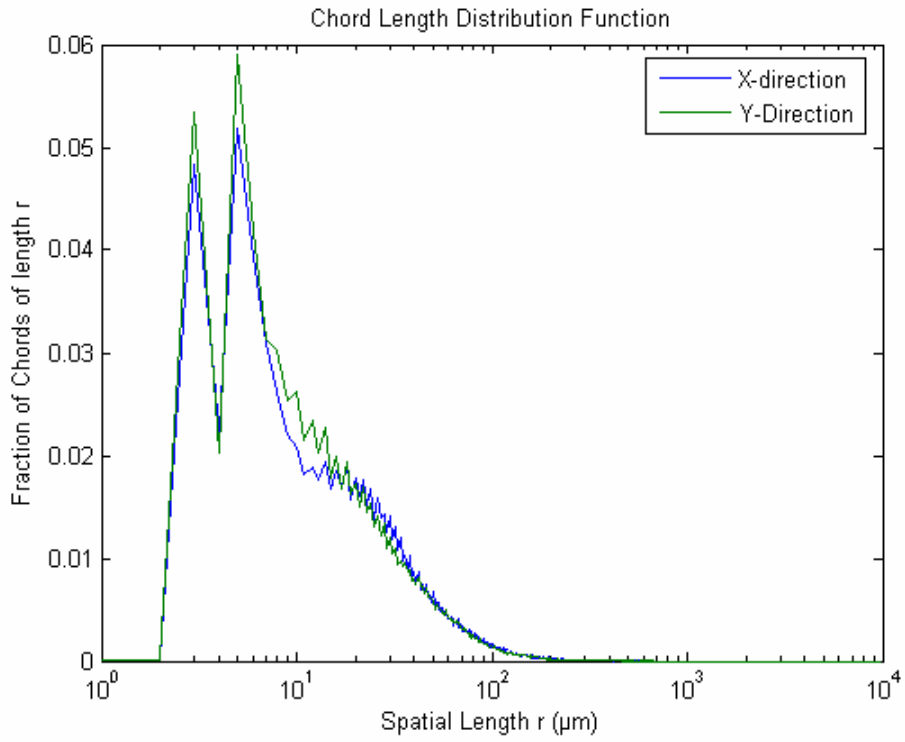
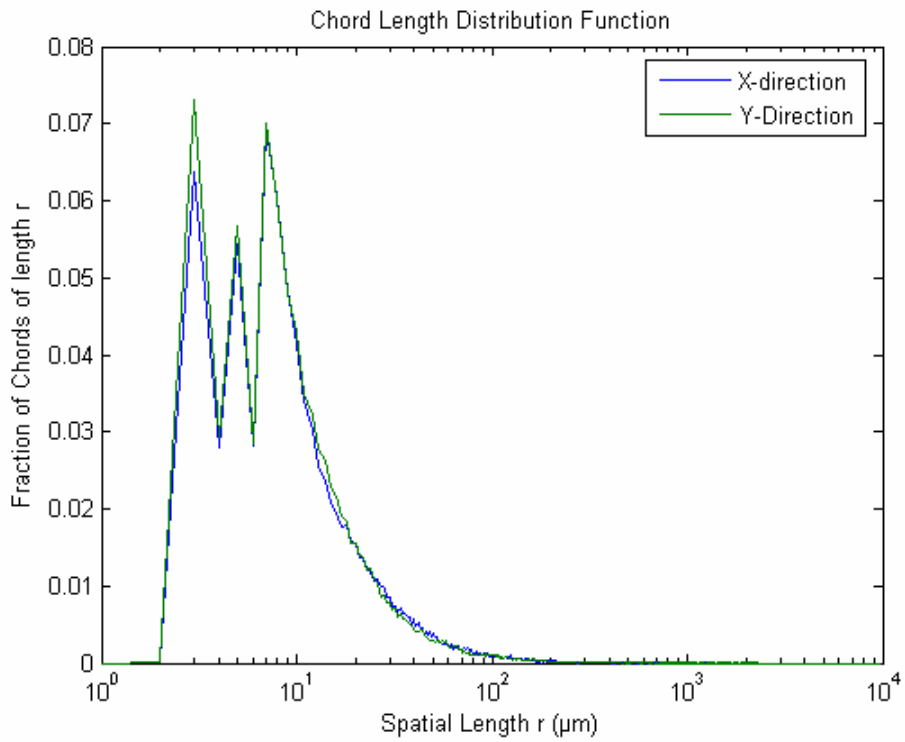


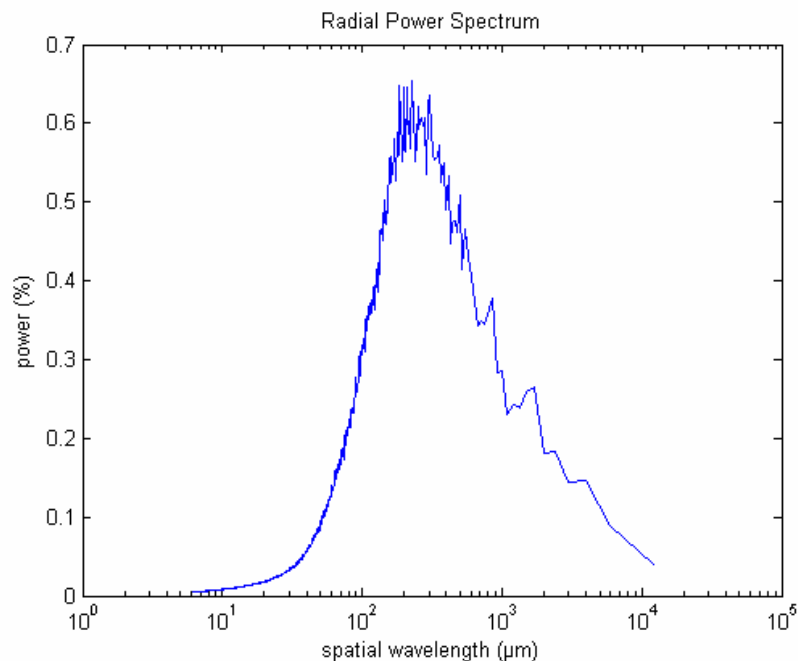
Figure 50 Chord Number Distribution for 7626B Vertical Thin Section



2.6 Fourier Transform

In the mechanism of grain deposition and subsequent diagenesis, the grains compact well to form clusters with the flaws between clusters providing the channels for flow. These channels can be differentiated from an inter-granular pore in a 2-D image using radial power spectrum derived from Fourier transform which gives a characteristic peak associated with grain size and another associated with the grain clusters at about 1.2 times the grain peak. A filter based on the power spectrum can then be used to distinguish between the two types of porosities. Figure 51 shows the radial power spectrum of a sample of Berea sandstone.

Figure 51 Radial Power Spectrum for Berea Sandstone



Since a carbonate undergoes drastic changes during diagenesis, the original grain deposition pattern is altered. In general for the carbonate samples studied, the peak is not as sharp as in the case of sandstones indicating absence of a dominant grain size. Figures 52-63 show the radial power spectrum for the six sandstone samples for the horizontal and vertical sections.

Figure 52. Radial Power Spectrum for Limestone 1 Horizontal Section

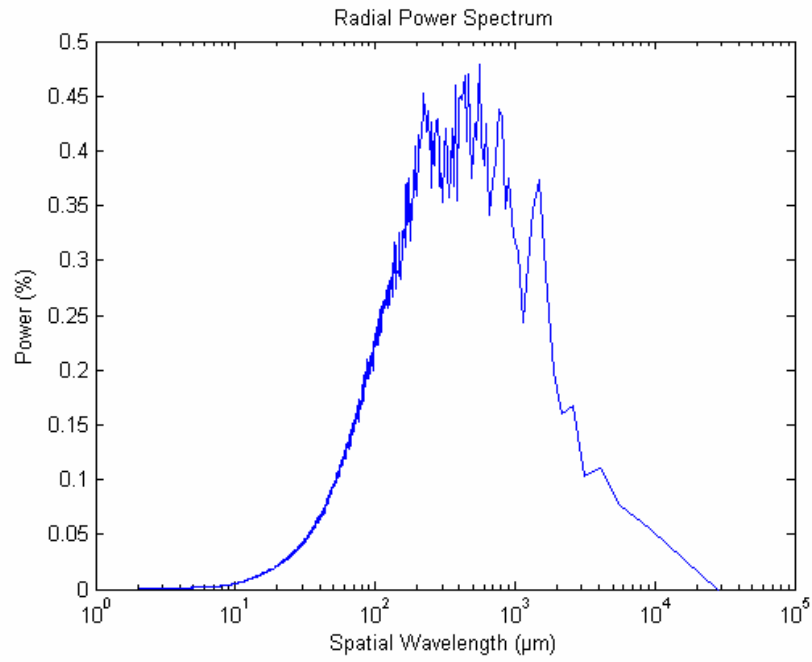


Figure 53. Radial Power Spectrum for Limestone 1 Vertical Section

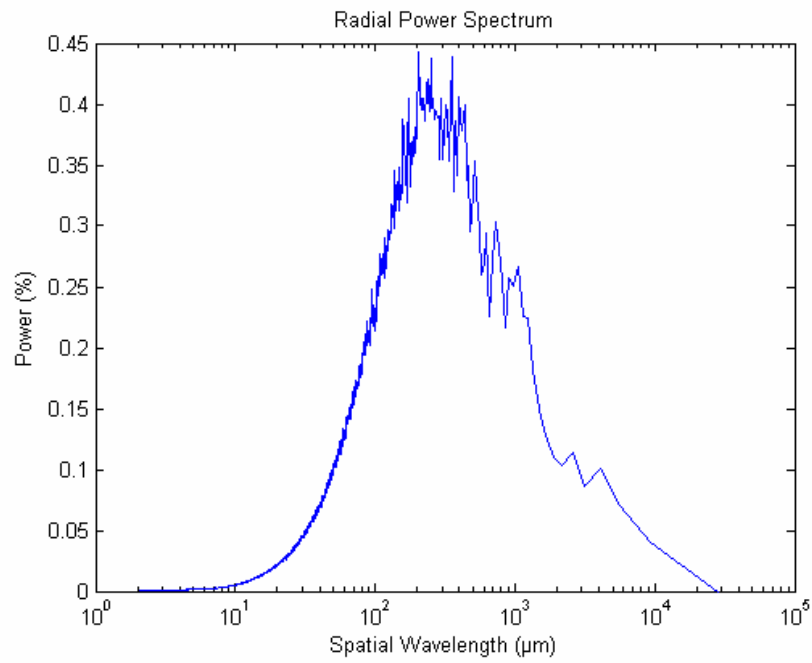


Figure 54. Radial Power Spectrum for Limestone 2 Horizontal Section

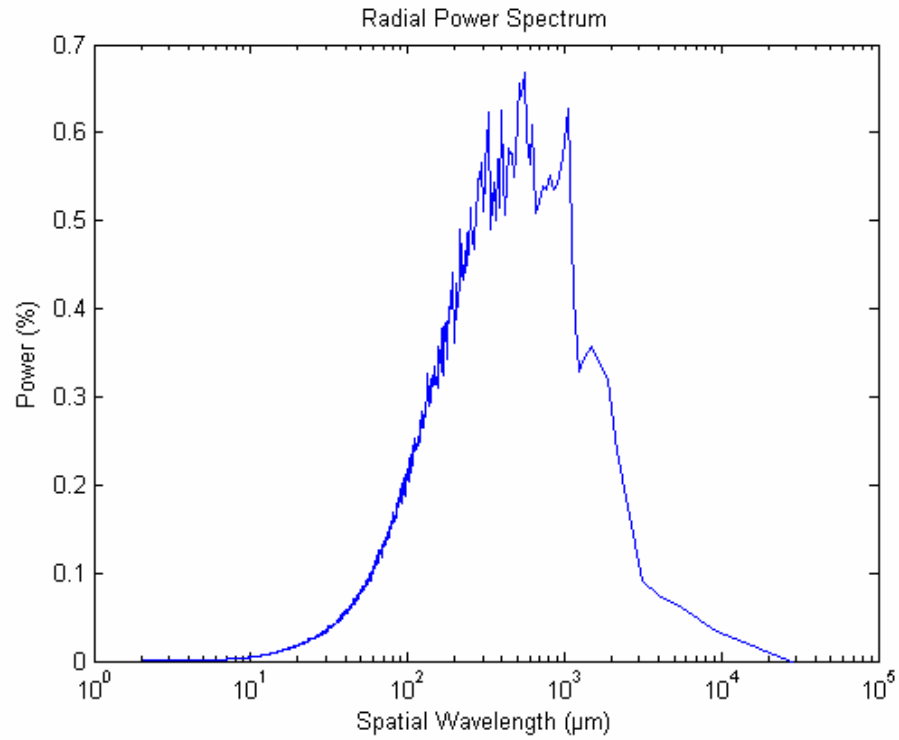


Figure 55. Radial Power Spectrum for Limestone 2 Vertical Section

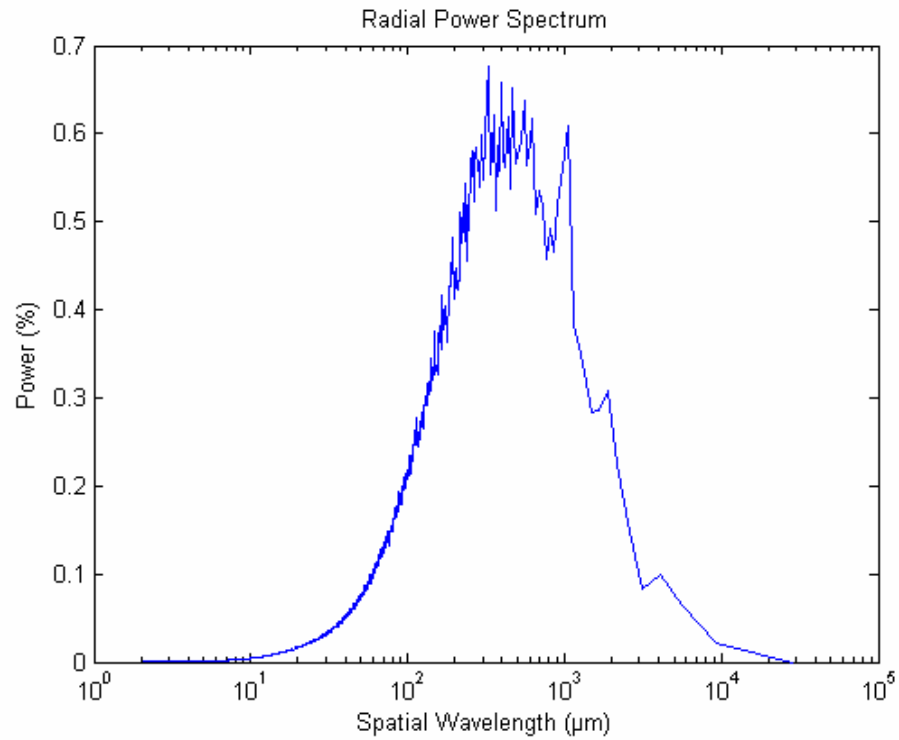


Figure 56. Radial Power Spectrum for 7536 B Horizontal Thin Section

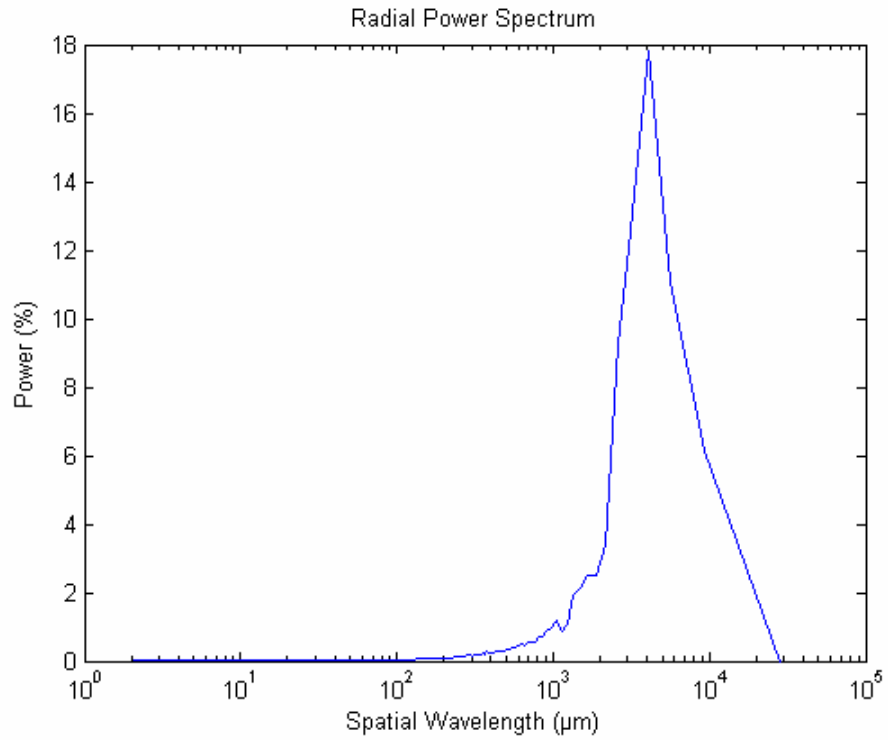


Figure 57. Radial Power Spectrum for 7536 B Vertical Thin Section

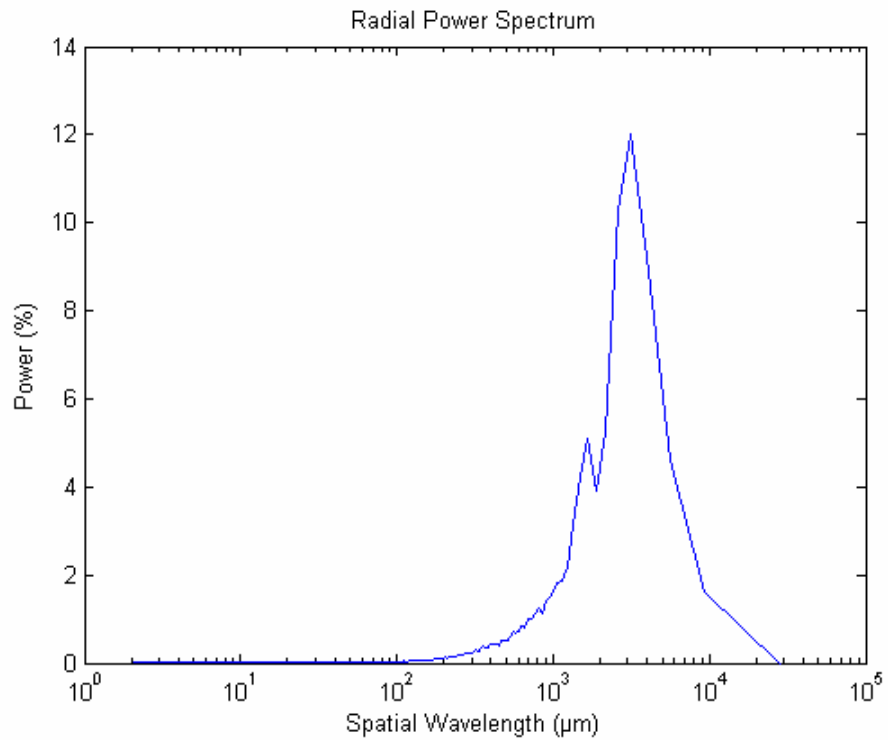


Figure 58. Radial Power Spectrum for 2416 Horizontal Thin Section

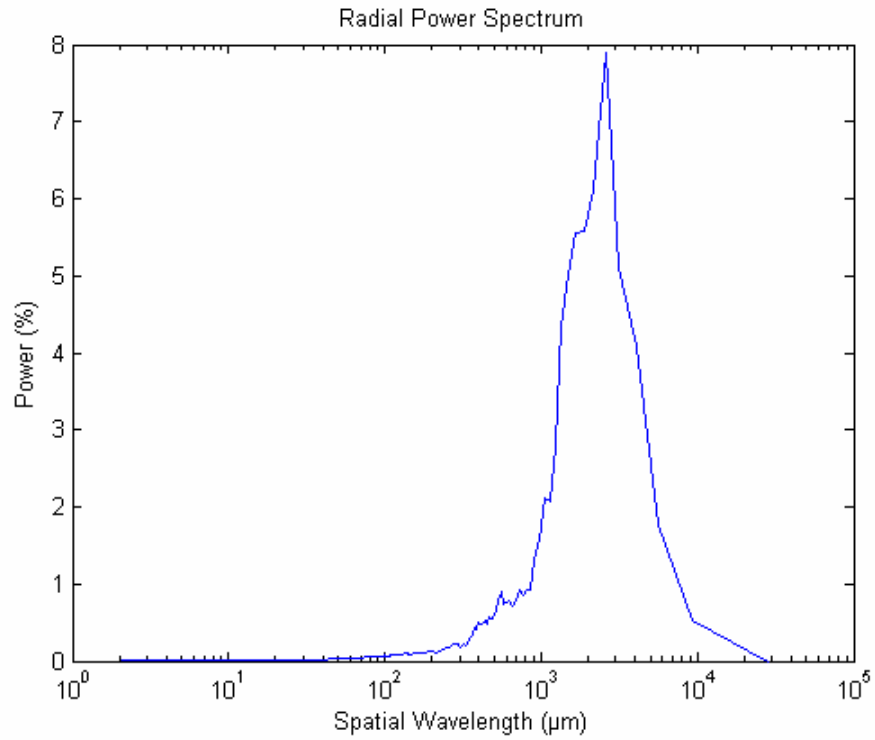


Figure 59. Radial Power Spectrum for 2416 Vertical Thin Section

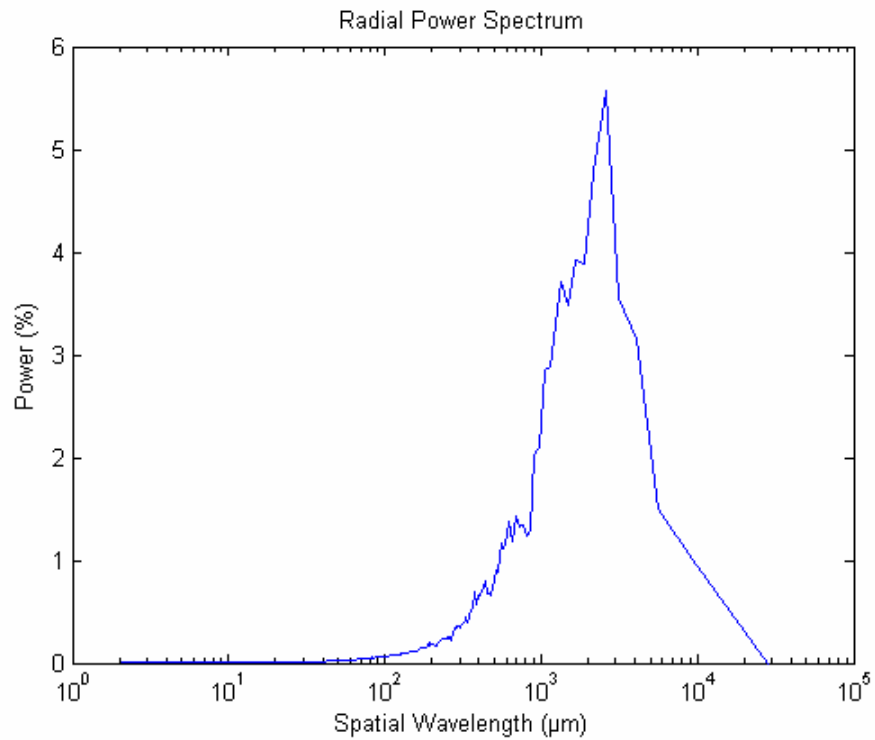


Figure 60. Radial Power Spectrum for 7626A Horizontal Thin Section

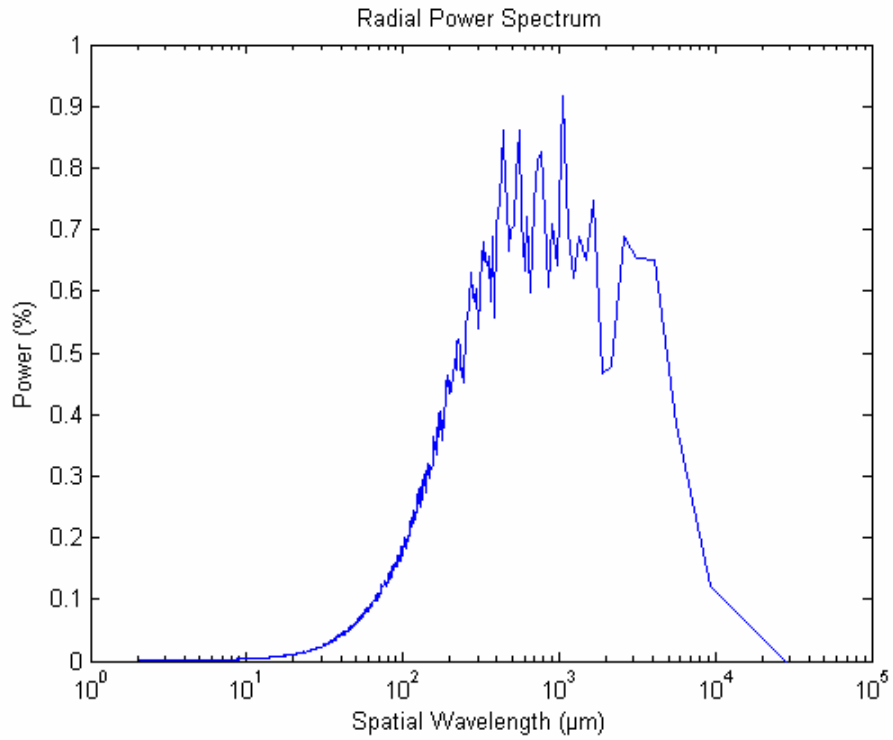


Figure 61. Radial Power Spectrum for 7626A Vertical Thin Section

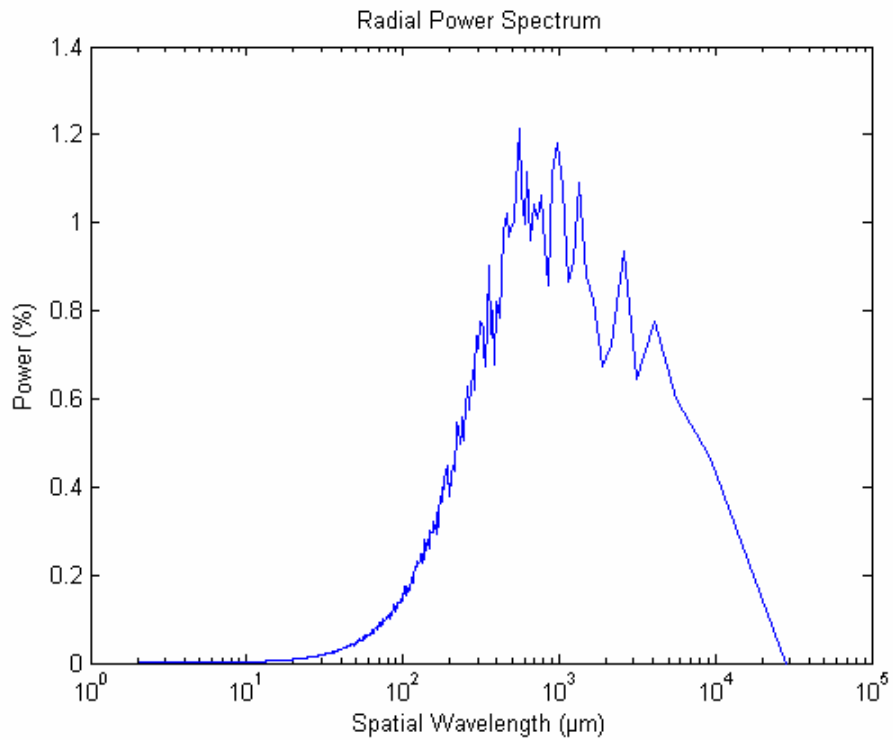


Figure 62. Radial Power Spectrum for 7626B Horizontal Section

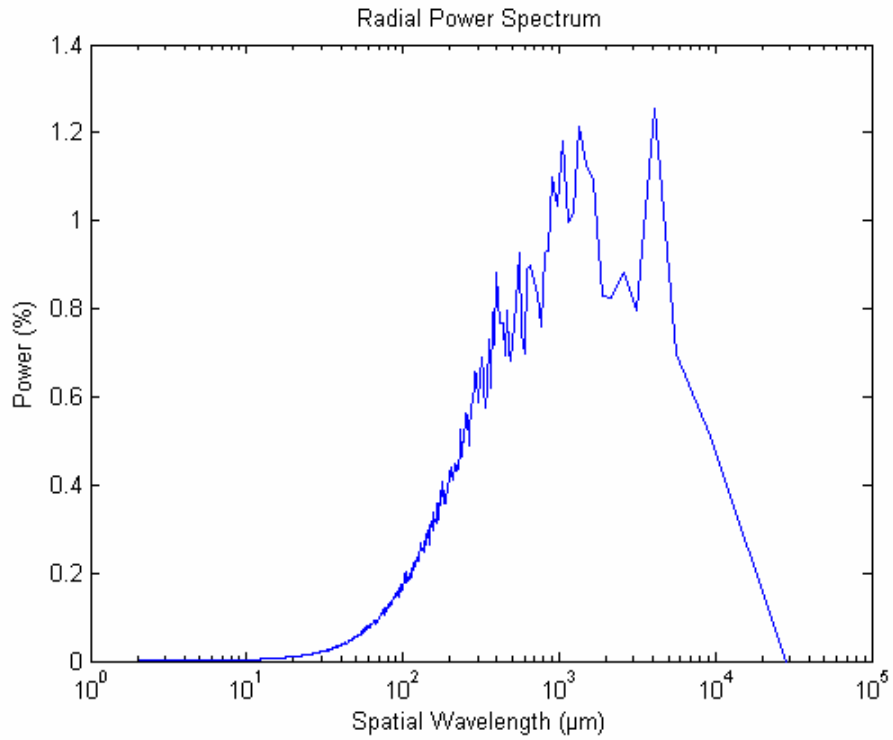
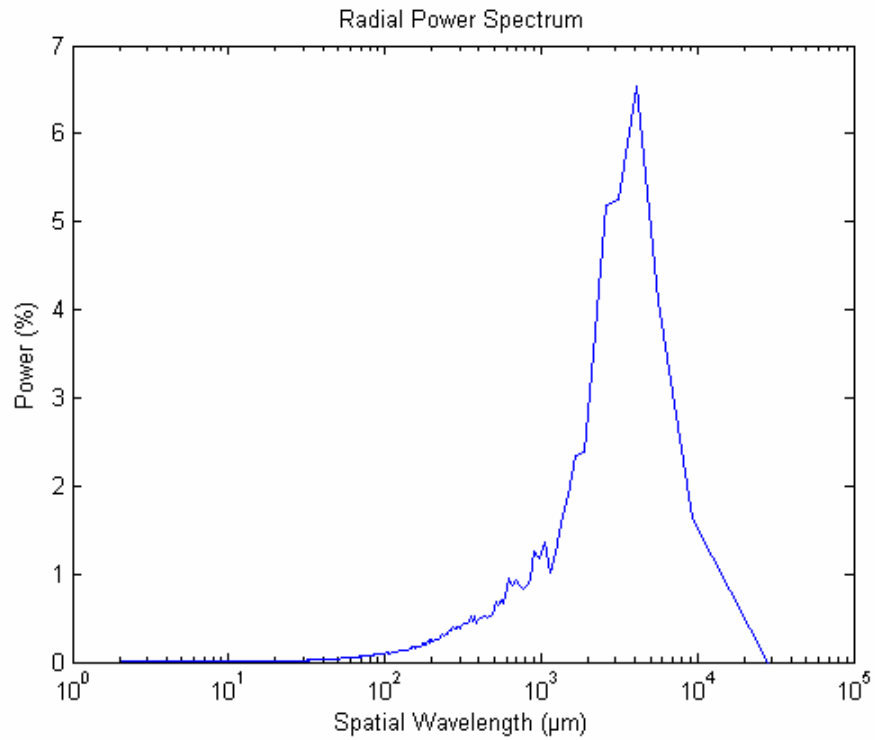


Figure 63. Radial Power Spectrum for 7626B Vertical Section



2.7 Fractal Dimension

The fractal dimension of each set of images is calculated using the box counting method. Three different types of features in an image are studied – the fraction of image occupied rock, the fraction of image occupied by pore and the fraction of image having the interface between rock and pore. The fractal dimensions are calculated by counting the number of boxes containing the respective feature F and plotting the box count vs box size. The fractal dimension is given by

$$D = - \frac{\log(N_B(F))}{\log(L_B)}$$

where D is the fractal dimension for feature F , N_b is the number of boxes of size L_b which contain the feature F . In the following figures D_m is the fractal dimension of the matrix, D_p is the fractal dimension of the pore space and D_s is the fractal dimension of the interface between pore and rock. Figures 64 – 99 show the fractal dimension calculation and values for matrix, pore and surface dimensions for the horizontal and vertical section of 6 carbonate samples at a resolution of $1 \mu\text{m}/\text{pixel}$.

Figure 64 Matrix Fractal Dimension for Limestone 1 Horizontal Section

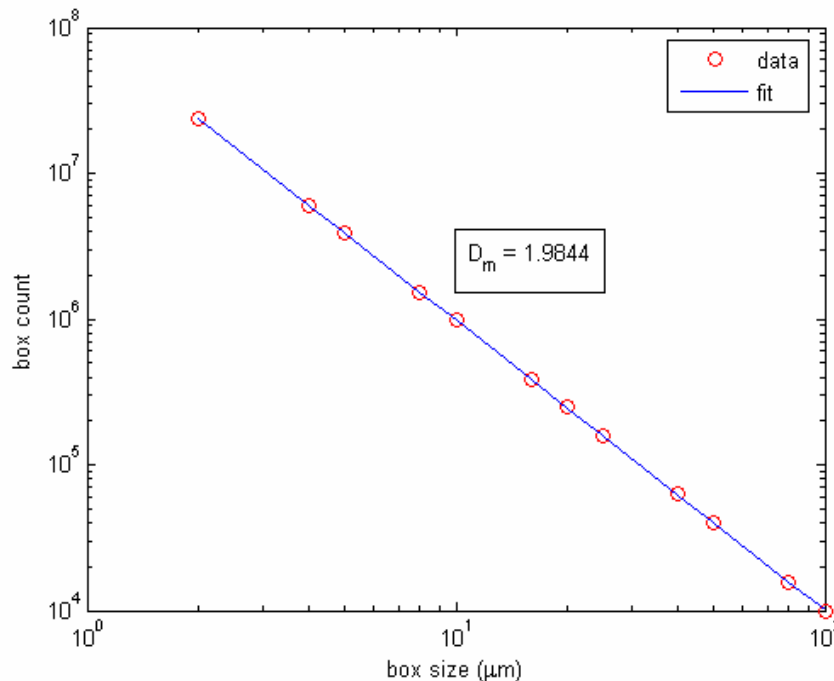


Figure 65 Pore Space Fractal Dimension for Limestone 1 Horizontal Section

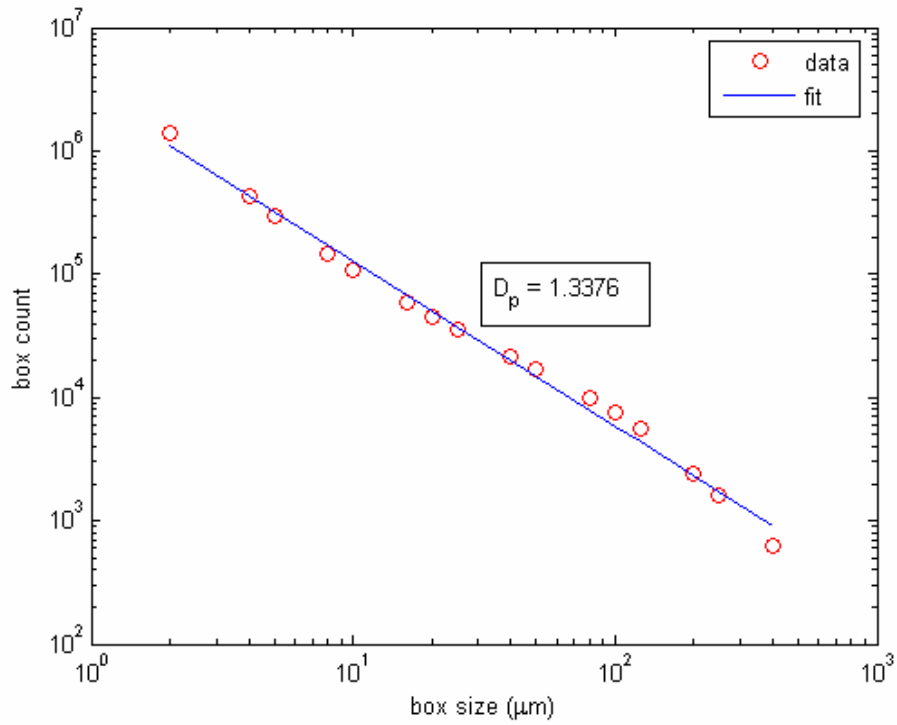


Figure 66 Surface Fractal Dimension for Limestone 1 Horizontal Section

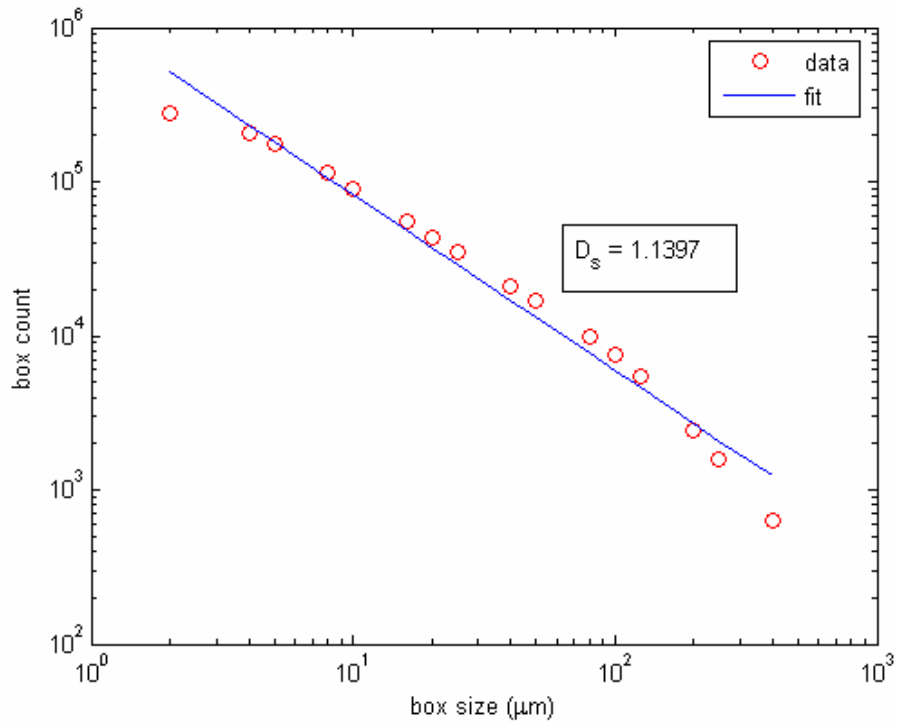


Figure 67 Matrix Fractal Dimension for Limestone 1 Vertical Section

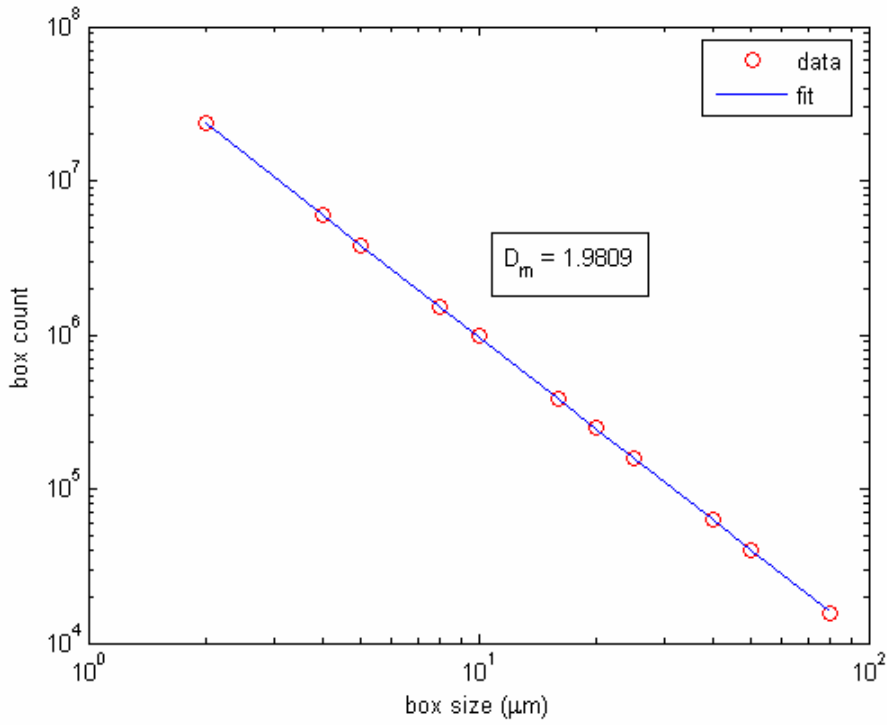


Figure 68 Pore Space Fractal Dimension for Limestone 1 Vertical Section

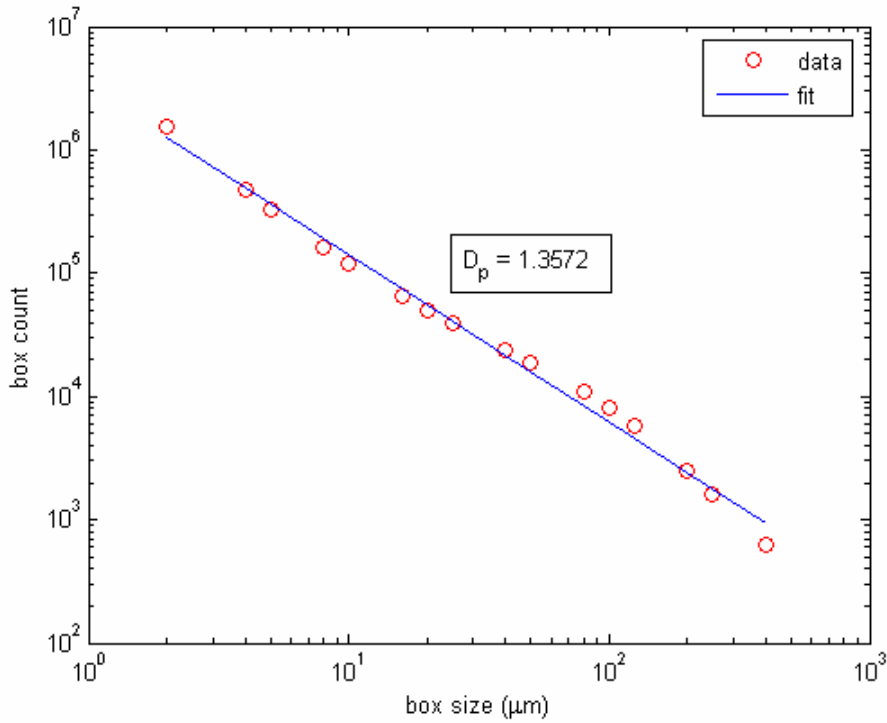


Figure 69 Surface Fractal Dimension for Limestone 1 Vertical Section

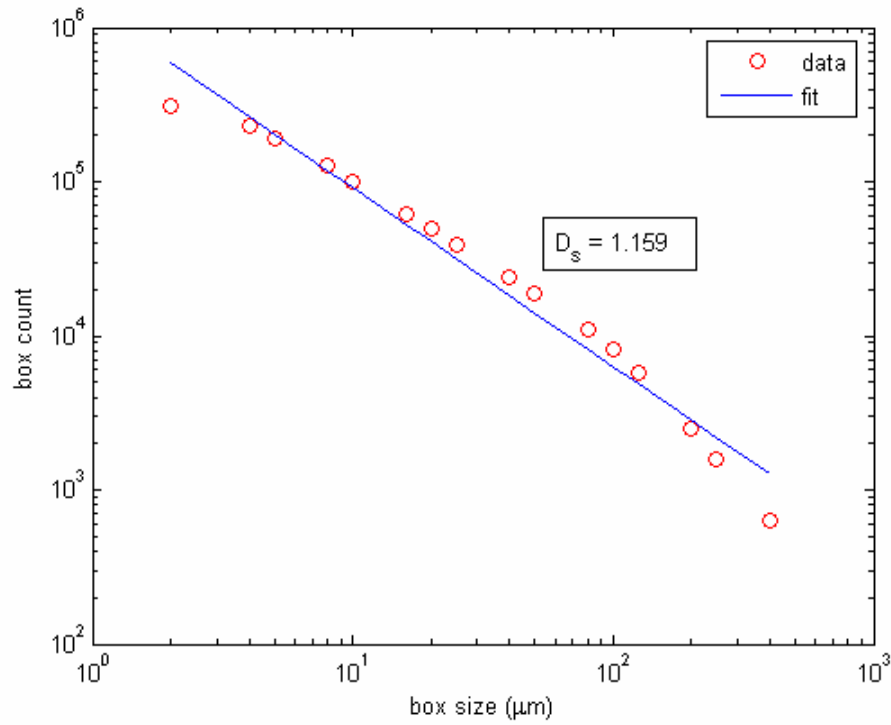


Figure 70 Matrix Fractal Dimension for Limestone 2 Horizontal Section

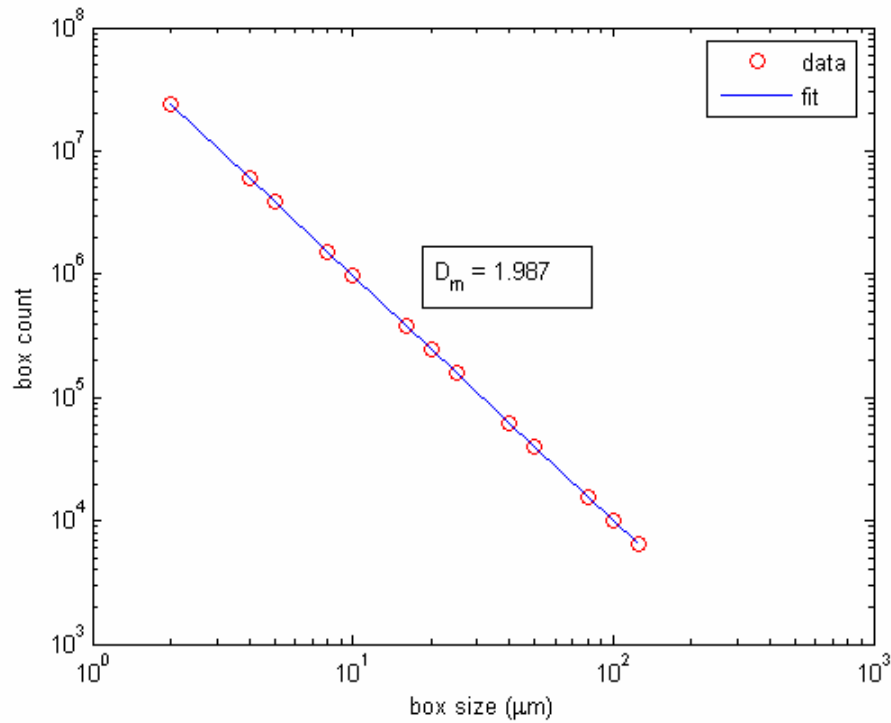


Figure 71 Pore Space Fractal Dimension for Limestone 2 Horizontal Section

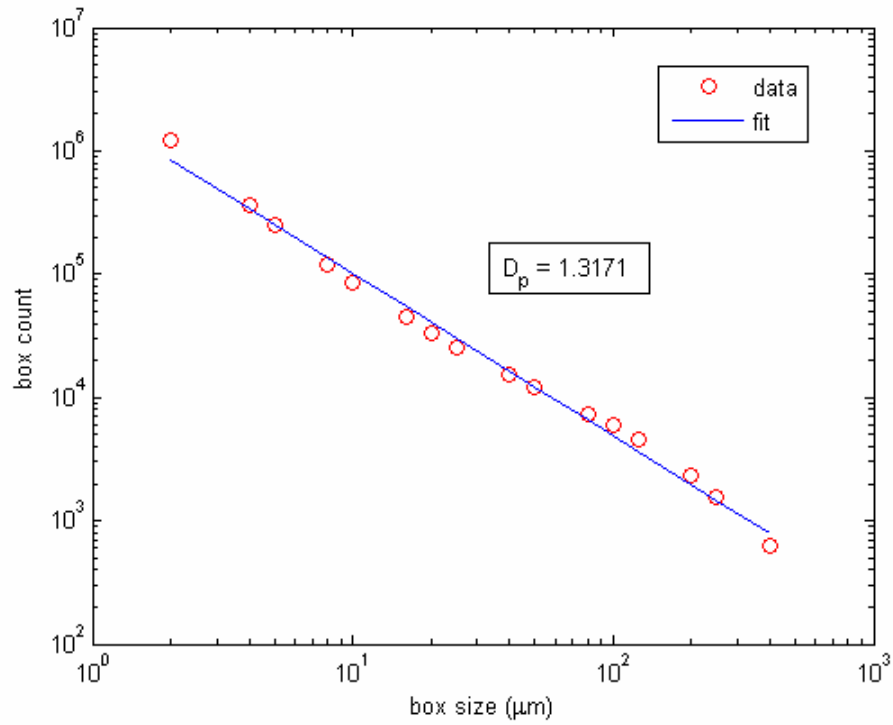


Figure 72 Surface Fractal Dimension for Limestone 2 Horizontal Section

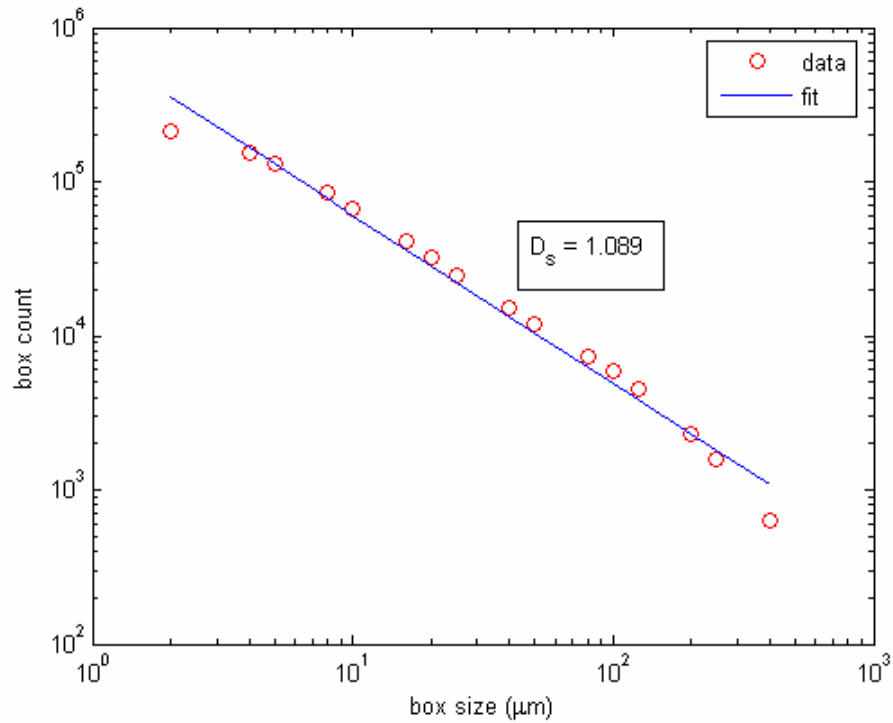


Figure 73 Matrix Fractal Dimension for Limestone 2 Vertical Section

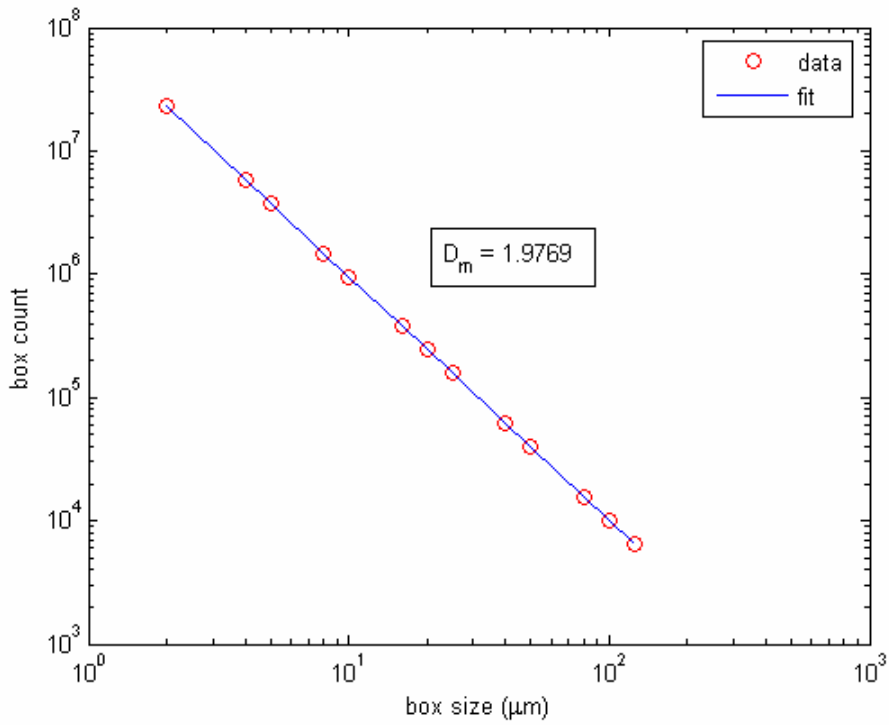


Figure 74 Pore Space Fractal Dimension for Limestone 2 Vertical Section

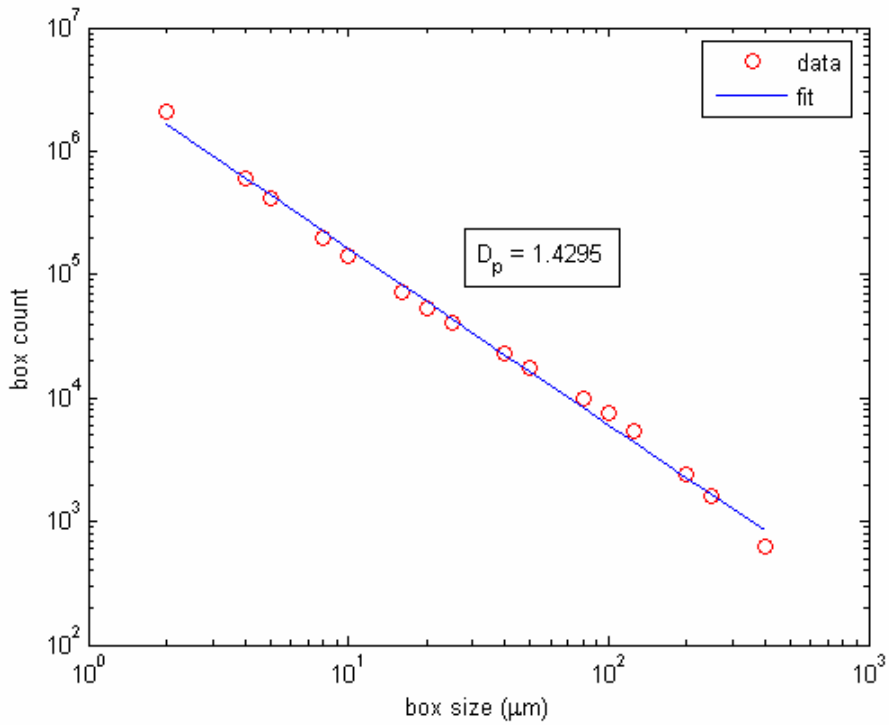


Figure 75 Surface Fractal Dimension for Limestone 2 Vertical Section

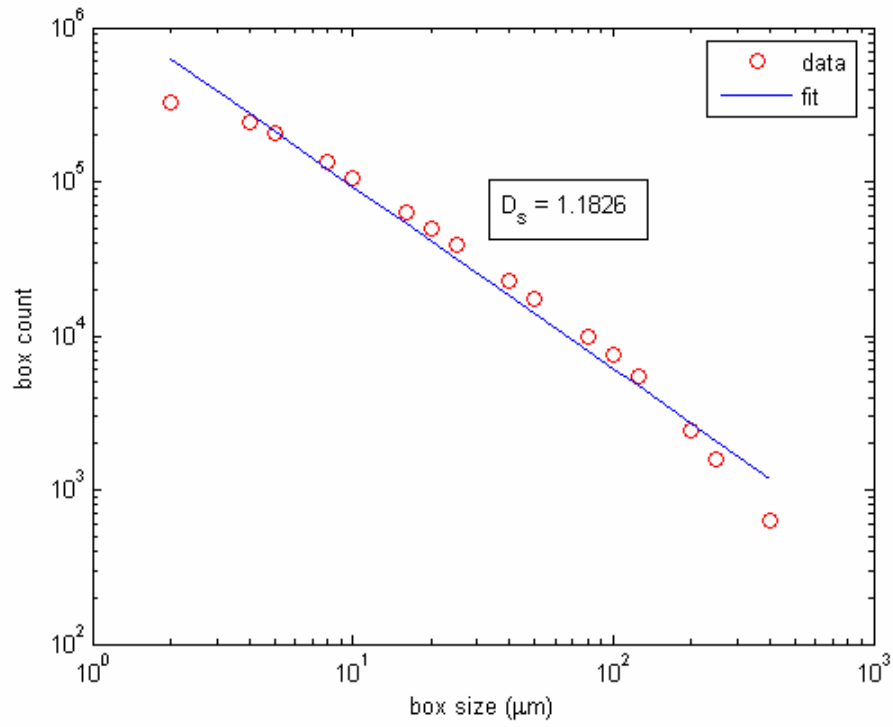


Figure 76 Matrix Fractal Dimension for 7536 B Horizontal Section

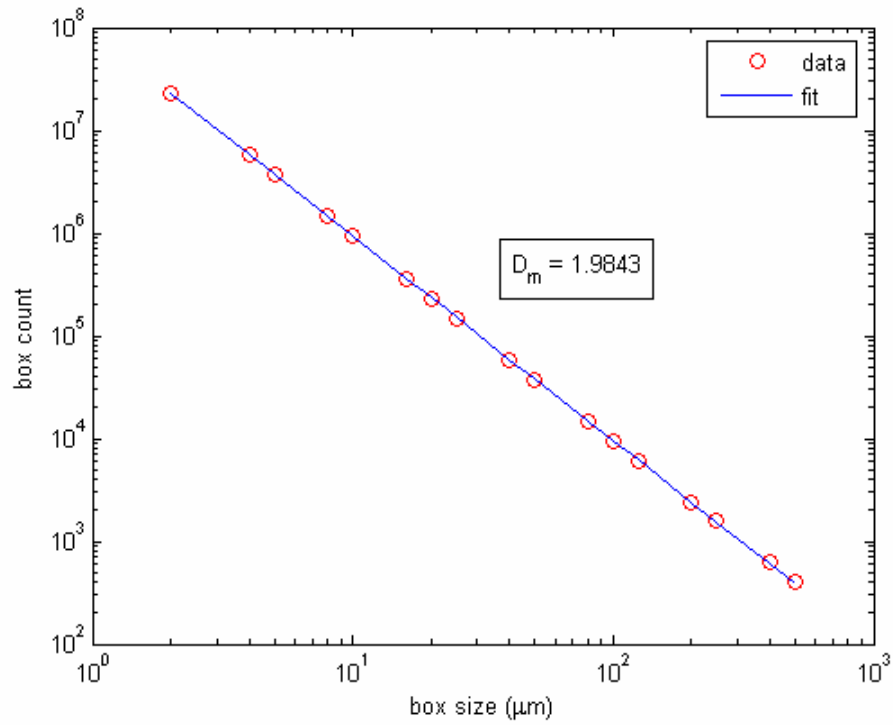


Figure 77 Pore Space Fractal Dimension for 7536 B Horizontal Section

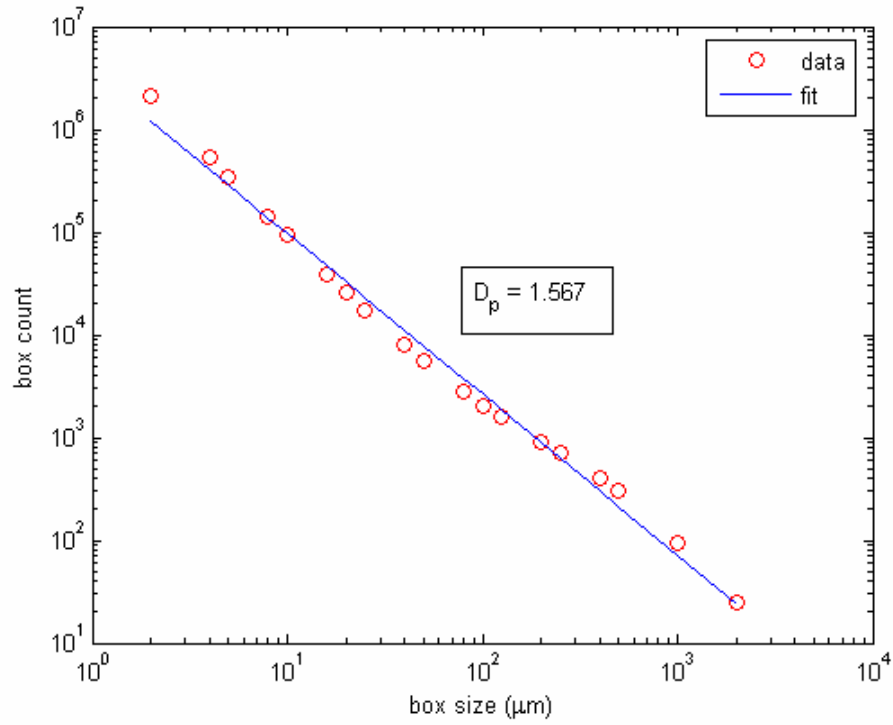


Figure 78 Surface Fractal Dimension for 7536 B Horizontal Section

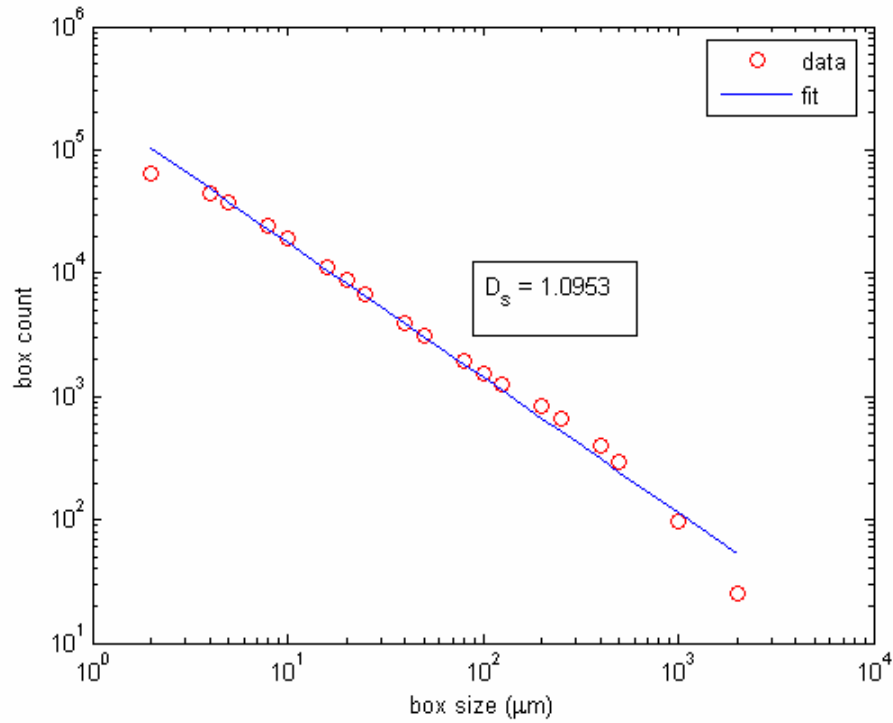


Figure 79 Matrix Fractal Dimension for 7536 B Vertical Section

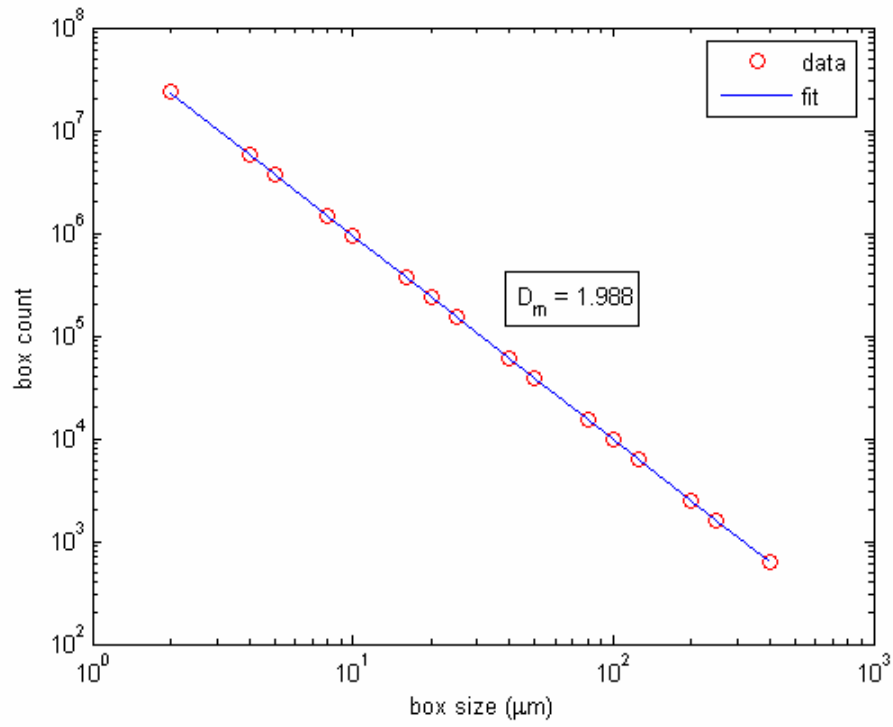


Figure 80 Pore Space Fractal Dimension for 7536 B Vertical Section

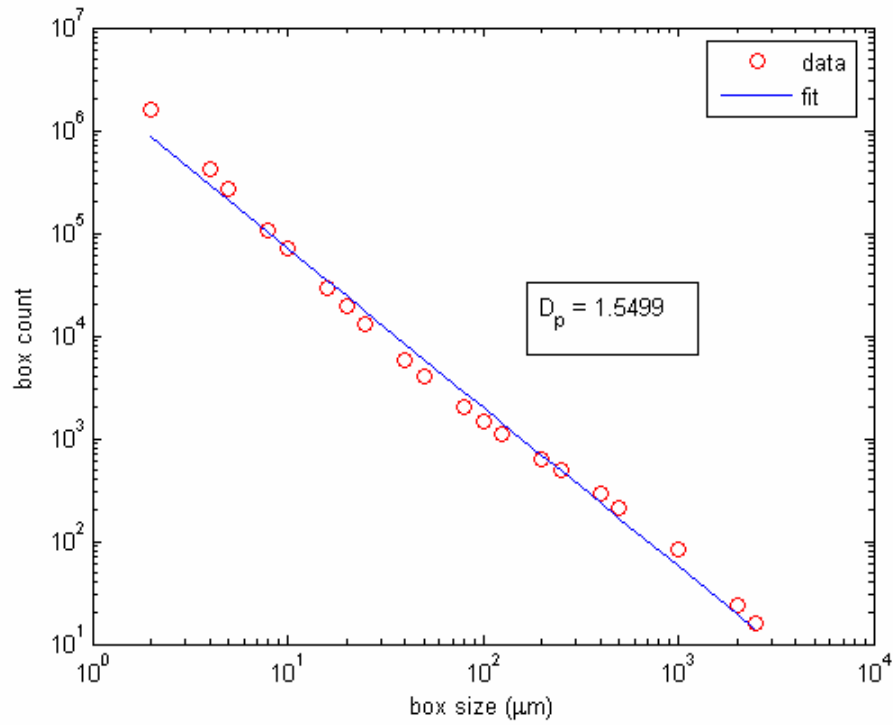


Figure 81 Surface Fractal Dimension for 7536 B Vertical Section

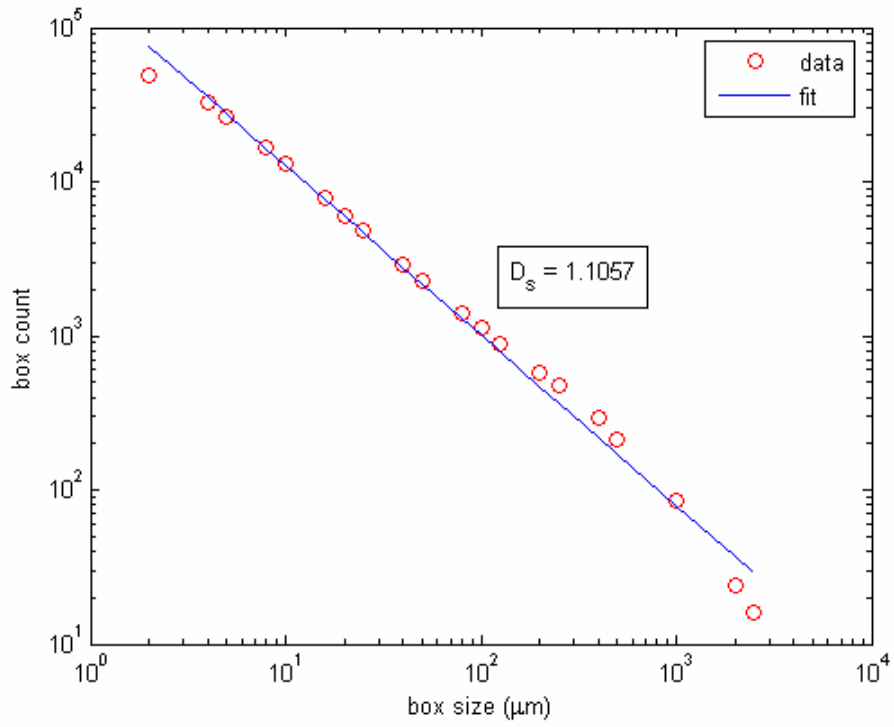


Figure 82 Matrix Fractal Dimension for 2416 Horizontal Section

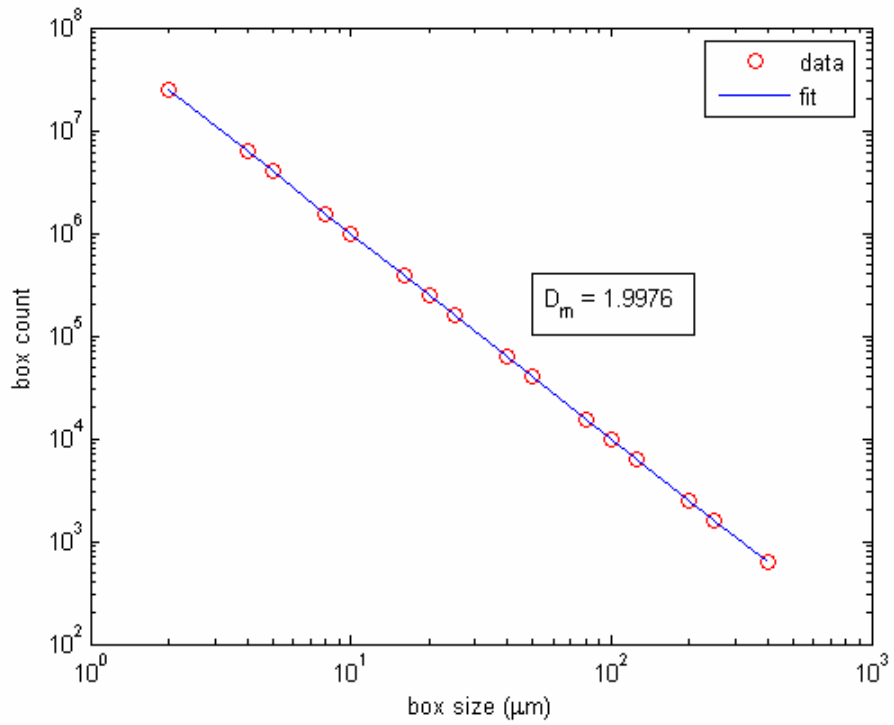


Figure 83 Pore Space Fractal Dimension for 2416 Horizontal Section

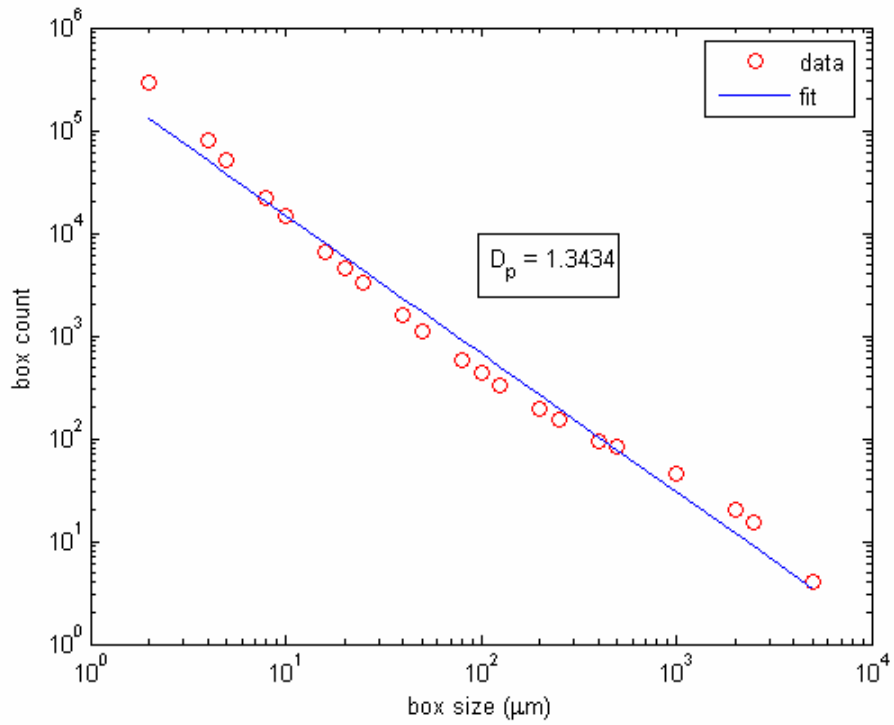


Figure 84 Surface Fractal Dimension for 2416 Horizontal Section

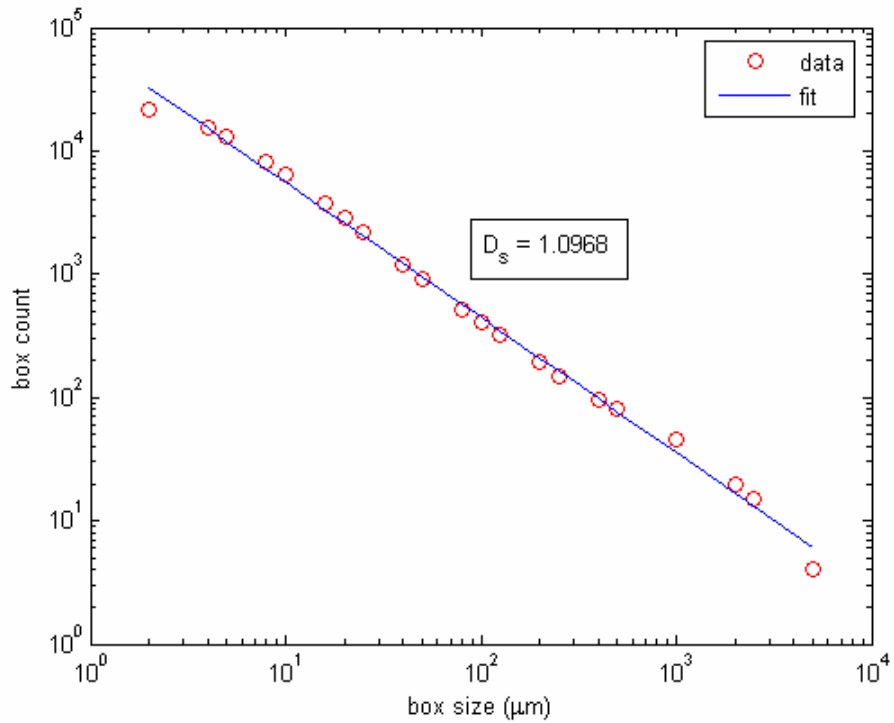


Figure 85 Matrix Fractal Dimension for 2416 Vertical Section

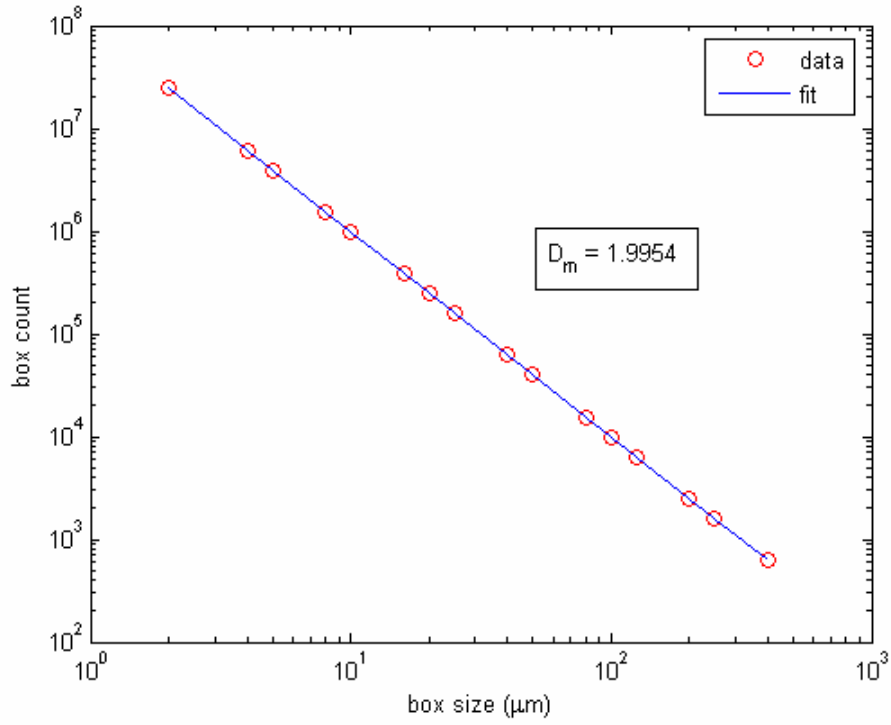


Figure 86 Pore Space Fractal Dimension for 2416 Vertical Section

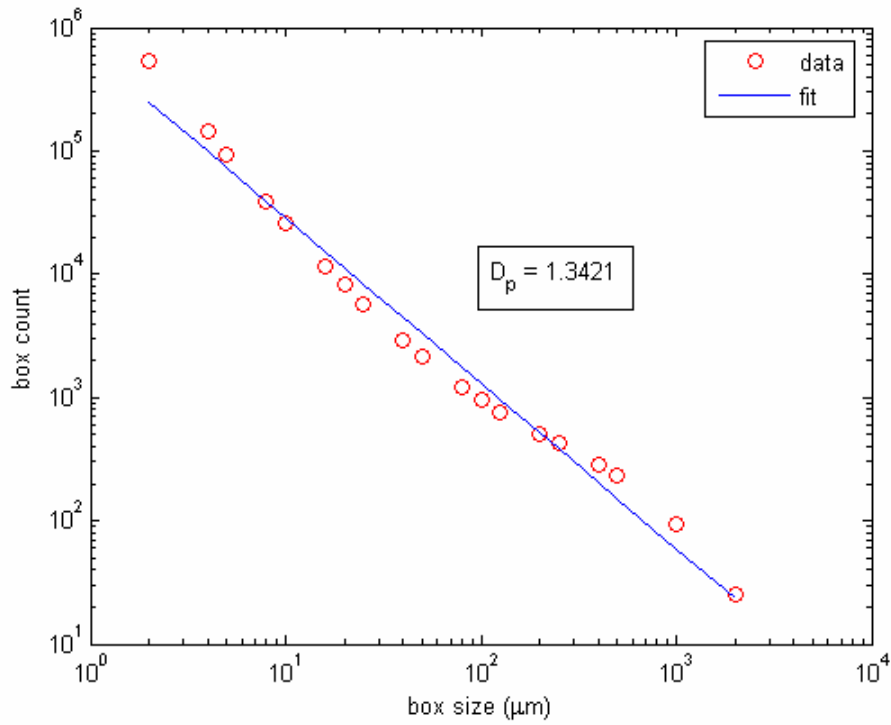


Figure 87 Surface Fractal Dimension for 2416 Vertical Section

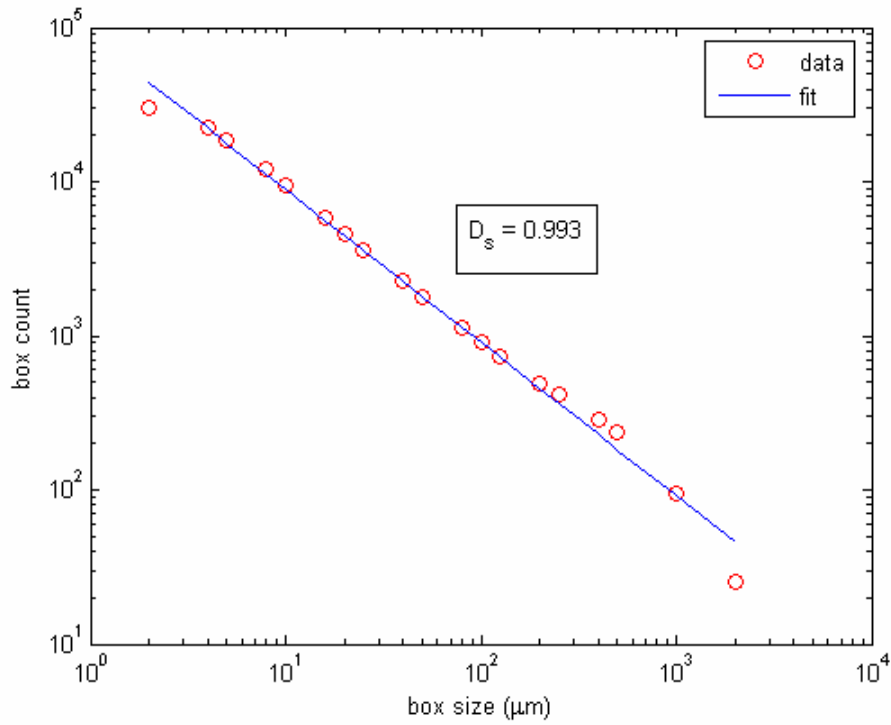


Figure 88 Matrix Fractal Dimension for 7626A Horizontal Section

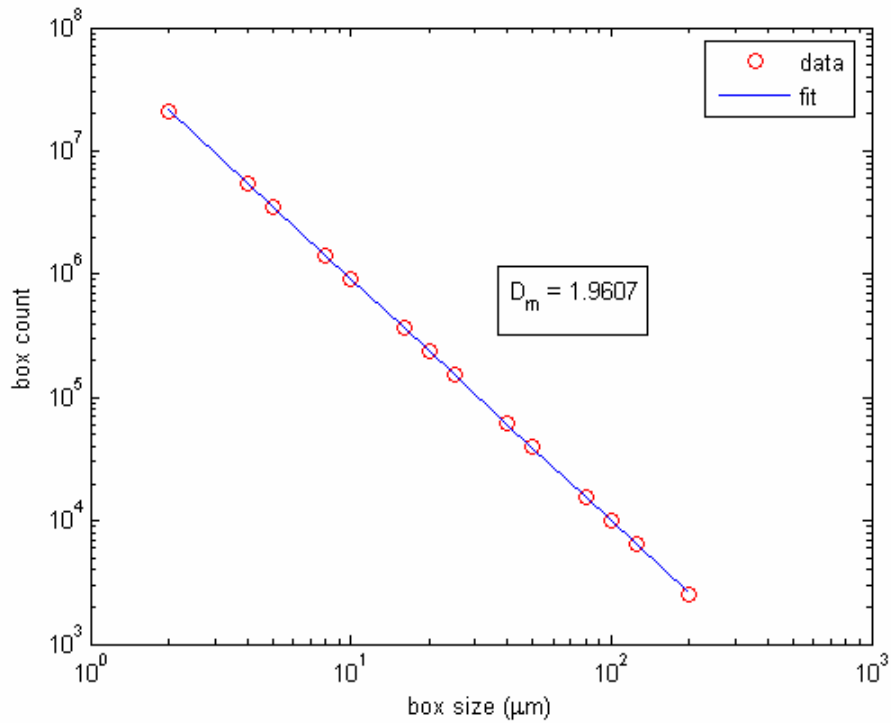


Figure 89 Pore Space Fractal Dimension for 7626A Horizontal Section

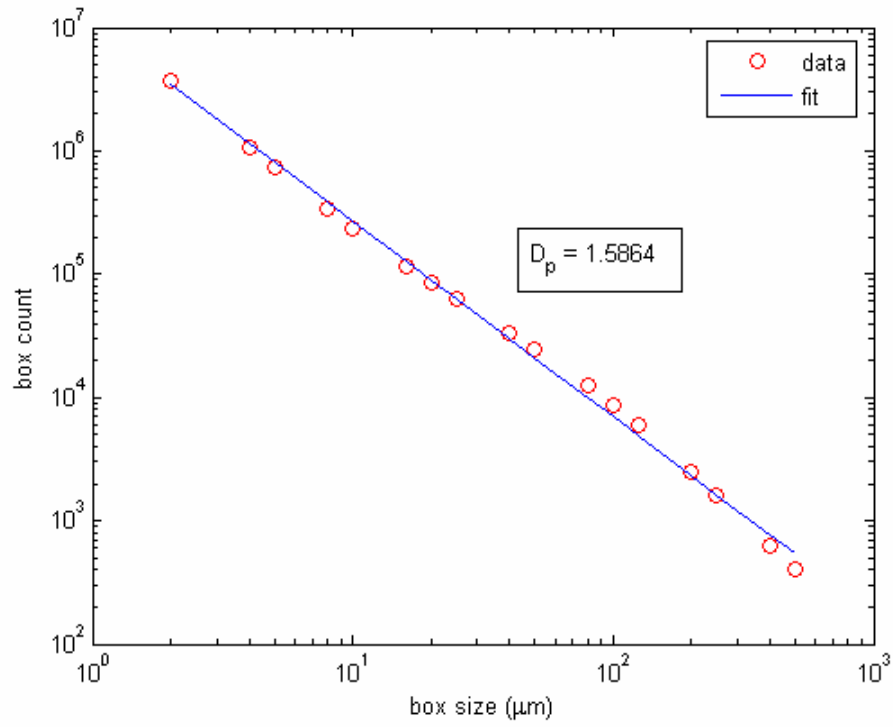


Figure 90 Surface Fractal Dimension for 7626A Horizontal Section

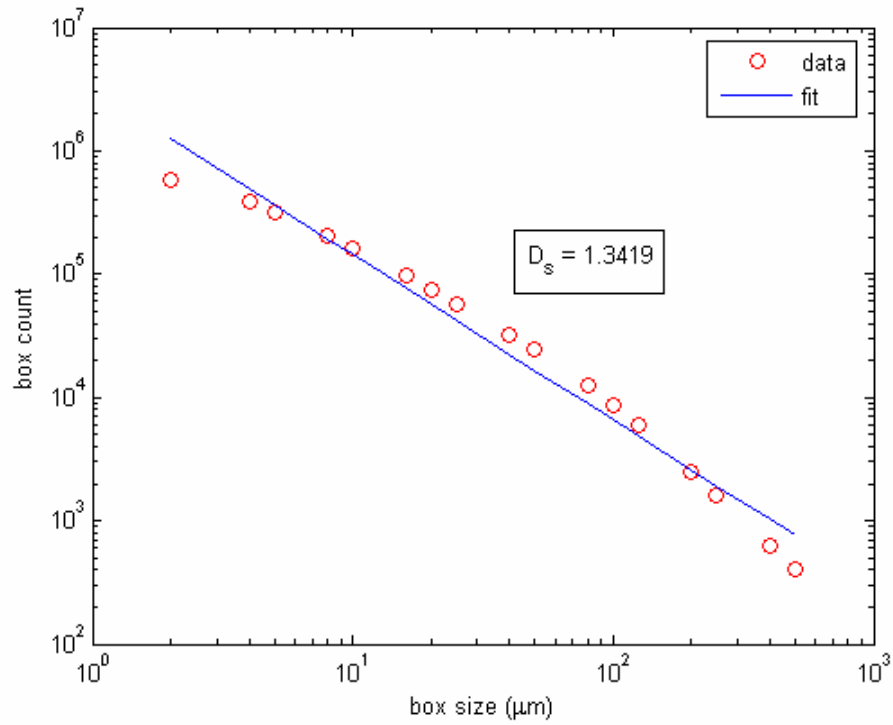


Figure 91 Matrix Fractal Dimension for 7626A Vertical Section

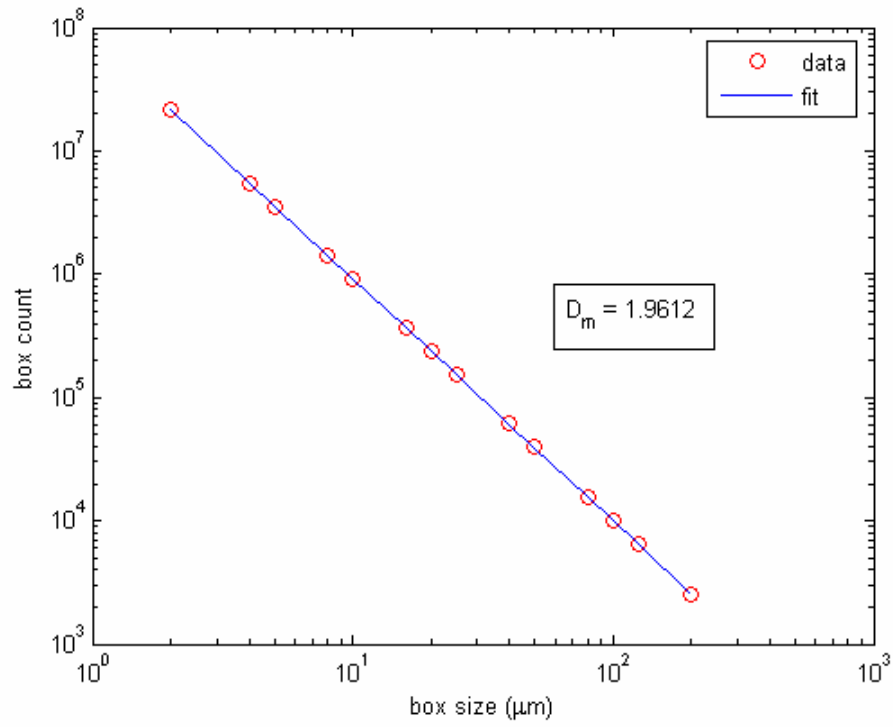


Figure 93 Pore Space Fractal Dimension for 7626A Vertical Section

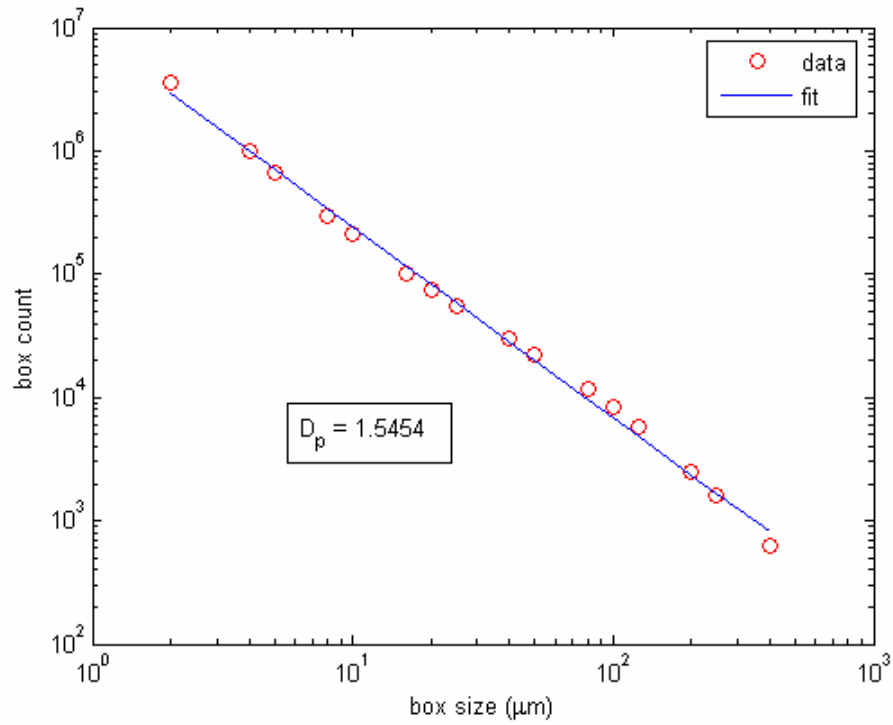


Figure 93 Surface Fractal Dimension for 7626A Vertical Section

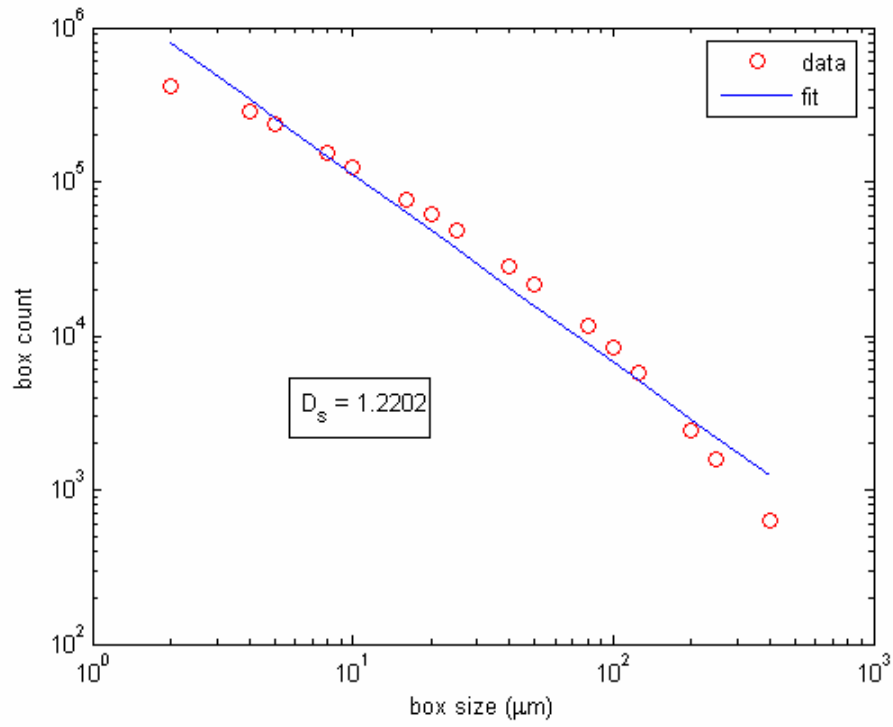


Figure 94 Matrix Fractal Dimension for 7626B Horizontal Section

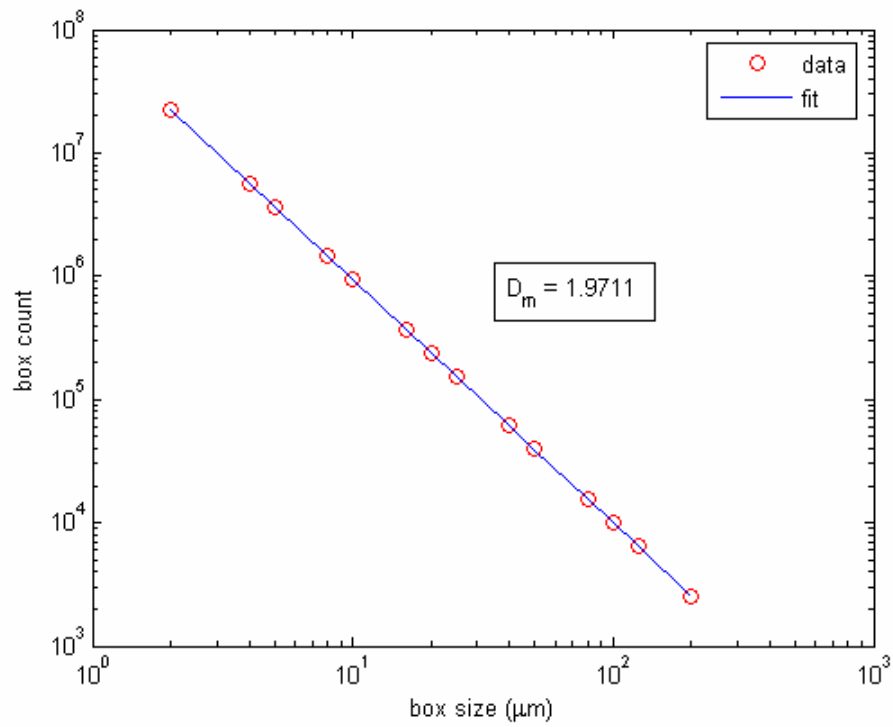


Figure 95 Pore Space Fractal Dimension for 7626B Horizontal Section

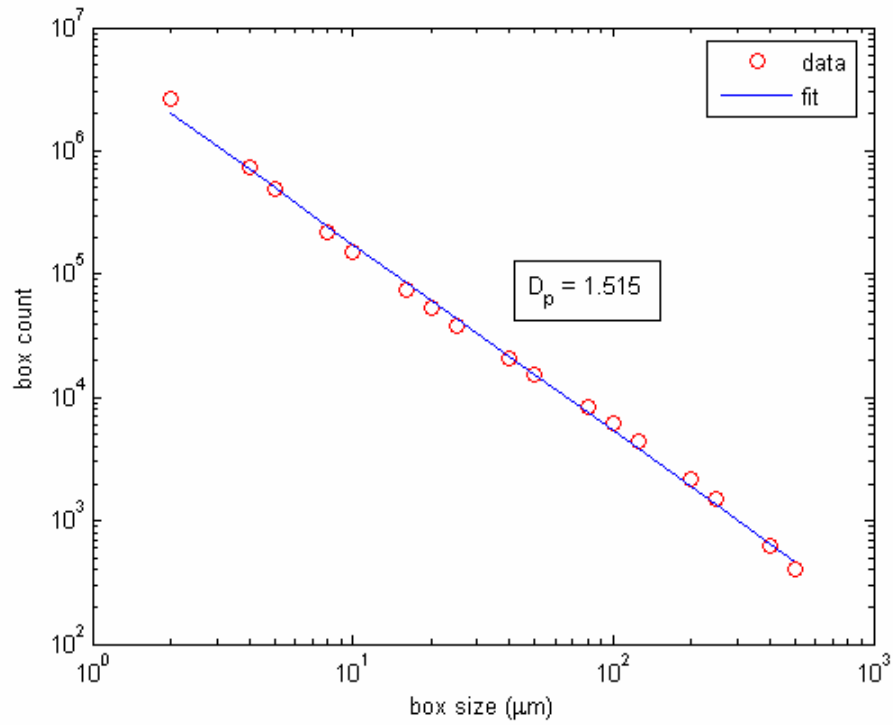


Figure 96 Surface Fractal Dimension for 7626B Horizontal Section

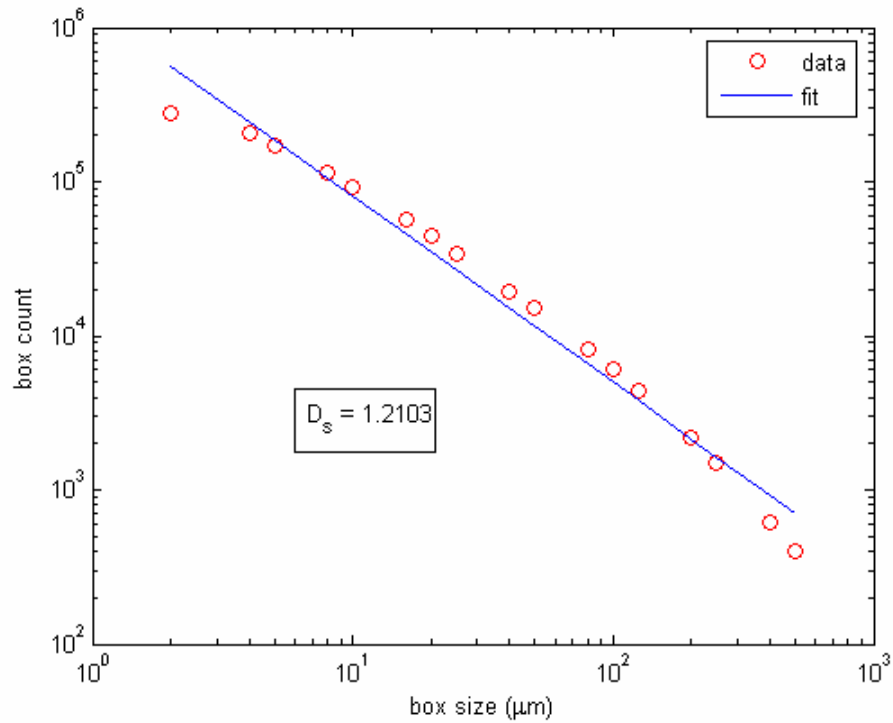


Figure 97 Matrix Fractal Dimension for 7626B Vertical Section

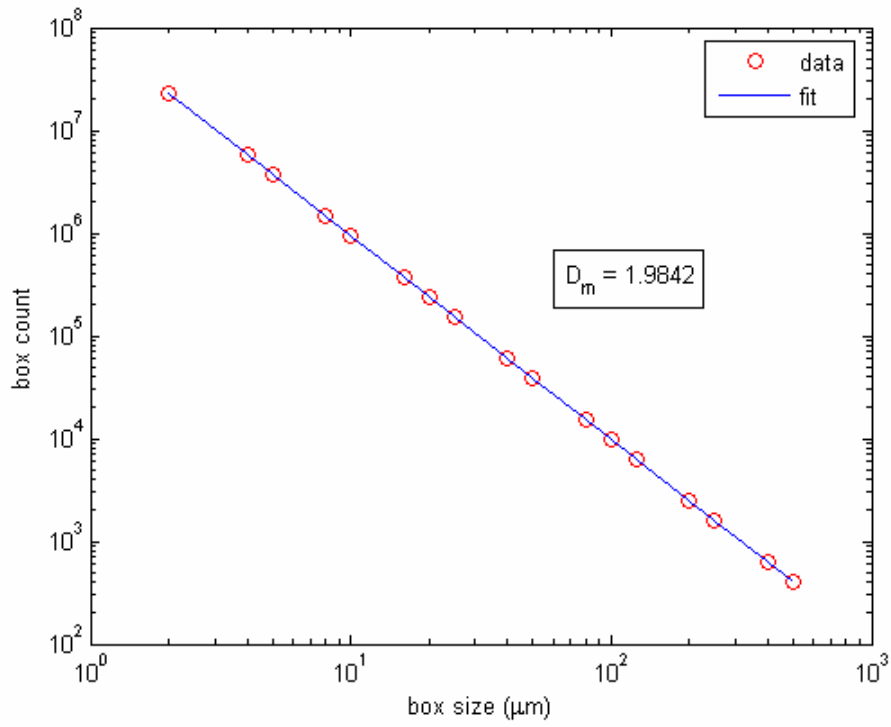


Figure 98 Pore Space Fractal Dimension for 7626B Vertical Section

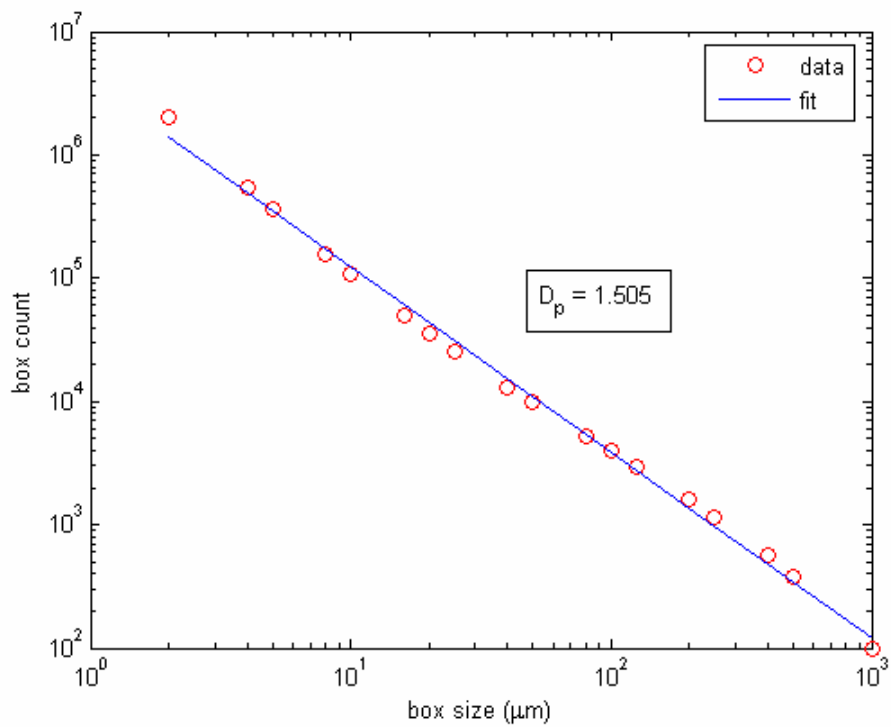
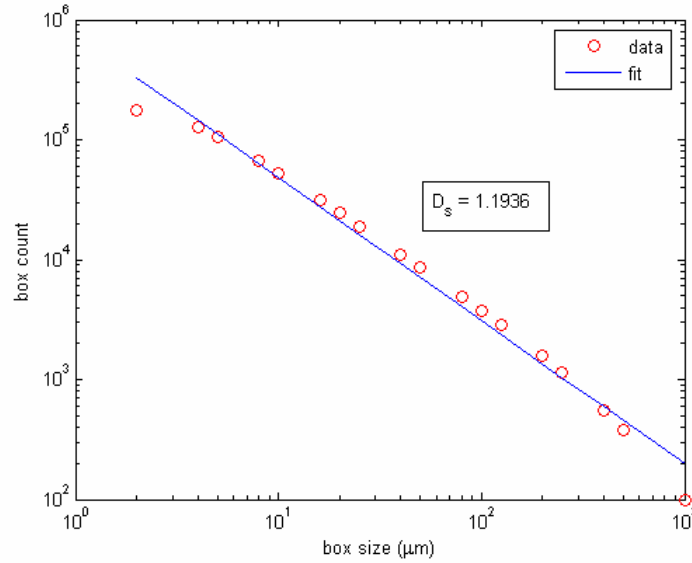


Figure 99 Surface Fractal Dimension for 7626B Vertical Section



2.8 3-D Reconstruction

The procedure of simulated annealing has been used to reconstruct 3-D porous media from 2-D sections. In this procedure, the statistical functions described in sections 2.2-2.5 are calculated for a thin section image. Then a random 3-D structure is constructed so that it has the same porosity as given by the thin section. The same statistical functions are calculated for the 3-D structure and the procedure involves evolving the structure using simulated annealing so that its statistical properties are closer to that from the 2-D image.

For the functions $f_i^0(r)$; $i = [1, n]$ from the 2-D image, it is assumed that they are independent of the direction of r so that they can be applied to the reconstructed direction as well. Now, the energy in the step s is defined as

$$E^s = \sum_{i=1}^N \sum_j [f_i^0(r_j) - f_i^s(r_j)]^2 .$$

To minimize E^s , 2 random points are chosen in different phases and their phases are interchanged to calculate $E^{s'}$. Now ΔE is defined as,

$$\Delta E = E^s - E^{s'}$$

This phase interchange of last step is accepted with the probability $p(\Delta E)$ given by

$$p(\Delta E) = \begin{cases} 1 & \Delta E \leq 0 \\ \exp(-\Delta E / T) & \Delta E > 0 \end{cases}$$

where T is the temperature, whose value and rate of change is chosen to minimize E^s to the global minimum. The functions used for reconstruction include porosity, two point auto-correlation function, chord length distribution and lineal path function. Figure 100 shows the 100 μm X 100 μm X 100 μm reconstructed structure of Limestone 1 and Figure 101 shows the reconstructed structure for Limestone 2 of the same size. In both these images white represents rock and blue represents pore space.

Figure 100 Reconstructed Structure for Limestone 1

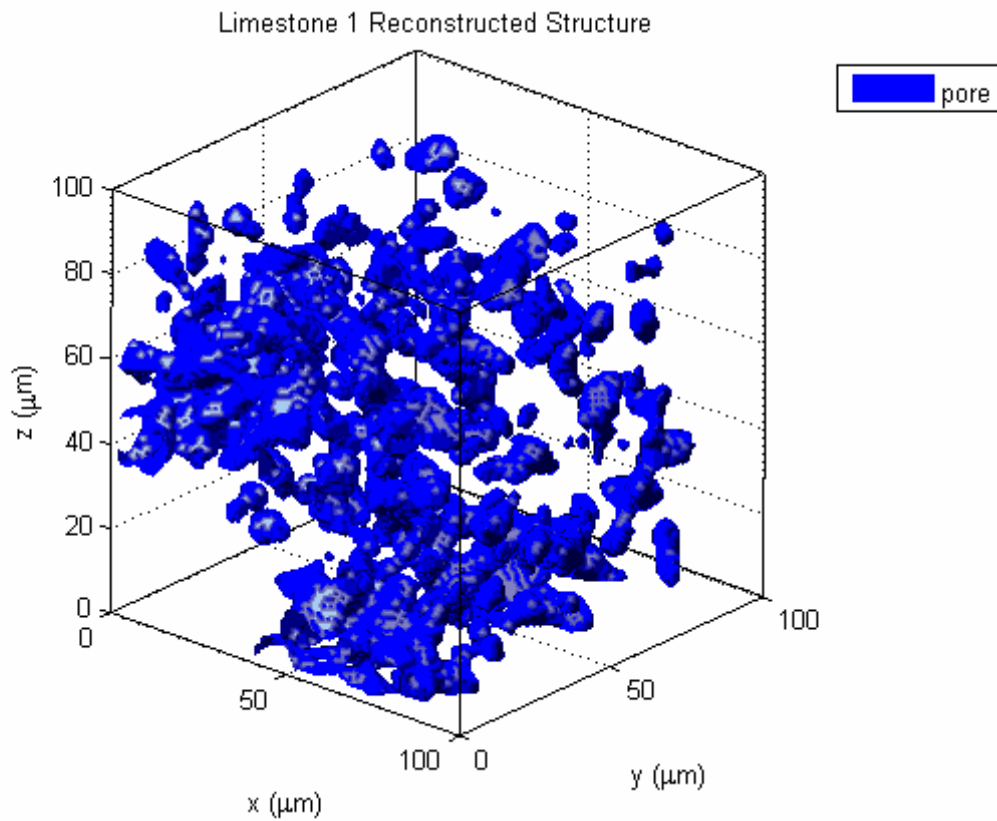
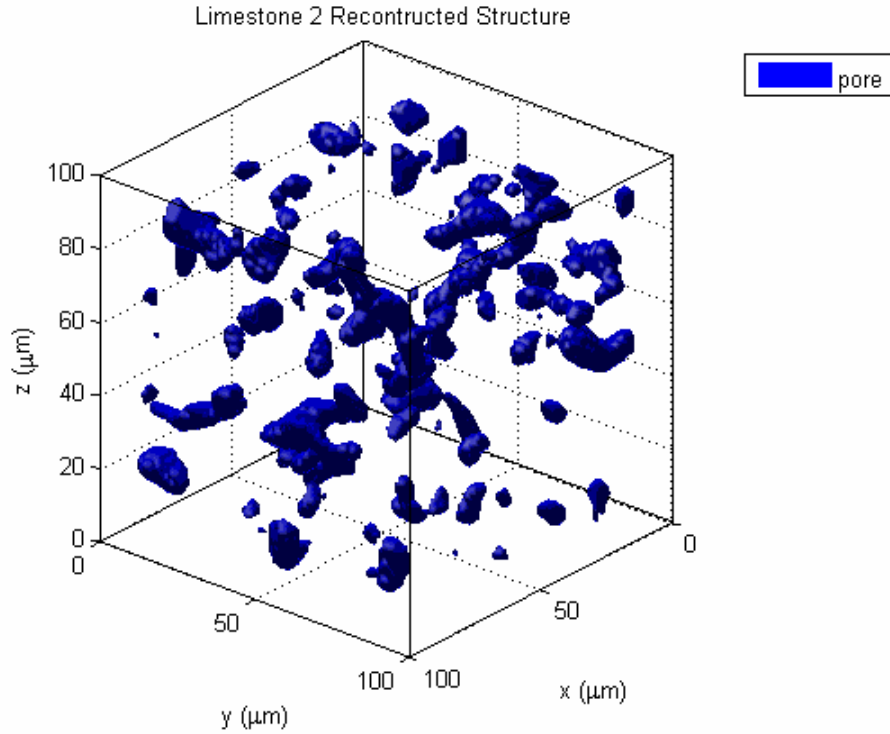


Figure 101 Reconstructed Structure for Limestone 2



2.9 Flow calculations

The single phase permeability (k) for the porous medium is given by the Darcy's law

$$\bar{u} = -\frac{\bar{k}}{\mu} \cdot (\bar{\nabla}P + \rho \bar{g})$$

Where \bar{u} is the superficial velocity given by

$$\bar{u} = \frac{Q}{A}$$

where Q = volumetric flow rate

A = macroscopic cross-sectional area

k = permeability

μ = fluid viscosity

$\bar{\nabla}P$ = pressure gradient

For comparison, for flow along a tube,

$$k = \frac{R^2}{8}$$

The typical fluid flow rate in an oil-field is about 1ft/day. Because the typical diameter of the flow channels is of the order of microns, the Reynold's number for flow of water is less than 1.0. This shows that the flow is in the Stokes flow regime. For a 3-D porous medium, the single phase permeability can be calculated by solving the Stokes flow equations using the staggered grid method. The equation of continuity and equation of motion give for the case of incompressible flow (neglecting gravity)

$$\begin{aligned} \frac{\partial u}{\partial x} + \frac{\partial v}{\partial y} + \frac{\partial w}{\partial z} &= 0 \\ -\frac{1}{\rho} \frac{\partial P}{\partial x} + \nu \left(\frac{\partial^2 u}{\partial x^2} + \frac{\partial^2 u}{\partial y^2} + \frac{\partial^2 u}{\partial z^2} \right) &= 0 \\ -\frac{1}{\rho} \frac{\partial P}{\partial y} + \nu \left(\frac{\partial^2 v}{\partial x^2} + \frac{\partial^2 v}{\partial y^2} + \frac{\partial^2 v}{\partial z^2} \right) &= 0 \\ -\frac{1}{\rho} \frac{\partial P}{\partial z} + \nu \left(\frac{\partial^2 w}{\partial x^2} + \frac{\partial^2 w}{\partial y^2} + \frac{\partial^2 w}{\partial z^2} \right) &= 0 \end{aligned}$$

Using second order finite difference on a staggered grid, the Laplace equation for pressure is solved with the velocity equations above to get the velocity profile. The input and output pressures are specified and the normal and tangential velocities on a solid surface are taken to be zero. The permeability can be calculated from the velocity profile using Darcy's Law.

For the case of both water and oil flowing through a porous medium, relative permeabilities are calculated using a pore network model. For this the 3-D pore structure is converted to pore-network using skeletonization software 3DMA. Then this network can be used to simulate multiphase psuedo-static displacements (as in the case of mercury porosimetry experiments) or dynamic displacements (as in the case of core floods).

2.10 Core Floods

The rock is cored in the form of a cylinder of diameter 1.5 inches. The height varies for different samples from about 1.5 inches to 3 inches. For the flow experiment the core is confined on the outside surface by a rubber sleeve using an overburden pressure of about 1500psi leaving the 2 circular faces open to flow along the axial direction. Fluid distributors are placed in contact with these surfaces to evenly distribute the fluid on the

surface for flow. The pressure drop across the core and the flow rate of the flowing fluid is measured.

Formation factor for a sample is defined as the resistivity of rock filled with brine divided by the resistivity of the brine.

$$F = \frac{R_{rock+brine}}{R_{brine}}$$

Formation factor is considered a measure of the tortuosity of the fluid flow path in the sample and is used in a number of permeability correlations. The formation factor for the 6 carbonates are listed in Table 3. Electrical conductivity of the sample can be measured during the fluid flow experiments by using a LCZ meter connected to 2 rings placed in contact with the sample (Figure 102).

Figure 102. Core Flood Apparatus

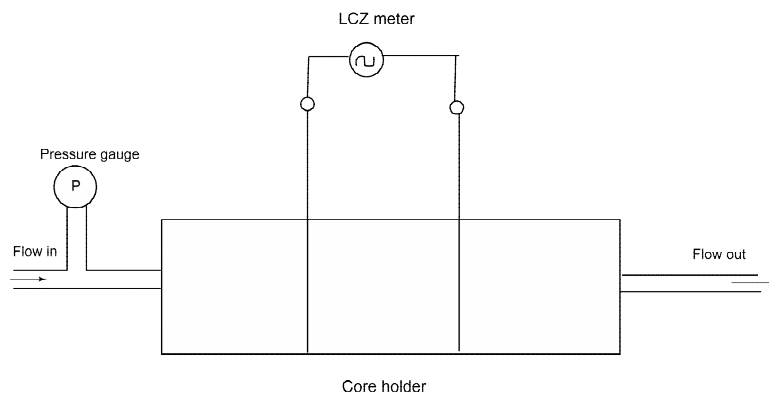


Table 3. Measured Formation Properties for samples

| Sample | K (mD) | F | Porosity (%) |
|--------|--------|--------|--------------|
| 2416 | 0.023 | 190.71 | 5.97 |
| 7536A | 0.022 | 303.89 | 9.53 |
| 7536B | 0.08 | 500.53 | 4.55 |
| 17C9 | 56.13 | 69.4 | 17.5 |
| 7626A | 140.17 | 54.41 | 19.5 |
| 7626B | 2313 | 26.93 | 24.4 |
| Berea | 482 | 16.43 | 23 |

For single phase permeability, 1wt% NaCl brine is flowed through the sample at a known flow rate. The pressure drop is measured to estimate the permeability of the rock using the Darcy's Law

$$\frac{Q}{A} = \frac{k_w}{\mu_w} \frac{\Delta P}{L}$$

where Q = flow rate of brine,

A = cross-section area of core,

L = length of core,

ΔP = pressure drop across the core,

k_w = brine permeability of sample,

μ_w = viscosity of water .

Once the rock is saturated with brine, it is flooded with the crude oil and the pressure drop and exit fractional flow is noted as a function of time. The drainage relative permeability can be calculated from this experiment using the JBN method. As oil continues to flow into the sample, water is displaced from the pores until oil saturation becomes constant and the water reaches its residual saturation. At this point the experiment is terminated and the core is aged with oil for about 2 months. During this time the wettability of the core changes from water wet to mixed wet due to deposition of asphaltene type of materials from the oil on the pore surface which is occupied by oil. Thus the pores occupied by oil become partly oil wet. Then this core is flooded with brine until the core reaches the residual oil saturation and the measurement of pressure drop and exit composition can be used to estimate the imbibition relative permeability from the JBN method.

2.11 JBN Method

This method is based on the Darcy's Law and can be used for calculation of relative permeability as a function of phase saturation using the data obtained from core flood experiments. For a water flood,

$$S_{w2} = \bar{S}_w + Q_i (f_{w2} - f_{w1})$$

where subscript 2 denotes the exit face and subscript 1 denotes the entry face for fluid flow. Since water is the only fluid that is injected, $f_{w1} = 1.0$, so

$$S_{w2} = \bar{S}_w - Q_i f_{o2} .$$

For ratio of the relative permeabilities at the saturation S_{w2}

$$\left(\frac{k_{ro}}{k_{rw}} \right)_{S_{w2}} = \frac{\mu_o}{\mu_w} \left(\frac{1}{f_{w2}} - 1 \right).$$

Now

$$f_{o2} = \frac{dV_{o2}}{dV_{w1}} = \frac{d\bar{S}_w}{dQ_i}$$

and

$$S_{w2} = \bar{S}_w - Q_i \frac{d\bar{S}_w}{dQ_i}.$$

The value of f_{o2} can be found from the plot of \bar{S}_w vs Q_i . For this we draw tangents to the curve at $Q_i > 1.0$ and the intercept of the tangent with the \bar{S}_w axis is the value of S_{w2} . At any time, the total pressure drop across the core is given by

$$\Delta P = \int_0^L \frac{\frac{q_t}{A} dx}{k \left(\frac{k_{ro}}{\mu_o} + \frac{k_{rw}}{\mu_w} \right)}.$$

If permeability (k) is measured by another experiment on the same core using single phase flow of a base fluid b, then

$$\Delta P = \frac{q_t \Delta P_b}{q_b \mu_b L} \int_0^L \frac{dx}{\left(\frac{k_{ro}}{\mu_o} + \frac{k_{rw}}{\mu_w} \right)} = \frac{q_t \Delta P_b}{q_b \mu_b} \bar{\lambda}_2^{-1}$$

$$\bar{\lambda}_2^{-1} = \frac{\int_0^L \lambda_r^{-1} dx}{\int_0^L dx}$$

$$\lambda_r^{-1} = \left(\frac{k_{ro}}{\mu_o} + \frac{k_{rw}}{\mu_w} \right)^{-1}$$

Using the above with the equation

$$\lambda_2^{-1} = \bar{\lambda}^{-1} - Q_i \frac{d\bar{\lambda}^{-1}}{dQ_i}.$$

We can calculate

$$k_{ro} = \frac{\mu_o f_{o2}}{\lambda_2^{-1}}$$

$$k_{rw} = \frac{\mu_w f_{w2}}{\lambda_2^{-1}}$$

where k_{ro} is the relative permeability of oil at water saturation S_{w2} and k_{rw} is the relative permeability oil water at the same saturation. In a similar manner the relative permeability for water and oil can be calculated from the oil flood as well. Figures 103 and 104 show the relative permeability curves calculated for Limestone 2 during oil flood and water flood respectively.

Figure 103. Relative Permeability for oil flood for Limestone Sample 2

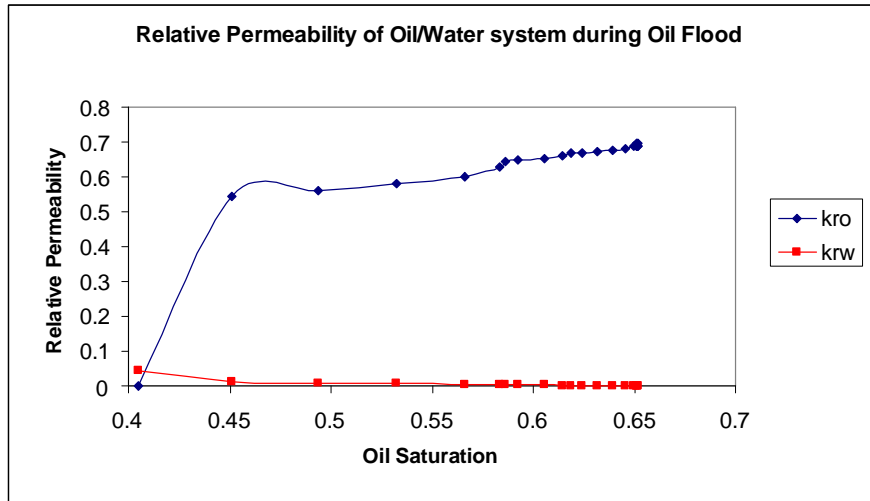
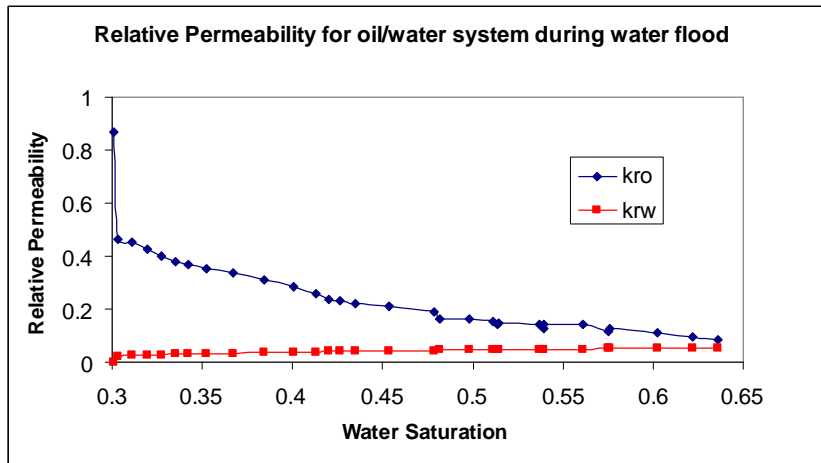


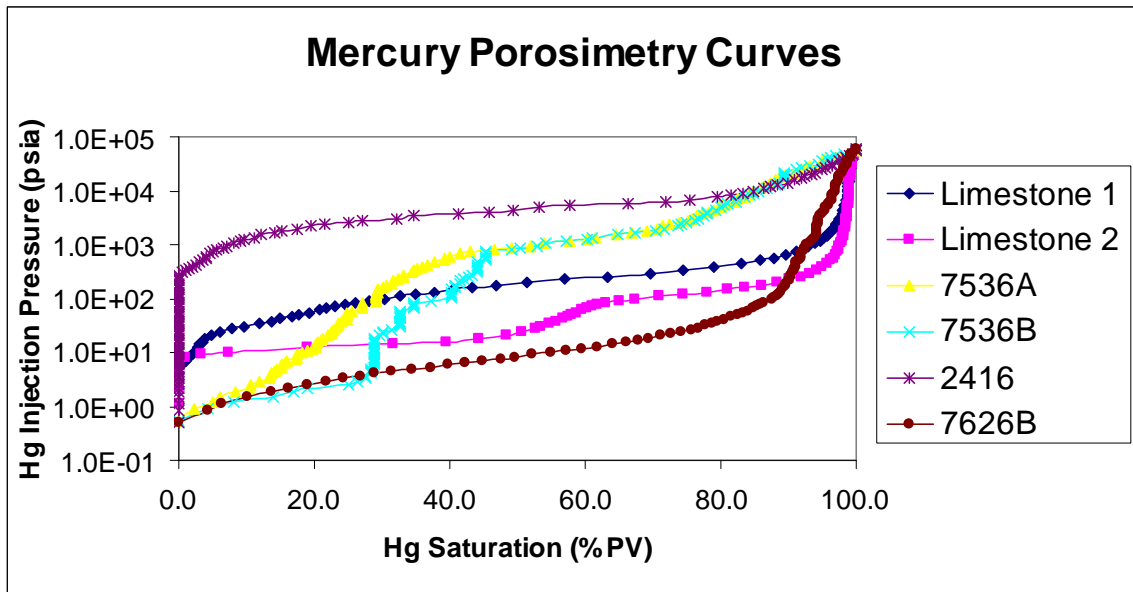
Figure 104. Relative Permeability for water flood for Limestone Sample 2



2.12 Mercury Capillary Pressure

In these experiments, mercury is a non-wetting fluid for the surface and has to be injected into the pores of the rock. The pressure required for the injection of mercury in a pore is governed by the capillary force in the throat connecting the pore which can give an estimate of the throat size. The mercury capillary pressure measurements of the end pieces were conducted and the graphs for all the samples are shown in Fig 105.

Figure 105. Mercury Porosimetry Curves for 6 Carbonate Samples



Permeability can be estimated from the mercury capillary pressure experiments using the following correlations. The Swanson's correlation estimates permeability from the mercury capillary pressure using

$$k_w = 290 \left(\frac{S_b}{P_c} \right)_{\max}^{1.901}$$

where S_b is the mercury saturation in percent bulk volume and P_c is the mercury capillary pressure in psi. At the maximum point S_b is indicative of the pore space effectively contributing to the fluid flow and the reciprocal capillary pressure is proportional to the pore size connecting this effective pore space. The Winland correlation uses the pore throat size invaded when 35% of the pore space is saturated with mercury, to give

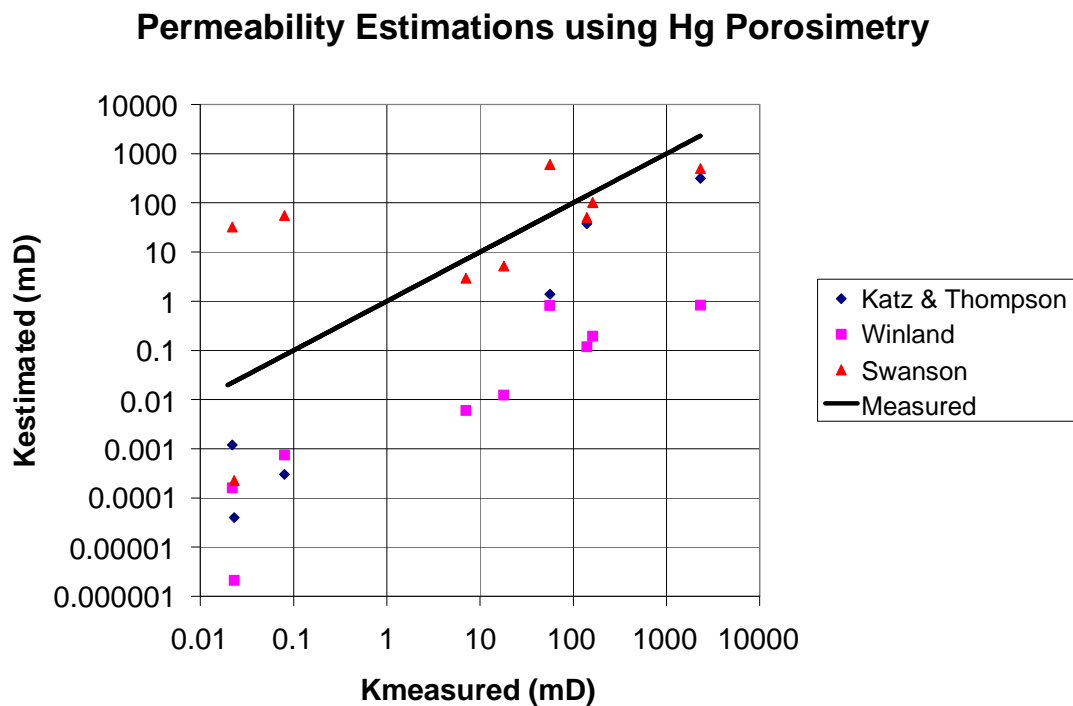
$$k = \phi^{1.47} r_{35}^{1.701} / 17.6.$$

The correlation given by Katz and Thompson uses the throat size associated with the inflection point on the Hg injection curve (l_c) and the formation factor (F) of the sample to estimate permeability by

$$k = \frac{1}{226} \frac{l_c}{F}$$

Figure 106 shows the actually measured permeability for these samples vs. the permeability estimated from these correlations.

Figure 106. Permeability Estimation from Mercury Porosimetry Correlations



2.13 NMR Response

When an atomic nucleus is subjected to magnetic fields it results in nuclear magnetic resonance. In well-logging applications, the response of a hydrogen (H) nucleus in the fluids is measured. This H atom can be present either in the brine or the hydrocarbons. In general, the H-nucleus will precess around a static magnetic field B_0 with the Larmor frequency f given by

$$f = \frac{\gamma B_0}{2\pi}$$

Where γ is the gyromagnetic ratio and for hydrogen

$$\frac{\gamma}{2\pi} = 42.58 \text{MHz} / \text{Tesla}$$

From the theory of quantum mechanics, when a large number of protons are precessing about a static magnetic field B_0 , with spins that can be parallel or anti-parallel to the direction of B_0 , the net macroscopic magnetization of the system M_0 is given by the Curie's law

$$M_0 = N \frac{\gamma^2 h^2 I(I + 1)}{3(4\pi^2)kT} B_0$$

where M_0 = net magnetic moment per unit volume,

N = nuclei per unit volume,

k = Boltzman's constant,

T = absolute temperature (K),

h = Plank's constant,

I = spin quantum number of the nucleus.

When the field B_0 is applied the magnetization is not instant but follows an exponential growth

$$M_z(t) = M_0(1 - \exp(-t / T_1))$$

where T_1 is the longitudinal relaxation time constant. When an oscillating field B_1 with frequency equal to the Larmor frequency is applied in a direction perpendicular to B_0 the macroscopic magnetization tips at an angle given by

$$\theta = \gamma B_1 \tau$$

where τ is the time over which B_1 is applied. When diffusion can be ignored, the irreversible decay of transverse magnetization can be measured using a CPMG pulse sequence. The time constant of this decay is called the transverse relaxation time (T_2) and the equation is

$$M_x(t) = M_{0x} \exp(-t / T_2)$$

where M_{0x} is the equilibrium transverse magnetization.

For fluids in pores, 3 types of relaxation contribute to the total decay in the signal

1. Bulk Relaxation,
2. Surface Relaxation, and

3. Diffusion-Induced Relaxation.

And the total transverse relaxation is given by

$$\frac{1}{T_2} = \frac{1}{T_{2bulk}} + \frac{1}{T_{2surface}} + \frac{1}{T_{2diffusion}}$$

$$T_{2bulk} \approx c \frac{T_K}{\eta}$$

$$T_{2surface} = \rho_2 \frac{S}{V}$$

$$T_{2diffusion} = \frac{D (\gamma * G * TE)^2}{12}$$

The Pulsed Field Gradient Diffusion Editing pulse sequence (Figure 109) can be used to measure the D and T₂ in the presence of a magnetic field gradient. Using this information it is possible to separate out the T₂ signal for oil and water.

The NMR response of the rocks is measured using a 2 MHz Maran Ultra NMR spectrometer. The response of the system to CPMG pulse sequence and a Pulsed Field Gradient sequence is noted and diffusion coefficient and transverse relaxation times can be estimated.

Permeability Estimation from NMR

The SDR correlation estimates permeability from formation porosity and the log mean of the brine T₂ distribution to give

$$k = 4\phi^4 T_{2m}^2$$

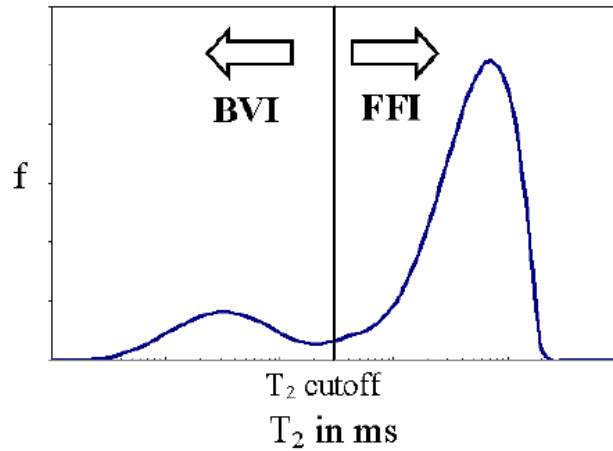
Coates *et al.* developed the Free Fluid Model which estimates the permeability based on the Free Fluid Index (*FFI*) (or free-moving water in the porous media) and the Bulk Volume Irreducible (*BVI*) (or the bound water in the porous media) to give

$$k = 10^4 \phi^4 \left(\frac{FFI}{BVI} \right)^2$$

$$FFI + BVI = \phi$$

For a carbonate T₂ distribution the cut-off between FFI and BVI was taken to be 92ms in the absence of laboratory data.

Figure 107. Distinction between BVI and FFI using T_2 cutoff

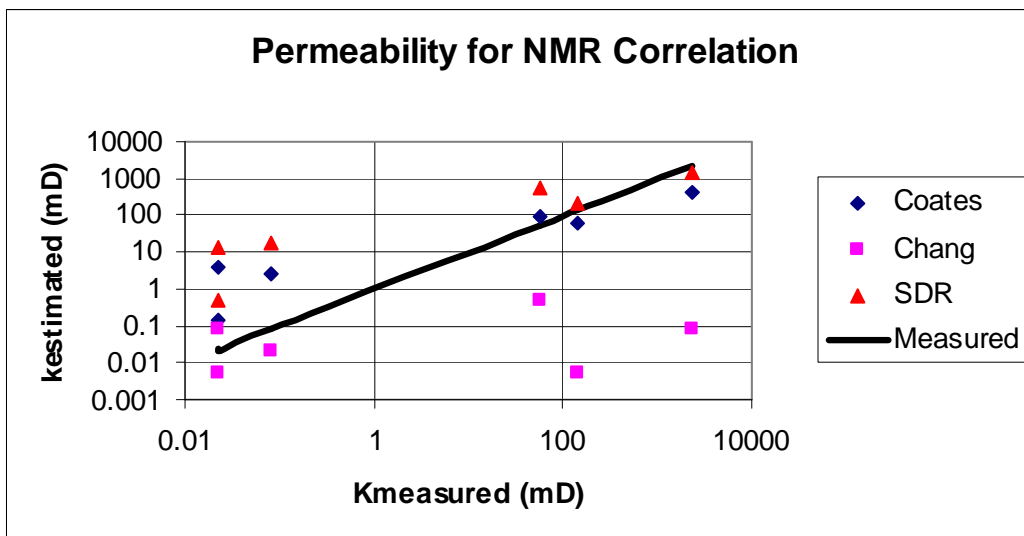


The model by Chang et al., takes the vulgar cut-off of 750 ms and excludes the contribution of vugs to the T_2 log mean used for calculation of permeability. Their correlation gives k from

$$k = 4.75\phi_{750}^4 T_{2lm,750}^2$$

The permeability value estimated from these samples is plotted against the value measured for the samples using single phase brine flood in Figure 108.

Figure 108. Permeability Estimation from NMR T_2 Correlations



The PFG pulse sequence used for measuring D-T₂ maps for samples saturated with brine and crude oil is shown in Figure 109. The subsequent figures 110-115 show the D-T₂ and the T₂ distributions for sample 7626B at S_{wr} before wettability alteration, at S_{wr} after wettability alteration and at S_{or} after brine flood respectively. Similar graphs for Limestone 1 are shown in Figure 116-119 and for Limestone 2 in Figure 120-125.

Figure 109. Pulsed Field Gradient NMR Pulse Sequence

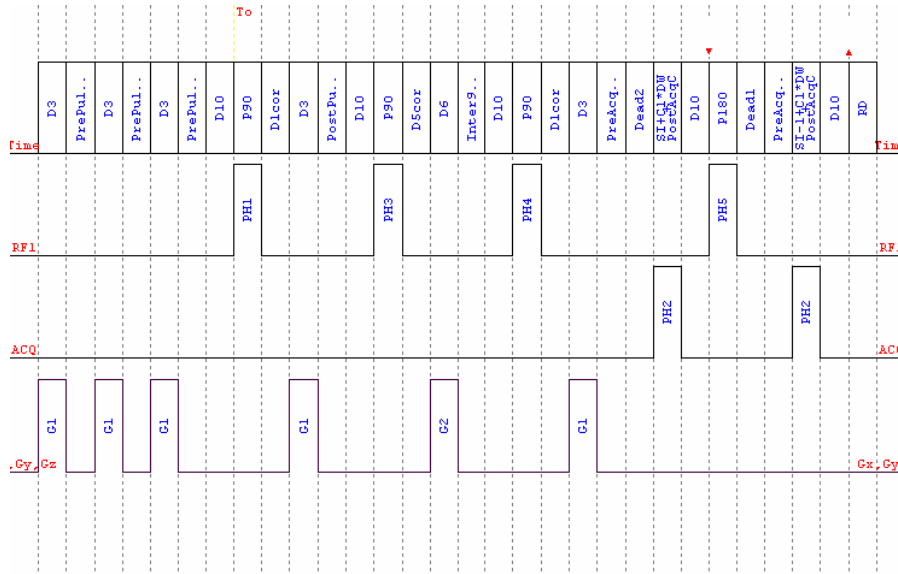


Figure 110. D-T₂ Map for 7626B at S_{wr} before wettability alteration

Stimulated Echo : 7626B t_D = 53.3 ms

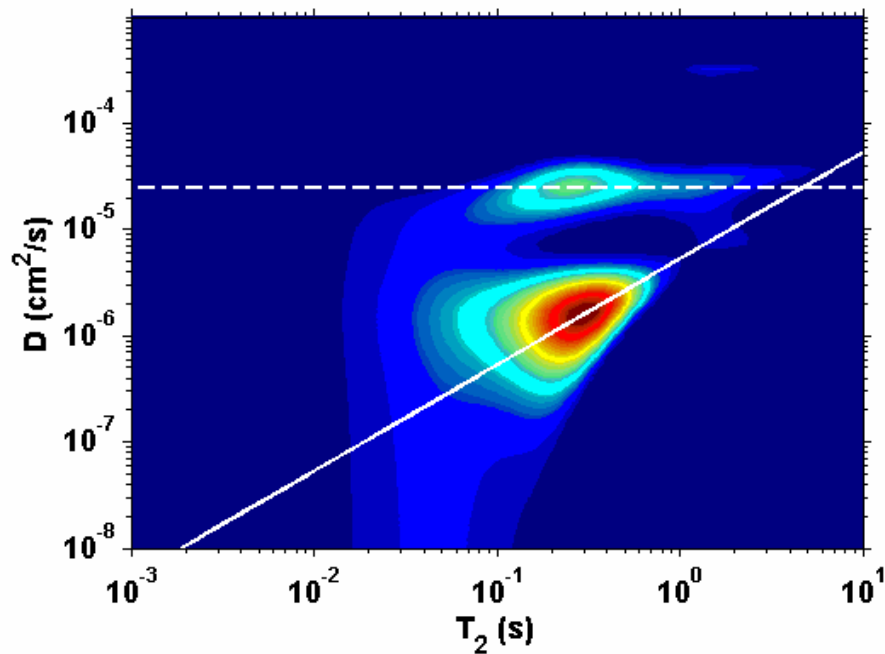


Figure 111. T_2 Distribution for 7626B at S_{wr} before wettability alteration

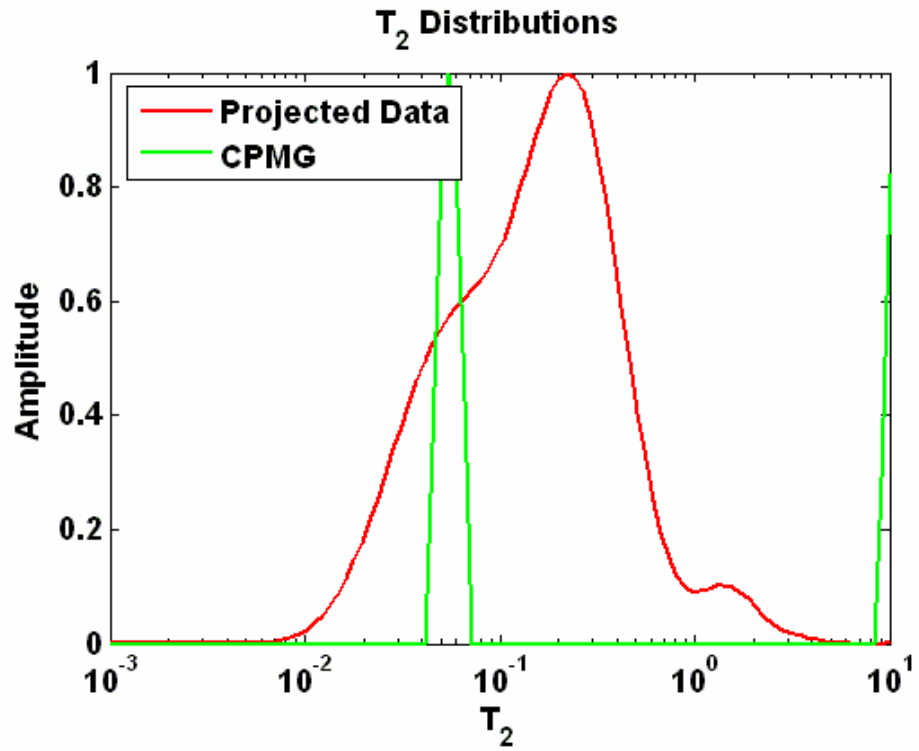


Figure 112. D-T₂ Map for 7626B at S_{wr} after wettability alteration

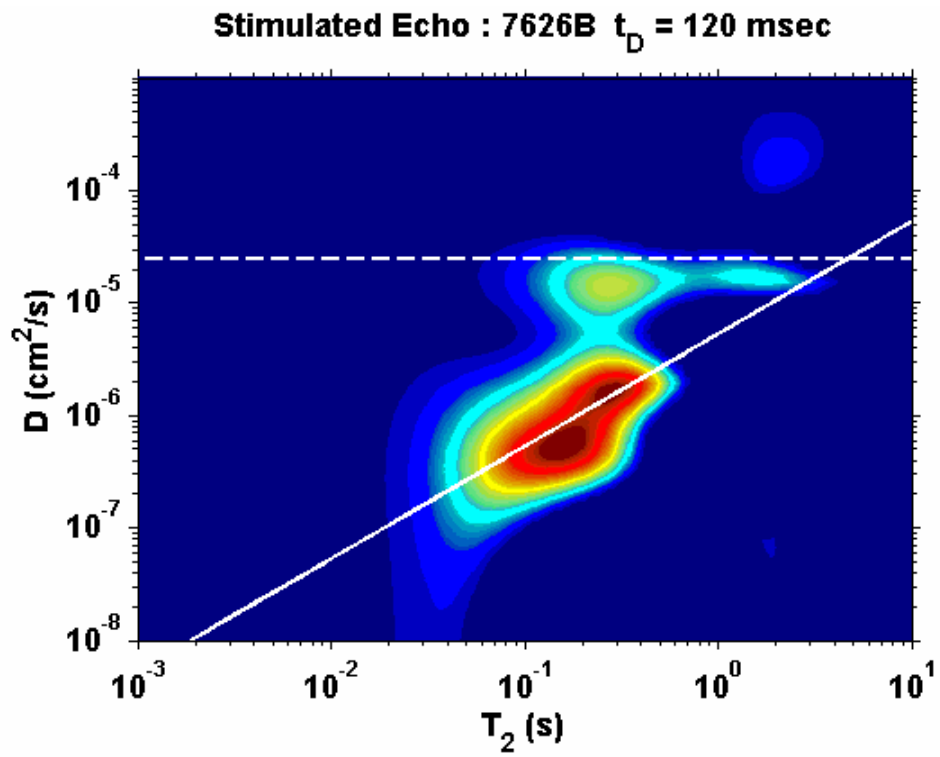


Figure 113. T_2 Distribution for 7626B at S_{wr} after wettability alteration

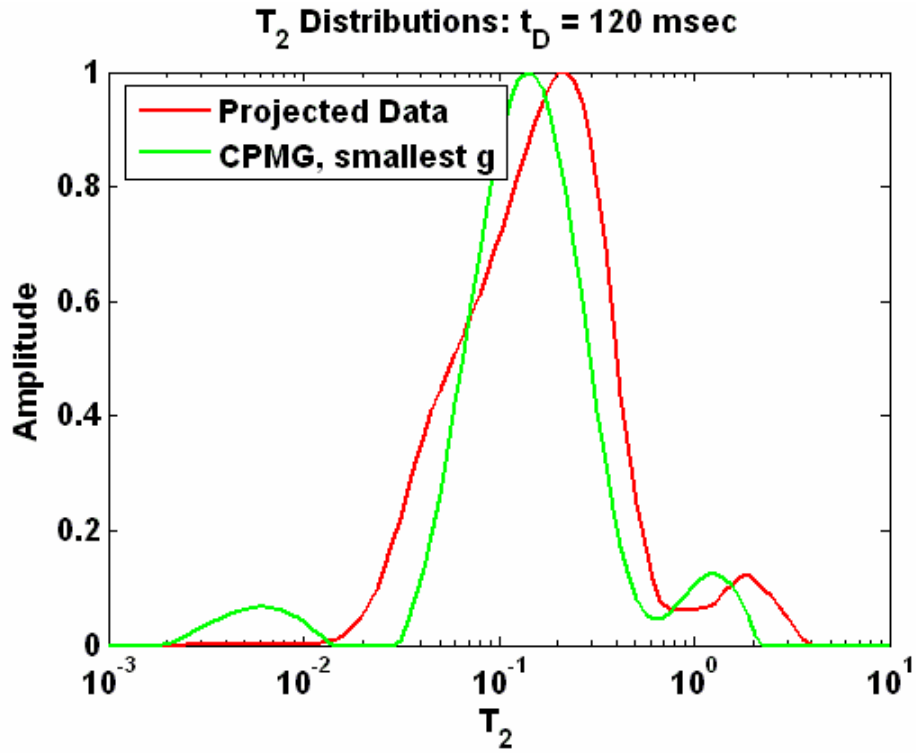


Figure 114. D- T_2 Map for 7626B at S_{or} after brine flood

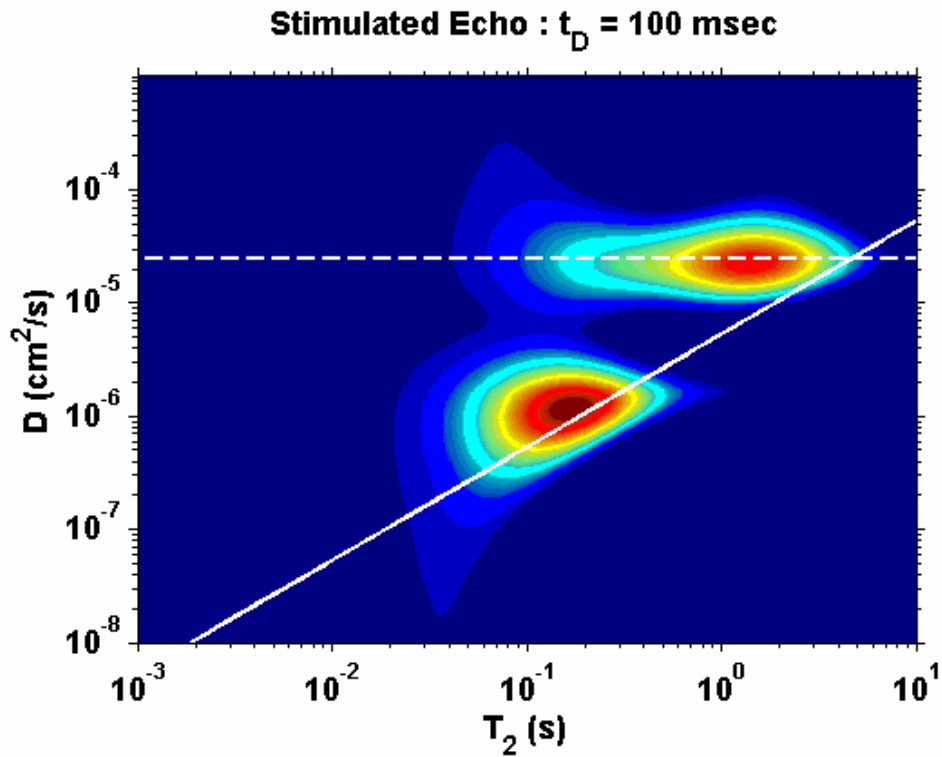


Figure 115. T_2 Distribution for 7626B at S_{or} after brine flood

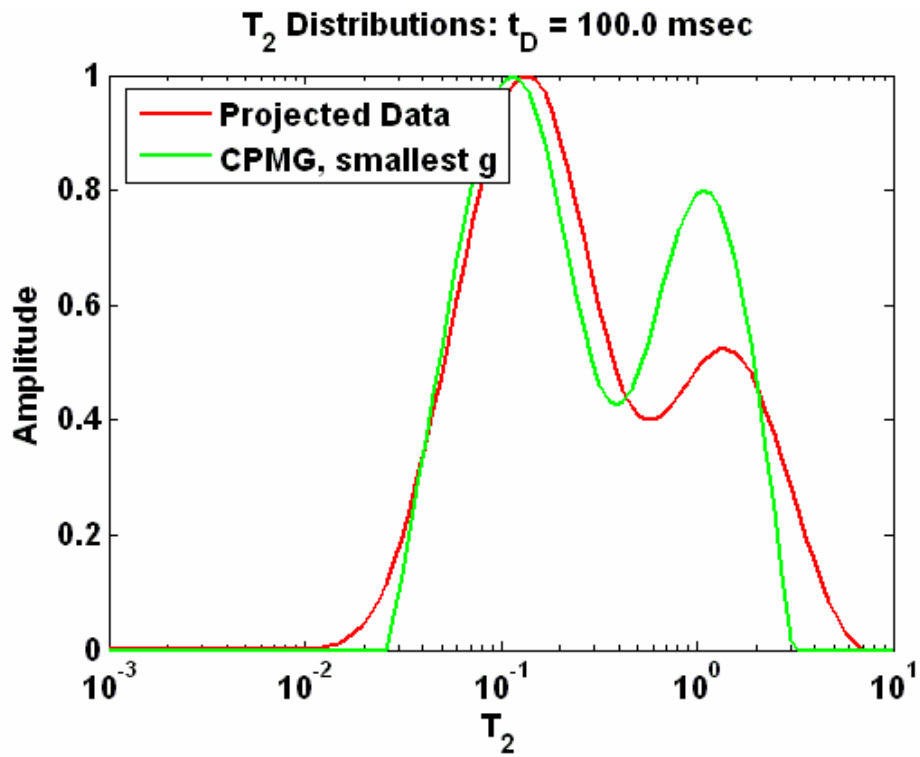


Figure 116. D- T_2 Map for Limestone 1 at S_{wr} before wettability alteration

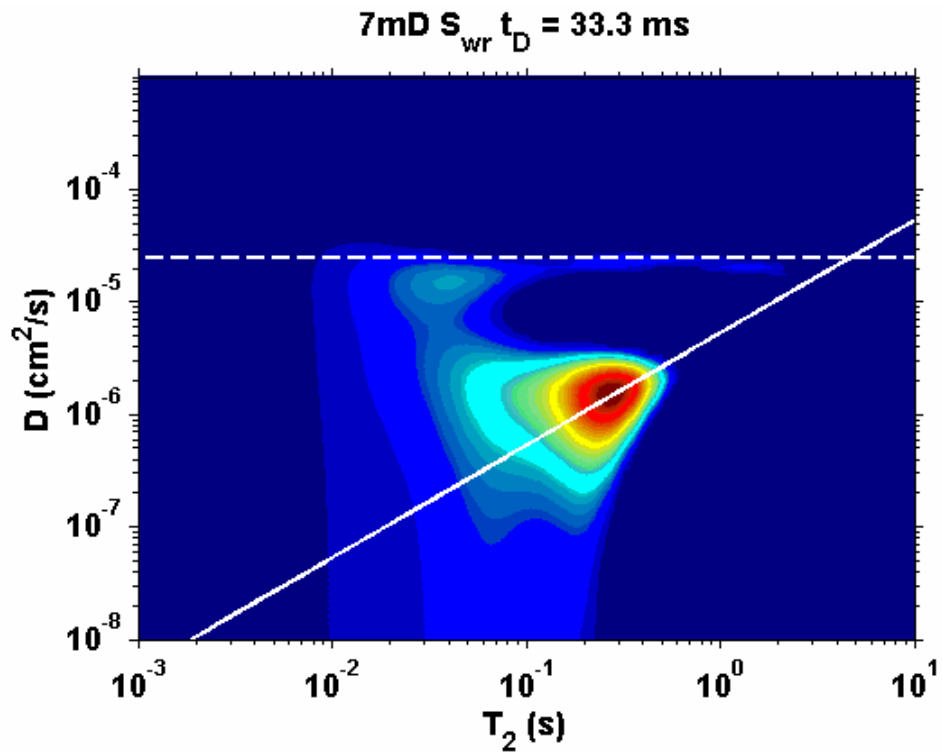


Figure 117. T_2 Distribution for Limestone 1 at S_{wr} before wettability alteration

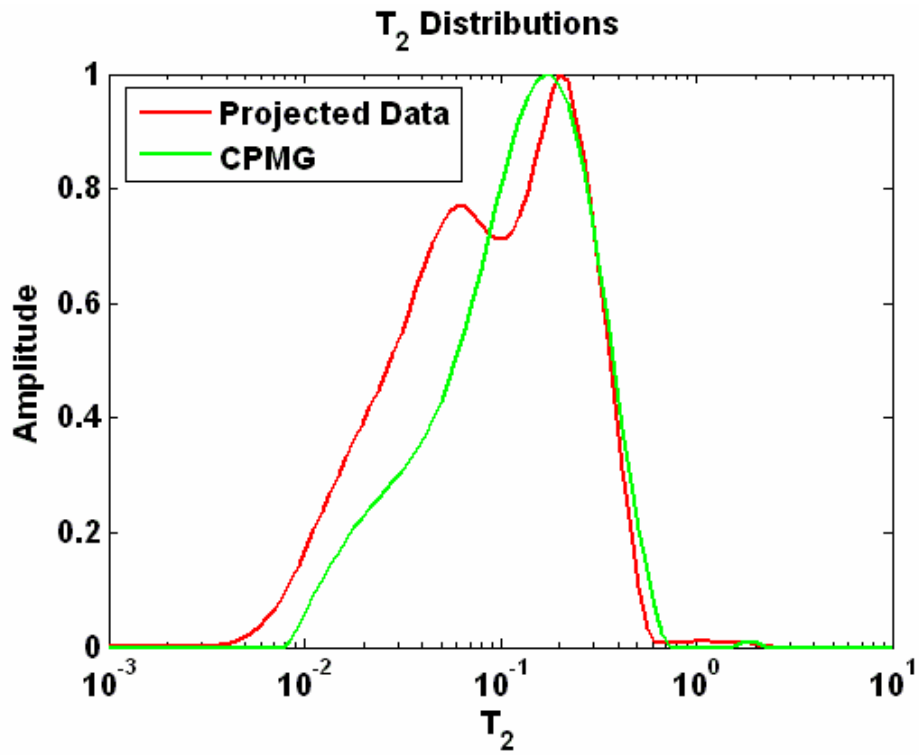


Figure 118. D-T₂ Map for Limestone 1 at S_{wr} after wettability alteration

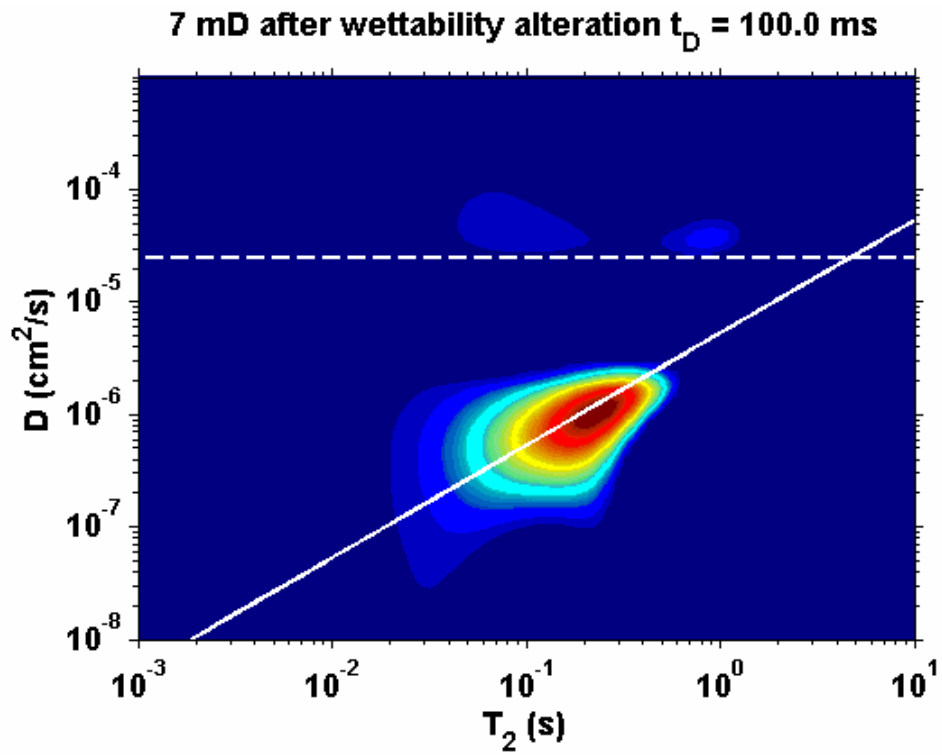


Figure 119. T_2 Distribution for Limestone 1 at S_{wr} after wettability alteration

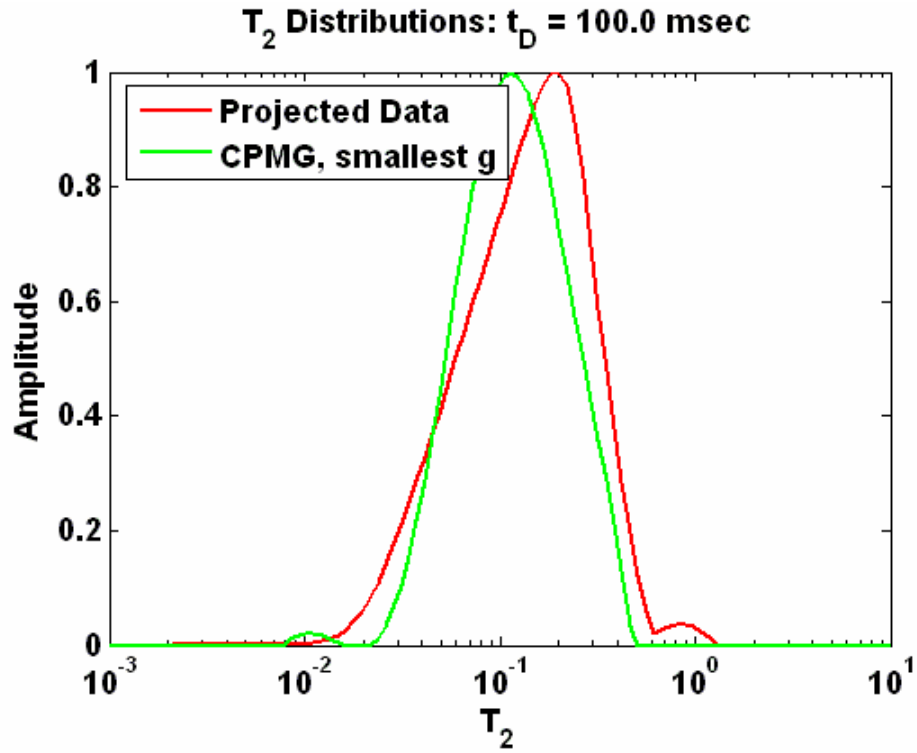


Figure 120. D- T_2 map for Limestone 2 at S_{wr} before wettability alteration

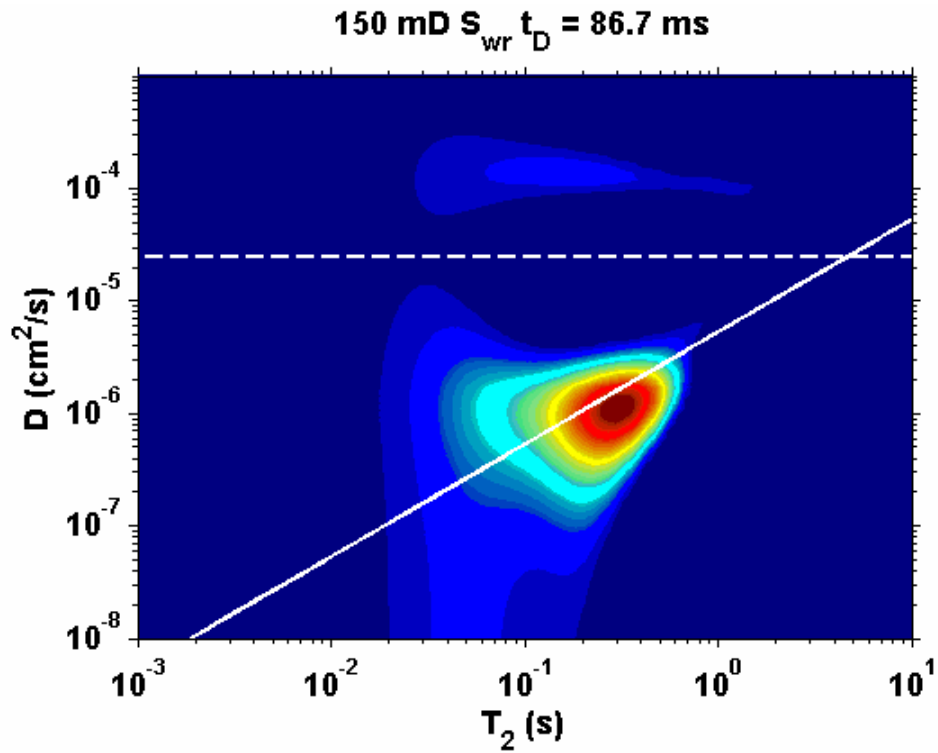


Figure 121. T_2 Distribution for Limestone 2 at S_{wr} before wettability alteration

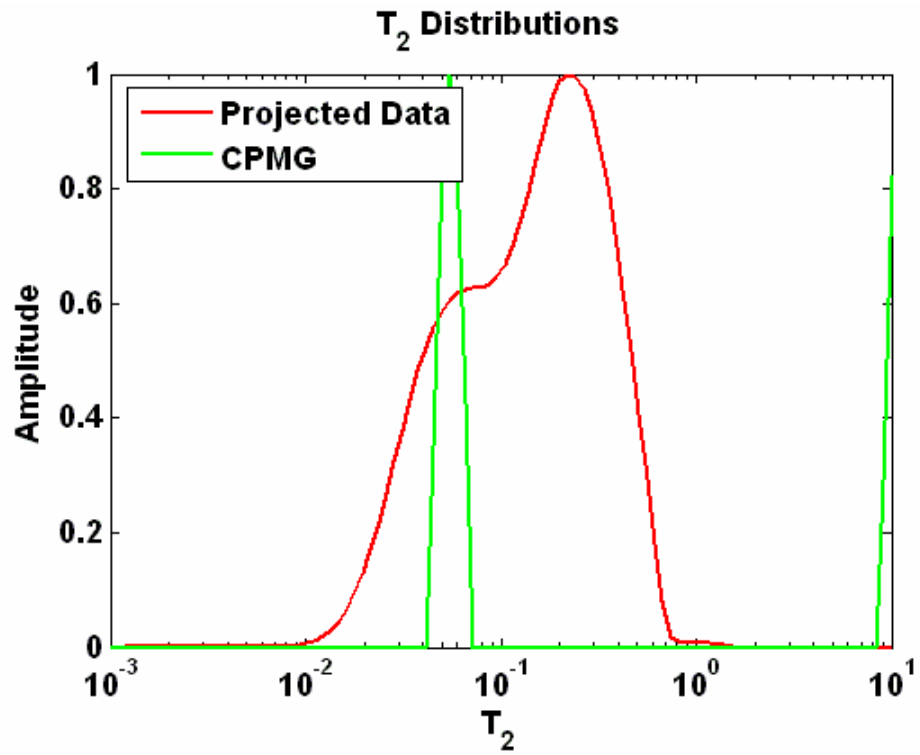


Figure 122. D-T₂ Map for Limestone 2 at S_{wr} after wettability alteration

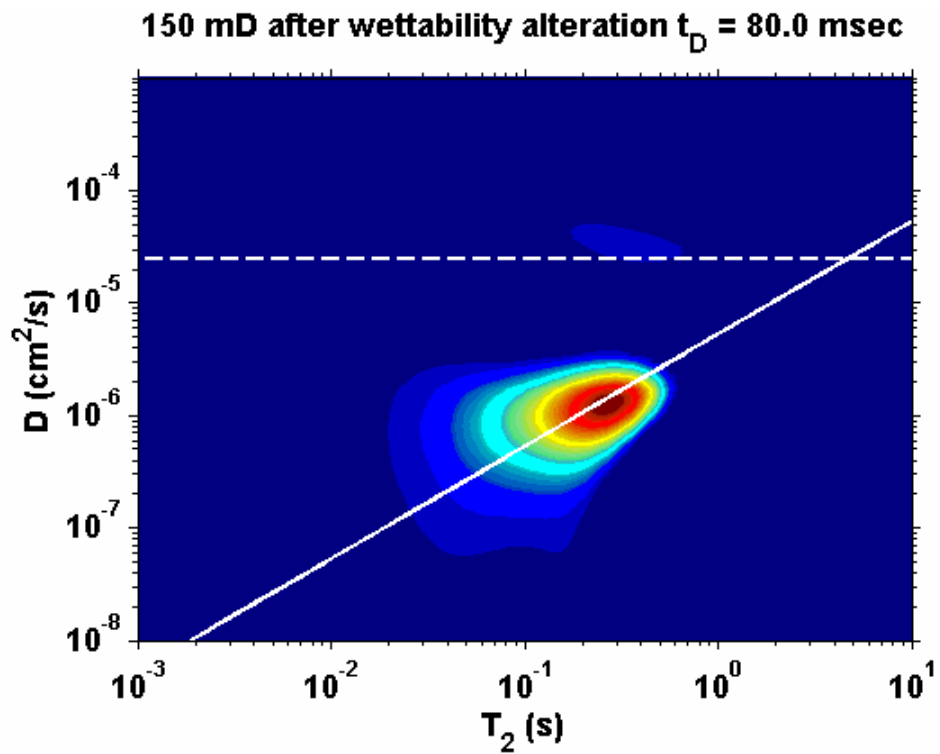


Figure 123. T_2 Distribution for Limestone 2 at S_{wr} after wettability alteration

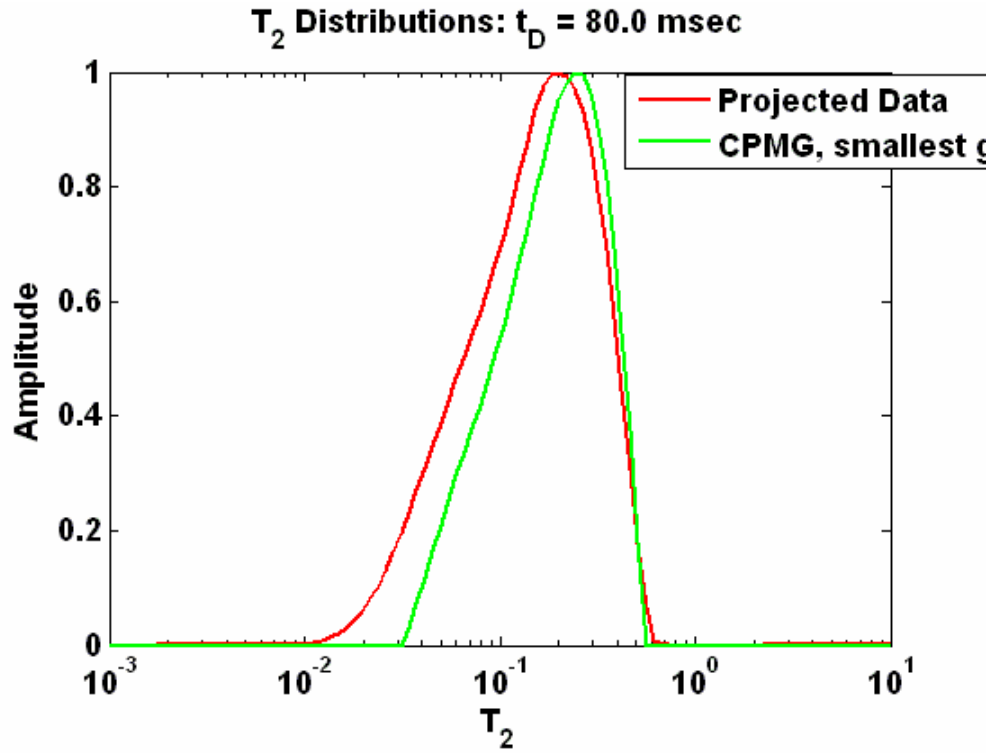


Figure 124. D- T_2 Map for Limestone 2 at S_{or} after brine flood

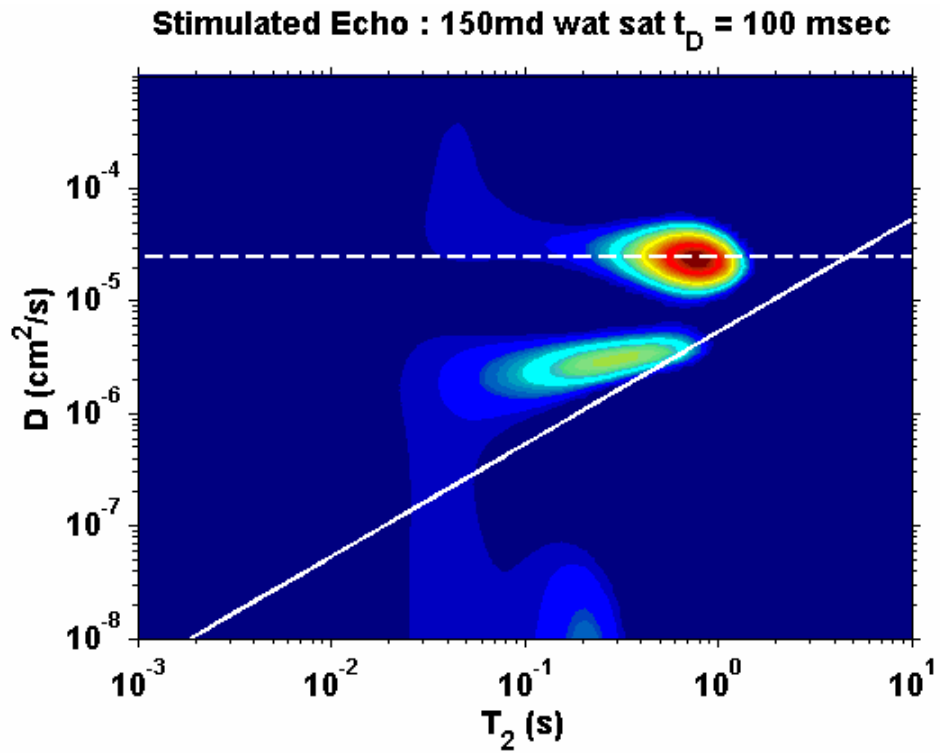
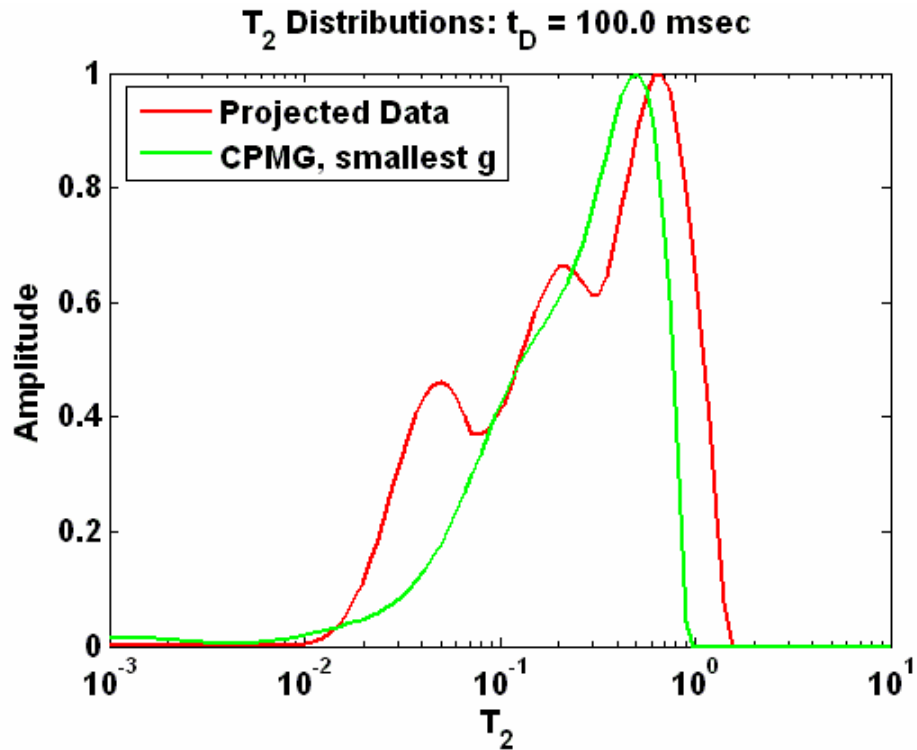


Figure 125. T_2 Distribution for Limestone 2 at S_{or} after brine flood



The T_2 distributions for brine saturated samples 2416, 7536B, 7626A and 7626B are shown in Figures 125-129. These were measured using the CPMG pulse sequence.

Figure 126. T_2 Distribution for Sample 2416 at 100% brine saturation

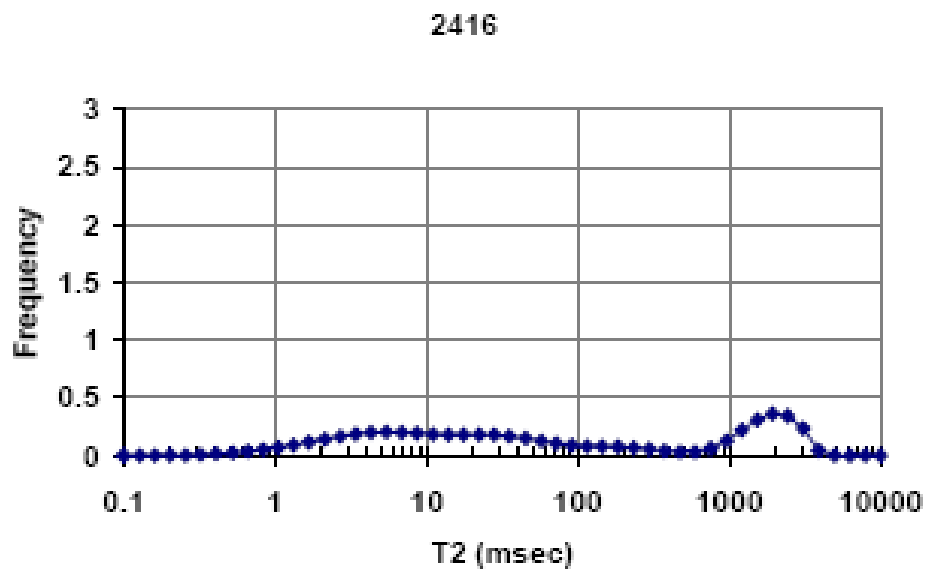


Figure 127. T2 Distribution for Sample 7536B at 100% brine saturation

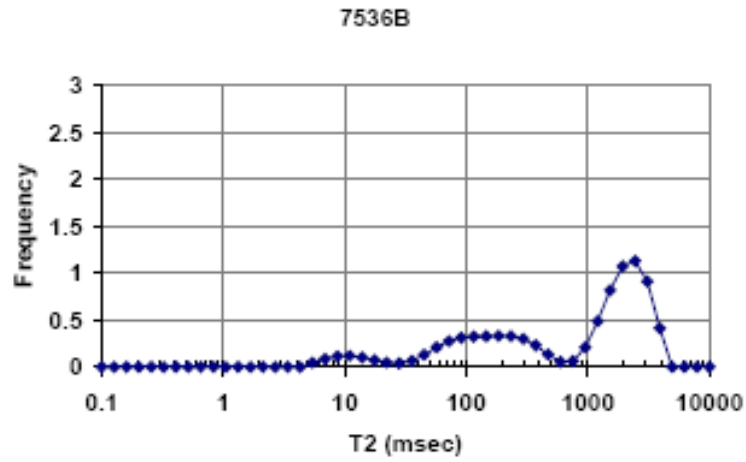


Figure 128. T2 Distribution for Sample 7626A at 100% brine saturation

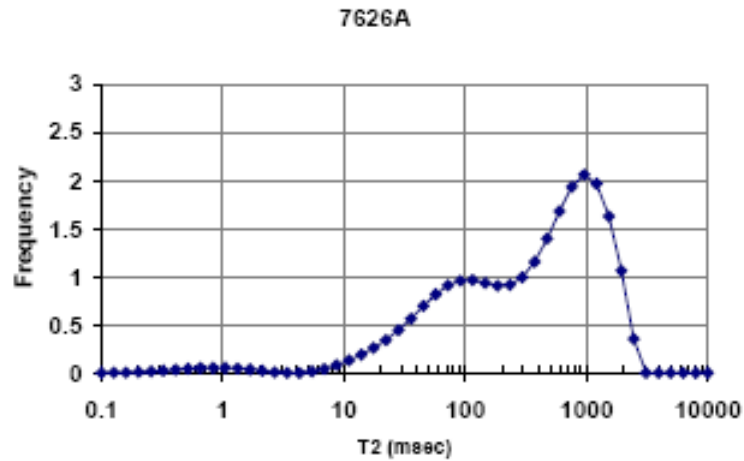
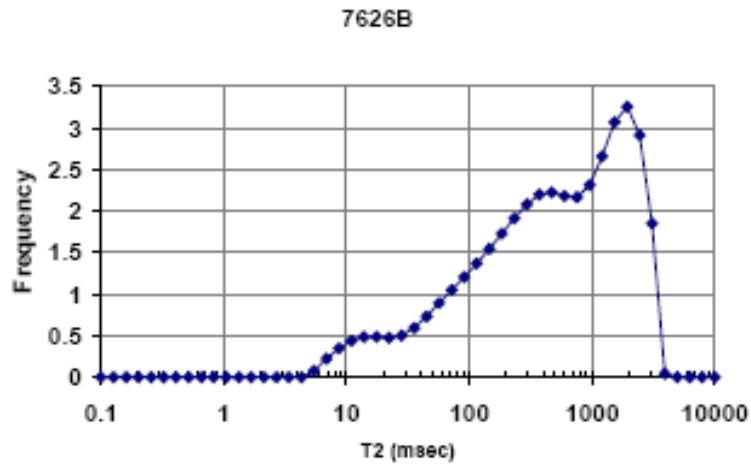


Figure 129. T2 Distribution for Sample 7626B at 100% brine saturation



III. Conclusion

NMR response, relative permeability and electrical conductivity measurements for 3 carbonate samples (Limestone 1, Limestone 2 and 7626B) are completed. The single phase permeability, formation factor and NMR response for the other three samples are measured. Images for the horizontal and vertical thin-sections of all 6 samples have been acquired at three optical resolutions. These have been stitched together to form the composite images and their segmentation into binary images is complete. The statistical analysis comprising of optical porosity, two-point autocorrelation function, lineal path function and chord length is completed. The Fourier Power Spectrum and fractal dimension of images is computed. The 3-D reconstruction of two samples (Limestone 1 and Limestone 2) based on statistical properties from thin-section analysis is completed.

Integrated, Multi-Scale Characterization of Imbibition and Wettability Phenomena Using Magnetic Resonance and Wide-Band Dielectric Measurements

NMR 1-D Profiling

Michael Rauschhuber and George Hirasaki

Abstract

T_2 profiles can be generated by implementing the rapid acquisition with relaxation enhancement (RARE) pulse sequence. The RARE sequence is a multi-echo imaging sequence used to construct a one-dimensional profile of T_2 relaxation times. Experimental parameters, such as sample size, gradient strength and duration, and the number and spacing of the acquired data points, must be selected to ensure that useful information can be extracted from the profiles. The sample must be centered within the Maran's sweet spot. The gradient strength relates the precession frequency to sample position. Attenuation due to diffusion is dependent on the product of gradient strength (g) and duration (δ). Therefore, g and δ should be selected in order to reduce the amount of the relaxation due to diffusion. The dwell time (DW), or spacing between acquired data points, needs to be selected so that the sample plus a small region above and below is resolved by the experiment. The number of data points collected per echo will influence the image resolution; as more points are collected per echo, the resolution will increase. Experiments were performed on both a water sample and a layered water-squalane (C-30 oil, $\mu = 22$ cP) system using the RARE sequence. T_2 was calculated by fitting the decaying profiles to a single exponential model. The difference between the T_2 profiles acquired via RARE and the T_2 of the bulk samples found using CPMG is due to diffusion and thus needs to be minimized.

While standard NMR techniques, such as CPMG or gradient CPMG, tend to look at either the whole sample or only a thin slice, NMR profiling relies on the application of imaging techniques in order to attain spatially resolved measurements. Spatial resolution of properties such as magnetization and relaxation times will allow for the determination of saturation profiles and sample heterogeneities, such as changes in local porosity or pore size distribution. The goal of this project is to develop profiling techniques for a low-field NMR (2 MHz Maran Ultra) allowing for the determination of T_2 as a function of sample position.

Outline of Report

Each section in this report addresses an essential topic for the generation of 1-D NMR profiles. First, the concept that spatial realization can be imparted onto a measurement via frequency encoding gradients will be addressed. Then, the basic spin echo imaging pulse sequence will be introduced as well as the necessary parameter selection in order to generate a single 1-D image. The final topic covered will be the collection of multiple echoes using the rapid acquisition with relaxation enhancement (RARE) to produce a series of profiles from which T_2 can be extracted.

Frequency-Encoding Gradients

Frequency encoding is a standard MR technique used to detect spatial information from a desired sample. In a uniform magnetic field, protons precess at the same frequency, known as the Larmor frequency.

$$f_L = \frac{\gamma}{2\pi} B_0 \quad (0.1)$$

When a magnetic gradient is applied, the intensity of the magnetic field and subsequently, the precession frequency varies with spatial position. For instance, under the application of a linear gradient field, the spatially dependent precession frequency can be represented by

$$f(x) = \frac{\gamma}{2\pi} (B_0 + g_x x) \quad (0.2)$$

or

$$f(x) = f_L + \frac{\gamma}{2\pi} g_x x \quad (0.3)$$

where g_x designates the gradient strength and x denotes position. Therefore, spatial information can be extracted from the sample's various precession frequencies. Consequently, g_x is referred to as a frequency-encoding gradient (Bernstein et al., 2004).

Basic Spin Echo (SE) Imaging Pulse Sequence

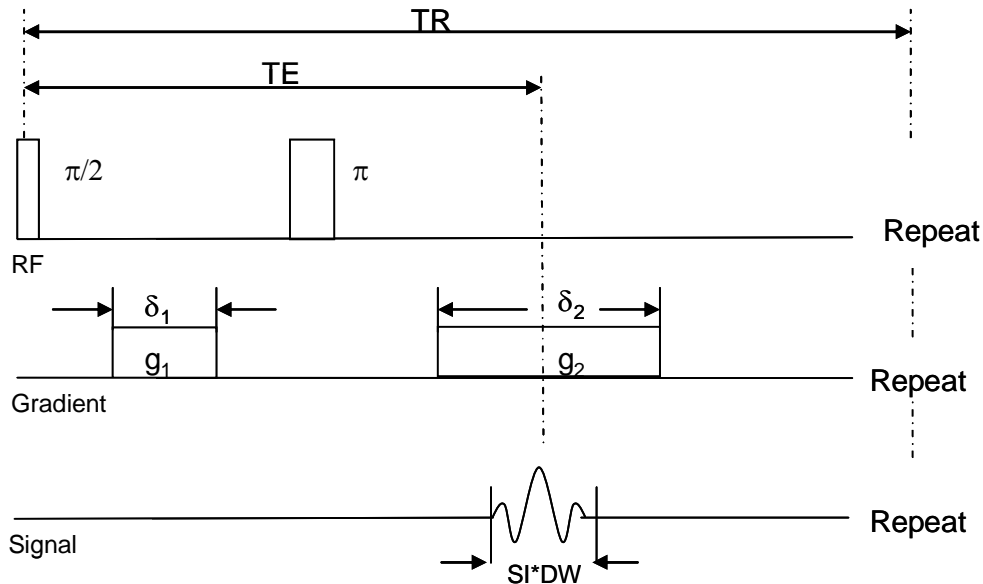


Figure 1 - One Dimensional Profiling Pulse Sequence (PROFILE) (Liang & Lauterbur, 2000)

This sequence is comprised of two gradient pulses, the prephasing and readout pulses, which are separated by a refocusing RF pulse. The prephasing gradient pulse prepares the system for an echo to occur later. The prephasing gradient pulse causes the magnetic field to be stronger at one position than another resulting in non-uniform precession frequencies throughout the sample. Therefore, spin isochromats, regions of constant precession frequency, will begin to precess at different rates and thus get out of phase with the other isochromats. Then, the RF refocusing pulse flips all of the spins by 180° . The subsequent readout gradient pulse plays a similar role as the prephasing gradient pulse, causing different isochromats to gather phase at different rates. The application of the readout gradient pulse after the 180° RF pulse causes the spins to refocus resulting in the formation of an echo (Bernstein et al., 2004).

The temporal location of the echo does not depend on the spacing of the RF pulses, but on the duration and magnitude of the gradient pulses. When the area under the readout pulse equals the area under the prephasing pulse, the echo will reach its maximum amplitude (Bernstein et al., 2004). A one dimensional profile is then attained by performing a fast Fourier transform (FFT) reconstruction of the acquired signal (Liang & Lauterbur, 2000). For instance, a collected echo is depicted in Figure 2 and its corresponding 1-D profile in Figure 3. Note that the scale of the ordinate in Figure 3 is in centimeters not Hertz; the conversion between the two is made via the linear relationship described in equation (1.4).

$$f - f_{Larmor} = \frac{\gamma}{2\pi} g_x (x - x_{Larmor}) \quad (0.4)$$

where x_{Larmor} corresponds to the sample height at which $f = f_{Larmor}$.

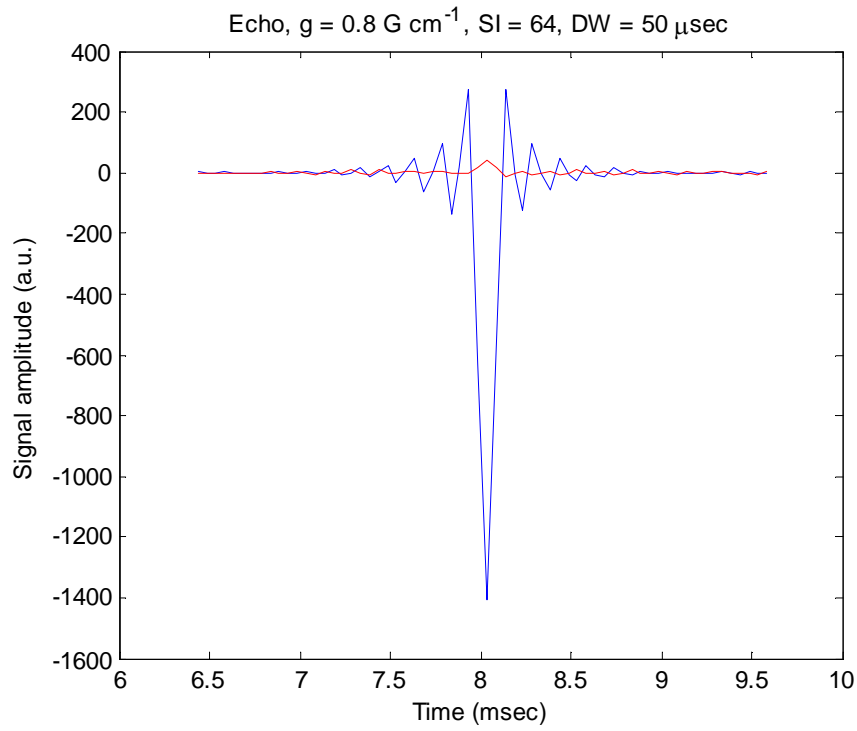


Figure 2 - Collected Echo for a Water Sample with a height of 4 cm.

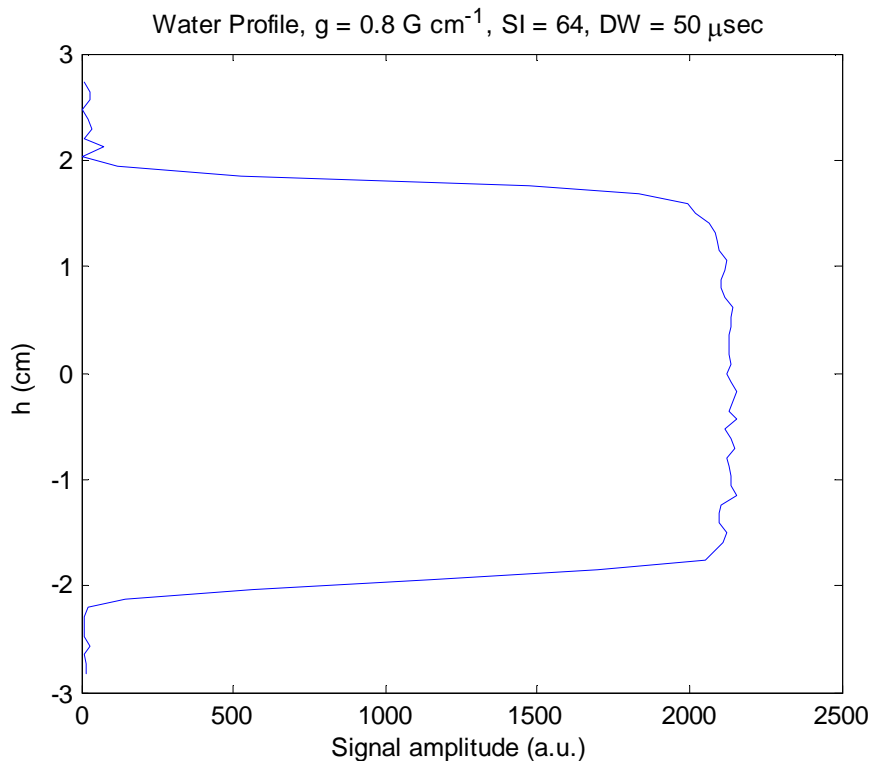


Figure 3 - Profile of 4 cm water sample generated after FFT reconstruction of the collected echo.

Parameter Selection

NMR 1-D Profiles are sensitive to the selected measurement parameters. These include the sample size and location, the gradient strength (g) and duration (δ), and the number (S) and spacing (DW) of the collected data points.

Sample Size and Location

The sample should be located within the sweet spot of the NMR and centered about f_{Larmor} . In order to determine the size and location of the sweet spot, a series of FID experiments were performed with water. The water sample has a height 0.5 cm and was moved in 0.5cm increments through the probe; an FID was performed at each location. The results are illustrated in Figure 4. From these results, it was determined the sweet spot was about 5 cm long. Therefore, for all subsequent measurements, the sample will be located within the sweet spot and have a height of 4 cm.

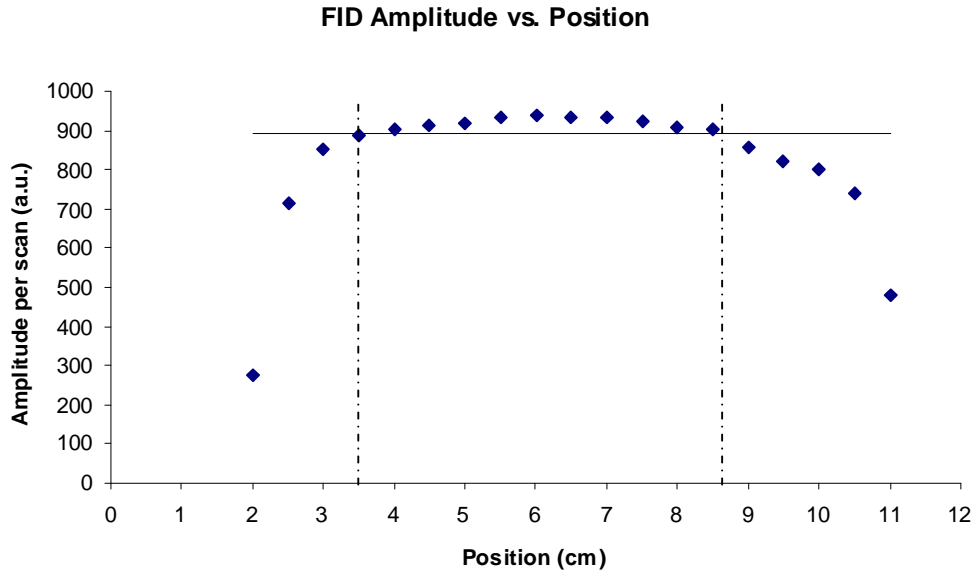


Figure 4 – Results of a series of FID experiments performed on a 0.5 cm sample of water used to determine the sweet spot of the MARAN-M. The horizontal line denotes a 5% percent deviation from the maximum amplitude.

Gradient Strength

The gradient used for imaging should be the lowest value that will give reliable results. Strong gradients can cause attenuation due to diffusion. However, this effect can be minimized by selecting to use weaker gradients. Therefore, it is necessary to properly characterize the behavior of the gradient over a range of values. For instance, at very low gradients, the expected behavior deviates from what is observed. By using a low, reliable gradient strength, 0.800 G cm^{-1} , attenuation due to diffusion can be reduced.

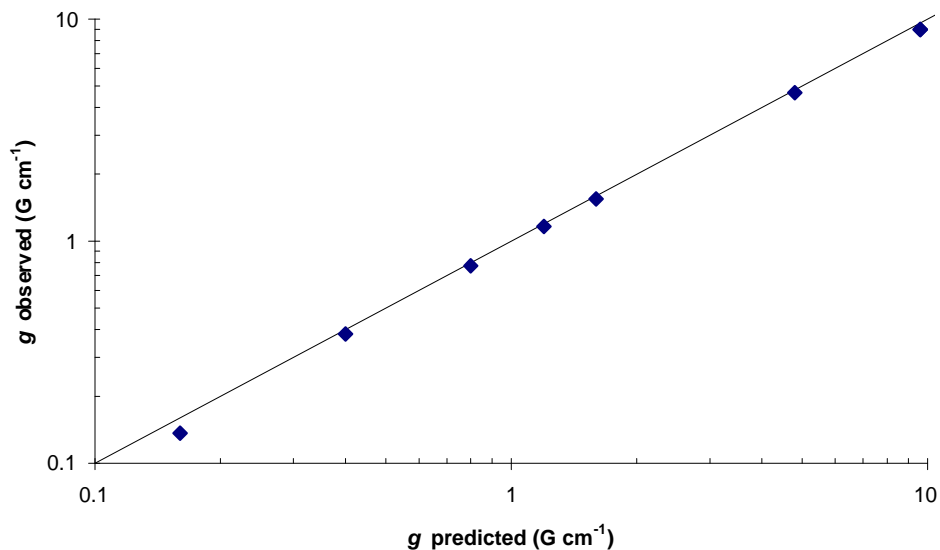


Figure 5 - Observed vs. Predicted behavior of the MARAN-M's gradient. Deviations are observed at very low values of g .

Dwell Time

The dwell time (DW), or the spacing between the acquired data points, should be selected to acquire data over the length of the sample and a small distance beyond. If the dwell time is too short, the distance which the measurement can identify is much longer than the length of the sample (Figure 6).

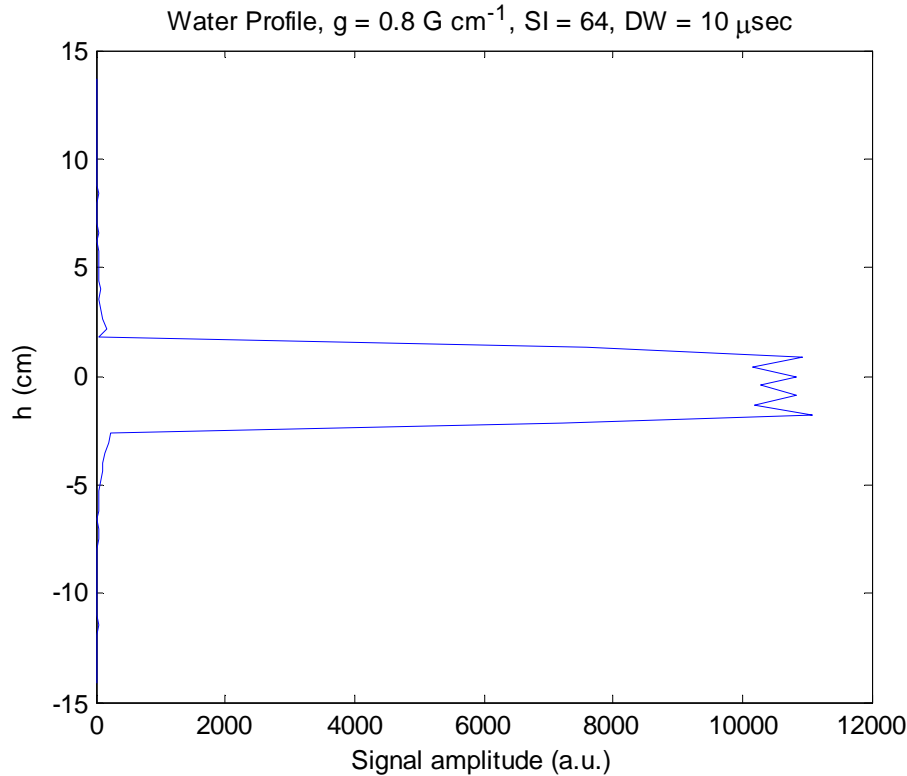


Figure 6 – Improper selection of DW. The measurement resolved a length much greater than the sample height.

The dwell time can be determined from the size of the sample and the strength of the gradient pulses used, and equation (1.6) gives a means of calculating an appropriate DW. This equation is based on the Nyquist sampling theorem which states that the sampling rate, SR, should be at least twice the maximum frequency encoded in the signal where the maximum encoded frequency, f_{max} , corresponds to half the sample height plus a small distance outside for a centered sample (Bernstein et al., 2004). If this criterion is not met, aliasing can occur.

$$SR = \frac{1}{DW} = 2f_{\max} \quad (0.5)$$

$$DW = \frac{1}{2f_{\max}} = \frac{1}{2\left(\frac{\gamma}{2\pi} g_x \frac{h_s + h_\epsilon}{2}\right)} = \frac{2\pi}{\gamma g_x (h_s + h_\epsilon)} \quad (0.6)$$

where h_s is the sample height and h_ϵ is the length outside of the sample to be measured. For example, Figure 7 depicts a profile in which the dwell time has been chosen so that the sample plus about half a centimeter above and below the sample is resolved. Note that only DW has changed between Figure 6 and Figure 7.

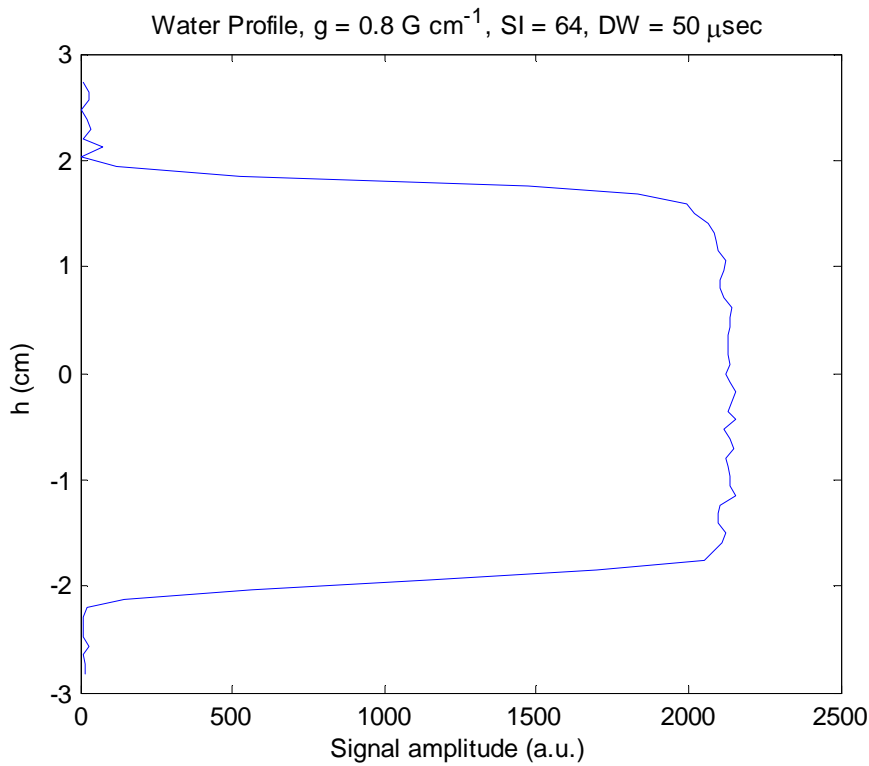


Figure 7 - Dwell time selected so that the sample plus an excess of about half a centimeter above and below the sample is measured. All other parameters remain the same as the profile depicted in Figure 6.

Number of Acquisition Points

The number of acquisition point (SI) is also a vital parameter when performing a profiling measurement. While DW determined the range of frequencies resolved, SI governs the number of points spanning that range. Therefore, increasing SI increases the image resolution.

$$resolution \left[\frac{points}{cm} \right] = \frac{SI}{h_s + h_e} \quad (0.7)$$

$$(h_s + h_e) = \frac{2\pi}{\gamma g DW} \quad (0.8)$$

$$resolution \left[\frac{points}{cm} \right] = \frac{\gamma g DW (SI)}{2\pi} \quad (0.9)$$

However, acquisition must occur under a gradient and is therefore limited by the readout gradient duration (δ_2). Therefore, the duration of the gradient pulse must be greater than or equaled to the product of SI and DW (Eq. 1.10). Increasing the gradient duration to accommodate more points will increase resolution at the cost of greater attenuation due to diffusion.

$$\delta_2 \geq SI(DW) \quad (0.10)$$

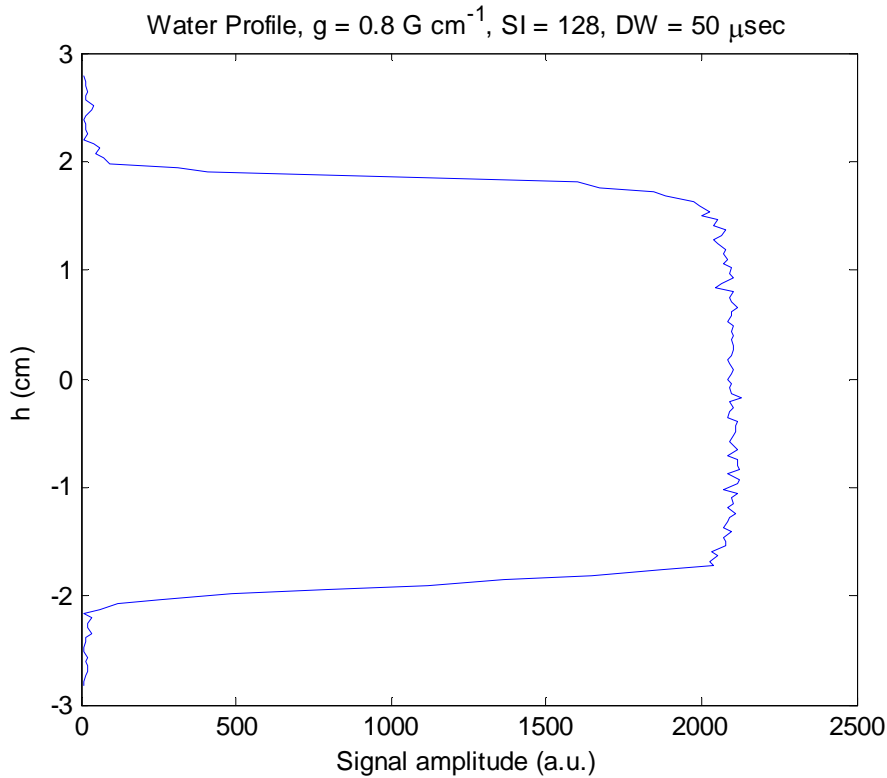


Figure 8 – Increasing SI increases the resolution of the profile. The only parameter changed from Figure 7 to this figure was SI from 64 (Figure 7) to 128. Resolution has been increased from $2.2 \text{ points cm}^{-1}$ (Figure 7) to $4.4 \text{ points cm}^{-1}$.

Therefore, several parameters must be appropriately chosen when performing profiling measurements. The gradient strength determines the range of encoded frequencies (equation(0.4)), but the use of strong gradient pulses results in greater attenuation due to diffusion. Therefore, weak gradients can be implemented to diminish the effect of diffusion. Once the gradient strength has been selected, the dwell time can be determined using equation(0.6). Then the number of acquisition points, SI , can be selected based on the desired resolution of the image, equation

Image Contrast

Image contrast is a technique which can be used to help differentiate fluids with varying relaxation times. Three types of contrast methods are readily applicable to this pulse sequence: spin-density, T_1 -weighting, and T_2 -weighting. The easiest way to understand how to generate an image with the desired contrast method is to first consider the magnetization equation. For the previously described basic spin echo imaging pulse sequence, the magnetization is described by equation (1.11).

$$M = M_0 \left[1 - \exp\left(\frac{-T_R}{T_1}\right) \right] \left[\exp\left(\frac{-T_E}{T_2}\right) \right] \quad (0.11)$$

where T_E is the time at which the echo center occurs and T_R is the repetition time between scans (Liang & Lauterbur, 2000). Therefore, the parameters T_E and T_R can be selected in such a manner so that the profile is representative of M_0 or is either weighted by the T_1 or T_2 terms. In Table 1, guidelines for selecting T_E and T_R for a given method of contrast are given.

Table 1 - Parameters for desired image contrast (Liang & Lauterbur, 2000)

T_A : relaxation time of fast relaxing component

T_B : relaxation time of slow relaxing component

| Method of Contrast | T_E | T_R |
|---------------------------|-------------------------|-------------------------|
| Spin Density | $T_E \ll T_A$ | $T_R > T_B$ |
| T_1 -weighted | $T_E \ll T_A$ | $T_B > T_R > T_A$ |
| T_2 -weighted | $T_A < T_E < T_B$ | $T_R \gg T_B$ |

For T_1 contrast, selection of T_R should allow for one fluid to be fully polarized while the other is only partially polarized. Similarly, for T_2 contrast, the proper choice of T_E allows for greater relaxation of one fluid than the other. The difference between the various contrast methods are illustrated in the figures below. All profiles are of the same layered water ($T_2 = 2.80$ sec) and squalane ($T_2 = 120$ msec) system, and the only parameters varying are T_E and T_R . Figure 9 represents a spin-density image. The two phases cannot be distinguished from

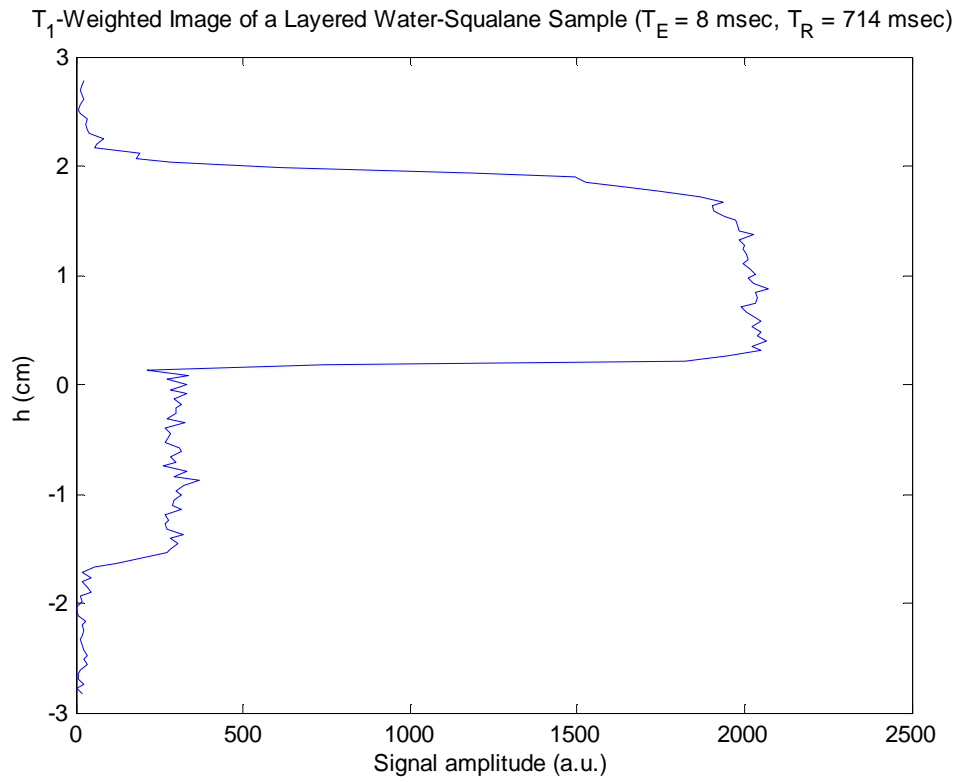


Figure 10 – T_1 -weighted image of a layered water and squalane system

T_2 -Weighted Image of a Layered Water-Squalane Sample ($T_E = 140$ msec, $T_R = 15,000$ msec)

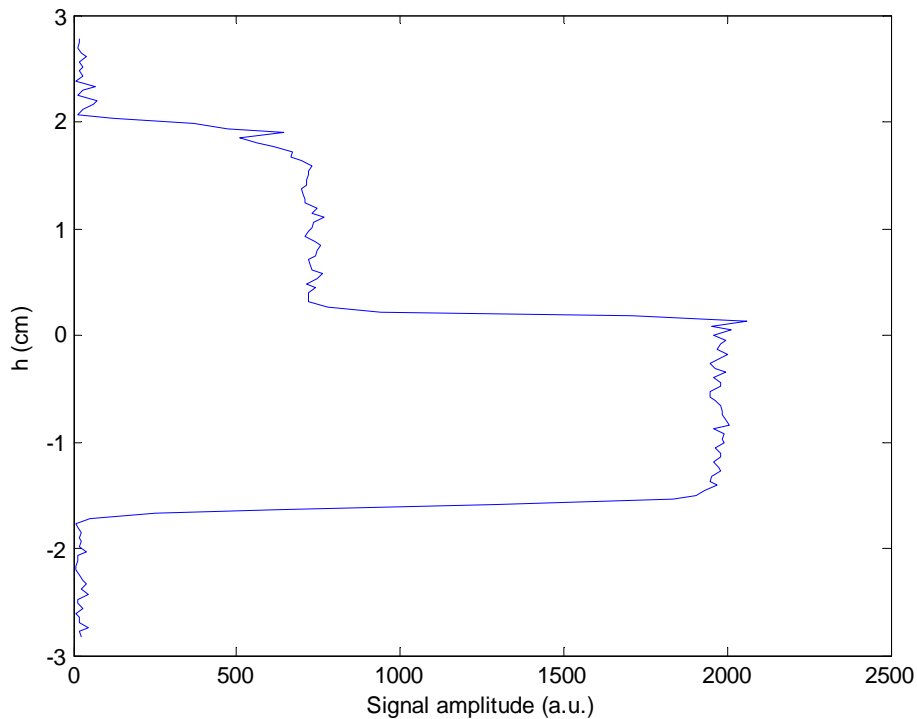


Figure 11 – T_2 -weighted image of a layered water and squalane system

T_2 Profiling via Rapid Acquisition with Relaxation Enhancement (RARE)

The rapid acquisition with relaxation enhancement pulse sequence (RARE) is a CPMG-style extension of the one dimensional profile measurement first proposed by Henning et al (1986). It is commonly used for clinical imaging, but modifications to the sequence must be made in order to accommodate the use of a MARAN. Presented below is a schematic of the pulse sequence created for the MARAN.

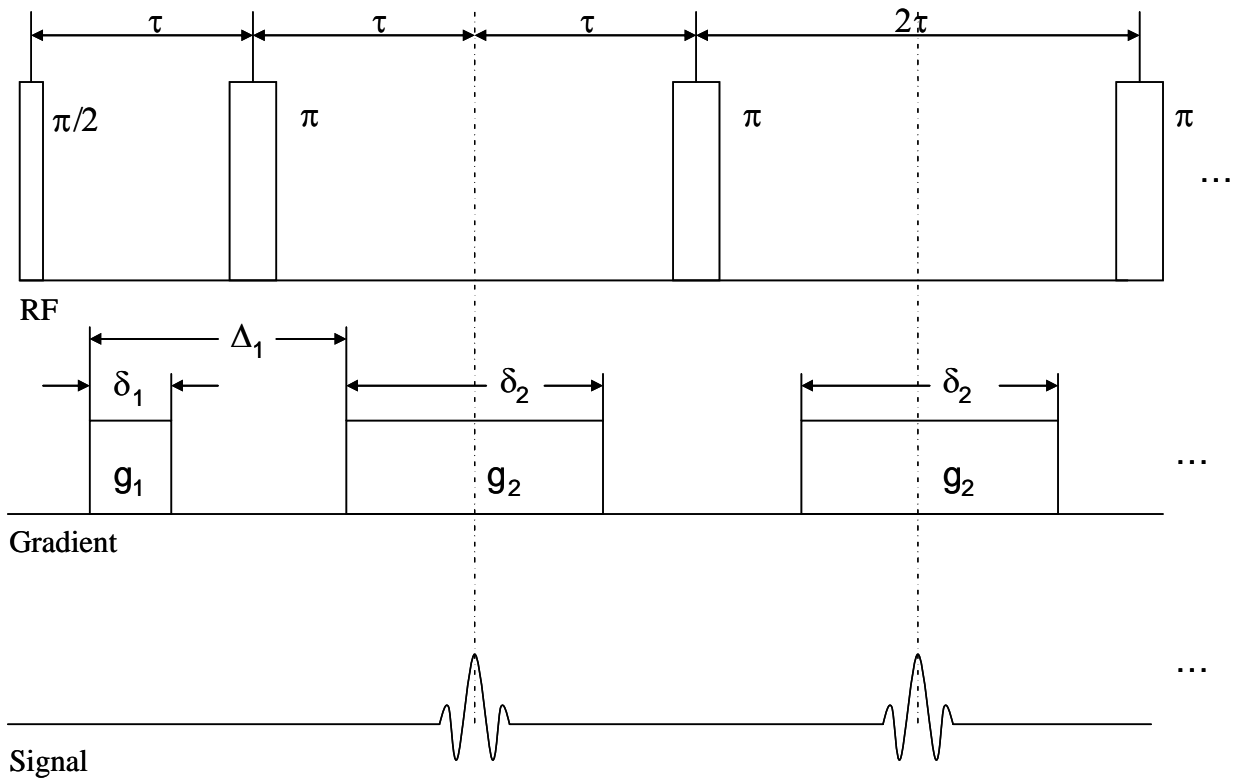


Figure 12 - RARE Pulse Sequence Diagram (Bernstein et al., 2004)

In the above schematic, the first gradient pulse is known as the prephasing pulse and all subsequent gradient pulses are referred to as readout or imaging pulses. Both pulses play analogous roles as their counterparts in the one dimensional profiling pulse sequence with one significant exception. As in the profiling sequence, the temporal location of the echo occurs when the area of the readout pulse is equivalent to the area under the prephasing pulse. Therefore, the remainder of the readout pulse acts as a prephasing pulse for the next echo. Resulting from this fact stems a careful balance between the two gradient pulses. In other words, the readout pulse should have twice the area of the prephasing pulse. In Figure 12, note that $2g_1\delta_1 = g_2\delta_2$.

The Fourier transform can be taken for each individual echo to obtain a series of one-dimensional profiles. The attenuation in the signal is also observable in the profiles. Therefore, the goal behind using such a sequence is to take advantage of the frequency encoding gradients and extract T_2 information as a function of position within the sample. A series of profiles with an increasing amount of T_2 relaxation generated by the RARE sequence is shown in Figure 13.

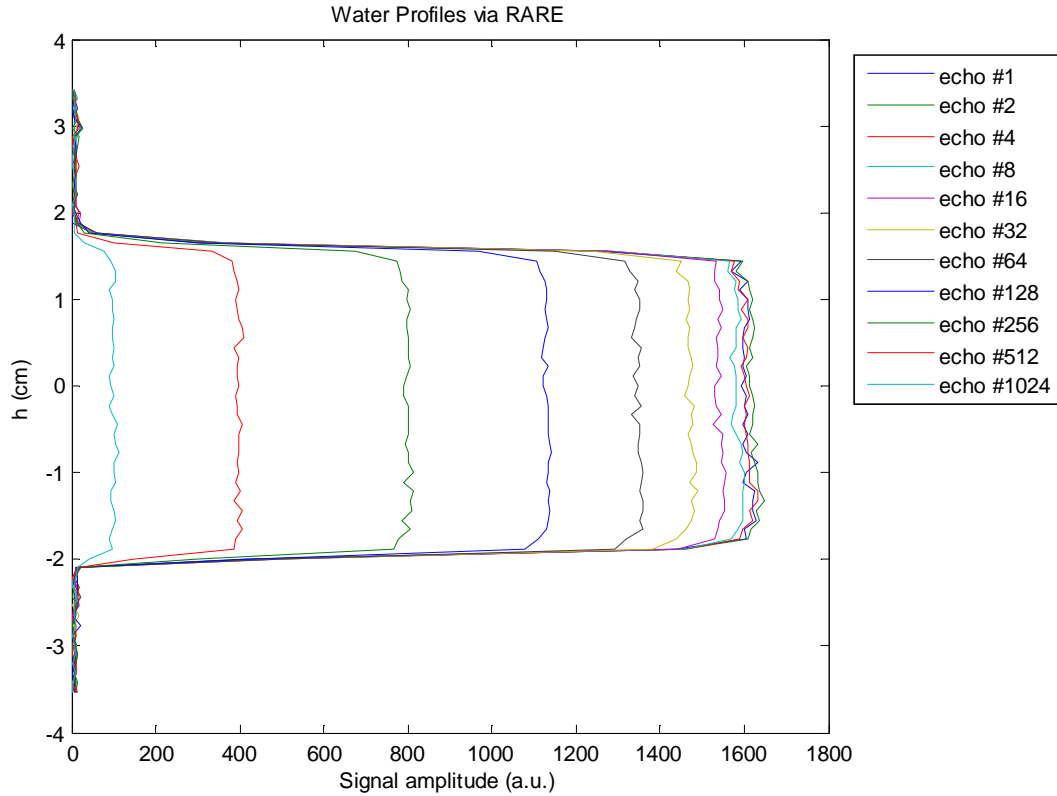


Figure 13 – RARE Profiles of a water sample with a 4 cm height. $g_1 = g_2 = 0.800 \text{ cm}^{-1}$, $\delta_1 = 1.30 \text{ msec}$, $\tau = 3.00 \text{ msec}$, $DW = 40.0 \text{ msec}$, $SI = 64$

Effect of Diffusion

Due to the presence of multiple gradient pulses, attenuation due to diffusion can become significant. Therefore, it is necessary to develop a suitable model describing the attenuation in terms of the relevant parameters of the pulse sequence. Callaghan (1991) suggests that one method which can be used to determine the effect of self-diffusion is the application of the Bloch-Torrey equations. In the rotating reference frame, the effect of self-diffusion and velocity on the transverse magnetization, M_T , can be represented by (Torrey, 1956)

$$\frac{\partial M_T}{\partial t} = -i\gamma \mathbf{r} \cdot \mathbf{g} M_T - \frac{M_T}{T_2} + D \nabla^2 M_T - \nabla \cdot \mathbf{v} M_T \quad (0.12)$$

With the solution (Stejskal and Tanner, 1965)

$$M_T(\mathbf{r}, t) = A(t) \exp \left[-i\gamma \mathbf{r} \cdot \int_0^t \mathbf{g}(t') dt' \right] \exp \left(\frac{-t}{T_2} \right) \quad (0.13)$$

At the echo center, $\int_0^t \mathbf{g}(t') dt'$ is equal to zero. Therefore, equation (0.13) reduces to

$$M_T(\mathbf{r}, t) = A(t) \exp \left(\frac{-t}{T_2} \right) \quad (0.14)$$

Substituting equation (0.14) into equation (0.12) yields an expression for $A(t)$.

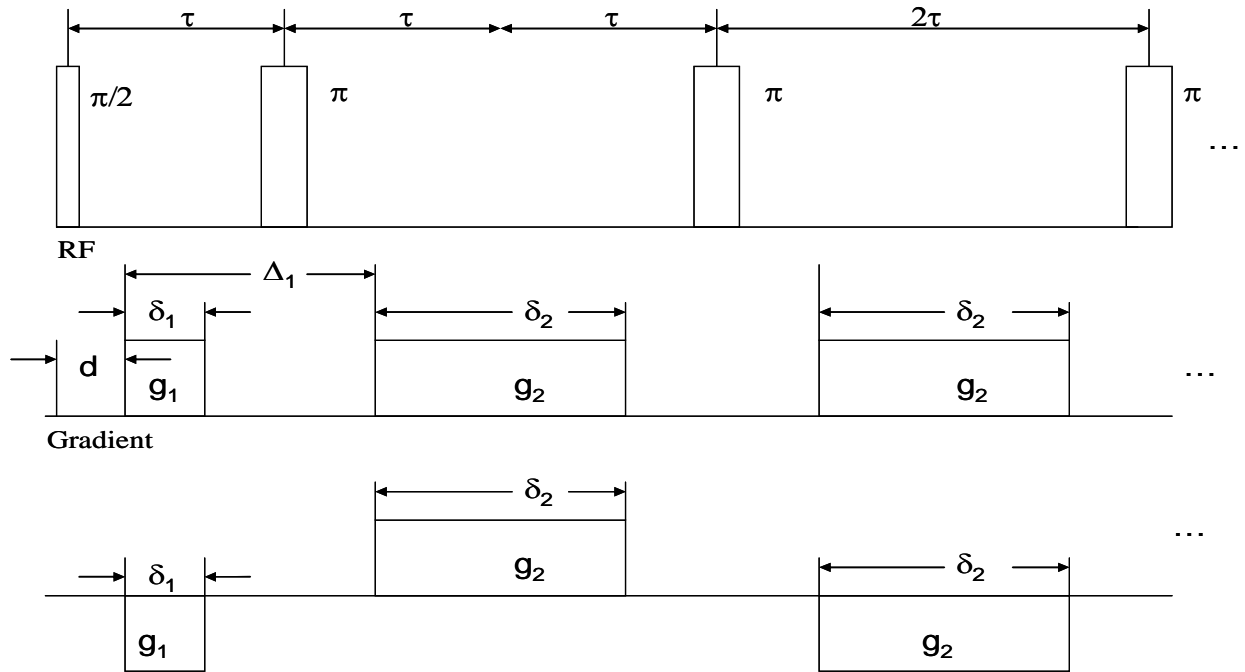
$$\frac{\partial A(t)}{\partial t} = -D\gamma^2 \left(\int_0^t \mathbf{g}(t') dt' \right) \exp \left(\frac{-t}{T_2} \right) \quad (0.15)$$

$$A(t) = \exp \left[-D\gamma^2 \int_0^t \left(\int_0^{t'} \mathbf{g}(t'') dt'' \right)^2 dt' \right] \exp \left[i\gamma \mathbf{v} \cdot \int_0^t \left(\int_0^{t'} \mathbf{g}(t'') dt'' \right) dt' \right] \quad (0.16)$$

If there is no flow, this expression can be reduced to

$$A(t) = \exp \left[-D\gamma^2 \int_0^t \left(\int_0^{t'} \mathbf{g}(t'') dt'' \right)^2 dt' \right] \quad (0.17)$$

This formulation neglects the presence of RF pulses. However, the effect of the RF pulses can be accounted for by examining the “effective gradient”. When a π pulse is applied, the phase shift due to the presence of the gradient is flipped. This is equivalent to applying a gradient pulse with the opposite polarity. Therefore, the effective gradient, g^* , can be thought of as gradient pulses required to refocus the signal in the absence of 180° RF pulses, and is represented in the following figure for the RARE sequence.



Effective Gradient

Figure 14 – Representation of the effective gradient, g^* , in the RARE sequence.

Or the effective gradient, $g^*(t)$, can be defined as

- 0 when $0 < t < d$
- $-g_1$ when $d < t < d + \delta_1$
- 0 when $d + \delta_1 < t < d + \delta_1$
- g_2 when $d + \delta_1 < t < 2\tau + \delta_2/2$
- 0 when $2\tau + \delta_2/2 < t < 4\tau - \delta_2/2$
- $-g_2$ when $4\tau - \delta_2/2 < t < 4\tau + \delta_2/2$
- 0 when $4\tau + \delta_2/2 < t < 6\tau - \delta_2/2$
- g_2 when $6\tau - \delta_2/2 < t < 6\tau + \delta_2/2$
- ...
- $-g_2$ when $2n\tau - \delta_2/2 < t < 2n\tau + \delta_2/2$, where n , the number of echoes is even.

Using these facts and imposing the stipulation that $g_1 = g_2 = g$ and $2\delta_1 = \delta_2$, $A(t)$ takes the form

$$A(t) = \exp \left[-D\gamma^2 g^2 \delta_1^2 \left(2(n-1)\tau + \Delta_1 - \frac{(n-1)}{3} \delta_2 \right) \right] \quad (0.18)$$

Therefore, the magnetization at the echo center of the RARE sequence can be described by

$$\frac{M}{M_0} = \exp \left[-D\gamma^2 g^2 \delta_1^2 \left(2(n-1)\tau + \Delta_1 - \frac{(n-1)}{3} \delta_2 \right) \right] \exp \left(\frac{-t}{T_2} \right) \quad (0.19)$$

Where n is the number of echoes. A comparison of this equation to experimental results can be seen in Figure 15 and Figure 16. Water was used as the sample. The blue curve represents the CPMG decay, the green curve is the decay of the RARE profiles at the specified sample location, and the red curve is the calculated behavior.

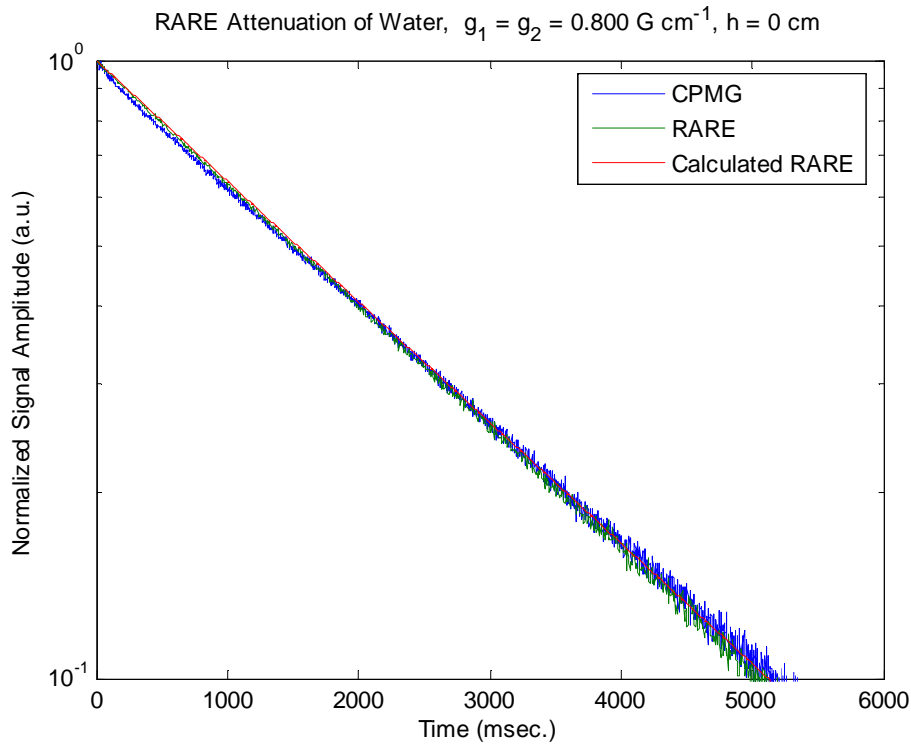


Figure 15 Comparison of CPMG with RARE for $g = 0.8 \text{ G/cm}$

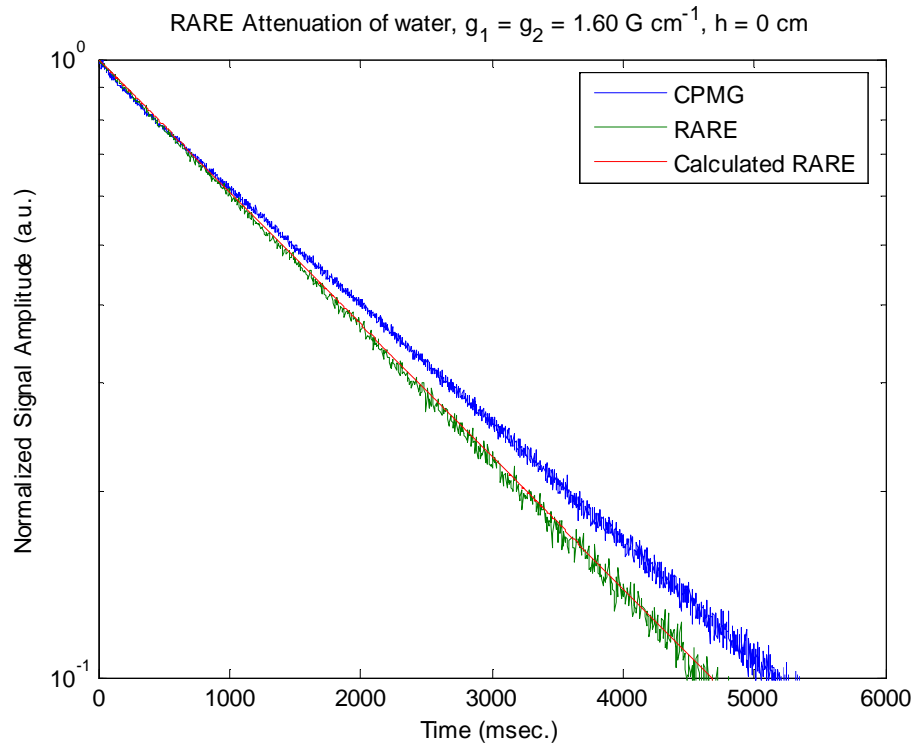


Figure 16 Comparison of CPMG with RARE for $g = 1.6 \text{ G/cm}$

Calculation of T_2

T_2 is estimated using a single exponential fit of the RARE profiles at a specific height within the sample. For instance, the T_2 profile corresponding to the data in Figure 13 is shown below.

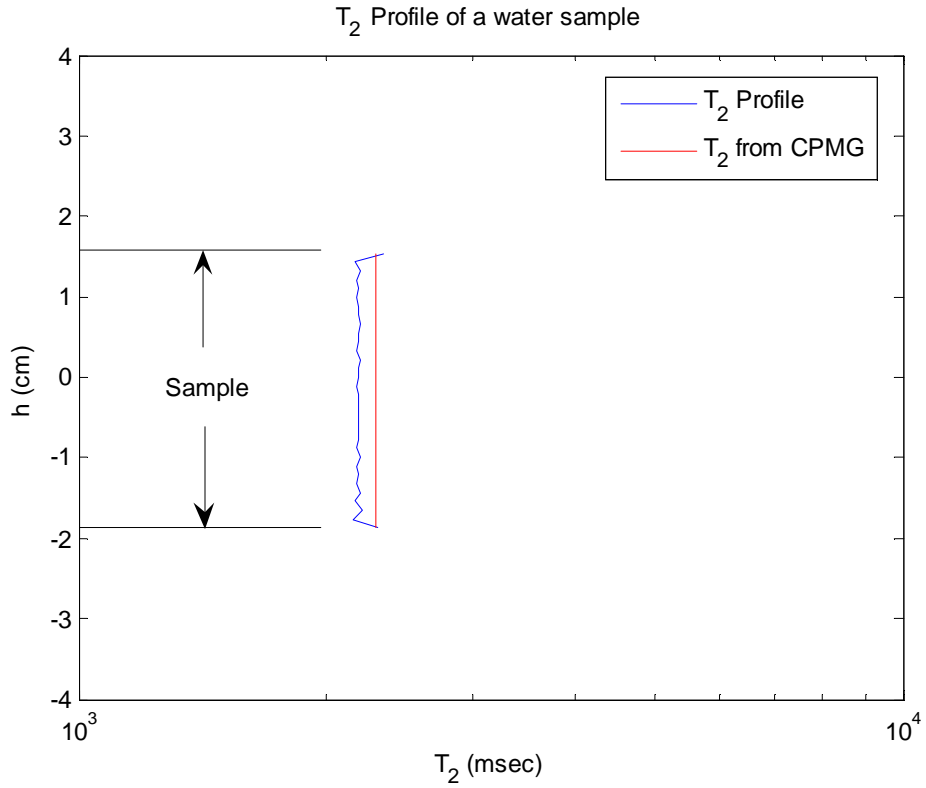


Figure 17 - T₂ profile of a water sample with a height of 4 cm

The T₂ profile of a layered water and squalane sample was also generated via RARE. The series of T₂-weighted images is presented in Figure 18 and the corresponding T₂ profile in Figure 19.

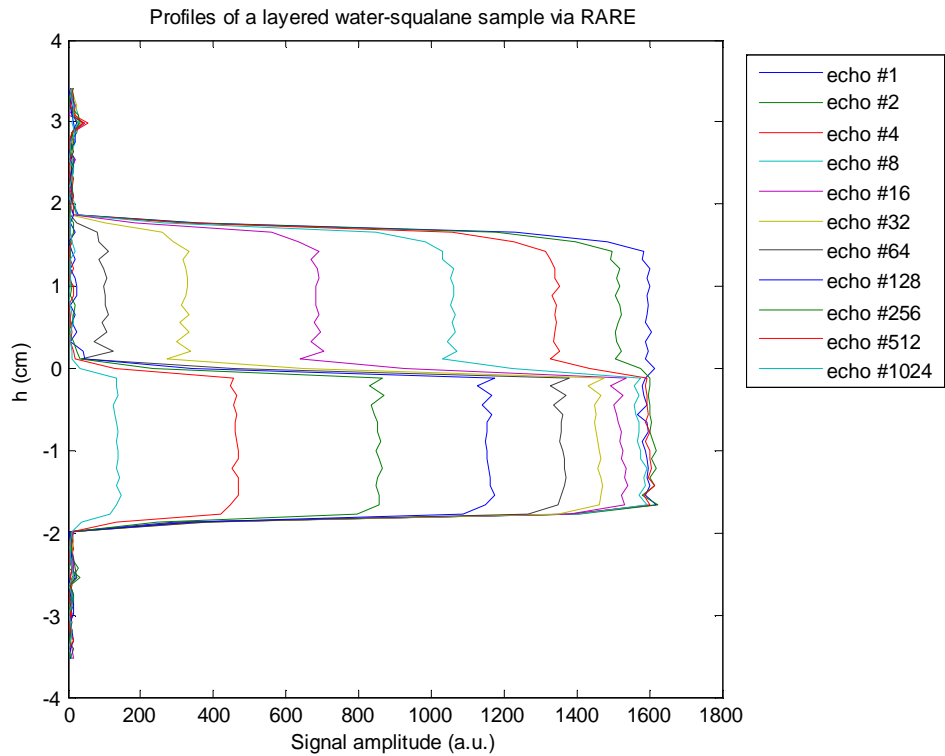


Figure 18 - RARE Profiles of a layered water and squalane sample. Each layer has a height of 2 cm. $g_1 = g_2 = 0.824 \text{ G cm}^{-1}$, $\delta_1 = 1.30 \text{ msec}$, $\tau = 3.00 \text{ msec}$, $DW = 39.0 \text{ msec}$, $SI = 64$

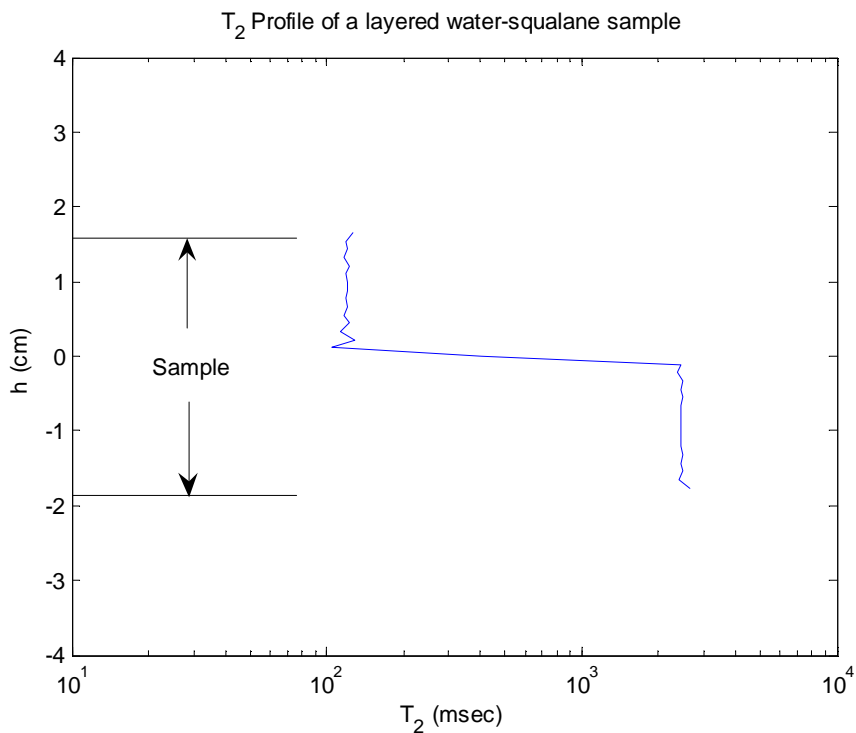


Figure 19 - T_2 profile of layered water and squalane system. Each layer has a height of 2 cm.

Conclusion

In summary, NMR profiling is a valuable tool enabling for the determination of spatial characteristics of a sample. When parameters are properly selected, useful information can be extracted from NMR profiles. These parameters include the gradient strength, dwell time, and the number of acquisition points. The gradient imparts spatial realization upon the measurements, but can also cause attenuation due to diffusion. Therefore, g and δ should be chosen to reduce the effect of relaxation due to diffusion. Also, DW and SI affect the resolution of the 1-D profiles. DW should narrow the range of the measurement to a span which is a little greater than the sample length, and SI will determine the number points over the range set by DW .

Furthermore, by taking advantage of differing relaxation times within a sample, images with different types of contrast, such as spin-density, T_1 -weighted, and T_2 -weighted, can be generated. By comparing several images which have undergone various amounts of relaxation, T_2 can be calculated as a function of time. The rapid acquisition with relaxation enhancement (RARE) pulse sequence can be used to generate multiple profiles each with a different amount of T_2 -weighting. Experiments have been performed with both a water sample and a layered water-squalane system. The results are in good agreement with the expected behavior for the RARE sequence and indicate that this is an effective method for obtaining T_2 profiles.

References

Bernstein, M.A., King, K.F., & Zhou, X.J. (2004). *Handbook of MRI pulse sequences*. Amsterdam: Elsevier Academic Press.

Callaghan, P.T. (1991) *Principles of nuclear magnetic resonance microscopy*. New York: Oxford University Press, Inc.

Henning, J., Nauerth, A., & Friedburg, H. (1986). RARE imaging: A fast imaging method for clinical MR. *Magnetic Resonance in Medicine*, **3**, 823-833.

Liang, Z.P., & Lauterbur, P.C (2000). *Principles of magnetic resonance imaging: A, signal processing perspective*. New York, NY: IEEE Press.

Stejskal, E.O., & Tanner, J.E. (1965). Spin diffusion measurements: Spin-echoes in the presence of a time-dependent field gradient. *The Journal of Chemical Physics*, **42**(1), 288-292.

Torrey, H.C. (1956). Bloch equations with diffusion terms. *Physical Review*, **104**(3), 563-565